Analysis of Optimum Lamb Wave Tuning

by

Yijun Shi

Bachelor of Science, Materials Science
Tongji University, China (1993)

Master of Science, Materials Science
Tongji University, China (1996)

Master of Science, Civil Engineering
Massachusetts Institute of Technology, MA (1998)

Submitted to the Department of Civil and Environmental Engineering
in partial fulfillment of the requirements for the degree of

Doctor of Philosophy in Structures and Materials

at the

MASSACHUSETTS INSTITUTE OF TECHNOLOGY

February 2002

Author .....
Department of Civil and Environmental Engineering
September 17, 2001

Certified by.....
Shi-Chang Wooh
Associate Professor of Civil and Environmental Engineering
Thesis Supervisor

Accepted by
Oral Buyukozturk
Chairman, Department Committee on Graduate Students

Analysis of Optimum Lamb Wave Tuning

by

Yijun Shi

Submitted to the Department of Civil and Environmental Engineering
on September 17, 2001, in partial fulfillment of the
requirements for the degree of
Doctor of Philosophy in Structures and Materials

Abstract

Guided waves are of enormous interest in the nondestructive evaluation of thin-walled structures and layered media. Due to their dispersive and multi-modal nature, it is desirable to tune the waves by discriminating one mode from the others. The objectives of this thesis are (1) to develop schemes and procedures for Lamb wave tuning, (2) to develop tools for understanding and analyzing the mechanism of various tuning techniques, and (3) to provide suggestions and guidelines for selecting optimum tuning parameters.

In order to remedy the inherent problems of traditional tuning techniques using angle wedge and comb transducers (such as the inability to tune the modes with low phase velocities, and the inability to control the propagation direction of tuned waves), a novel dynamic phase tuning concept using phased arrays is proposed. In this approach, the constructive interference of desired modes is achieved by properly adjusting the time delays. As an extension to this concept, the *synthetic phase tuning* (SPT) scheme is introduced, in which the tuning effect is achieved by constructing virtual waves. The effectiveness of SPT against other techniques is experimentally demonstrated, which shows its feasibility.

To understand the mechanism of tuning, an analytical model is developed to study transient waves, based on the Fourier integral transform method. The excitation conditions for both angle wedge and array transducers are taken into account. The surface displacements of individual modes and their temporal and spatial Fourier spectrum are derived and used to study the tuning behavior. The analytical results are compared with the experimental results as well as the numerical results obtained from the finite element simulation studies.

In dealing with broadband signals, laser generated Lamb waves are investigated. Both line and circular source loading models are developed to study the behavior in the ablation regime. The predicted waveforms and dispersion curves are in good agreement with the experimental results. Based on the same SPT scheme, virtually-tuned waves are constructed by processing a set of broadband signals.

Finally, Lamb waves in a transversely isotropic composite plate are investigated. Although the analysis is limited only to the waves propagating in the principal directions, it could serve as the basis for future work on tuning of Lamb waves in composites.

It is concluded from this thesis that the SPT method enjoys advantages over

other methods including its low operation cost, ability to tune the modes of low phase velocities, and capability to control the propagation direction of tuned waves. The analysis of transient waves allows us to examine various tuning scenarios. The investigation of the tuning effectiveness enables us to select optimum modes for the given conditions.

Thesis Supervisor: Shi-Chang Wooh
Title: Associate Professor of Civil and Environmental Engineering

Acknowledgments

I would sincerely like to thank Prof. Shi-Chang Wooh for continuously advising my research at the Massachusetts Institute of Technology. It is his keen insight and unlimited enthusiasm that makes this thesis eventually possible. His rigorous attitude towards research is a good source to benefit my whole life.

I am indebted to Profs. Jerome Connor, Kevin Amaratunga, and Franz-Josef Ulm for their precious advice on my research. The encouragement from Profs. Chiang C. Mei and Oral Buyukozturk is also very much appreciated.

I am grateful to Joonsang Park for providing remarkable discussions on the wave propagation theory, and Ji-Yong Wang and Mark Orwat for offering invaluable assistance to my experimental work.

It has been a rewarding and enjoyable experience to work with the former and current graduate students of the Nondestructive Evaluation Laboratory, namely Arthur Clay, Kecheng Wei, Casey Kim, Lawrence Azar, Quanlin Zhou, Jung-Wuk Hong, Mark Orwat and Ji-Yong Wang.

The financial support from the Korean Highway Corporation (KHC) and National Science Foundation (NSF) is highly acknowledged.

Finally, I would like to thank my wife and parents, whose love, passion, and patience are very crucial to my work. I owe them a lot for their whole-hearted support.

Contents

List of Figures

List of Tables

Chapter 1

Introduction

1.1 Conventional Ultrasonic Techniques

Nondestructive evaluation (NDE) has been recognized as an indispensable and powerful tool for the inspection of a broad range of structures and materials from the aerospace industry to civil infrastructure. Among the various NDE techniques, ultrasonic methods are perhaps the most robust and flexible methods available. They play an important role in the flaw detection and material characterization. In ultrasonic testing, elastic waves are impinged into the structure and the response is measured, using transducers made of piezoelectric material. The integrity of the structure is then assessed by analyzing the response.

Common waves used in ultrasonic testing are bulk waves, e.g., *longitudinal* (L or P) and *transverse* (T or S) waves [1]. In some inspection cases, Rayleigh surface waves are also utilized.

There are two basic types of transducers commonly used in NDE: *straight beam transducers* and *angle wedge transducers.* A straight beam transducer impinges longitudinal waves at normal incidence to the material; an angle wedge transducer impinges incident waves through a wedge to produce refracted longitudinal and transverse waves propagating in the material.

There are three types of common operation configurations: (1) *pulse-echo*: a single transducer acts as both transmitter and receiver, (2) *through-transmission*: a pair of

transducers are positioned on opposite sides of each other, acting as transmitter and receiver, respectively, (3) *pitch-catch*: a pair of transducers are situated on the same side of the material, acting as transmitter and receiver, respectively.

Material flaws are typically presented in three forms: A-scan, B-scan, and C-scan [1]. An A-scan is an amplitude-time display. A B-scan is an image representing the cross-sectional view, which is obtained from a set of A-scans along a line. A C-scan image shows a planar view of the material and flaws, which is obtained by scanning over an area of interest.

Traditional ultrasonic NDE techniques have been effectively used for inspecting bulk materials or assessing materials in the thickness direction. The primary advantage of using such techniques is the easy interpretation of signals since bulk wave signals do not change their shape as they propagate in acoustic media. As an example, Fig. 1.1(a) shows a typical ultrasonic signal obtained from the normal incident pulse-echo testing of an aluminum specimen, which exhibits multiple echoes traveling back and forth in the specimen. Measuring the thickness is relatively simple so long as the echoes are clearly separable.

However, these traditional ultrasonic techniques are limited to monitoring local areas. It is very time consuming and cumbersome to use such techniques for inspecting large-scale structures. Guided wave techniques are among the techniques developed to address this problem.

1.2 Guided Wave Techniques

Guided waves refer to the waves propagating in bounded media. One of the greatest merits of guided waves is that they can travel long distances along the plane of the members. Hence, with guided waves, the entire thickness of the plate is interrogated, instead of only that of a single point on the surface. This implies that guided waves are able to interact with both surface and internal defects. Thus, a significant amount of inspection time can be saved, thanks to the merits of guided waves.

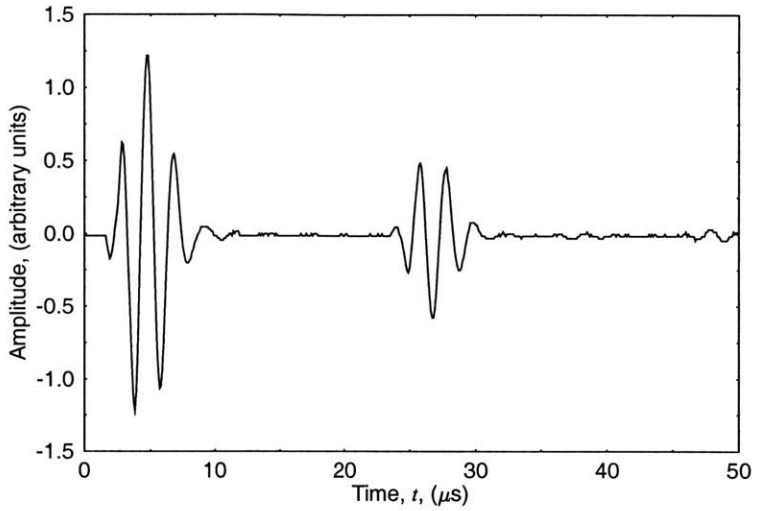

(a)

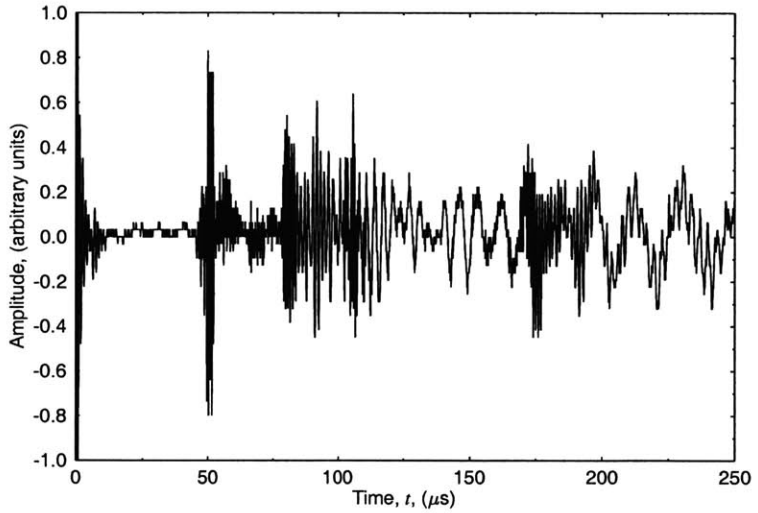

(b)

Figure 1.1: One typical signal of (a) longitudinal waves, where the signal comes from the multiple reflection from an aluminum block back face, and (b) guided (Lamb) waves, where the signal is laser-generated in an aluminum plate.

Compared with bulk waves, guided waves provide a very attractive solution for the assessment of large structures consisting of thin or slender members, such as pipes, shells, membranes, rods, plate girders, slabs and even multilayered structures. Considering the abundance of such structures, the importance of these techniques can not be over-emphasized. Some examples of the numerous works on guided wave NDE include the detection of defects in boiler and heat exchange pipings [2], spot welds [3], bridge girders [4], long steel pipes [5], aircraft components [6], etc. Guided waves are also used in determining the elastic properties of composite materials [7–12].

Lamb waves are a special form of guided waves, propagating in a solid plate with traction-free boundaries, which result in the interference of multiple reflections and mode conversion of longitudinal waves and transverse waves at the plate surface. The wave propagation in bounded structures is governed by the well-known Rayleigh-Lamb dispersion relations [13, 14]. Understanding the complicated propagation mechanism of Lamb waves is vital to their application.

Interpretation of guided wave signals is complicated by the two fundamental natures of guided waves: dispersion and multi-modality. Due to the dispersion, wave shapes change during the propagation. Furthermore, there are an infinite number of wave modes, categorized into two different groups: (1) longitudinal plate waves having symmetric displacements, and (2) flexural plate waves having antisymmetric displacements with respect to the center of the plane [13,14]. For example, Fig. 1.1(b) shows a typical ultrasonic wave propagating in a thin plate, generated and detected by laser sources separated by a distance. The signal consists of two events: one arrived directly from the generation point to the detection point on the specimen, and the other that is reflected from a discontinuity and returned to the detection point. The signal clearly shows that the dispersive and multi-modal nature of guided waves. It will be difficult to analyze such signals.

In dealing with guided waves, signals of different spectral characteristics can be used: broadband and narrowband signals. Broadband pulses contain rich information over a wide range of frequencies [15]. However, such signals are often complicated and difficult to analyze. This makes it unwieldy to utilize guided waves with con-

ventional pulse-echo or pitch-catch setups, particularly for broadband transducers. Despite these complications, there are several tools available for analyzing the dispersion of broadband signals, e.g., the two-dimensional Fourier transform (2-D FT) technique [16–18], pseudo-Wigner-Ville distribution method [19], reassigned spectrogram method [20], and the wavelet transform method [21]. These techniques, which manipulate the data in the transformation domain, are powerful, but they often give erroneous results in certain frequency ranges and are also quite sensitive to the given signal processing parameters.

On the other hand, the narrowband signal approach enables the processing of Lamb waves directly in the time domain. In this case, the dispersion effect is reduced and the waves may retain their shape as they propagate in the medium. However, due to the existence of multiple modes (with different velocities) even for a single frequency, it is mandatory to distinguish one desired mode from the coexisting modes. This technique is called "tuning" of Lamb wave modes. With mode tuning, the pitch-catch and pulse-echo setups may find practical applications in Lamb wave inspection. By measuring the time-of-flight (TOF) of the tuned wave, Lamb waves can be easily interpreted to detect flaws in structural members. Hence, investigation of tuning techniques is important for the proper applications of Lamb waves, which is one of the main objectives of this thesis work.

The tuning effect is normally achieved using either angle wedge transducers [13,17] or comb transducers [13, 22]. These approaches are based on similar physical mechanisms, in that both of them are to enhance the mode(s) of interest and suppress the other modes, despite that they are implemented in different ways. The angle wedge transducer approach is simple but less capable than the comb transducer approach. However, when operated properly, angle wedge transducers may allow for long-distance inspection of thin members.

Although these methods work in principle, their inherent limitations make it difficult to meet the requirements for effective tuning. The drawbacks of angle wedge transducers include (1) inability to tune all the modes, (2) sensitivity to the misalignment of incident angles, and (3) numerous interfaces in the wedge assembly reducing

the inspection zone and signal transmission efficiency. The major problems associated with the comb transducer tuning are that the wave propagation direction is not controllable and that the transducer cannot be used effectively as receiver.

1.3 Objectives

This research is motivated by the need to develop effective ultrasonic techniques for assessing large thin-walled structures. The objectives are summarized into three aspects:

- to develop schemes and procedures for Lamb wave tuning;
- to develop tools for understanding and analyzing the mechanism of various tuning techniques;
- to provide suggestions and guidelines for selecting optimum tuning parameters.

1.4 Thesis Structure

This thesis consists of 10 chapters. An overview of the thesis structure is as follows:

- Chapter 1 outlines the objectives of the research. The traditional ultrasonic NDE techniques are reviewed, and their limitations are pointed out. Then the guided (Lamb) wave techniques are introduced. The importance of wave mode tuning is highlighted. The problem associated with current Lamb wave tuning techniques are briefly reviewed, followed by the objectives of the thesis. Finally, the thesis structure is outlined.
- Chapter 2 provides the readers with the fundamentals of Lamb waves necessary for understanding the concepts in subsequent chapters. The equations of motion in acoustic media are reviewed. The concepts of phase and group velocities are introduced to understand the dispersion of elastic waves. The wave propagation in plates with free boundaries is reviewed, which gives rise to the Rayleigh-Lamb

dispersion equations. Dispersion curves for an aluminum plate are constructed to illustrate the dispersive and multi-modal nature of Lamb waves, from which the significance of mode tuning is emphasized.

- Chapter 3 presents the various tuning techniques of Lamb waves. The traditional angle wedge and comb transducer tuning techniques are introduced first. Their principles of wave mode tuning are explained, and their limitations are summarized. In order to remedy the drawbacks, an innovative approach – *phased array tuning* technique is proposed. The principle of mode tuning is explained, the background of phased arrays is reviewed, and the phased array system development is introduced. Experimental work is done using this new technique. While certain wave modes have been successfully tuned, the limitations of this technique are pointed out — delay circuits are expensive and the signal bandwidth is not easy to control. This gives rise to the brief remarks on another phase tuning technique using array transducers — *synthetic phase tuning* which will be described in Chapter 4.

- Chapter 4 studies the synthetic phase tuning technique. The principle of this technique is introduced, in which numerical time delays are provided to array elements. The operational schemes for the synthetic phase tuning, including the pseudo pitch-catch (PPC) and pseudo pulse-echo (PPE) setups are introduced. The construction of virtually tuned waves is described for the PPE scheme, including the signal generation and recording, synthetic construction of emitting waves, synthetic construction of receiving waves, and real-time reconstruction of synthetic signals. Experimental results on the PPE testing are obtained to demonstrate the effectiveness of this new technique as compared to the other tuning techniques. It is also observed that some wave modes are tuned well while some are not. This demands a quantitative study of the transient response of Lamb waves in a plate subject to external loadings.

- In Chapter 5, a theoretical model is developed to analyze the transient response of an elastic plate to external loadings, using an integral transform method.

Analytical expressions are derived for computing the Lamb wave displacements and their 2-D FTs. The physical meaning of the overall and modal excitation efficiencies is enunciated. The effect of loading conditions is investigated using a Gaussian spike pulse of different bandwidths to demonstrate the possibility of wave mode selection. Finally, the analytical results are compared with those obtained from the finite element simulation studies, and an excellent agreement is observed. The analytical model of transient Lamb waves described in this chapter is the basis for quantitatively examining the angle beam transducer tuning, array transducer tuning and laser generation of Lamb waves.

- Chapter 6 examines quantitatively the tuning mechanism of angle wedge transducers, based on the analytical model in Chapter 5. The theoretical model is applied by taking into account the excitation conditions for both straight beam and angle wedge transducers. The tuning effect of angle wedge transducers against straight beam transducers is theoretically demonstrated through the 2-D FTs and waveforms. Experimental waveforms from both the straight beam and angle wedge transducer excitation are obtained. Consistency is observed between the experimental observations and theoretical predictions.

- Chapter 7 examines quantitatively the synthetic phase tuning technique proposed and experimentally validated in Chapter 4, using the analytical model in Chapter 5. Based on the formulation results of single element excitation, the phase-tuned Lamb wave displacements and their 2-D FTs are derived for the *half-way tuning* (array as transmitter) and *full tuning* (arrays as both transmitter and receiver) operated in the PPC scheme, using the superposition principle. Theoretical examples are given to illustrate the tuning effect for the half-way tuning and full tuning in both the frequency-wavenumber domain (2-D FT) and time domain (waveform). It is shown that the tuning effect is improved from the half-way tuning to full tuning. Experimental waveforms are obtained, and compared with theoretical predictions for the half-way tuning, and a good agreement is observed.

- Chapter 8 examines quantitatively the laser generation of (broadband) Lamb waves. An analytical model is proposed to study the propagation of transient waves originated from a circular source. Solutions for the wave mode displacements are obtained using the Fourier and Hankel transform. The loading conditions are prescribed to represent the line and circular sources. Predicted waveforms based on the line source loading model are analyzed using the group dispersion curves and 2-D FT of displacements. Laser-generated Lamb waves in an aluminum plate are obtained and compared with the predicted waveforms due to the line and circular source loadings. Also, the experimental dispersion curves (2-D FFT) are constructed and compared with the theoretical dispersion curves (2-D FT). The SPT scheme is applied to a set of laser-generated signals to construct virtually tuned waves. Excellent agreement is observed between experimental and theoretical results. It is shown that both the line and circular source loading models are valid for lasers in the ablation regime, and the line source model enables the link between the theoretical dispersion curves and experimental dispersion curves. Also shown is that it is feasible to tune laser-generated Lamb waves.

- Chapter 9 initially investigates the transient Lamb waves in transversely isotropic composite plates. This is intended to serve as a basis for the future study of Lamb wave tuning in composites. To help understand the principle of ultrasonic measurement of elastic constants, the propagation of plane (bulk) waves in the composite principal directions is reviewed first, which results in the relationship between the wave velocities and the 3 out of totally 5 elastic constants (the remaining 2 constants can be determined using Lamb waves). The dispersion equations of Lamb waves in the principal directions are then introduced, and sample dispersion curves are constructed. Using an integral transform method, transient waves in the principal directions of composite plates subjected to arbitrary external loadings are analyzed. Analytical expressions are derived for the Lamb wave displacements and their 2-D FTs. Laser-generated Lamb waves

in the principal directions are also obtained. It is observed that only A_0 and S_0 modes of low frequency exist. Experimental dispersion curves are also obtained and compared with theoretical ones.

- Chapter 10 summarizes the research work and draws conclusions. Recommendations are given regarding future study of Lamb wave reflection from discontinuities, influence of the laser beam size, tuning of Lamb waves in composites, etc.

Chapter 2

Wave Propagation in Elastic Plates

2.1 Introduction

Lamb waves represent one of the types of normal or plate modes in an elastic waveguide with free boundaryies. For a given plate thickness and frequency, there are many propagation modes which are grouped into two fundamental families: symmetric modes and antisymmetric modes. Each mode is associated with an infinite number of orders. This characteristic distinguishes Lamb waves from bulk waves. Besides plates, other examples of waveguides include rods, cylindrical shells, and layered elastic solids. In this research, only the plate waveguide is considered.

The mechanism of Lamb wave generation can be explained as follows [23]. A plate is considered as a half space bounded by a second boundary parallel to the other surface. One can imagine that longitudinal (P), vertically polarized transverse (SV) and horizontally polarized transverse (SH) waves are reflected back and forth from one boundary to the other. Generally, the P and SV waves undergo mode conversion at each reflection, and progress along the plane of the plate. The neighboring parallel boundaries are in effect guiding the waves along the plate.

The investigation of harmonic wave propagation in an elastic plate dates back to the initial work by Rayleigh [24] and Lamb [25] over one century ago. The dispersion relations were obtained for the symmetric and antisymmetric modes, and are often refered to as the Rayleigh-Lamb dispersion equations. Later, Lamb investigated the

SH waves whose particle displacements are polarized parallel to the surface of the plate [26]. However, the detailed analysis of the Rayleigh-Lamb dispersion relations was not well established until the investigation work by Mindlin and his colleagues in the 1950s [27], which included the thorough enunciation of the real, imaginary and complex branches of the equations. Detailed theoretical and experimental work on Rayleigh and Lamb waves was conducted by Viktorov [13]. For the problem of Lamb wave propagation in anisotropic plates, Solie and Auld [28] introduced the partial wave or transverse resonance technique. The investigation of Lamb wave propagation in composites was performed by Datta [29], Nayfeh [30] and many others.

In the following, the background of Lamb waves will be introduced. The equations of motion in acoustic media are reviewed first. The concept of dispersion is then illustrated along with those of the phase and group velocities. Afterwards, the Rayleigh-Lamb dispersion relations are derived by applying the traction-free boundary conditions to the equations of motion. Finally, the dispersion relations are interpreted along with the dispersion curves. Note that this chapter only gives a brief introduction about the wave propagation in plates. The detailed knowledge on guided waves in elastic plates can be found in the reference books by Viktorov [13], Graff [14], Miklowitz [23], Auld [31], Achenbach [32], and Rose [33].

2.2 Equations of Motion in Acoustic Media

The theory of elasticity for a homogeneous, isotropic elastic solid may be summarized using the Cartesian tensor notation as the stress equations of motion, Hooke's law and the strain-displacement relations:

$$\sigma_{ij,j} + \rho f_i = \rho \ddot{u}_i \tag{2.1}$$

$$\sigma_{ij} = \lambda \varepsilon_{kk} \delta_{ij} + 2\mu \varepsilon_{ij} \tag{2.2}$$

$$\varepsilon_{ij} = \frac{1}{2}(u_{i,j} + u_{j,i}) \ , \tag{2.3}$$

where σ_{ij} and ε_{ij} are the stress and strain tensors, and u_i is the displacement vector. ρ is the mass density, f is the body force per unit mass, λ and μ are the Lamé constants, and δ_{ij} is the Kronecker delta defined as

$$\delta_{ij} = \begin{cases} 1, & \text{for } i = j \\ 0, & \text{for } i \neq j \ . \end{cases} \tag{2.4}$$

The displacement equations of motion are obtained by substituting the strain-displacement relations, Eq. (2.3), into Hooke's law, Eq. (2.2), and subsequently substituting the stresses into the stress equations of motion, Eq. (2.1), as

$$(\lambda + \mu)u_{j,ji} + \mu u_{i,jj} + \rho f_i = \rho \ddot{u}_i \ , \tag{2.5}$$

which are also known as Navier's equations. The equivalent vector form of this expression is

$$(\lambda + \mu)\nabla\nabla \cdot \mathbf{u} + \mu\nabla^2\mathbf{u} + \rho\mathbf{f} = \rho\ddot{\mathbf{u}} \ . \tag{2.6}$$

In the absence of body forces, the equation can be rewritten as

$$(\lambda + \mu)\nabla\nabla \cdot \mathbf{u} + \mu\nabla^2\mathbf{u} = \rho\ddot{\mathbf{u}} \ . \tag{2.7}$$

Using the vector identity

$$\nabla^2\mathbf{u} = \nabla\nabla \cdot \mathbf{u} - \nabla \times \nabla \times \mathbf{u} \ , \tag{2.8}$$

the equation of motion can be alternatively expressed as

$$(\lambda + 2\mu)\nabla\nabla \cdot \mathbf{u} - \mu\nabla \times \nabla \times \mathbf{u} = \rho\ddot{\mathbf{u}} \ . \tag{2.9}$$

The equation of motion may be further represented in a simpler form. The vector displacement $\mathbf{u}$ can be expressed via Helmholtz decomposition as the gradient of a

scalar and the curl of the zero divergence vector

$$\mathbf{u} = \nabla\phi + \nabla \times \mathbf{\Psi} \,, \quad \text{and} \quad \nabla \cdot \mathbf{\Psi} = 0 \,, \tag{2.10}$$

where ϕ and $\mathbf{\Psi}$ are the scalar and vector potentials, respectively. By substituting Eq. (2.10) into the Navier's equation of motion, Eq. (2.7), we obtain

$$(\lambda + \mu)\nabla\nabla \cdot (\nabla\phi + \nabla \times \mathbf{\Psi}) + \mu\nabla^2(\nabla\phi + \nabla \times \mathbf{\Psi}) = \rho\left(\nabla\frac{\partial^2\phi}{\partial t^2} + \nabla \times \frac{\partial^2\mathbf{\Psi}}{\partial t^2}\right) . \tag{2.11}$$

In view of the following identities

$$\nabla \cdot \nabla\phi = \nabla^2\phi \,; \quad \nabla \times \nabla \times \nabla\phi = 0 \,; \quad \nabla \cdot \nabla \times \mathbf{\Psi} = 0 \,, \tag{2.12}$$

we have the following equation

$$\nabla\left[(\lambda + 2\mu)\nabla^2\phi - \rho\frac{\partial^2\phi}{\partial t^2}\right] + \nabla \times \left[\mu\nabla^2\mathbf{\Psi} - \rho\frac{\partial^2\phi}{\partial t^2}\right] = 0 \,, \tag{2.13}$$

which will be satisfied if each bracketed term vanishes. This leads to the decomposed equations

$$\nabla^2\phi = \frac{1}{c_L^2}\frac{\partial^2\boldsymbol{\phi}}{\partial t^2} \tag{2.14}$$

$$\nabla^2\mathbf{\Psi} = \frac{1}{c_T^2}\frac{\partial^2\mathbf{\Psi}}{\partial t^2} \,, \tag{2.15}$$

where c_L and c_T are the longitudinal (primary, dilatational, compression) and transverse (secondary, distortional, shear) wave velocities, respectively given as

$$c_L = \sqrt{\frac{\lambda + 2\mu}{\rho}} \,, \qquad c_T = \sqrt{\frac{\mu}{\rho}} \,. \tag{2.16}$$

It can be seen that the components ψ_x, ψ_y, ψ_z of the vector potential $\mathbf{\Psi}$ satisfy the equations

$$\nabla^2\psi_x = \frac{1}{c_T^2}\frac{\partial^2\psi_x}{\partial t^2}\ ; \quad \nabla^2\psi_y = \frac{1}{c_T^2}\frac{\partial^2\psi_y}{\partial t^2}\ ; \quad \nabla^2\psi_z = \frac{1}{c_T^2}\frac{\partial^2\psi_z}{\partial t^2}\ . \tag{2.17}$$

Thus, the wave equations can be written in terms of the potentials ϕ, ψ_x, ψ_y, ψ_z as

$$\frac{\partial^2\phi}{\partial x^2} + \frac{\partial^2\phi}{\partial y^2} + \frac{\partial^2\phi}{\partial z^2} = \frac{1}{c_L^2}\frac{\partial^2\phi}{\partial t^2} \tag{2.18}$$

$$\frac{\partial^2\psi_x}{\partial x^2} + \frac{\partial^2\psi_x}{\partial y^2} + \frac{\partial^2\psi_x}{\partial z^2} = \frac{1}{c_T^2}\frac{\partial^2\psi_x}{\partial t^2} \tag{2.19}$$

$$\frac{\partial^2\psi_y}{\partial x^2} + \frac{\partial^2\psi_y}{\partial y^2} + \frac{\partial^2\psi_y}{\partial z^2} = \frac{1}{c_T^2}\frac{\partial^2\psi_y}{\partial t^2} \tag{2.20}$$

$$\frac{\partial^2\psi_z}{\partial x^2} + \frac{\partial^2\psi_z}{\partial y^2} + \frac{\partial^2\psi_z}{\partial z^2} = \frac{1}{c_T^2}\frac{\partial^2\psi_z}{\partial t^2}\ . \tag{2.21}$$

Also, from Eq. (2.10), the displacement components u_x, u_y and u_z can be related to the potentials as

$$u_x = \frac{\partial\phi}{\partial x} + \frac{\partial\psi_z}{\partial y} - \frac{\partial\psi_y}{\partial z} \tag{2.22}$$

$$u_y = \frac{\partial\phi}{\partial y} - \frac{\partial\psi_z}{\partial x} + \frac{\partial\psi_x}{\partial z} \tag{2.23}$$

$$u_z = \frac{\partial\phi}{\partial z} + \frac{\partial\psi_y}{\partial x} - \frac{\partial\psi_x}{\partial y}\ . \tag{2.24}$$

2.3 Dispersion of Elastic Waves

The same governing equations shown above, are also be used in investigating the propagation of waves in plates. Dispersion is one of the most important features of Lamb waves. Thus, before we go to the detail of Lamb waves, it is worthwhile to introduce the general concept of dispersion.

The concept of dispersion can be well explained by introducing the concepts of phase velocity and group velocity. As we will see, these two properties play an

important role in the context of wave dispersion, especially for the analysis of wave propagation in an elastic plate.

2.3.1 Phase Velocity

Consider a typical harmonic wave traveling in a medium. The longitudinal displacement is then expressed as

$$u(x,t) = A\cos[k(x-ct)] = A\cos(kx-\omega t)\ , \tag{2.25}$$

where the amplitude A is independent of the space x and time t, and the term $k(x-ct)$ is the phase of the wave. For increasing values of time t, increasing values of x are required to maintain a constant phase. The propagation velocity of this constant phase is c, which is defined as the *phase velocity*[1].

2.3.2 Group Velocity

In contrast to the phase velocity, group velocity is associated with the propagation of a group of wave packets. Consider two propagating harmonic waves of the same amplitudes but slightly different frequencies, i.e.,

$$\begin{aligned} u_1(x,t) &= A\cos(k_1x-\omega_1t) \\ u_2(x,t) &= A\cos(k_2x-\omega_2t)\ . \end{aligned} \tag{2.26}$$

The superposition of the displacements yields the total displacement

$$u(x,t) = 2A\cos\left(\frac{k_1-k_2}{2}x-\frac{\omega_1-\omega_2}{2}t\right)\cos\left(\frac{k_1+k_2}{2}x-\frac{\omega_1+\omega_2}{2}t\right)\ . \tag{2.27}$$

[1] In the following we designate c_p as the phase velocity to distinguish it from the group velocity.

By introducing the following definitions

$$\Delta k = \frac{k_1 - k_2}{2}, \qquad \Delta\omega = \frac{\omega_1 - \omega_2}{2} \tag{2.28}$$

$$k = \frac{k_1 + k_2}{2}, \qquad \omega = \frac{\omega_1 + \omega_2}{2}, \tag{2.29}$$

Eq. (2.27) can be rewritten as

$$u(x,t) = 2A \underbrace{\cos(\Delta k x - \Delta\omega t)}_{\text{lower frequency}} \underbrace{\cos(kx - \omega t)}_{\text{higher frequency}}, \tag{2.30}$$

where $\cos(\Delta kx - \Delta\omega t)$ is the term containing the lower frequency and $\cos(kx - \omega t)$ is the term containing the higher frequency. As shown in Fig. 2.1, what we obtain is a wave system oscillating at a frequency $(\omega_1 + \omega_2)/2$ which is very close to the frequency of either component but with a maximum amplitude of $2A$, modulated in space and time by a very slowly varying envelope of frequency $(\omega_1 - \omega_2)/2$ and wavenumber $(k_1 - k_2)/2$.

Note that the higher frequency term, $\cos(kx - \omega t)$, propagates at the phase velocity $c_p = \omega/k$, while the lower frequency term $\cos(\Delta kx - \Delta\omega t)$ moves at a velocity, defined as

$$c_g = \frac{\Delta\omega}{\Delta k}. \tag{2.31}$$

This velocity is referred to as the *group velocity*, The modulation imposed on the carrier results in the creation of groups traveling at the group velocity c_g. In the limit, the group velocity approaches

$$c_g = \frac{d\omega}{dk}. \tag{2.32}$$

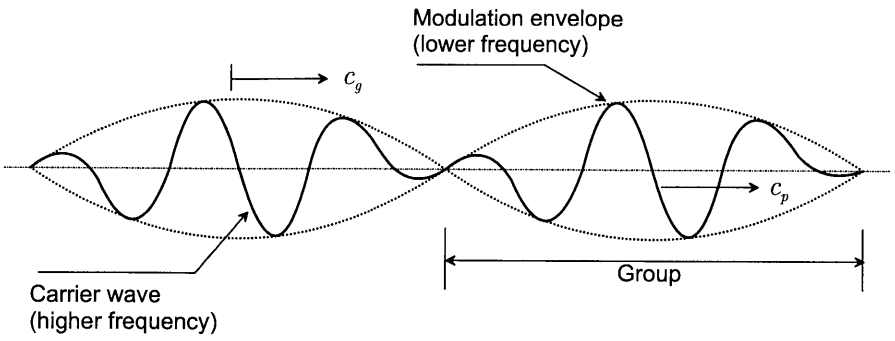

Figure 2.1: The superposition of two harmonic waves of slightly different frequencies, ω_1 and ω_2, forms a wave packet. The faster oscillation occurs at the average frequency of the two components $(\omega_1 + \omega_2)/2$ and the slowly varying group envelope has a frequency equal to half the frequency difference between the components $(\omega_1 - \omega_2)/2$.

Up to npow, the superposition of two harmonic waves are considered. However, any number of waves with similar frequency can also be considered, in which

$$u(x,t) = \sum_{i=1}^{n} A\cos(k_i x - \omega_i t) \ , \tag{2.33}$$

where the frequency ω_i and wavenumber k_i differ slightly from one wave to another.

From the definitions, we can obtain the following relationship

$$c_g = \frac{d(kc_p)}{dk} = c_p + k\frac{dc_p}{dk} \ . \tag{2.34}$$

By virtue of the relationship, $\lambda = 2\pi/k$, an alternative form of group velocity is obtained as

$$c_g = c_p - \lambda\frac{dc_p}{d\lambda} \ . \tag{2.35}$$

2.3.3 Dispersion Relation

A medium is called dispersive if the phase velocity is frequency dependent (i.e., ω/k not constant); the dispersion relation expresses the variation of ω as a function of k. Understanding dispersion is important because it governs the change of shape of a

pulse as it propagates through a dispersive medium. Dispersion occurs not only in inelastic bodies but also in elastic waveguides. Figure 2.2 schematically illustrates

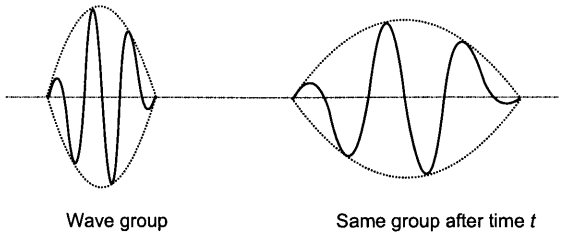

Figure 2.2: A wave group showing the dispersion after a certain time t.

the change of the wave shape after some travel time t in a dispersive medium.

The comparison of the group velocity, and the phase velocity gives rise to three different conditions

- Normal dispersion ($c_g < c_p$) : the carrier waves appear behind the group, travel to the front, and disappear.
- No dispersion ($c_g = c_p$) .
- Anomalous dispersion ($c_g > c_p$) : the carrier waves appear ahead of the group, travel to the rear, and then disappear.

The dispersion relations of these conditions are illustrated in Fig. 2.3.

2.4 Wave Propagation in an Infinitely Long Plate

Elastic waves in an infinitely long plate have the same governing equations of motion as those in a full space, yet with free boundary conditions. In this section, the method of displacement potentials is reviewed to obtain the solutions.

2.4.1 Rayleigh-Lamb Dispersion Equations

Consider a plane harmonic wave propagating in a homogeneous elastic plate of thickness $2h$ and of infinite in-plane dimensions, as shown in Fig. 2.4. Since the plate is

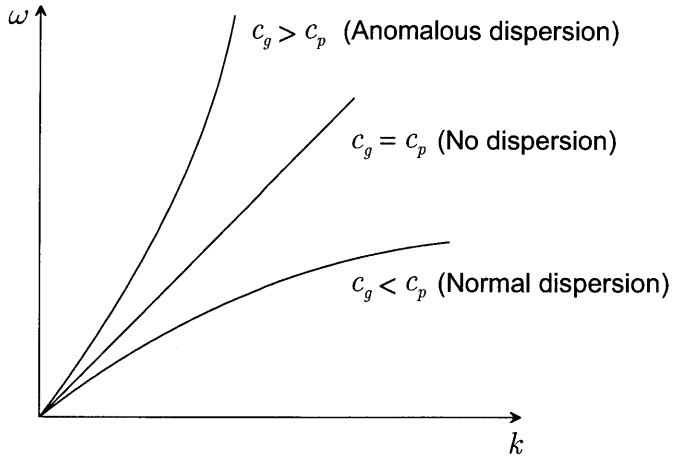

Figure 2.3: Curves illustrating dispersion: (a) a straight line representing a non-dispersive medium, $c_g = c_p$; (b) a normal dispersion relation where $c_g < c_p$; (c) an anomalous dispersion relation where $c_g > c_p$.

considered to be traction free, the boundary conditions would be written as

$$\sigma_{zz} = \sigma_{xz} = 0 \tag{2.36}$$

at the top and bottom surfaces ($z = \pm h$). In the case of plane strain in the xz plane, we have the conditions

$$u_y = 0\,, \quad \frac{\partial}{\partial y} = 0\,. \tag{2.37}$$

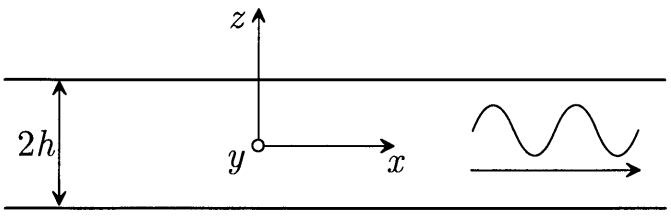

Figure 2.4: Propagation of a plane harmonic wave in a plate of thickness $2h$.

The Helmholtz decomposition of the displacement vector as shown in Eq. (2.10) is reduced to the equations

$$u_x = \frac{\partial \phi}{\partial x} - \frac{\partial \psi}{\partial z} \tag{2.38}$$

$$u_z = \frac{\partial \phi}{\partial z} + \frac{\partial \psi}{\partial x} , \tag{2.39}$$

where the subscript y has been omitted from ψ for simplicity. Since the wave motion in the y axis is not considered, the vector potential $\mathbf{\Psi}$ has a nonzero magnitude in that direction.

Also, from Hooke's law, the stress components σ_{xx}, σ_{zz} and σ_{xz} can be expressed in terms of ϕ and ψ as

$$\sigma_{xx} = \lambda \left(\frac{\partial^2 \phi}{\partial x^2} + \frac{\partial^2 \phi}{\partial z^2} \right) + 2\mu \left(\frac{\partial^2 \phi}{\partial x^2} - \frac{\partial^2 \psi}{\partial x \partial z} \right) \tag{2.40}$$

$$\sigma_{zz} = \lambda \left(\frac{\partial^2 \phi}{\partial x^2} + \frac{\partial^2 \phi}{\partial z^2} \right) + 2\mu \left(\frac{\partial^2 \phi}{\partial z^2} + \frac{\partial^2 \psi}{\partial x \partial z} \right) \tag{2.41}$$

$$\sigma_{xz} = \mu \left(2\frac{\partial^2 \phi}{\partial x \partial z} + \frac{\partial^2 \psi}{\partial x^2} - \frac{\partial^2 \psi}{\partial z^2} \right) . \tag{2.42}$$

The potentials ϕ and ψ satisfy the two-dimensional wave equations for plane strain,

$$\frac{\partial^2 \phi}{\partial x^2} + \frac{\partial^2 \phi}{\partial z^2} = \frac{1}{c_L^2} \frac{\partial^2 \phi}{\partial t^2} \tag{2.43}$$

$$\frac{\partial^2 \psi}{\partial x^2} + \frac{\partial^2 \psi}{\partial z^2} = \frac{1}{c_T^2} \frac{\partial^2 \psi}{\partial t^2} . \tag{2.44}$$

To find the solutions to these equations, we assume that ϕ and ψ are of the form,

$$\phi = \phi(z) \exp[j(kx - \omega t)] \tag{2.45}$$

$$\psi = \psi(z) \exp[j(kx - \omega t)] , \tag{2.46}$$

which represents waves standing in the z-direction and traveling in the x-direction. Substituting Eqs. (2.45) and (2.46) into Eqs. (2.43) and (2.44), and dropping the

factor $e^{j(kx-\omega t)}$, we obtain the resulting solutions as

$$\phi = A_s \cosh(\alpha z) + B_a \sinh(\alpha z) \tag{2.47}$$

$$\psi = C_a \cosh(\beta z) + D_s \sinh(\beta z) \ , \tag{2.48}$$

where A_s, B_a, C_a, D_s are arbitrary constants, k is the wavenumber and

$$\alpha^2 = k^2 - \frac{\omega^2}{c_L^2} = k^2 - k_L^2 \tag{2.49}$$

$$\beta^2 = k^2 - \frac{\omega^2}{c_T^2} = k^2 - k_T^2 \ . \tag{2.50}$$

The constants k_L and k_T are the wavenumbers of longitudinal and transverse waves, respectively given as

$$k_L = \omega\sqrt{\frac{\rho}{\lambda + 2\mu}} \ , \qquad k_T = \omega\sqrt{\frac{\rho}{\mu}} \ . \tag{2.51}$$

From Eqs. (2.47) and (2.48), we can rewrite the displacement and stress components in terms of the potentials as

$$u_x = jk\phi - \frac{d\psi}{dz} \tag{2.52}$$

$$u_z = \frac{d\phi}{dz} + jk\psi \ , \tag{2.53}$$

and

$$\sigma_{zz} = \lambda\left(-k^2\phi + \frac{d^2\phi}{dz^2}\right) + 2\mu\left(\frac{d^2\phi}{dz^2} + jk\frac{d\psi}{dz}\right) \tag{2.54}$$

$$\sigma_{xz} = \mu\left(2jk\frac{d\phi}{dz} - k^2\psi - \frac{d^2\psi}{dz^2}\right) \ . \tag{2.55}$$

From Eqs. (2.52) and (2.53), we can observe that the motion in the x-direction is symmetric (antisymmetric) with regard to $z = 0$, if u_x only contains hyperbolic cosines (sines); the displacement in the z-direction is symmetric (antisymmetric) if

u_z only contains hyperbolic sines (cosines). Thus, the modes are grouped into two systems: symmetric and antisymmetric modes.

1. For symmetric modes, the resulting potentials, displacements, and stresses are:

$$\phi = A_s \cosh(\alpha z) \tag{2.56}$$

$$\psi = D_s \sinh(\beta z) \tag{2.57}$$

$$u_x = jkA_s \cosh(\alpha z) - \beta D_s \cosh(\beta z) \tag{2.58}$$

$$u_z = \alpha A_s \sinh(\alpha z) + jkD_s \sinh(\beta z) \tag{2.59}$$

$$\sigma_{zz} = \lambda[(-k^2 + \alpha^2)A_s \cosh(\alpha z)] + 2\mu[\alpha^2 A_s \cosh(\alpha z) + jk\beta D_s \cosh(\beta z)] \tag{2.60}$$

$$\sigma_{xz} = \mu[2jk\alpha A_s \sinh(\alpha z) - (k^2 + \beta^2)D_s \sinh(\beta z)] \; ; \tag{2.61}$$

2. For antisymmetric modes, the resulting potentials, displacements, and stresses are:

$$\phi = B_a \sinh(\alpha z) \tag{2.62}$$

$$\psi = C_a \cosh(\beta z) \tag{2.63}$$

$$u_x = jkB_a \sinh(\alpha z) - \beta C_a \sinh(\beta z) \tag{2.64}$$

$$u_z = \alpha B_a \cosh(\alpha z) + jkC_a \cosh(\beta z) \tag{2.65}$$

$$\sigma_{zz} = \lambda[(-k^2 + \alpha^2)B_a \sinh(\alpha z)] + 2\mu[\alpha^2 B_a \sinh(\alpha z) + jk\beta C_a \sinh(\beta z)] \tag{2.66}$$

$$\sigma_{xz} = \mu[2jk\alpha B_a \cosh(\alpha z) - (k^2 + \beta^2)C_a \cosh(\beta z)] \; . \tag{2.67}$$

The expression relating the frequency ω to the wavenumber k, or so called frequency equation, is now obtained from the boundary conditions, Eq. (2.36). For the symmetric modes this yields a system of two homogeneous equations for the constants

A_s and D_s,

$$(k^2+\beta^2)\cosh(\alpha h)A_s + 2jk\beta\cosh(\beta h)D_s = 0 \tag{2.68}$$

$$2jk\alpha\sinh(\alpha h)A_s - (k^2+\beta^2)\sinh(\beta h)D_s = 0\ . \tag{2.69}$$

Since the systems are homogeneous, the determinant of the coefficients must vanish, which yields the frequency equation

$$\frac{(k^2+\beta^2)\cosh(\alpha h)}{2jk\beta\cosh(\beta h)} = \frac{2jk\alpha\sinh(\alpha h)}{-(k^2+\beta^2)\sinh(\beta h)}\ , \tag{2.70}$$

This can be simplified as

$$\frac{\tanh(\beta h)}{\tanh(\alpha h)} = \frac{4k^2\alpha\beta}{(k^2+\beta^2)^2}\ , \tag{2.71}$$

which is the Rayleigh-Lamb frequency equation for symmetric modes in the plate.

Similarly, for the antisymmetric modes, the boundary conditions yield a system of two homogeneous equations for the constants B_a and C_a,

$$(k^2+\beta^2)\sinh(\alpha h)B_a + 2jk\beta\sinh(\beta h)C_a = 0 \tag{2.72}$$

$$2jk\alpha\cosh(\alpha h)B_a - (k^2+\beta^2)\cosh(\beta h)C_a = 0\ , \tag{2.73}$$

which yields the frequency equation

$$\frac{(k^2+\beta^2)\sinh(\alpha h)}{2jk\beta\sinh(\beta h)} = \frac{2jk\alpha\cosh(\alpha h)}{-(k^2+\beta^2)\cosh(\beta h)}\ . \tag{2.74}$$

This can be further simplified as

$$\frac{\tanh(\beta h)}{\tanh(\alpha h)} = \frac{(k^2+\beta^2)^2}{4k^2\alpha\beta}\ , \tag{2.75}$$

which is the Rayleigh-Lamb frequency equation for antisymmetric modes in the plate.

For the symmetric mode, the boundaries of the plate periodically dilate and contract; these modes are, therefore, often called *longitudinal*; The antisymmetric modes

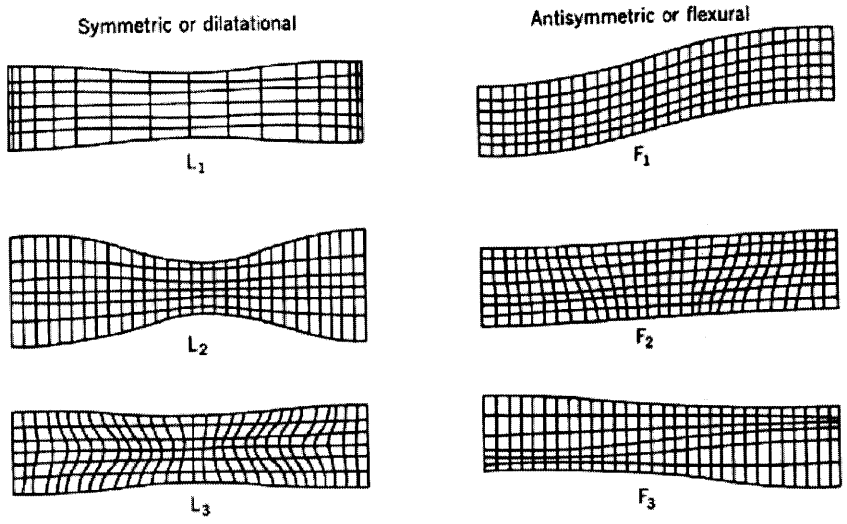

Figure 2.5: Field distributions for the lowest modes on an traction-free isotropic plate ($k \approx 0$), where L stands for symmetric or longitudinal modes, and F stands for antisymmetric or flexural modes [31].

are called *flexural* because of the periodic flexing motion of the boundaries. Figure 2.5 shows the displacement patterns of the three lowest symmetric and antisymmetric modes for a small value of the wavenumber k [31].

2.4.2 Analysis of Rayleigh-Lamb Frequency Equations

It can be observed from the frequency equations that there exists no known analytical solution. This is due to the fact tha both P and SV waves exist for any given mode owing to the mode conversion at the traction-free surfaces.

Displacements of Lamb Wave Modes

The displacements for symmetric and antisymmetric modes have been expressed in terms of the four constants A_s, D_s, B_a and C_a. Here we can rewrite them in a further expression.

1. Symmetric modes: From Eq. (2.69) we obtain the amplitude ratio

$$\frac{D_s}{A_s} = \frac{2jk\alpha \sinh(\alpha h)}{(k^2+\beta^2)\sinh(\beta h)} \,. \tag{2.76}$$

Thus, the displacements can be expressed as

$$u_x^s = jkA\left(\frac{\cosh(\alpha z)}{\sinh(\alpha h)} - \frac{2\alpha\beta}{k^2+\beta^2}\cdot\frac{\cosh(\beta z)}{\sinh(\beta h)}\right)e^{j(kx-\omega t)} \tag{2.77}$$

$$u_z^s = A\alpha\left(\frac{\sinh(\alpha z)}{\sinh(\alpha h)} - \frac{2k^2}{k^2+\beta^2}\cdot\frac{\sinh(\beta z)}{\sinh(\beta h)}\right)e^{j(kx-\omega t)} \,, \tag{2.78}$$

where A is a new constant.

2. Antisymmetric modes: From Eq. (2.73) we obtain the amplitude ratio

$$\frac{C_a}{B_a} = \frac{2jk\alpha \cosh(\alpha h)}{(k^2+\beta^2)\cosh(\beta h)} \,. \tag{2.79}$$

or the displacements can be expressed as

$$u_x^a = jkB\left(\frac{\sinh(\alpha z)}{\cosh(\alpha h)} - \frac{2\alpha\beta}{k^2+\beta^2}\cdot\frac{\sinh(\beta z)}{\cosh(\beta h)}\right)e^{j(kx-\omega t)} \tag{2.80}$$

$$u_z^a = B\alpha\left(\frac{\cosh(\alpha z)}{\cosh(\alpha h)} - \frac{2k^2}{k^2+\beta^2}\cdot\frac{\cosh(\beta z)}{\cosh(\beta h)}\right)e^{j(kx-\omega t)} \,, \tag{2.81}$$

where B is a new constant.

Various Regions of the Rayleigh-Lamb Equations

It is noted that the variables, α and β, defined as

$$\alpha^2 = k^2 - \frac{\omega^2}{c_L^2} = \frac{\omega^2}{c_p^2} - \frac{\omega^2}{c_L^2} \tag{2.82}$$

$$\beta^2 = k^2 - \frac{\omega^2}{c_T^2} = \frac{\omega^2}{c_p^2} - \frac{\omega^2}{c_T^2} \,, \tag{2.83}$$

are either real or imaginary numbers, depending on the value of c_p relative to c_L and c_T.

1. $0 < c < c_T < c_L$: In this case, both α and β are real, and the frequency equations are of the same form as before,

$$\frac{\tanh(\beta h)}{\tanh(\alpha h)} = \frac{4k^2\alpha\beta}{(k^2+\beta^2)^2} \qquad \text{(symmetric)} \tag{2.84}$$

$$\frac{\tanh(\beta h)}{\tanh(\alpha h)} = \frac{(k^2+\beta^2)^2}{4k^2\alpha\beta} \qquad \text{(antisymmetric)} \, . \tag{2.85}$$

2. $0 < c_T < c < c_L$: In this case, α is real and β is imaginary, The frequency equations become:

$$\frac{\tan(\bar{\beta} h)}{\tanh(\alpha h)} = \frac{4\alpha\bar{\beta}k^2}{(k^2-\bar{\beta}^2)^2} \qquad \text{(symmetric)} \tag{2.86}$$

$$\frac{\tan(\bar{\beta} h)}{\tanh(\alpha h)} = -\frac{(k^2-\bar{\beta}^2)^2}{4\alpha\bar{\beta}k^2} \qquad \text{(antisymmetric)} \tag{2.87}$$

where $\bar{\beta}$ is the complex conjugate of β

$$\bar{\beta} = \sqrt{\frac{\omega^2}{c_T^2} - k^2} \, . \tag{2.88}$$

3. $0 < c_T < c_L < c$: In this case, both α and β are imaginary. The frequency equations are written as

$$\frac{\tan(\bar{\beta} h)}{\tan(\bar{\alpha} h)} = -\frac{4\bar{\alpha}\bar{\beta}k^2}{(k^2-\bar{\beta}^2)^2} \qquad \text{(symmetric)} \tag{2.89}$$

$$\frac{\tan(\bar{\beta} h)}{\tan(\bar{\alpha} h)} = -\frac{(k^2-\bar{\beta}^2)^2}{4\bar{\alpha}\bar{\beta}k^2} \qquad \text{(antisymmetric)} \tag{2.90}$$

where $\bar{\alpha}$ and $\bar{\beta}$ are the complex conjugates of α and β, respectively,

$$\bar{\alpha} = \sqrt{\frac{\omega^2}{c_L^2} - k^2} \, , \qquad \bar{\beta} = \sqrt{\frac{\omega^2}{c_T^2} - k^2} \, . \tag{2.91}$$

Cutoff Frequencies

The cutoff frequencies for various wave modes are obtained by limiting the wavenumber $k \to 0$. At this limiting value, the Rayleigh-Lamb equations are reduced to:

$$\cos(\bar{\alpha}_c h)\sin(\bar{\beta}_c h) = 0 \qquad \text{(symmetric)} \tag{2.92}$$

$$\sin(\bar{\alpha}_c h)\cos(\bar{\beta}_c h) = 0 \qquad \text{(antisymmetric)}\ . \tag{2.93}$$

1. Symmetric modes:

$$\cos(\bar{\alpha}_c h) = 0, \qquad \bar{\alpha}_c h = \frac{p\pi}{2} \qquad (p = 1, 3, 5, \dots) \tag{2.94}$$

$$\sin(\bar{\beta}_c h) = 0, \qquad \bar{\beta}_c h = \frac{q\pi}{2} \qquad (q = 0, 2, 4, \dots)\ . \tag{2.95}$$

In view of the fact that $\bar{\alpha}_c = \omega_c / c_L$ and $\bar{\beta}_c = \omega_c / c_T$ in this case, we have the condition for the cutoff frequencies

$$\frac{\omega_c h}{c_T} = \begin{cases} \dfrac{p\pi}{2}\dfrac{c_L}{c_T} & (p = 1, 3, 5, \dots) \\ \dfrac{q\pi}{2} & (q = 0, 2, 4, \dots) \end{cases}\ . \tag{2.96}$$

or in terms of the frequency and thickness product

$$2 f_c h = \begin{cases} \dfrac{p c_L}{2} & (p = 1, 3, 5, \dots) \\ \dfrac{q c_T}{2} & (q = 0, 2, 4, \dots) \end{cases}\ . \tag{2.97}$$

2. Antisymmetric modes:

$$\sin(\bar{\alpha}_c h) = 0, \qquad \bar{\alpha}_c h = \frac{p\pi}{2} \qquad (p = 0, 2, 4, \dots) \tag{2.98}$$

$$\cos(\bar{\beta}_c h) = 0, \qquad \bar{\beta}_c h = \frac{q\pi}{2} \qquad (q = 1, 3, 5, \dots)\ . \tag{2.99}$$

Likewise, in view of the fact that $\bar{\alpha}_c = \omega_c/c_L$ and $\bar{\beta}_c = \omega_c/c_T$, the condition for the cutoff frequencies are

$$\frac{\omega_c h}{c_T} = \begin{cases} \frac{p\pi}{2}\frac{c_L}{c_T} & (p = 0, 2, 4, \dots) \\ \frac{q\pi}{2} & (q = 1, 3, 5, \dots) \end{cases}, \tag{2.100}$$

or in terms of the frequency and thickness product

$$2f_c h = \begin{cases} \frac{pc_L}{2} & (p = 0, 2, 4, \dots) \\ \frac{qc_T}{2} & (q = 1, 3, 5, \dots) \end{cases}. \tag{2.101}$$

2.4.3 Dispersion Curves

From the Rayleigh-Lamb frequency equations, the relationship between the frequency (ω) and wavenumber (k) of the Lamb waves, or between the phase velocity (c_p) or group velocity (c_g) and the frequency ω can be detremined numerically, resulting in the so-called *dispersion curves*. For a given frequency there are infinite number of wavenumbers that satisfy the frequency relations, but only a finite number of these wavenumbers are purely real or imaginary, while the others are complex [33]. The behavior of the real, imaginary and complex branches of the frequency equations was discussed by Mindlin [27]. In many cases, only the real solutions of the frequency equations are displayed in the dispersion curves since they represent the propagating modes. Dispersion curves are very important in analyzing Lamb waves.

Figure 2.6(a) is the dispersion curves for aluminum, showing the relationship between the phase velocity and frequency-thickness product. The solid lines represent symmetric modes while the dashed liness represent antisymmetric modes. The dispersion curves reflect the aforementioned characteristics of Lamb waves: dispersion and multi-modality. For a given mode, the phase velocity changes with the frequency-thickness product. For a given frequency-thickness product, there exist at least two modes, i.e., they are multi-modal. It is therefore important to take into account both the influence of dispersion and multi-modality in analyzing Lamb waves.

Shown in Fig. 2.6(b) are the dispersion curves relating the group velocity and frequency-thickness product. As shown in this figure, each mode has a maximum group velocity. For example, $c^g_{max} = 3168$ m/s for A_0 mode and $c^g_{max} = 5438$ m/s for S_0 mode. It is also noted that the group velocities of the symmetric modes are larger than those of the antisymmetric modes. In addition, the group velocities of the lowest symmetric and antisymmetric modes (S_0 and A_0) asymptotic approach the Rayleigh wave velocity (c_R). By contrast, the group velocities of all the other modes approach the transverse wave velocity (c_T). No group velocity exceeds the longitudinal wave velocity (c_L).

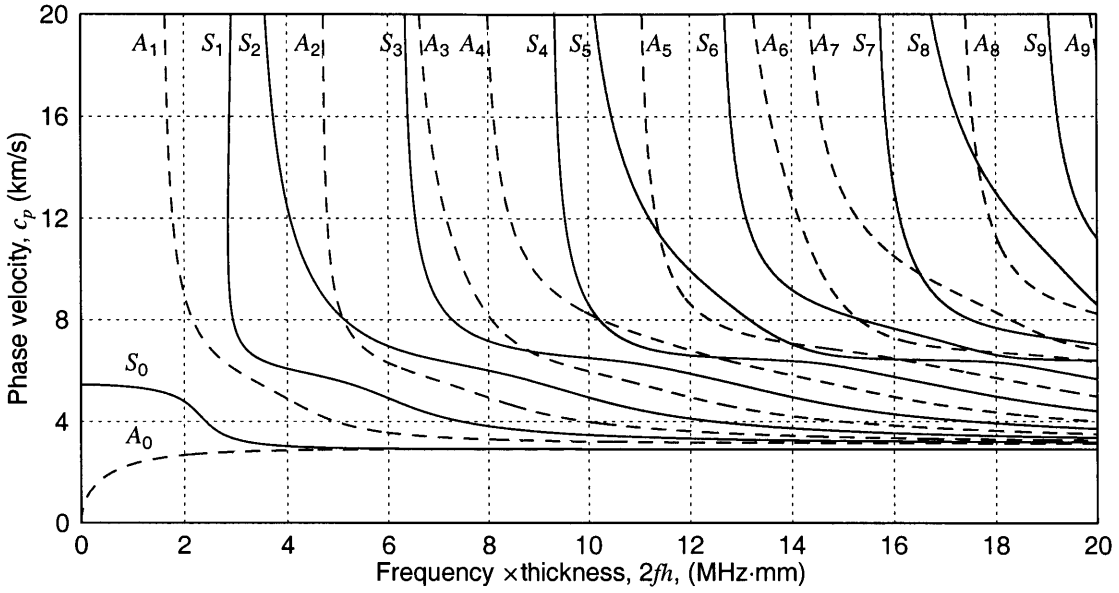

(a)

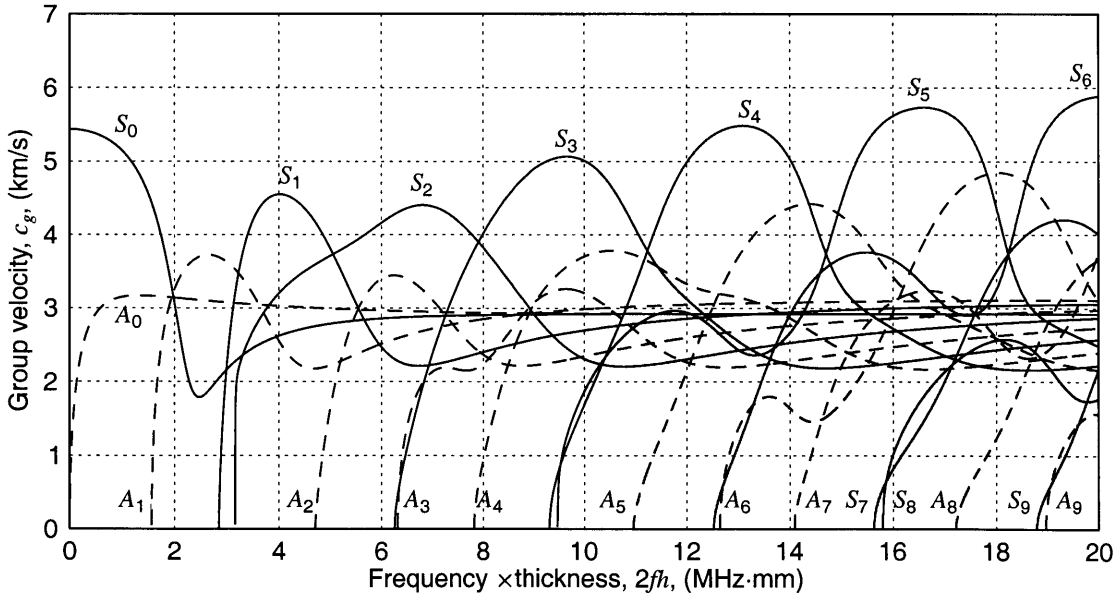

(b)

Figure 2.6: Dispersion curves for an aluminum plate of thickness $2h$: (a) phase velocity and (b) group velocity. The longitudinal wavespeed is $c_L = 6320$ m/s and transverse wavespeed is $c_T = 3130$ m/s.

Chapter 3

Wave Mode Tuning Techniques

3.1 Introduction

As mentioned in Chapter 1, Lamb waves offer an attractive solution for inspecting thin-walled structural members mainly because they can travel long distances in the plane of the members. However, the analysis is complex due to their dispersive and multi-modal nature. Unlike bulk waves, the propagation velocity of Lamb waves is a function the frequency. This means that the shape of a propagating waves could be changed as it travel in the medium. In addition, at least two modes exist at a single frequency, and the number of co-existing modes increases as the frequency increases. Hence, the application of Lamb waves depends on the way we deal with these two features. Two approaches are generally used for this purpose, including those using broadband signals and those using narrowband signals.

Broadband signals are attractive since they contain rich information over a wide range of frequency. An example of applications in this category is the construction of experimental dispersion curves from the laser generated Lamb waves, which will be discussed in Chapter 8. However, this approach involves advanced signal processing algorithms such as two-dimensional Fourier transform and continuous wavelet transform. Furthermore, in-plane pulse-echo or pitch-catch operations (used for bulk waves) require much more sophisticated signal processing techniques since it is not easy to extract useful information directly in the time domain.

On the other hand, the narrowband signal approaches enable the processing of signals directly in the time domain. In this case, the waves retain their shapes as they propagate in the medium so that the dispersion effect is small. However, due to the existence of multiple modes traveling at different velocities, it is preferred to discern one desired mode from the other modes. This procedure is called mode tuning. With successful mode tuning, the pitch-catch or pulse-echo setups can be simple and useful. For example, Lamb waves can be conveniently used to detect flaws in structural members, by detecting and measuring the time of flight (TOF) of a single reflection from a flaw. One of the main objective of this thesis work is to develop an effective tuning method.

In this chapter, we will presents the various tuning techniques of Lamb waves. Two major state-of-the-art tuning techniques used in Lamb wave inspection will be reviewed first, including the *angle beam transducer tuning* or *angle wedge transducer tuning* and *comb transducer tuning*. Tuning examples will be given to illustrate the effect and disadvantages of these two techniques. Then we will propose our innovative dynamic phase tuning technique using linear phased arrays, or the *phased array tuning* technique. A comparison between our approach and the ones reviewed is included. To assist the understanding of the phase tuning concept, the background of phased arrays will be introduced along with the prototype system development. Experimental results will be obtained for the phased array tuning, and the limitations of this technique will be also pointed out. Remarks will be given on alternative phase tuning technique, *synthetic phase tuning* method, which will be discussed in great detail in Chapter 4.

3.2 Angle Wedge Transducer Tuning

The most common and economical way to tune Lamb waves is to control the incident angle using a variable or fixed angle wedge transducer [13, 17]. Fig. 3.1 shows a normal contact transducer mounted on an angle wedge (usually made of perspex).

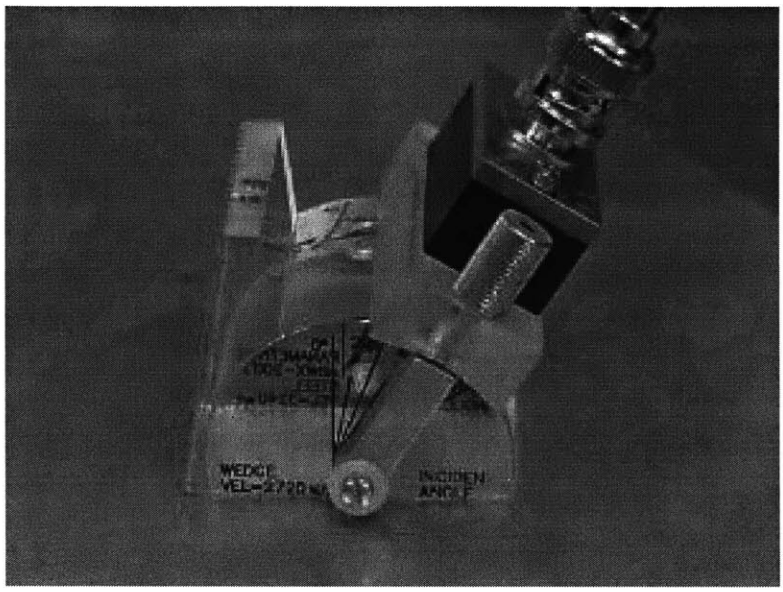

Figure 3.1: Conventional variable angle wedge transducer used for tuning Lamb waves.

3.2.1 Principle

As schematically shown in Fig. 3.2, Snell's law governs the principle of this tuning technique, which gives rise to the computation of the required angle of incidence θ_w [17]. The transducer generates a plane wave of wavelength λ_w in the wedge. Upon arrival of this plane wave at the interface between the wedge and the plate, Lamb wave modes are excited with different wavelength or velocities. Among all the generated modes, only the mode with a wavelength of λ_p (which is the mode to be tuned) is

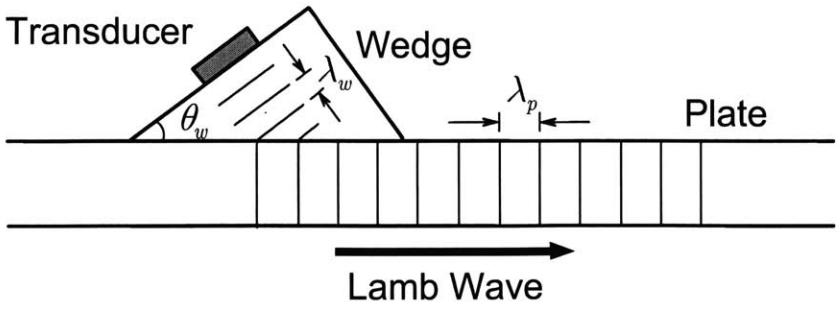

Figure 3.2: Schematic diagram of angle wedge transducer tuning of Lamb waves.

efficiently generated due to the delayed arrival times of the wave. This requires the angle of incidence to be set at

$$\sin\theta_w = \frac{\lambda_w}{\lambda_p} \ . \tag{3.1}$$

By virtue of the relationship:

$$\lambda_p = c_p/f \ , \qquad \lambda_w = c_w/f \ , \tag{3.2}$$

we may further express the incident angle as

$$\sin\theta_w = \frac{c_w}{c_p} \ , \tag{3.3}$$

where c_p is the phase velocity of the desired wave mode, and c_w is the longitudinal wave velocity in the wedge. The other modes which do not follow Shell's law are not constructively interfered. This is how the tuning effect is achieved through the angle control in the angle wedge transducer tuning technique.

It should be pointed out that the angle wedge transducer can be used as both a transmitter and receiver in pulse-echo. Sometimes, a second angle wedge transducer can be used as receiver especially in pitch-catch. The effect of oblique incident angle can be achieved by directly placing an angle wedge in contact with the surface or by using an immersion [10] or air-coupled transducer [34, 35] techniques.

As an example, Fig. 3.3 shows a typical Lamb wave tuned for A_1 mode, and the conditions set for this experiment are shown in Table 3.1. Although it was possible to obtain the other modes successfully, only the results for this mode are presented here for discussion. In this experiment, a variable angle wedge transducer, excited by a toneburst signal tuned at a carrier frequency $f_0 = 2.25$ MHz, is placed on a thin aluminum plate of 2 mm thickness ($2f_0h = 4.5$ MHz-mm). The wedge-transducer assembly is positioned to send waves toward the edge of the plate and receive signals reflected from the edge. The phase and group velocities are obtained from the dispersion curves shown in Fig. 2.6: $c_p = 4{,}269$ m/s, $c_g = 2{,}161$ m/s. Substituting c_p

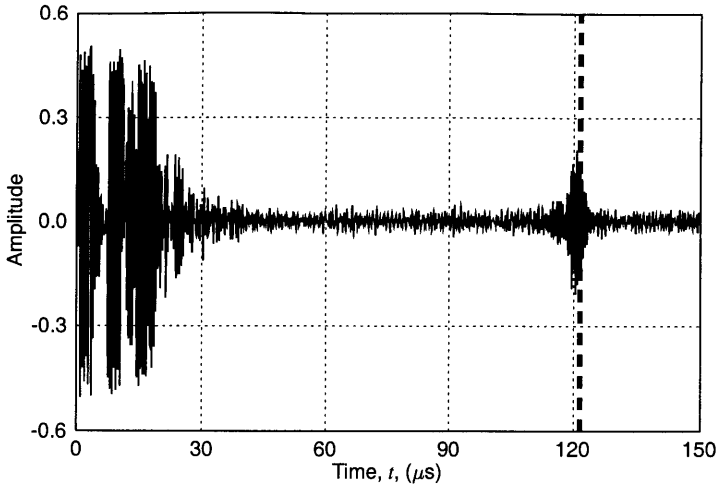

Figure 3.3: A typical pulse-echo Lamb wave signal, tuned for A_1 mode by a variable angle wedge and toneburst signals.

and c_w = 2,720 m/s into Eq. (3.3), the incident angle is set at $\theta_w = 39.6°$ to produce the desired mode (A_1). Knowing the group velocity and the distance from the center of the transducer to the plate edge (x = 104 mm), it is possible to measure the time (group delay) for a round trip: t_g=122.0 μs. This arrival time is indicated in the figure as a thick dashed line.

Table 3.1: Experimental conditions used for angle wedge tuning experiment.

Parameter	Value
Material	Aluminum
Toneburst frequency, f_0, (MHz)	2.25
Plate thickness, $2h$, (mm)	2.0
$2f_0h$ value (MHz-mm)	4.5
Wedge angle, θ_w, (degree)	39.6
Longitudinal wavespeed in the wedge, c_w, (m/s)	2720
Transducer-edge distance, x, (mm)	104
Time of travel, t_g, (μs)	122.0

3.2.2 Limitations

From this experiment, one can observe that the arrival time of the wedge-tuned signal corroborates the theoretical prediction; however, there are some annoying drawbacks and limitations to this technique. Firstly, since it is usually manipulated manually, it is difficult to set the angle of incidence with any appreciable accuracy. The sensitivity due to misalignment is uncertain and error levels may vary for different modes and frequencies.

Another drawback is attributed to the numerous interfaces that the signal must traverse in the wedge assembly. As shown in Fig. 3.1, a typical variable angle wedge consists of two parts: a main wedge and a block rotating around the wedge. Since the transducer is mounted on a plastic block, three interfaces exist in the transducer-wedge assembly: (1) one between the transducer and the rotating block, (2) one between the block and the main wedge, and (3) one between the wedge and the specimen. These interfaces introduce reflections, producing high peaks near the main bang. Although the acoustic impedances between the two wedge pieces are equivalent, reflections are still likely, especially if there is poor coupling. The reflections from the interface between the wedge and the test material could be pronounced due to the potentially high impedance mismatches. The problem may become more noticeable for smaller angles of incidence, where strong multiple reflections may occur. This not only diminishes the inspection zone in the vicinity of the transducer but also decreases the transmission efficiency.

There are additional limitations of the wedge-tuning technique. For example, it may be noted that Eq. (3.3) becomes invalid for $c_p < c_w$. Consequently, angle wedge transducers cannot tune the modes whose phase velocity falls below that of the longitudinal waves in the wedge. Specifically, the A_0 mode in the low frequency range (approximately below 2–3 MHz-mm) cannot be tuned in this fashion because $c_p < 2{,}720$ m/s, as shown in Fig. 2.6.

One remaining disadvantage stems from the fact that the wedge works as a delay block as a whole, requiring additional travel time that should be taken into account in

the analysis. Furthermore, the signal may be attenuated significantly before impinging the inspection material. All of the aforementioned limitations make angle wedge transducers rather cumbersome in certain situations, even though the device is widely used. The advantage and disadvantage of this technique are listed in Table 3.2.

Table 3.2: Advantages and disadvantages of angle wedge and comb transducer tuning techniques

	Angle wedge transducer tuning	Comb transducer tuning
Advantages	It is simple to operate.	Wave modes of low phase velocities can be tuned, mode selectivity is increased and penetration potential is enhanced.
Disadvantages	Difficult to set the angle of incidence with any appreciable accuracy. The numerous interfaces in the wedge assembly causes the reverberations, which introduces high peaks near the main bang. This not only diminishes the inspection zone in the vicinity of the transducer but also decreases the transmission efficiency. It only applies to the modes whose phase velocity is bigger than the longitudinal velocity in the wedge.	The wave inherently propagates bi-directionally, resulting in a symmetric excitation pattern. The arrays cannot be effectively used as a receiver since the inter-element spacing is fixed. The control of frequency characteristics of the propagating wave is not flexible. The produced signals generally have a long time duration, resulting in poor spatial resolution.

3.3 Comb Transducer Tuning

As an alternative to angle transducers, comb transducers have been explored for single mode excitation of Lamb waves [13, 22, 36, 37]. Comb transducers are in fact linear

arrays whose elements are equally spaced. The tuning effect is achieved by adjusting the element spacing or the frequency of the excitation signal.

3.3.1 Principle

Figure 3.4 schematically depicts the principle of Lamb wave tuning using a comb transducer. A gated sinusoidal signal of carrier frequency f_c excites all the elements at the same time. Or, in some cases, the elements are divided into two groups by activating every other element. By adjusting the distance between the elements, d, it is possible to generate guided waves of wavelength equal to d with the vibration (or carrier) frequency f_c, i.e., the inter-element spacing can be chosen such that $d = c_p/f_c$. Similarly, by adjusting f_c, it is possible to control the signal in such a way that the signal peaks are synchronized with the travel velocity of the mode to be tuned. In other words, the sinusoidal period of the excitation signal is to be set at

$$T_c = \frac{1}{f_c} = \frac{d}{c_p} \,. \tag{3.4}$$

There is another type of array transducer similar to the comb transducer, which is the *interdigital transducer*. Such transducer was originally developed as a surface acoustic wave (SAW) device for filters and delay lines used in radar and communication [38], but it was demonstrated that they could also be used to excite other waves such as Love and Lamb waves [39,40]. It is believed that interdigital transducers will

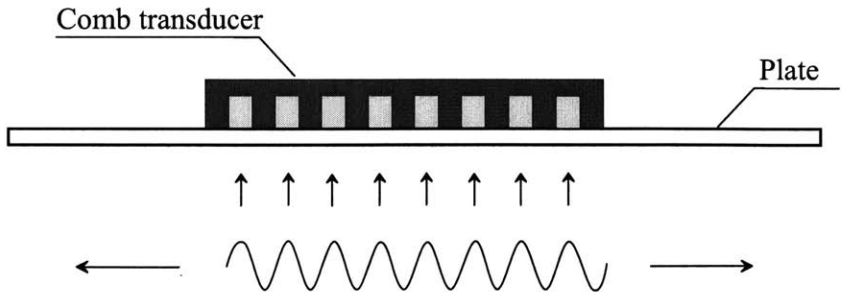

Figure 3.4: Schematic diagram of comb transducer tuning of Lamb waves.

find more and more applications in nondestructive evaluation with the advancement of micro-electro-mechanical system (MEMS) technology.

3.3.2 Limitations

Comb transducers have several benefits over wedge transducers [36], but there are several limitations as well. The most critical problem is that the wave inherently propagates bi-directionally. This is because all the elements are simultaneously activated by the same signal, resulting in a symmetric excitation pattern. Consequently, waves of commensurable energy emanate from both sides of the transducer.

The other critical disadvantage is that the arrays cannot be effectively used as a receiver. Since the inter-element spacing of the transducer is fixed and all the elements are engaged together, the constructive interference occurs only for the wave whose wavelength is equal to the inter-element spacing. It is not possible to control the wavelength and hence these arrays are not suitable for dynamically tuning the signals in the receiving mode.

Figure 3.5 shows a signal obtained from an experiment using a combination of array and wedge transducer. The experimental conditions are shown in Table 3.3. In this experiment, the array transducer works as a transmitter, while the wedge is placed on one side of the transducer to receive the signal. Both T_c and θ_w are set for tuning the S_0 mode. There are two main groups of the waves appearing in the signal. The first one arriving at $t_{g1} = 48.0$ μs represents the signal directly transmitted to the wedge transducer, and the one arriving later at approximately $t_{g2} = 131.2$ μs corresponds to the wave initially traveling in the opposite direction and then reversing upon contact with the edge of the plate. It is important to observe the significant amplitude of the second signal which has actually been attenuated due to reflection. This phenomenon is quite deleterious since the signals arriving from the unwanted direction (opposite direction in this case) may also appear in the waveform and corrupt the real data.

In addition to these problems, it may be noted that the control of frequency characteristics of the propagating wave is not flexible. Also, the produced signals generally

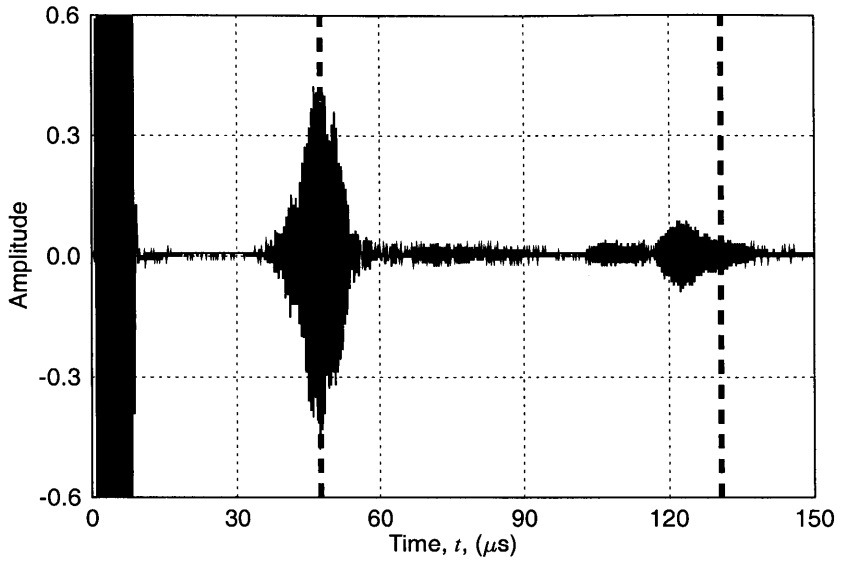

Figure 3.5: An S_0 mode-tuned pitch-catch signal transmitted by a comb transducer and received by a variable angle wedge transducer.

have a long duration time, resulting in poor spatial resolution. The advantage and disadvantage of comb transducer tuning technique are also listed in Table 3.2.

3.4 Phased Array Tuning

To overcome the drawbacks of the two aforementioned tuning techniques, we propose the innovative dynamic phase tuning method using linear phased arrays. This technique is referred to as the phased array tuning method. In contrast to comb transducers, all the elements of the array are isolated and excited individually according to a prescribed time delay profile. This allows dynamic tuning of a multi-mode dispersive wave without repositioning or realigning the transducer.

Before proceeding to explain the principle of phased array tuning in detail, we will review the background of ultrasonic phased arrays, including the geometry parameters and beam forming principle. This will help us understand the principle of phased array tuning. Note that in the following review, bulk waves (non-dispersive) instead of guided waves (dispersive) are considered.

Table 3.3: Experimental conditions used for the comb transducer tuning experiment.

Property	Value
Period of sine function, T_c, (ns)	473
Vibration frequency, f_c, (MHz)	2.1
Phase velocity, c_p, (m/s)	2961
Group velocity, c_g, (m/s)	2704
Velocity in the wedge, c_w, (m/s)	2720
Wedge Angle, θ_w, (deg)	66.7
Group delay of direct wave, t_{g1}, (μs)	48.0
Group delay of edge-reflected wave, t_{g2}, (μs)	131.2

3.4.1 Background of Phased Arrays

Ultrasonic phased arrays are made of multiple piezoelectric elements which are subsequently activated by time-delayed pulses. In general, phased arrays can be categorized as *linear arrays*, *planar arrays* and *annular arrays* by their geometry [41]. A linear array is composed of a number of individual elements arranged in a single line assembly. A planar array is basically a two-dimensional linear array. An annular array consists of concentric rings. Among these three arrays, only the linear arrays are considered in this thesis.

A representative linear phased array with eight elements is schematically shown in Fig. 3.6 viewed from upside-down, where D is the *lateral dimension* or the *aperture*, L is the *elevation dimension*, d is the *inter-element spacing*, and a is the *element size* or *width*. The lateral dimension of the array is always larger than its elevation dimension ($D > L$), and the individual element is always smaller than its elevation dimension ($L > a$). Also, it is observed that the lateral dimension can be expressed as

$$D = (N-1)d + a\,, \tag{3.5}$$

where N is the number of elements ($N = 8$ for this particular case).

The above design parameters, especially the number of elements(N), inter-element spacing (d), element size (a), as well as the frequency (f) are very important for the

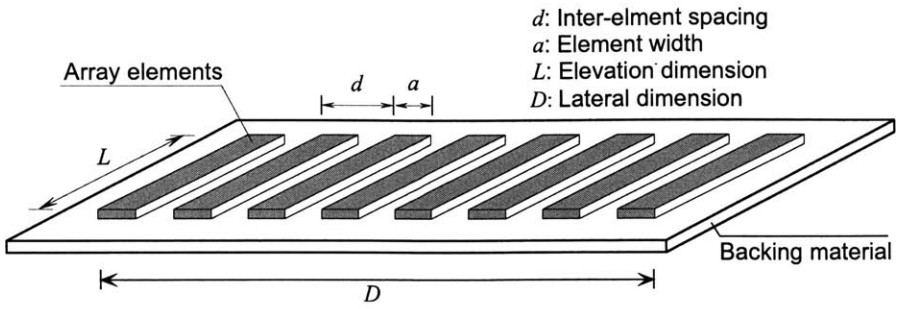

Figure 3.6: Geometry of a linear phased array transducer.

performance of phased arrays. There have numerous research done on this regard [42–53].

Beamforming is the most significant advantage of phased arrays over conventional ultrasonic transducers, which is achievable by adjusting the time delays between array transducer elements. The beamforming includes beam steering and focusing.

Beam steering of a linear phased array can be achieved by sequentially exciting individual elements with fixed time delay. The sound field of such configuration can be represented by the synthesis of pressure contributed by individual elements, according to *Huygens'* principle. Figure 3.7(a) illustrates the schematic concept of beam steering of a phased array. The propagation angle or the *steering angle* (θ_s) of the beam can be written as a function of wavespeed in the medium (c), time delay between adjacent elements ($\Delta\tau$), and the spacing between the elements or the inter-element spacing (d), such that

$$\Delta\tau = \frac{d \sin\theta_s}{c} \,. \tag{3.6}$$

Beam Focusing is accomplished by variably delaying a group of elements with respect to the center element. For example, when a delay profile takes a quadratic form, as shown in Fig. 3.7(b), the beam is converging at a focal point aligned with the transducer center. If the linear and quadratic time delay profiles are superposed, beam steering and focusing are obtained at the same time.

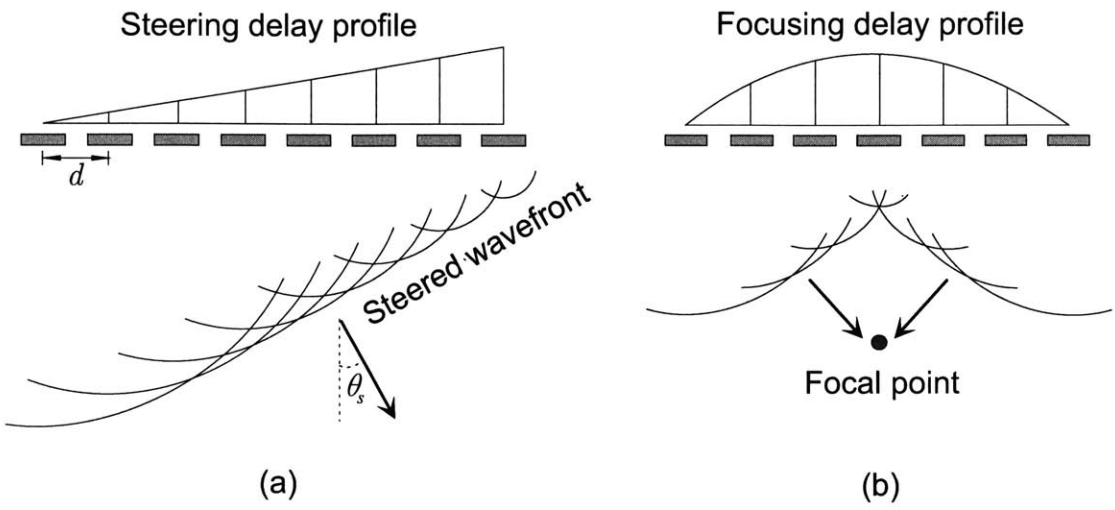

Figure 3.7: Principle of electronic beam forming: (a) a linear delay line creates a deflected beam, (b) a parabolic delay line results in a focused beam.

3.4.2 Principle

Figure 3.8 illustrates the basic concept of the phased array tuning. In this scheme, the element located farthest from the direction of the desired propagation is excited first at certain time, e.g., at $t = 0$. The wave generated by this element is multi-modal, bi-directional and dispersive. In other words, the activated element sends several different waves traveling at different speeds in both directions. An illustrative waveform is shown in the right-hand side of the topmost figure. The next step is to excite the adjacent element exactly when the wavefront of the desired mode arrives beneath that element, i.e., at $t = \Delta\tau$. At this moment, the other modes traveling at different speeds may have already passed that element, or they may not have reached it yet. Now, the desired wave mode is constructively interfered, while the other modes are not systematically modified. Progressive repetition of this sequence for all the elements increases the energy so that the amplitude of the desired mode can be significantly boosted. The required time delay between adjacent elements is given by a relationship similar to Eq. (3.4),

$$\Delta\tau = d/c_p \ . \tag{3.7}$$

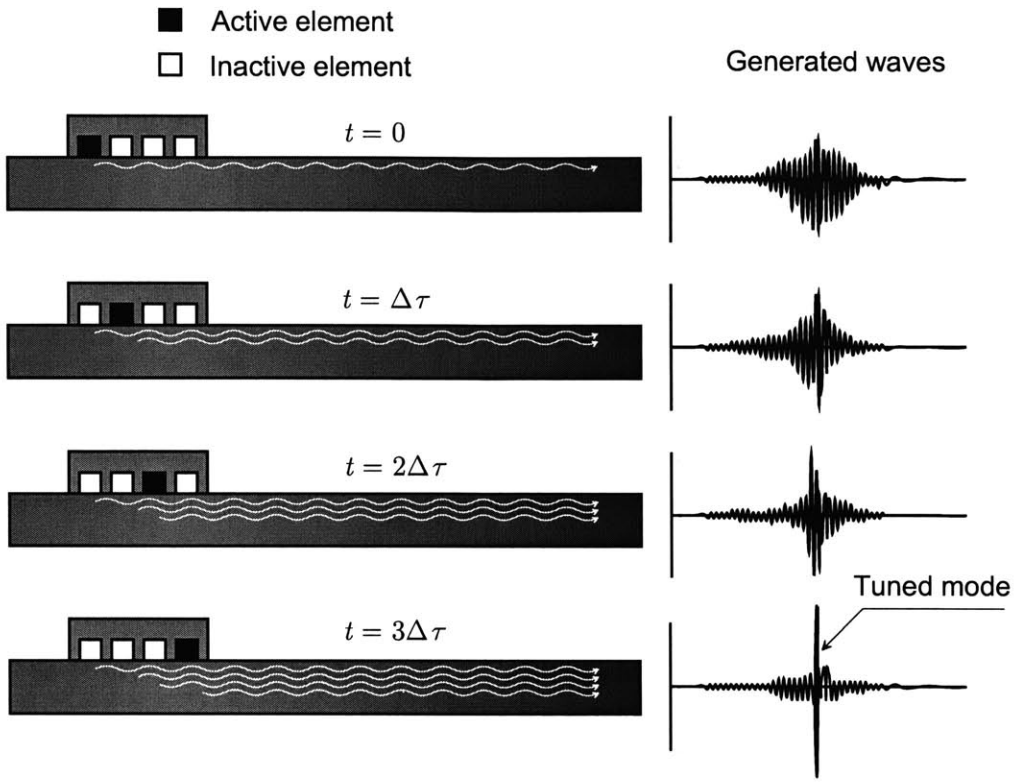

Figure 3.8: The concept of phase-tuning mechanism using a linear phased array.

If we compare Eq. (3.6) with Eq. (3.7), we can see that the phased array tuning is equivalent to steering the mode being tuned at an angle of 90°. The only difference between our phased array tuning method and the aforementioned comb transducer tuning approach is that the electronics for driving individual element is completely isolated. In our approach, only the target wave mode requires a systematic and sequential firing scheme. In this fashion, the amplitudes of the waves traveling in the opposite direction are suppressed while the ones traveling in the intended direction are enhanced. Increasing the number of repetitions will further squelch the unwanted signals.

3.4.3 Experimental Setup

From the principle, we emphasize that the key to phased array tuning is the time delay between array elements. For this, a sophisticated time delay circuit is required

to provide accurate time delays for tuning various wave modes. Before introducing the experimental setup for phased array tuning, we will have a brief review of the 16-channel phased array control system developed in the NDE Laboratory at the Massachusetts Institute of Technology.

Like most other phased array systems developed for biomedical imaging or NDE applications [54–62], our system is composed of essentially four main components: (1) delay circuit, (2) pulser circuit, (3) array transducers, and (4) computer interfacing. The system electronic hardware is composed of the 16-channel delay generator and high-voltage pulser circuit. Each of the 16 channels is dedicated to pulsing a specific array element. Many of the parts used in the hardware are controllable, and therefore require computer interfacing through parallel I/O cabling, GPIB for data acquisition, and RS-232 for serial port communication. The result is an electronically controllable ultrasonic beam.

Figure 3.9 schematically illustrates the conceptual diagram of the system layout. TTL (transistor-transistor logic) trigger signals, output from an HP function generator, are used as inputs to all 16 channels. Data from a 192-bit I/O board installed in a computer manipulates individual delay channels to generate a delayed trigger source for each of the 16 pulser units. Finally, each piezo element is excited by a delayed high voltage pulse from each pulser unit. More detailed information on the system development can be found in elsewhere [63].

Figure 3.10 schematically shows the experimental setup for the phased array tuning operated in pitch-catch configuration. The experimental conditions are tabulated in Table 3.4. An eight-element linear phased array transducer of center frequency $f_0 = 2.25$ MHz, made of piezo lead zirconate titanate (PZT), was used to tune Lamb wave modes in an aluminum plate of thickness $2h = 3.2$ mm. For the purpose of simplicity, an angle wedge transducer of center frequency $f_0 = 2.25$ MHz was used as the receiver with appropriate angles of incidence corresponding to the tuned wave modes. The inter-element spacing of the array was $d = 2.03$ mm. The distance between the first element (leftmost) and the angle wedge was set at x and the propagation distance in the wedge was $h_w = 35.0$ mm. Hence, the theoretical time of arrival (or

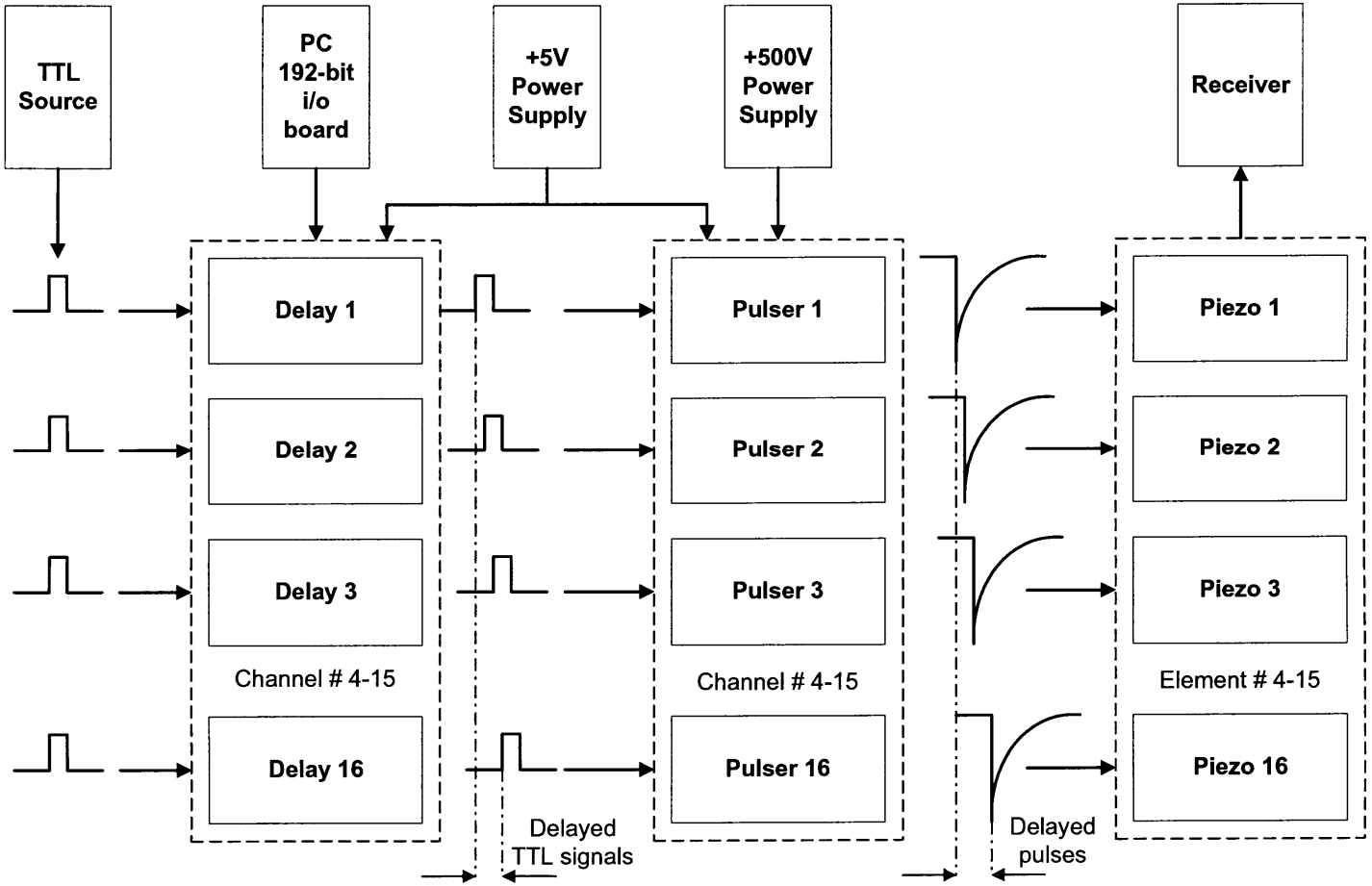

Figure 3.9: Schematic diagram of the 16-channel phased array system.

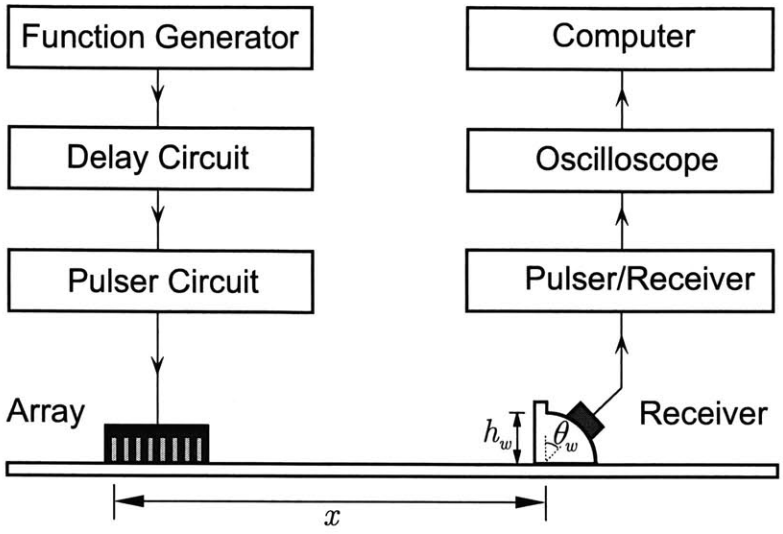

Figure 3.10: Experimental setup for the phased array tuning of Lamb waves operated in pitch-catch configuration, where tuned Lamb waves are generated by an array of eight elements and received by an angle wedge transducer.

group delay) for a tuned wave mode can be expressed as

$$t_g = x/c_g + h_w/c_w \ . \tag{3.8}$$

With suitable choice of time delays, Lamb wave modes were tuned in the aluminum plate and received by the angle wedge receiver. After going through the pre-amplifier, the received signals were displayed in an oscilloscope and further transferred into a computer for storage and analysis.

3.4.4 Experimental Results

Table 3.5 lists the required parameters for tuning various wave modes, including the phase and group velocities from Fig. 2.6, calculated time delays according to Eq. (3.7), and the angles of incidence according to Eq. (3.3). Among all the seven modes, only four modes: S_1, S_2, S_3 and A_2 were chosen for the experiment. This is because the capacity of our delay circuit was 500 ns, well below the required time delays for S_0, A_0 and A_1. Among the four modes of choice, the two modes — S_1 and S_3 display

Table 3.4: Experimental conditions used for phased array tuned pitch-catch testing.

Parameter	Value
Material	Aluminum
Number of elements, N	8
Interelement spacing, d, (mm)	2.03
Element width, a, (mm)	1.0
Total transducer aperture, D, (mm)	15.2
Transducer frequency, f, (MHz)	2.25
Plate thickness, $2h$, (mm)	3.2
$2fh$ value, (MHz-mm)	7.2
Array-wedge distance, x, (mm)	235.0 (S_1)
	180.0 (S_3)
Wedge propagation distance, h_w, (mm)	35.0
Longitudinal wave velocity in wedge, c_w, (m/s)	2720

good tuning effect while the other two modes — A_2 and S_2 are not well tuned. In the following, we will only demonstrate the results for the well-tuned modes, S_1 and S_3.

Table 3.5: Required experimental parameters for tuning various wave modes.

Wave mode	Phase velocity c_p, (m/s)	Group velocity c_g, (m/s)	Time delay $\Delta\tau$, (ns)	Wedge Angle θ_w, (deg)
S_3	8,120	2,780	250	19.6
S_2	6,382	4,057	318	25.2
A_2	5,384	2,815	377	30.3
S_1	4,036	2,246	503	42.4
A_1	3,325	2,732	610	54.9
S_0	2,903	2,869	699	69.5
A_0	2,892	2,920	702	70.1

In Table 3.5, the required time delay for S_1 mode is $\Delta\tau = 503$ ns, which is just 3 ns above the circuit's delay capacity of 500 ns. Hence $\Delta\tau = 500$ ns was used as the time delay for S_1 mode. To illustrate the effect of time delay on the tuning in detail, we varied the time delay from 0 ns to 500 ns with a time step of 50 ns. Figure 3.11 depicts the waveforms of the tuned S_1 mode for various time delays, where the distance between the first element and the wedge was set as $x = 235.0$ mm. In these waveforms, the first peak stands for the triggering signal, and the second

signal represents the received Lamb waves. When $\Delta\tau < 450$ ns, no tuning effect is observed. For $\Delta\tau = 500$ ns, there is a clear high peak appearing in the waveform, which is the tuned S_1 mode. This is confirmed by the calculated theoretical time of arrival (or group delay) for S_1 mode, $t_g = 117.5$ μs according to Eq. (3.8). Thus, we can conclude that S_1 mode is well tuned using the phased array tuning approach.

For S_3 mode, the required time delay is $\Delta\tau = 250$ ns, which is one half of the capacity (500 ns) of the delay circuit. The waveforms of the tuned S_3 mode for various time delays are shown in Fig. 3.12, where the distance between the first element and the wedge was set as $x = 180.0$ mm. The peak appearing in the waveform at $\Delta\tau = 250$ ns indicates the tuned S_3 mode. However, in contrast to the case of S_1 mode tuning, the waveforms in this case are not very sensitive to the change of time delays. We can observe that there also exist relatively outstanding peaks corresponding to S_3 mode for other time delay values such as $\Delta\tau$= 0 ns, 50 ns, 300 ns and 350 ns. The reasons for this scenario are not totally understood yet, although one possibility might be that S_3 mode has high amplitude inherently. Recall that another objective of this research is to understand the tuning efficiencies of various wave modes. For this, we will analyze the transient response of plates to external loadings in Chapter 5.

3.4.5 Limitations

From the experimental results, we may conclude that Lamb wave modes can be tuned well using the phased array tuning approach. Since the tuned waves are physically obtained, this approach enables flexible operation and high signal-to-noise ratio (SNR), thanks to the time delay and pulser circuits. On the other hand, the cost of the circuits is high, and the time delay resolution and capacity are limited by the capability of the delay circuits. For instance, the delay resolution is 5 ns and the delay capacity is 500 ns in our phased array system, which excludes the possibility of tuning all the modes existing for the given frequency. Furthermore, phased array systems usually use spike pulses so that it is not quite easy to control the frequency bandwidth.

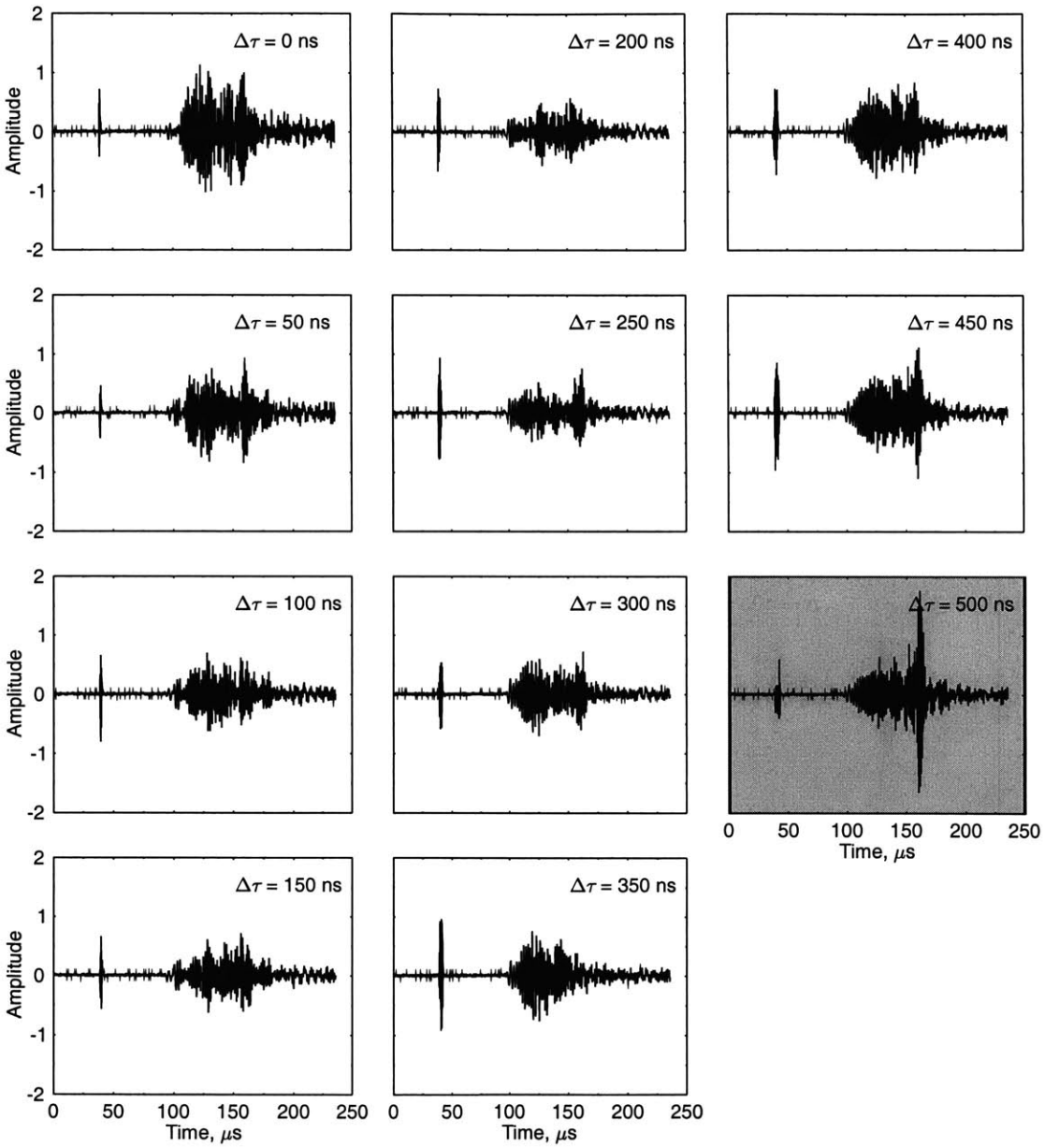

Figure 3.11: Phased array tuned S_1 mode in an aluminum plate for various time delays at $2fh = 7.2$ MHz-mm, where the required time delay is $\Delta\tau = 500$ ns.

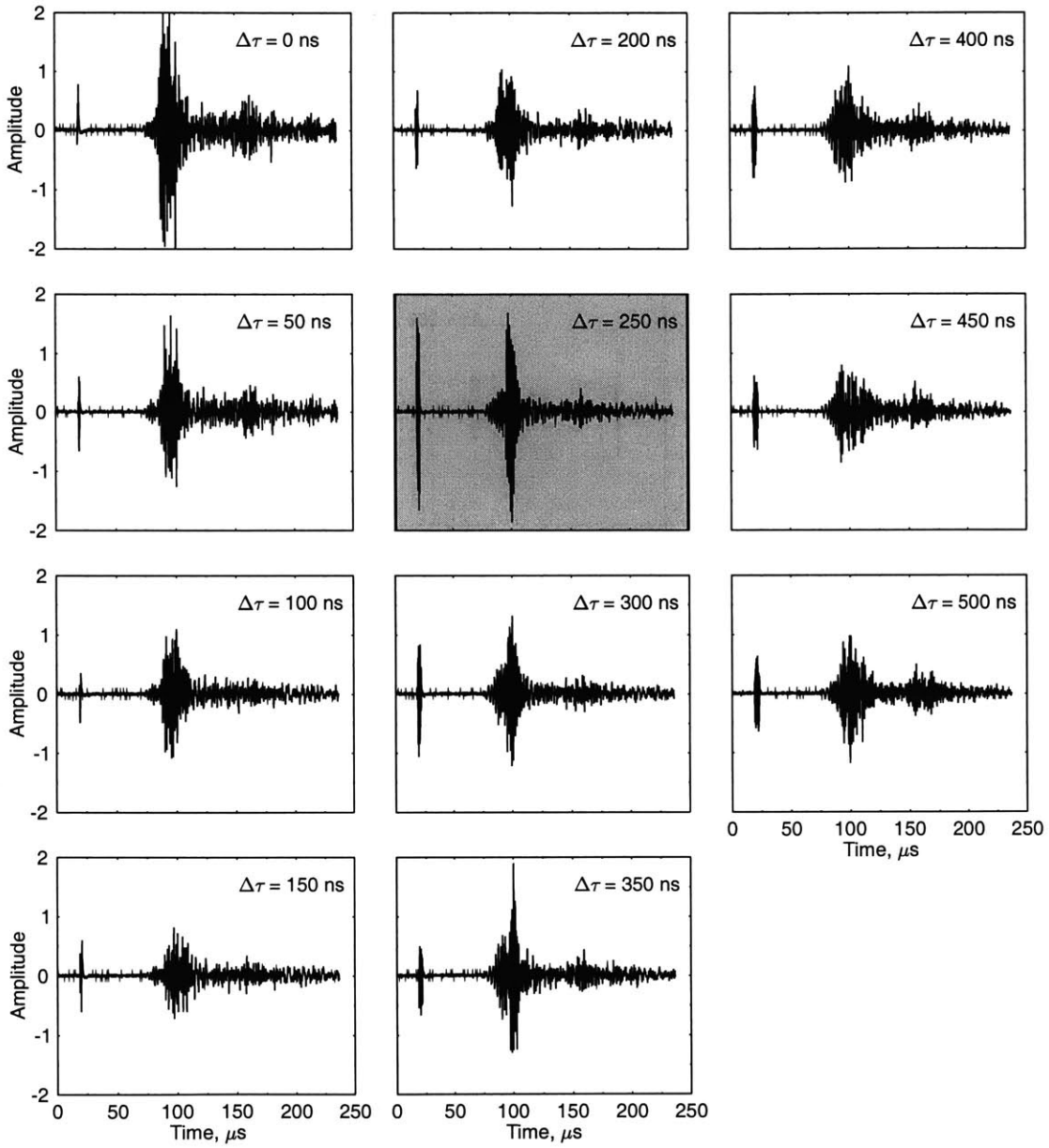

Figure 3.12: Phased array tuned S_3 mode in an aluminum plate for various time delays at $2fh = 7.2$ MHz-mm, where the required time delay is $\Delta\tau = 250$ ns.

3.5 Remarks on the Synthetic Phase Tuning

A natural way to remedy the limitations associated with the ultrasonic phased arrays system is to improve the delay capacity and resolution as well as the frequency bandwidth control capability. However, this solution could be extremely expensive, if not impossible. In response to this problem, we propose another dynamic phase tuning approach using the same array transducers, or the *synthetic phase tuning*. The phased array tuning and synthetic phase tuning have the same physical principle. The key difference is the way to provide the time delays for array elements. In the first approach, the time delay is provided by time delay circuits, while the time delay is provided numerically in the second approach. In this way, the aforementioned limitations imposed on the phased array array tuning by the system hardware could be eliminated. The details of the synthetic phase tuning technique will be discussed in Chapter 4.

3.6 Summary

In this chapter, various tuning methods of Lamb waves were presented. The traditional angle wedge transducer tuning method was firstly introduced. While the tuning effect was validated by an example, the limitations of this technique were pointed out, i.e., not all the wave modes can be tuned, and the tuning effect is influenced by the numerous interfaces in the wedge assembly, etc. Then the comb transducer tung technique was introduced. While this method offers several benefits over the angle wedge tuning method, it also has several limitations. One of the most limiting features is that the waves propagate bi-directionally.

In order to overcome the limitations of these methods, we proposed an innovative phased array tuning method whose tuning effect is achieved by adjusting time delays for controlling the excitation sequence of the array elements. The background of phased arrays and the system developed in the NDE Laboratory were introduced to help understanding the principle of the phased array tuning. While certain Lamb

wave modes were successfully tuned by this method in the experiment, it was shown that the tuning effect of this technique was severely limited by the capability of the hardware. Finally, we gave a brief remark on the synthetic phase tuning technique which will be further discussed in the next chapter.

Chapter 4

Synthetic Phase Tuning

4.1 Introduction

In Chapter 3, we have investigated three tuning techniques, including the angle wedge transducer tuning and comb transducer tuning, and the innovative phased array tuning techniques. The principles of mode tuning were explained, and experimental tuning results were obtained for each tuning technique. The advantages and disadvantages of each technique were also addressed.

As an alternative, we propose another dynamic phase tuning method using an array transducer, which is named the synthetic phase tuning (SPT). The principle of this method will be introduced followed by the description of the operating schemes. Afterwards, the procedure for constructing of virtually tuned waves is described in detail. Finally, experimental tuning results will be obtained using this method. A discussion of the comparison of SPT with other tuning techniques is included. This chapter is based on our previous research [64].

4.2 Principle of SPT

The SPT method essentially shares the same physical mechanism with the phased array tuning method. In other words, the tuning effect is achieved by adjusting the time delay to boost the mode of interest. The relationship between the required

time delay, the inter-element spacing and the mode phase velocity is represented by Eq. (3.6).

The key difference between these two methods is the way to provide the time delay for the excitation of array elements. For the phased array tuning, the time delay is provided by the delay circuit. For the SPT, the time delay is provided numerically rather than physically. Hence, the SPT technique deals with virtual or synthetic waves, in which the tuning is the result of manipulating a set of waveforms transmitted and received by individual elements.

4.3 Operating Schemes

There are basically two operating schemes in implementing the SPT: pseudo pulse-echo (PPE) and pseudo pitch-catch (PPC) schemes. The only difference between the PPC scheme and PPE scheme is that the former requires a second array transducer working as a receiver while the latter utilizes the same transducer working simultaneously as both both transmitter and receiver. Although it is possible to use either of them, we shall describe only the PPE scheme in this chapter because it may be better to demonstrate the capability of inspecting discontinuities in plates using the SPT technique. An SPT under PPC operating scheme will be considered later in Chapter 7.

Under the PPE operation, the array transducer behaves like a pulse-echo device. Figure 4.1 illustrates the concept of the PPE operation, in which an array transducer is mounted on the surface of the specimen at a distance x between the discontinuity and the center of the last element of the array. The transducer array consists of N elements of width a, separated by a center-to-center distance d. For convenience, we will use the edge of the plate to simulate a discontinuity or flaw in our study.

Since the array elements are operated independently, it is possible to transmit and receive signals, once at a time. The actual wave is (1) emitted from one of the transducer elements, (2) traveling in the desired direction, (3) reflected from discontinuities and traveling in the reverse direction, and (4) received by the same

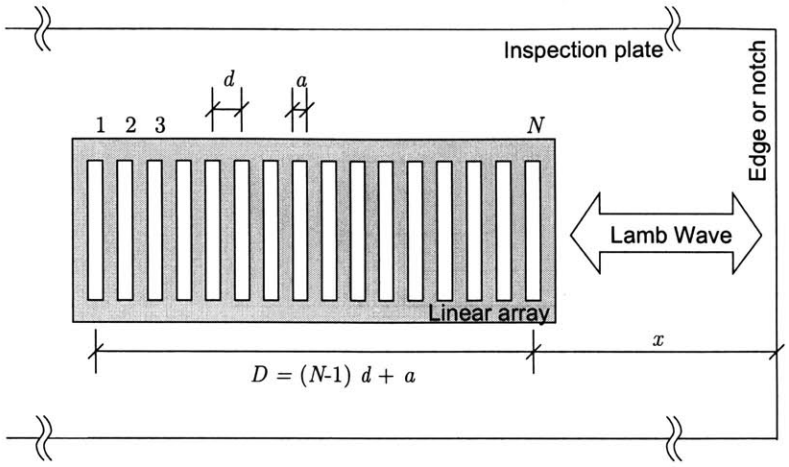

Figure 4.1: The concept of synthetic phase tuning under the pseudo pulse-echo operation. N=number of elements, d=inter-element spacing, a=element width, D=transducer width=$(N-1)d+a$, x=distance between the center of the last element and the discontinuity.

and other elements. By sequentially repeating the procedure, a total number of N^2 individual signals are obtained. Although all the elements participate independently, the synthetic construction brings about the overall effect as if the array transducer transmitted a single virtual wave and received the returning virtual wave off the discontinuity. This operating scheme or setup is therefore called "pseudo" pulse-echo or "synthetic" pulse-echo.

4.4 Construction of Virtually Tuned Waves

In the SPT testing, the tuning effect is achieved by manipulating the individually obtained signals. The procedure for constructing a virtually tuned signal consists of three basic steps: (1) signal generation and recording, (2) synthetic reconstruction of the emitted waves, and (3) synthetic reconstruction of the received waves. A high-resolution time-of-flight measurement, which can be achieved by this procedure, may be used to locate discontinuities or flaws for NDE purposes. It is also possible to combine steps (2) and (3) using a convenient formula given in this section. This will allow us to process signals in real-time immediately upon acquiring each waveform.

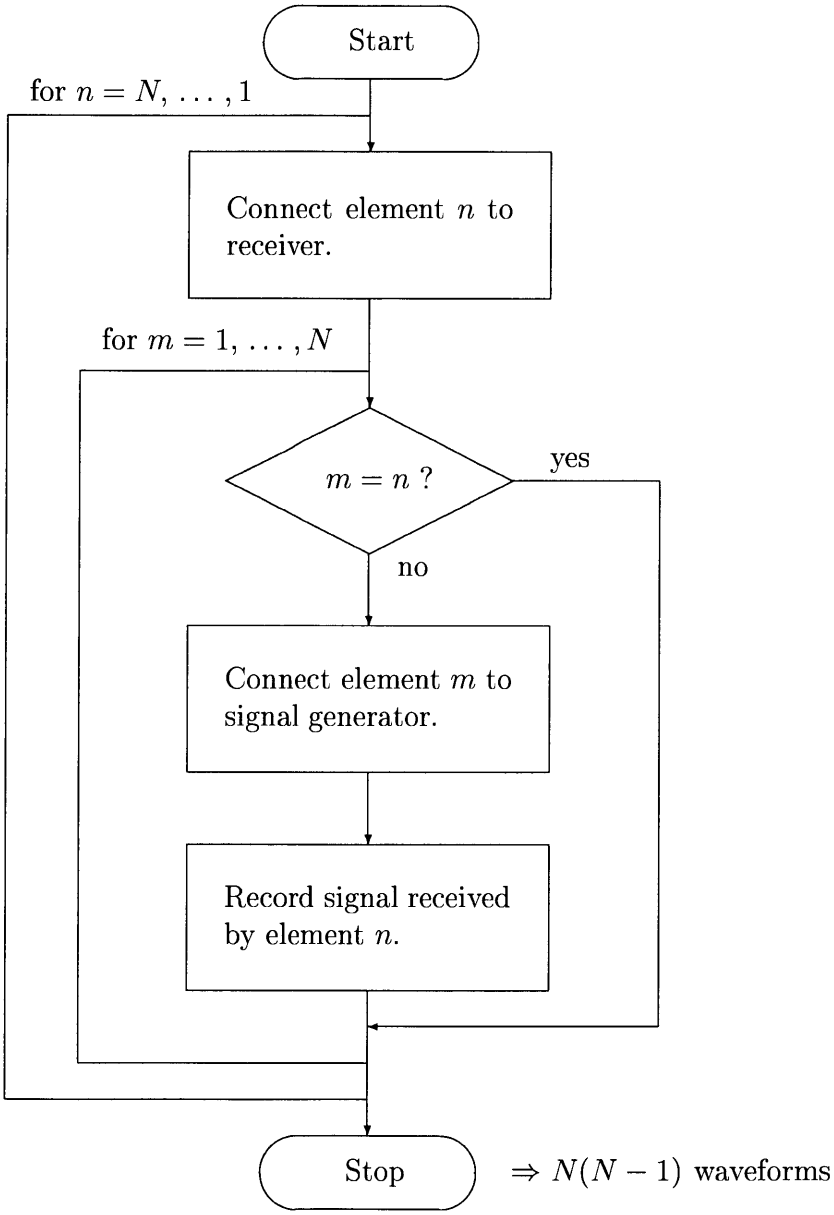

Figure 4.2: Flowchart for array data acquisition procedure.

4.4.1 Signal Generation and Recording

The first step is to generate signals and record them. The excitation sequence of the elements can be flexibly configured, e.g., pulse-echo (PE) or transmit-receive (TR) operations. The PE setup can be configured in such a way that each element is used to send and receive signals simultaneously and independently. The TR configuration, on the other hand, completely separates the elements. We adopt the TR configuration since one can achieve a higher SNR by separating the driving electronics. Figure 4.2 illustrates the procedure for the TR setup. A wave emitted by one element is received and recorded by each remaining array element, one at a time. The element index m denotes the transmitting element and n represents the index of the receiving elements. After completing the acquisition, we will have $N(N-1)$ waveforms to process.

Physically, indices m and n can be manipulated by multiplexers to switch the elements into different connection configurations. The transmitting elements are excited by a toneburst signal. Although one may excite the elements by a spike pulser, broadband signals will be produced, resulting in complicated waveforms. Recall that the tuning of Lamb waves requires narrow-band signals only.

4.4.2 Synthetic Construction of Emitting Waves

After the signals are acquired, the next step is to construct a synthetic wave. The waveform that we are constructing is a propagating virtual wave that is emitted from the transmitting array transducer, reflected off the discontinuity, and received by one of the array elements in the receiving transducer. We are constructing a total of N synthetic waveforms received by all elements.

Using the described setup, the signals are acquired with the same reference (triggering) position in time. For narrow-band signals, it is convenient to apply Huygen's principle directly in the time domain for constructing a new waveform. The signals are processed by the *time shift and delay algorithm* described as follows.

For an arbitrary inter-element time delay $\Delta\tau$, the corresponding time delay for the m-th element is given as

$$t_{m+1} = t_m + \Delta\tau\,, \quad m = 1, 2, 3, \ldots, N-1\,, \tag{4.1}$$

where the excitation time for the first element is taken as reference ($t_1 = 0$). Note that the first element is located at the extremity of the array with respect to the wave propagation direction, i.e, the wave erupts from element 1 to N. With this time delay profile, the synthetic wave received by the n-th element can be constructed by summing the time-shifted waveforms for all the elements, which can be written in the form

$$s_n(t) = \sum_{m=1,\, m\neq n}^{N} w_{mn} s_{mn}(t - t_m)\,, \quad n = 1, 2, 3, \ldots, N\,, \tag{4.2}$$

where $s_{mn}(t)$ are the waves transmitted by the m-th element and received by the n-th element, and w_{mn} is the *amplitude weighting function*. Note here that the signals $s_{mn}(t)$ encapsulate all the required information regarding the reflection coefficients and wave mode conversion occurring at the discontinuity. For convenience, we may take $w_{mn} = 1$, assuming that all elements are made equal. Noting this and by substituting t_m, Eq. (4.2) can be rewritten as

$$s_n(t) = \sum_{m=1,\, m\neq n}^{N} s_{mn}(t - (m-1)\Delta\tau)\,, \quad n = 1, 2, 3, \ldots, N\,. \tag{4.3}$$

Note that this equation is valid for any arbitrary time delay. By setting the time delay

$$\Delta\tau = \frac{d}{c_p}\,, \tag{4.4}$$

the constructed wave takes the form

$$s_n(t) = \sum_{m=1,\, m\neq n}^{N} s_{mn}\left(t - \frac{(m-1)d}{c_p}\right) , \tag{4.5}$$

for $n = 1, 2, 3, \ldots, N$. The synthetic signals constructed by this equation are tuned to a desired wave mode traveling in the plate at the phase velocity of c_p.

4.4.3 Synthetic Construction of Receiving Waves

Up to now, only the emitting wave has been conceptualized. When such a propagating wave encounters a discontinuity, it will reverse upon reflection. During the reflection, conversion between the modes may occur so that the incoming signal may spawn a variety of additional wave modes. Consequently, it behooves us to also tune the return signal in order to truly distinguish a particular mode of interest.

During reception, the time delay sequence has to be reversed since the wave travels backward, i.e.,

$$t_{n-1} = t_n + \Delta\tau' , \tag{4.6}$$

where $\Delta\tau'$ could be another arbitrary linear time delay profile. A fully constructed synthetic signal may then be expressed by the relationship:

$$s(t) = \sum_{n=N}^{1} s_n(t - (n-1)\Delta\tau') . \tag{4.7}$$

Although we are free to choose a different wave mode in receiving, we will only tune the same wave mode in both emitting and receiving stages. For this, we simply set

$$\Delta\tau' = \Delta\tau = \frac{d}{c_p} . \tag{4.8}$$

Note that the $N(N-1)$ number of waveforms are used to construct a synthetic PPE signal represented by Eq. (4.7). The wave constructed under this condition is now fully tuned to a desired wave mode.

4.4.4 Real-Time Reconstruction of Synthetic Signals

The procedure described above hinges on off-line processing, i.e., synthetic reconstruction ensues once the waveforms are recorded. This demands potentially large temporary storage space and the ongoing input/output operations may slow down the process. A more efficacious method is to process the acquired data immediately upon recording each waveform. This is possible by combining and recasting Eqs. (4.7) and (4.8) to create a real-time reconstruction formula as follows:

$$s(t) = \sum_{n=1}^{N} \sum_{m=1, m\neq n}^{N} s_{mn}\left(t - \frac{(m+n-2)d}{c_p}\right) . \tag{4.9}$$

For each (m,n) operation, the synthetic signal $s(t)$ is cumulatively constructed using this equation. At the end of acquisition, a fully synthesized PPE signal is readily available for display and analysis. This allows real-time processing of array signals.

4.4.5 Arrival Times of Tuned Waves

The group delay (travel time of the wave), measured from the main bang of element #1 to the receiver element n, can be expressed as:

$$(t_g)_n = \frac{2x + (2N-n-1)d + a}{c_g} + t_0 , \tag{4.10}$$

where x is the distance between the center of transducer element N and the discontinuity, c_g is the group velocity, d is the inter-element spacing, and t_0 is the trigger offset time that gives us a reference point. For small elements ($a \ll x$), Eq. (4.10)

can be approximated as

$$(t_g)_n = \frac{2x + (2N - n - 1)d}{c_g} + t_0 \ . \tag{4.11}$$

The total pulse-echo distance between element #1 and the discontinuity is $2(D+x)$ for a fully constructed wave and the corresponding travel time is given by the formula:

$$t_g = \frac{2[x + (N-1)d]}{c_g} + t_0 \ . \tag{4.12}$$

The advantage to this approach is that this sort of analysis provides excellent spatial resolution since the TOF is measured for a wave departing from element #1 and then received by the same element. In other words, the TOF can be exactly measured from the first element since it has negligible dimension. In fact, the overall dimension $(D = (N-1)d)$ of the array transducer does not affect the spatial resolution. Thus, this approach could enable us to enhance the transducer performance by increasing the number of elements without sacrificing the resolution.

4.5 Experimental Investigation

The experimental study is conducted in this section to prove the concept of synthetic phase tuning, where the pseudo pulse-echo operating scheme is used.

4.5.1 Experimental Setup

Figure 4.3 schematically shows the setup for the SPT experiment using the PPE configuration. In the experiment, a sixteen-element transducer made of flexible polyvinylidene fluoride (PVDF) piezo-polymer film was used. The inter-element spacing d was fixed at 1.4 mm, and the transducer was placed on an aluminum plate of 2 mm thickness at a location $x = 102$ mm (the distance between the 16-th element (rightmost) and the edge of the plate), as illustrated in Fig. 4.1. A five cycle toneburst signal of 2.25 MHz center frequency, generated by a function generator and power

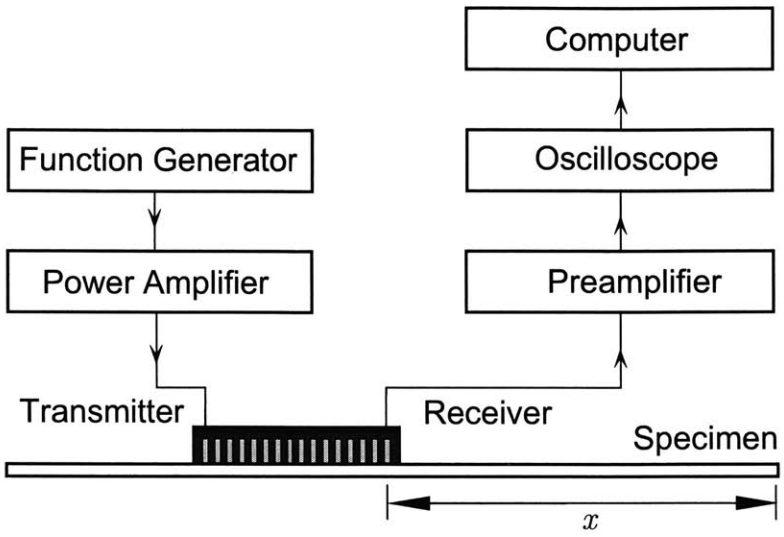

Figure 4.3: Experimental setup for the synthetic phase tuning of Lamb waves operated in the pseudo pulse-echo scheme, where the signal is generated by one element of the 16-element array transducer, and received by all the other elements.

amplifier, was used to excite each element. This yields a $2fh$ value of 4.5 MHz-mm. The conditions for the experiment are tabulated in Table 4.1. To facilitate the signal generation and recording, a single general-purpose pulser/receiver (or a function generator and pre-amplifier) unit can be used, combined with with a simple multiplexing unit or solid state switches that connect one element to the pulser/receiver unit at a time.

4.5.2 Experimental Results

As-Obtained Signals $s_{mn}(t)$

Figure 4.4 shows the respective waves obtained individually by exciting elements #1 through #15 and received by element #16. These waveforms respectively represent the signals $s_{mn}(t)$ where $n = N = 16$ and $m = 1, 2, 3, \ldots 15$. For the sake of brevity, the signals received by the other elements will not be reported but they have similar trends and features. In total, there will be $N(N-1)$ waveforms to be processed.

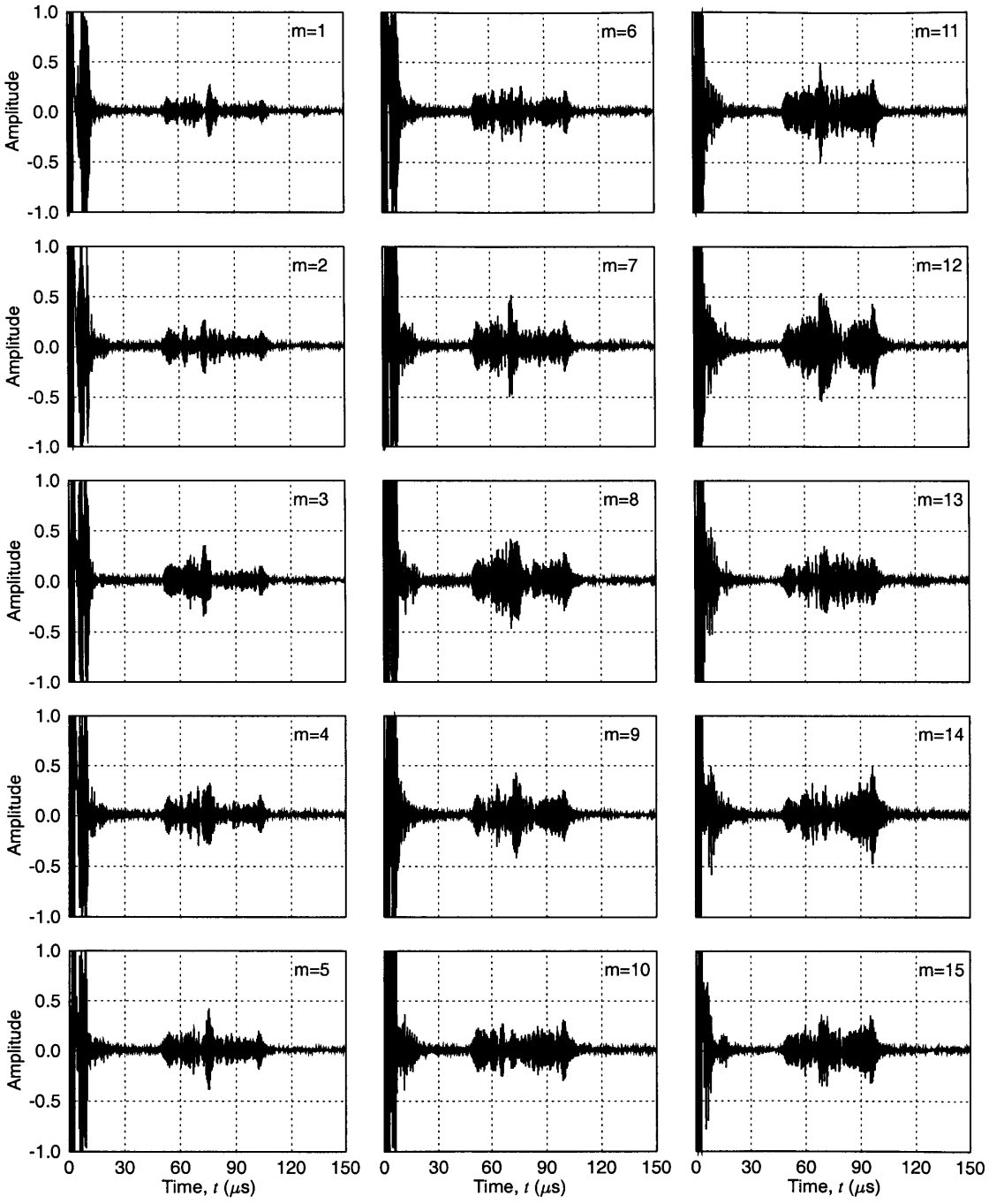

Figure 4.4: As-obtained individual waves emitted from elements 1 through 15 and received by the 16th element: $s_{mn}(t)$, $n = N = 16$, $m = 1, 2, 3, \ldots, 15$.

Table 4.1: Experimental conditions used for synthetic phase tuned pseudo pulse-echo testing.

Parameter	Value
Material	Aluminum
Number of elements, N	16
Inter-element spacing, d, (mm)	1.4
Element width, a, (mm)	0.5
Total transducer aperture, D, (mm)	22.0
Transducer frequency, f, (MHz)	2.25
Plate thickness, $2h$, (mm)	2.0
$2fh$ value, (MHz-mm)	4.5
Transducer-edge distance, x, (mm)	102.0

Reconstructed Signals $s_n(t)$

The waveforms shown in Fig. 4.5 are synthetic signals ($s_n(t)$ for $n = 16$) reconstructed using Eq. (4.3) with different $\Delta\tau$ values. In particular, the waveforms shown in the shadowed frames are the tuned signals obtained using specific time delays given by Eq. (4.4), i.e., they are the signals synthesized using Eq. (4.5). In all these plots, the first peaks appearing at near $t = 0$ are the waves arriving directly from the transmitting elements to the receiving element. Note that the shape of these peaks changes with varying $\Delta\tau$. This is caused by the numerical delay-sum operations used in the reconstruction processes, but these signals are of no interest to us and can be neglected. The remaining peaks, which capture our interest, arrive after significant delays and represent actual synthetic signals reflected from the discontinuity.

When there is no prescribed time delay between the elements, the array transducer functions similar to a single rectangular transducer directly placed on the surface of the plate. Thus, the signal shown on the upper left corner ($\Delta\tau = 0$) displays all untuned modes. As $\Delta\tau$ increases, the characteristics of synthetic waveforms, such as arrival times and peak amplitudes, are changing dramatically.

It should be pointed out that the synthetic wave is received by only one element (element #16) and the tuning procedure is only half-way through. The tuned signals synthesized up to this step still contain additional wave modes introduced by

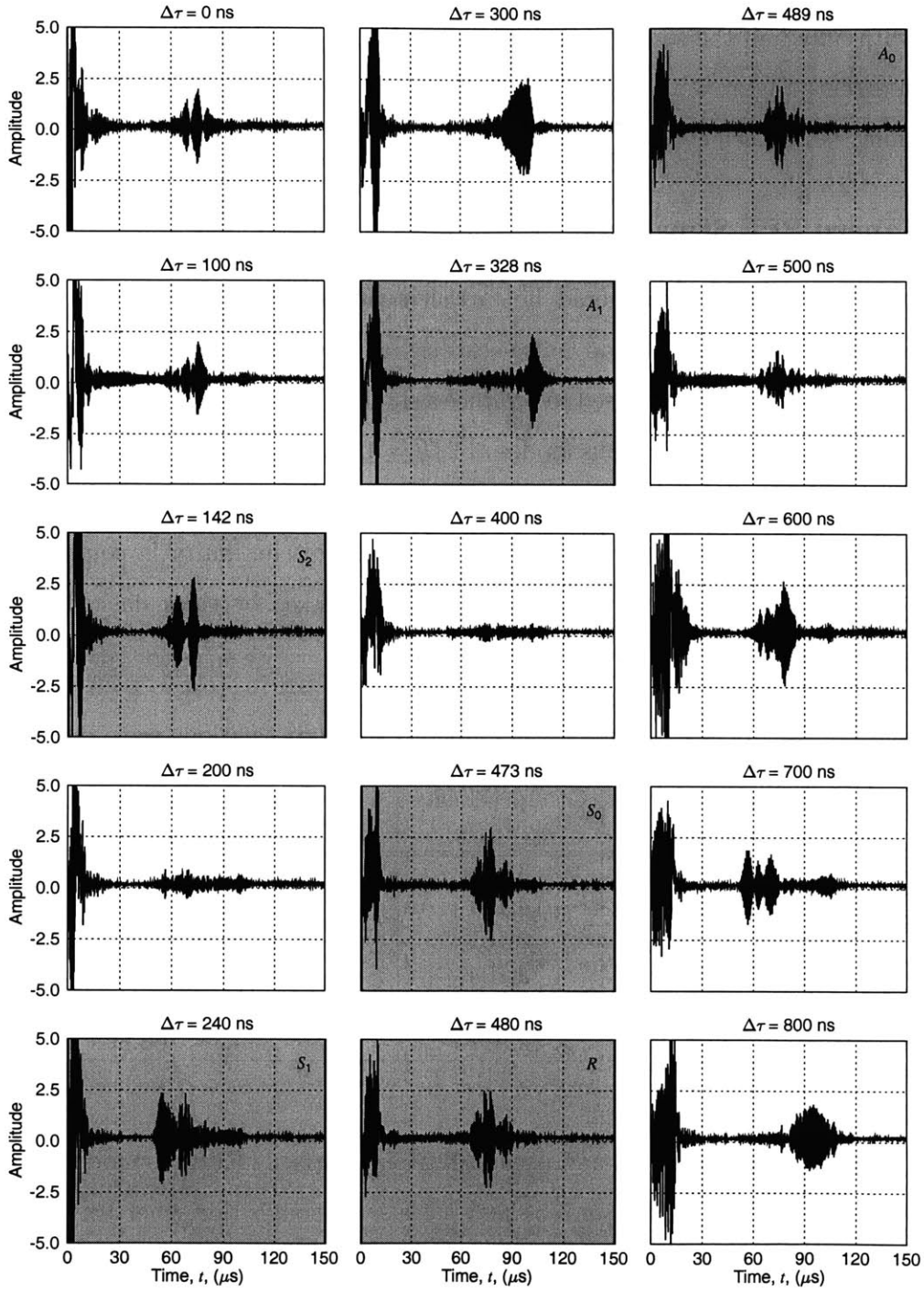

Figure 4.5: Synthetic waveforms reconstructed with different $\Delta\tau$: $s_n(t), n = 16$.

reflections, as explained earlier. The tuned waveforms displayed in the shaded frames reveal several tenacious wave modes coexisting with our desired mode of interest. Even with only half the tuning done, we can still appreciate the effect of tuning to a certain extent. Figure 4.6 shows the half-way tuned signals in the receiving mode. A full tuning can be achieved by combining these two as follows.

Fully-Tuned PPE Signal $s(t)$

The synthetic signals $s_n(t)$ should be further synthesized by Eqs. (4.7) and (4.8) to produce a fully-tuned pseudo pulse-echo signal. Note that the total number of $N(N-1)$ acquired signals are used to produce a single waveform $s(t)$. Figure 4.7 shows these tuned waveforms for various modes at $2fh = 4.5$ MHz-mm. The conditions used in the tuning experiment are tabulated in Table 4.2. The group delay t_g for a tuned wave to make a round trip from element #1 to the discontinuity is computed by Eq. (4.12) and the corresponding arrival times are marked by thick dashed lines in the figures.

Table 4.2: Required experimental parameters for tuning various wave modes.

Wave mode	Phase velocity c_p, (m/s)	Group velocity c_g, (m/s)	Time delay $\Delta\tau$, (ns)	Wedge Angle θ_w, (deg)
S_2	9,846	3,568	142	16.0
S_1	5,834	4,171	240	27.8
A_1	4,269	2,161	328	39.6
S_0	2,961	2,704	473	66.7
A_0	2,861	2,980	489	71.9
R	2,917	2,917	480	68.8

The tuning effect for S_2, S_1 and pseudo-Rayleigh surface (R) wave modes is quite clear as shown in Figs. 4.7(a), 4.7(b) and 4.7(f). Although the other wave modes are still observable, they have been significantly reduced and the desired tuning wave mode becomes dominant. Note the excellent agreement between the estimation and the true signal on arrival time. By contrast, it seems that the tuning effects for S_0 and A_0 modes are not as obvious. The required time delays for these modes ($\Delta\tau = 473$ ns

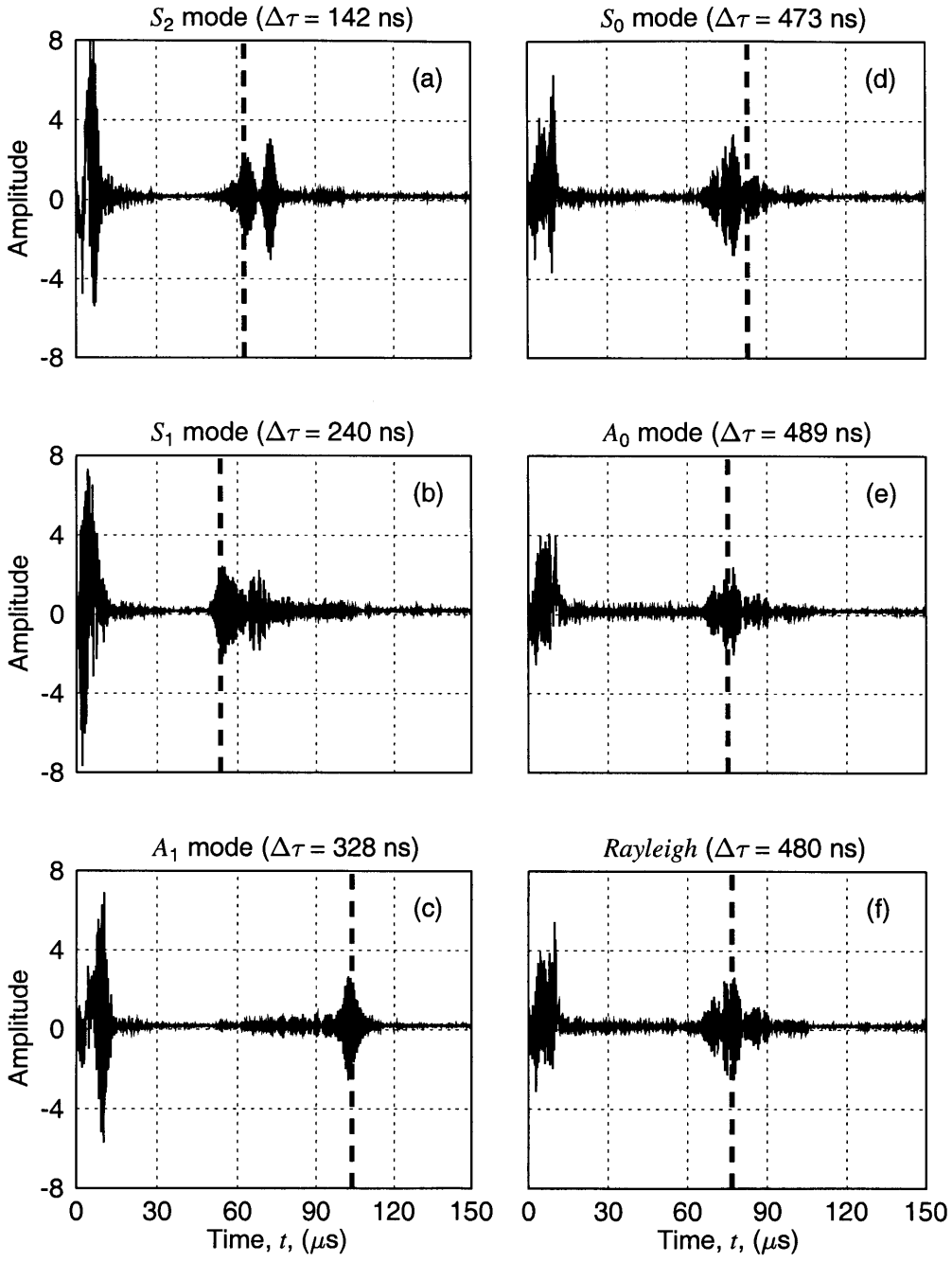

Figure 4.6: Synthetic waveforms reconstructed with different $\Delta\tau$: $s_n(t), n = 16$.

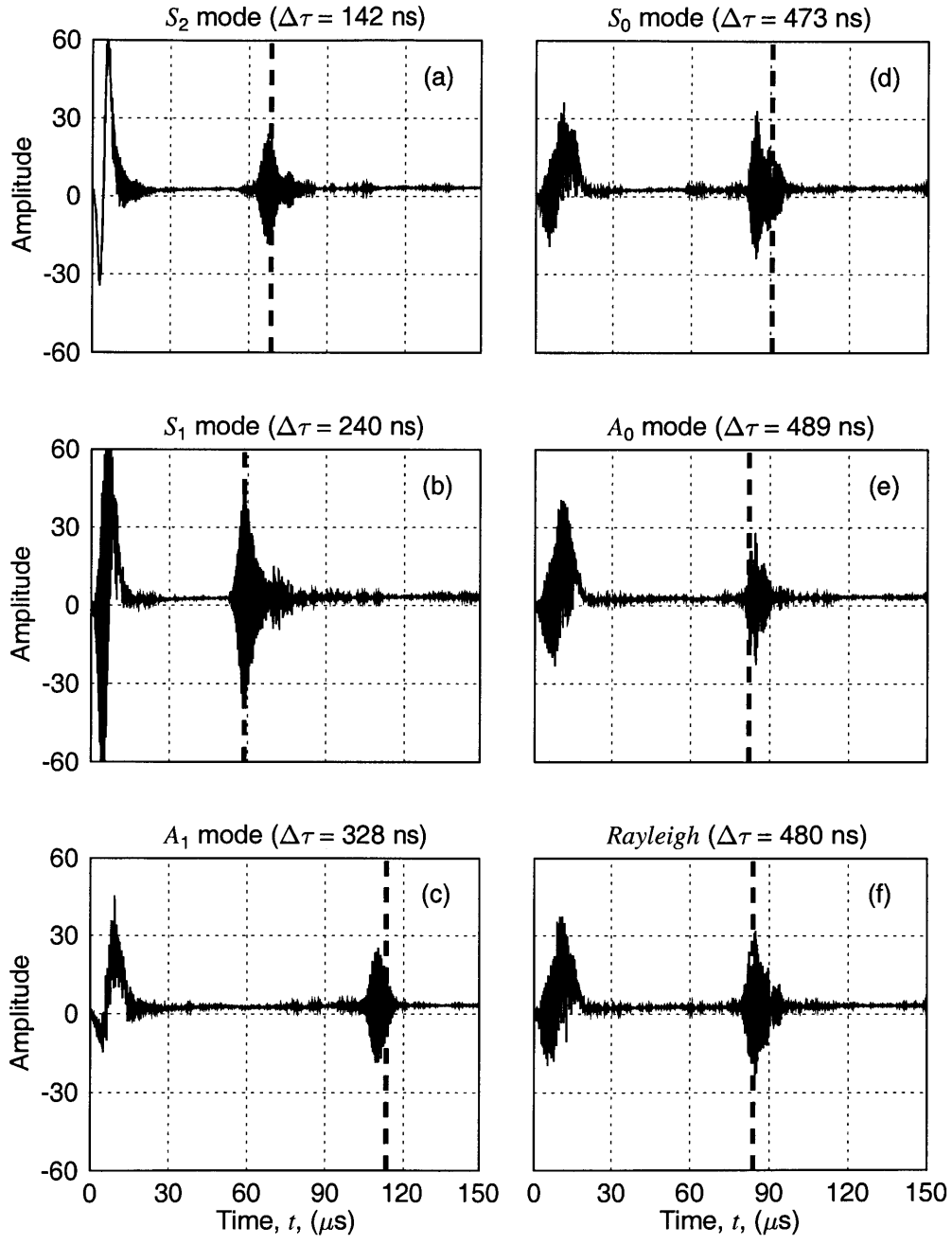

Figure 4.7: Phase-tuned PPE signals for various Lamb wave modes at $2fh = 4.5$ MHz-mm in aluminum.

for S_0, and $\Delta\tau = 489$ ns forA_0 mode, respectively) are close to that of the surface wave ($\Delta\tau = 480$ ns). As this occurs, the surface wave is always dominant in the waveforms shown in Figs. 4.7(d), 4.7(e) and 4.7(f). This may be explained by taking signal amplitudes into consideration in the analysis.

It is interesting to note that the S_1 mode disappears completely in the R-wave tuned waveform (Fig. 4.7(f)). This is another great advantage of our approach over traditional comb transducers. Since the required time delay ($\Delta\tau = 480$ ns) for the R-wave tuning is exactly twice that of the S_1 mode excitation ($\Delta\tau = 240$ ns), the elements of the comb transducer are activated for tuning the S_1 mode as well. By contrast, in our approach, the elements are individually energized exactly at the given time so that they are not interfering with each other. Figure 4.7(c) indicates that there is some difference between the actual arrival time of the maximum peak amplitude signal and the estimated arrival time of the A_1 mode.

Directionality of Emitting Waves

It was mentioned earlier that one of the main advantages of the SPT method is that we can choose the preferred direction of wave propagation. More specifically, it is possible for us to allow a synthetic wave to propagate in either direction using the same set of measured signals. This means that one can perform inspections in either direction. In order to allow the wave to propagate in the negative direction, we can use negative time delays

$$\Delta\tau' = \Delta\tau = -\frac{d}{c_p}\,, \tag{4.13}$$

or simply reverse the element index. In both cases, the wave propagation sequence is also reversed such that the wave is initiated by element N.

Although we intend to make a preferred propagation direction, there will always be some waves traveling in the opposite direction as well. However, we may argue that these waves are not sequentially amplified and their signal amplitudes may be much smaller than those of the tuned waves traveling in the given direction. In order

to study the significance of such waves traveling in the reverse direction, the following numerical experimentation is made.

Suppose that we want to inspect the negative direction of the transducer using the same set of data acquired by the same procedure. This mission can be achieved by entering the negative time delay given by Eq. (4.13). What is of our interest here is to construct another synthetic wave emitted in the positive direction and received by the transducer using the same receiving sequence set for the wave returning from the negative direction, i.e., we set the negative time delay

$$\Delta\tau' = -\Delta\tau = -\frac{d}{c_p} . \tag{4.14}$$

A signal constructed in this fashion appears as additional ghost peaks interfering with the PPE signal, if there exists a discontinuity in the direction opposite to the inspection direction. A comparison of the two waveforms with positive and negative delays may provide us with a clue as to how much energy travels in the reverse direction.

Figure 4.8 shows the waveforms, demonstrating the advantage of the SPT method over the other array techniques. Note that there is a slight time shift of the peaks between the two sets of signals. This is mainly because the starting element of the two configurations are different. That is, element #1 initiates the wave propagating in the forward direction, and likewise, element #16 initiates the wave in the opposite direction. We can observe from these waveforms that their signal amplitudes are generally smaller than those shown in Fig. 4.7. The cancellation effect for some wave modes (S_2 and A_1) is quite dramatic but the effect for the other modes is not entirely satisfactory.

Discussion

From these experimental results, we may make the following conclusions:

- The best wave mode for inspecting a 2 mm thick aluminum plate at 2.25 MHz is perhaps S_2. This conclusion is based on the observations that the amplitude

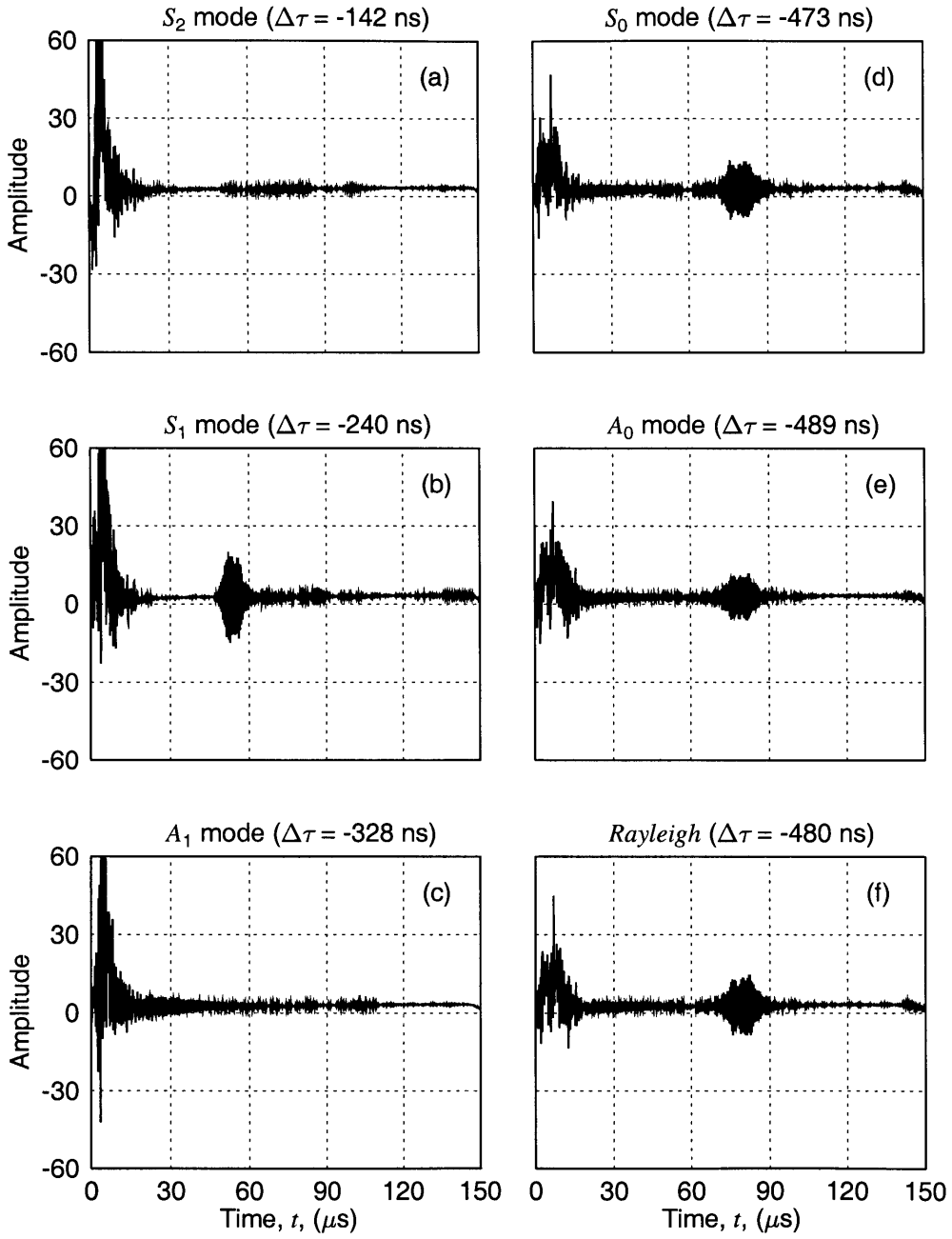

Figure 4.8: Synthetic waveforms emitted in the backward direction.

of the S_2 wave propagating in the desired direction is significantly boosted while the one in the negative direction is virtually canceled out, and that the predicted group delay for this mode exactly matches that of the main peak in the waveform. From the same point of view, the A_1 mode is a good choice but we have to first understand the error in the arrival time in the forward direction.

- The S_1 mode has good forward propagation characteristics, but in the reverse direction, it produces relatively high ghost signal amplitudes. The use of this mode may also be a good choice, but we should be aware of the potential existence of ghost signals if there is a reflection from the opposite side of the transducer.

- It is not recommended to use S_0 or A_0 modes, since the group velocities of these waves are close to that of surface wave velocity, resulting in close signal arrival times. These modes also produce considerably higher ghost signals.

These conclusions may be too hasty since these observations are valid only under this particular experimental condition and may not be generalized. It is certainly desirable to establish a general guideline for choosing frequency and wave mode, but for this, a more rigorous study is necessary. Nevertheless, suggestions for specific conditions can be made by a similar experimental procedure described in this investigation.

4.6 Conclusions

The SPT method allows us to enhance the tuning capability while adding more flexibility without sacrificing the advantages of angle wedge or comb transducer tuning techniques. Its validity and robustness have been demonstrated by the experimental results. Despite the fact that the noise introduced in SPT is higher than that in the phased array tuning approach, SPT is a preferred approach to implement the dynamic phase tuning concept. The benefits of SPT technique can be summarized as follows:

1. Given the plate thickness and transducer frequency, the array can tune virtually any Lamb wave mode.

2. The technique requires only one coupling interface between the transducer and the target material. This results in reduced dead zone and enhanced SNR.

3. Unlike the comb transducer technique, SPT technique can produce strong signals favoring a particular direction. Thus, we may inspect complex structures with minimized interference introduced by the reflections from the unwanted direction.

4. It is possible to tune different wave modes dynamically without mechanically aligning or relocating the transducer. Measurement is made only once and the dynamic tuning is performed numerically either by real-time or off-line processes. This may allow us to implement a fully automated inspection procedure, which may reduce the inspection times.

5. The SPT technique is capable of accurate control and recording of signals from individual elements. Isolated electronics allows for synthesized reconstruction of tuned signals with very high spatial resolution.

6. In the SPT scheme, the time delay profile can be set with high precision. It is only limited by the maximum sampling rate of the recording device. A delay shift and summing algorithm can be used in real-time without storing individual waveforms. This can be achieved using Eq. (4.9).

7. The implementation of the SPT scheme may be cost-effective since existing equipment setup for similar tests may be easily modified by adding a multiplexer.

Another noticeable point is that the tuning efficiency is different for different modes. In other words, some wave modes are tuned quite well while the others are not. Understanding this behavior is very important for selecting the modes. This

requires an analysis of transient Lamb waves under various loading conditions, which will be explored in Chapter 5.

Finally, it should be addressed that the time-domain processing technique described in this work is currently limited to narrow-band signals. Only one frequency is investigated at a time to be least disturbed from the dispersion effect. The entire dispersion can be studied by sweeping the frequency over the range of interest.

Chapter 5

Transient Waves in Elastic Plates

5.1 Introduction

It was shown in Chapter 4 that Lamb wave modes can be effectively tuned using the synthetic phase tuning (SPT) method. It is desired to select wave modes that have excellent tuning capability for achieving high SNR. However, we also notice that different wave modes demonstrated different tuning capabilities. In other words, some modes were tuned well while some were not. In essence, this necessitates the analysis of transient waves for a given source of excitation, which will help us understand the reason why one mode has higher amplitude than another. Since this is critical for the applications of Lamb waves, much efforts have been made to analyze transient Lamb waves in elastic plates. Currently there are two mainstream analytical approaches used widely in this regard, including the *integral transform* method, the *normal mode expansion* method or the equivalent *eigenfunction expansion* method. Besides, numerical methods such as the finite element method are also available.

In the earlier theoretical studies, the problem was generally resolved as a function of input force using the integral transform technique. For the integral transform method, the solutions are obtained by applying the Laplace transform in time and the exponential Fourier or Hankel transform in space. The inverse transformation integrals are carried out by the evaluation of residues in conjunction with the methods of stationary phase approximation or steepest-descent approximation. Viktorov [13] in-

vestigated the problem of Lamb wave generation under a single frequency (harmonic) excitation by an angle wedge transducer, where only the 1-D Fourier transform was applied. There are many other works on the transient wave propagation in elastic waveguides using the integral transform method [23, 32, 65–67].

The alternative analytical approach — normal mode expansion or eigen function expansion method was extensively discussed by Auld [31] and Kino [68], and Ering and Şububi [69]. The principle is to express the perturbed field as the sum of normal modes obtained in a traction free waveguide. The expansion amplitude of each mode is determined via the average power flow using the complex reciprocity relation and orthogonality of eigenmodes. Ditri and Rose [70] examined the excitation of guided wave modes by finite sources using the normal mode expansion method. The displacement response of the generated modes to a transient loading is the integral of the displacement response to a harmonic excitation over the frequency range. The amplitudes of the generated modes were expressed as the product of an "excitation function" and an "excitability function". With the normal mode expansion method, Jia [71] did modal analysis of Lamb wave generation in elastic plates by liquid wedge transducers, taking into account the effects of wave reflection and radiation. In their work, Núñez *et al* [72] used the normal mode expansion method to derive a tensorial transfer and Green functions for Lamb wave generation. The tensorial transfer function determined the impulse response (temporal and spatial) for symmetric and antisymmetric Lamb wave displacements. Li and Berthelot [73] formulated a normal mode expansion solution for transient excitation of circumferential waves in a thick annulus.

Besides the two above analytical methods, finite element method has been applied to transient Lamb waves. Al-Nasser *et al* [74] employed a combined finite element and normal mode expansion method to investigate the interaction of Lamb waves with defects in an elastic plate. Alleyne and Cawley [16–18] used finite element method to predict the propagation of Lamb waves in elastic plates with and without defects. Moser *et al* [75] studied Lamb wave propagation in an elastic plate and annular ring using the finite element method. To identify and measure the amplitudes of individual

Lamb wave modes, Alleyne and Cawley [16–18] also applied two-dimensional Fourier transform (2-D FT) to the predicted waves.

Among the analytical and experimental tools available, the 2-D FT method is of particular interest to us since it can used to measure the amplitudes and velocities of Lamb waves. The 2-D FT approach is based on the spectral analysis of Lamb wave signals in the frequency-wavenumber domain. In this method, signals measured at many sequential points along the wave propagation direction are processed in two phases. Individual signals are first transformed from the time domain to the frequency domain, and then the transformed set of signals are transformed again from the space domain to the wavenumber domain. The net result of this operation is a set of dispersion curves presented in the frequency-wavenumber domain, providing both the amplitude and phase velocity information of the Lamb wave modes.

In contrast to the treatment of experimental Lamb wave signals, however, theoretical treatments of transient Lamb waves using the 2-D FT are rarely found, according to our knowledge. A possible reason to this might be that the integral transform method and normal mode (eigenfunction) expansion method are dominant and do provide the solution of displacements for Lamb waves in an elastic plate subject to external loading.

This chapter is divided into two parts. In the first part, the 2-D FT will be used to analyze the transient Lamb waves. Instead of finding the displacements of individual modes and summing them, we directly obtain the 2-D FT of the displacements expressed in the frequency-wavenumber domain. This analysis is extended to derive the displacements induced by an arbitrary transient loading. The overall and modal excitation efficiencies are computed and the results are compared with those obtained by other methods. In the second part, the results from our analytical method will be compared with those from the finite element method.

5.2 Transient Response to an External Loading

5.2.1 Problem Statement

Consider an isotropic plate of thickness $2h$ loaded by an arbitrary traction $f(x,t)$. The problem geometry along with the coordinate system is shown in Fig. 5.1, in which the stress boundary conditions are prescribed as

$$\sigma_{zz}(x,t) = \begin{cases} f(x,t) & \text{at} \quad z = +h \\ 0 & \text{at} \quad z = -h \end{cases} \tag{5.1}$$

$$\sigma_{xz}(x,t) = 0 \qquad \text{at} \quad z = \pm h\,, \tag{5.2}$$

Assuming the state of plane strain, the equations of motion can be expressed in terms of displacements as:

$$\begin{aligned} (\lambda+\mu)\left(\frac{\partial^2 u_x}{\partial x^2} + \frac{\partial^2 u_z}{\partial x \partial z}\right) + \mu\left(\frac{\partial^2 u_x}{\partial x^2} + \frac{\partial^2 u_x}{\partial z^2}\right) &= \rho\frac{\partial^2 u_x}{\partial t^2} \\ (\lambda+\mu)\left(\frac{\partial^2 u_x}{\partial z \partial x} + \frac{\partial^2 u_z}{\partial z^2}\right) + \mu\left(\frac{\partial^2 u_z}{\partial x^2} + \frac{\partial^2 u_z}{\partial z^2}\right) &= \rho\frac{\partial^2 u_z}{\partial t^2}\,, \end{aligned} \tag{5.3}$$

where λ and μ are Lamé constants, and ρ is the mass density.

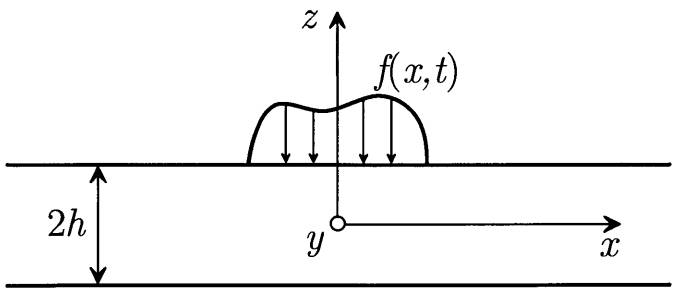

Figure 5.1: Problem geometry. An isotropic plate of thickness $2h$ is loaded by an arbitrary traction $f(x,t)$ on the top surface ($z = h$).

Our objective is to obtain the 2-D FT of the displacements $u_n(z,x,t)$ induced by the loading $f(x,t)$, which is defined as

$$\hat{u}_n(z,k,\omega) = \int_{-\infty}^{+\infty}\int_{-\infty}^{+\infty} u_n(z,x,t)e^{-j(kx-\omega t)}dxdt\ , \tag{5.4}$$

where k and ω are the wavenumber and angular frequency. The subscript n denotes the axis, i.e., $n = x$ (in-plane) or $n = z$ (out-of-plane). Correspondingly, the inverse FT is defined as

$$u_n(z,x,t) = \frac{1}{4\pi^2}\int_{-\infty}^{+\infty}\int_{-\infty}^{+\infty} \hat{u}_n(z,k,\omega)e^{j(kx-\omega t)}dkd\omega\ , \tag{5.5}$$

The solution $\hat{u}_n(z,k,\omega)$ can be obtained simply by substituting the displacements $u_n(z,x,t)$ in the form of inverse 2-D Fourier transform into the equations of motion and satisfying the boundary conditions. This procedure is described as follows.

5.2.2 Two-Dimensional Fourier Transform

The derivatives of $u_x(z,x,t)$ and $u_z(z,x,t)$ with respect to the variables x, z and t are obtained as

$$\frac{\partial u_x}{\partial x} = \frac{1}{4\pi^2}\int_{-\infty}^{+\infty}\int_{-\infty}^{+\infty} (jk)\hat{u}_x \exp[j(kx-\omega t)]dkd\omega \tag{5.6}$$

$$\frac{\partial^2 u_x}{\partial x^2} = \frac{1}{4\pi^2}\int_{-\infty}^{+\infty}\int_{-\infty}^{+\infty} (-k^2)\hat{u}_x \exp[j(kx-\omega t)]dkd\omega \tag{5.7}$$

$$\frac{\partial^2 u_x}{\partial x \partial z} = \frac{1}{4\pi^2}\int_{-\infty}^{+\infty}\int_{-\infty}^{+\infty} (jk)\frac{d\hat{u}_x}{dz} \exp[j(kx-\omega t)]dkd\omega \tag{5.8}$$

$$\frac{\partial^2 u_x}{\partial t^2} = \frac{1}{4\pi^2}\int_{-\infty}^{+\infty}\int_{-\infty}^{+\infty} (-\omega^2)\hat{u}_x \exp[j(kx-\omega t)]dkd\omega\ , \tag{5.9}$$

and

$$\frac{\partial u_z}{\partial z} = \frac{1}{4\pi^2}\int_{-\infty}^{+\infty}\int_{-\infty}^{+\infty}\frac{d\hat{u}_z}{dz}\exp[j(kx-\omega t)]dkd\omega \tag{5.10}$$

$$\frac{\partial^2 u_z}{\partial z^2} = \frac{1}{4\pi^2}\int_{-\infty}^{+\infty}\int_{-\infty}^{+\infty}\frac{d^2\hat{u}_z}{dz^2}\exp[j(kx-\omega t)]dkd\omega \tag{5.11}$$

$$\frac{\partial^2 u_z}{\partial z \partial x} = \frac{1}{4\pi^2}\int_{-\infty}^{+\infty}\int_{-\infty}^{+\infty}(jk)\frac{d\hat{u}_z}{dz}\exp[j(kx-\omega t)]dkd\omega \tag{5.12}$$

$$\frac{\partial^2 u_z}{\partial t^2} = \frac{1}{4\pi^2}\int_{-\infty}^{+\infty}\int_{-\infty}^{+\infty}(-\omega^2)\hat{u}_z\exp[j(kx-\omega t)]dkd\omega\ . \tag{5.13}$$

By substituting these into the governing equations of motion or Eqs. (5.3), we would have the ordinary differential equations:

$$\mu\frac{d^2\hat{u}_x}{dz^2} + [(\lambda+\mu)(jk)]\frac{d\hat{u}_z}{dz} + [\rho\omega^2 - k^2(\lambda+2\mu)]\hat{u}_x = 0 \tag{5.14}$$

$$(\lambda+2\mu)\frac{d^2\hat{u}_z}{dz^2} + [(\lambda+\mu)(jk)]\frac{d\hat{u}_x}{dz} + [\rho\omega^2 - k^2\mu]\hat{u}_z = 0\ . \tag{5.15}$$

Solving, the general solutions of $\hat{u}_n(z,k,\omega)$ can be written in the form:

$$\hat{u}_x = \{jA_sk\cosh(\alpha z) - D_s\beta\cosh(\beta z)\} + \{jB_ak\sinh(\alpha z) - C_a\beta\sinh(\beta z)\} \tag{5.16}$$

$$\hat{u}_z = \{A_s\alpha\sinh(\alpha z) + jD_sk\sinh(\beta z)\} + \{B_a\alpha\cosh(\alpha z) + jC_ak\cosh(\beta z)\}\ , \tag{5.17}$$

where the parameters α and β are defined as

$$\alpha^2 = k^2 - \frac{\omega^2}{c_L^2}\ , \qquad \beta^2 = k^2 - \frac{\omega^2}{c_T^2}\ , \tag{5.18}$$

and c_L and c_T are the longitudinal and transverse wave velocities, respectively. A_s, D_s, B_a and C_a are the constants to be determined from the stress boundary conditions. Then the displacements in terms of these constants using Eq. (5.5).

Since the stresses re related to the displacements by virtue of the constitutive law:

$$\sigma_{zz} = (\lambda+2\mu)\frac{\partial u_z}{\partial z} + \lambda\frac{\partial u_x}{\partial x}\ , \qquad \sigma_{zx} = \mu\left(\frac{\partial u_z}{\partial x} + \frac{\partial u_x}{\partial z}\right)\ , \tag{5.19}$$

the stresses can be expressed in terms of the constants A_s, D_s, B_a and C_a, i.e.,

$$\begin{aligned}\sigma_{zz} =& \frac{1}{4\pi^2}\int_{-\infty}^{+\infty}\int_{-\infty}^{+\infty}\Big[(\lambda+2\mu)\alpha^2-\lambda(k^2)\Big]\Big[A_s\cosh(\alpha z)+B_a\sinh(\alpha z)\Big]e^{j(kx-\omega t)}dkd\omega + \\ & \frac{1}{4\pi^2}\int_{-\infty}^{+\infty}\int_{-\infty}^{+\infty}\Big[2\mu k\beta\Big]\Big[jD_s\cosh(\beta z)+jC_a\sinh(\beta z)\Big]e^{j(kx-\omega t)}dkd\omega\ ,\end{aligned} \tag{5.20}$$

and

$$\begin{aligned}\sigma_{zx} =& \frac{\mu}{4\pi^2}\int_{-\infty}^{+\infty}\int_{-\infty}^{+\infty}\Big[2k\alpha\Big]\Big[jA_s\sinh(\alpha z)+jB_a\cosh(\alpha z)\Big]e^{j(kx-\omega t)}dkd\omega - \\ & \frac{\mu}{4\pi^2}\int_{-\infty}^{+\infty}\int_{-\infty}^{+\infty}\Big[k^2+\beta^2\Big]\Big[D_s\sinh(\beta z)+C_a\cosh(\beta z)\Big]e^{j(kx-\omega t)}dkd\omega\ .\end{aligned} \tag{5.21}$$

In the meantime, the stress boundary conditions can be expressed via the inverse 2-D FT as

$$\sigma_{zz}(x,t) = \begin{cases}\dfrac{1}{4\pi^2}\displaystyle\int_{-\infty}^{+\infty}\int_{-\infty}^{+\infty}\hat{f}(k,\omega)e^{j(kx-\omega t)}dkd\omega & \text{at} \quad z=+h \\ 0 & \text{at} \quad z=-h\end{cases} \tag{5.22}$$

$$\sigma_{xz}(x,t) = 0 \qquad \text{at} \quad z=\pm h \tag{5.23}$$

where $\hat{f}(k,\omega)$ is the 2-D FT of the traction $f(x,t)$:

$$\hat{f}(k,\omega) = \int_{-\infty}^{+\infty}\int_{-\infty}^{+\infty} f(x,t)e^{-j(kx-\omega t)}dxdt\ . \tag{5.24}$$

By satisfying the stress boundary conditions, the constants are determined as

$$A_s = \frac{(k^2+\beta^2)\sinh(\beta h)\cdot\hat{f}(k,\omega)}{2\mu\Delta_s}\ , \qquad D_s = \frac{jk\alpha\sinh(\alpha h)\cdot\hat{f}(k,\omega)}{\mu\Delta_s}\ , \tag{5.25}$$

$$B_a = \frac{(k^2+\beta^2)\cosh(\beta h)\cdot\hat{f}(k,\omega)}{2\mu\Delta_a}\ , \qquad C_a = \frac{jk\alpha\cosh(\alpha h)\cdot\hat{f}(k,\omega)}{\mu\Delta_a}\ , \tag{5.26}$$

where

$$\Delta_s = (k^2+\beta^2)^2 \cosh(\alpha h)\sinh(\beta h) - 4k^2\alpha\beta \sinh(\alpha h)\cosh(\beta h) \tag{5.27}$$

$$\Delta_a = (k^2+\beta^2)^2 \sinh(\alpha h)\cosh(\beta h) - 4k^2\alpha\beta \cosh(\alpha h)\sinh(\beta h)\ . \tag{5.28}$$

Note that the conditions for $\Delta_s = 0$ and $\Delta_a = 0$ represent the frequency equations for symmetric and antisymmetric Rayleigh-Lamb wave modes, respectively [13].

Using Eqs. (5.16) and (5.17), it is straightforward to compute $\hat{u}_n(z,k,\omega)$ at an arbitrary position z, which can be expressed as the sum of symmetric and antisymmetric parts:

$$\hat{u}_n(z,k,\omega) = \hat{u}_n^a(z,k,\omega) + \hat{u}_n^s(z,k,\omega)\ , \tag{5.29}$$

where

$$\hat{u}_x^s = jk\left[\frac{(k^2+\beta^2)\cosh(\alpha z)\sinh(\beta h) - 2\alpha\beta\cosh(\beta z)\sinh(\alpha h)}{2\mu\Delta_s}\right]\cdot \hat{f}(k,\omega) \tag{5.30}$$

$$\hat{u}_x^a = jk\left[\frac{(k^2+\beta^2)\cosh(\beta h)\sinh(\alpha z) - 2\alpha\beta\cosh(\alpha h)\sinh(\beta z)}{2\mu\Delta_a}\right]\cdot \hat{f}(k,\omega) \tag{5.31}$$

and

$$\hat{u}_z^s = \alpha\left[\frac{(k^2+\beta^2)\sinh(\alpha z)\sinh(\beta h) - 2k^2\sinh(\alpha h)\sinh(\beta z)}{2\mu\Delta_s}\right]\cdot \hat{f}(k,\omega) \tag{5.32}$$

$$\hat{u}_z^a = \alpha\left[\frac{(k^2+\beta^2)\cosh(\alpha z)\cosh(\beta h) - 2k^2\cosh(\alpha h)\cosh(\beta z)}{2\mu\Delta_a}\right]\cdot \hat{f}(k,\omega)\ . \tag{5.33}$$

This is the analytical solution representing the transient Lamb waves generated by an arbitrary traction. It can be observed that the 2-D FT $u_n^s(z,k,\omega)$ and $u_n^a(z,k,\omega)$ are the product of two independent terms: the first term is the material response which is dependent only on the material properties, and the second term is the loading in the transformed domain which is dependent only on the loading. For convenience, we denote $N_n^s(z,k,\omega)$ and $N_n^a(z,k,\omega)$ as the material responses for the symmetric and

antisymmetric wave modes, i.e.,

$$\hat{u}_n^s(z,k,\omega) = N_n^s(z,k,\omega)\cdot\hat{f}(k,\omega) \tag{5.34}$$

$$\hat{u}_n^a(z,k,\omega) = N_n^a(z,k,\omega)\cdot\hat{f}(k,\omega)\ , \tag{5.35}$$

where

$$N_x^s(z,k,\omega) = jk\left[\frac{(k^2+\beta^2)\cosh(\alpha z)\sinh(\beta h) - 2\alpha\beta\cosh(\beta z)\sinh(\alpha h)}{2\mu\Delta_s}\right] \tag{5.36}$$

$$N_x^a(z,k,\omega) = jk\left[\frac{(k^2+\beta^2)\cosh(\beta h)\sinh(\alpha z) - 2\alpha\beta\cosh(\alpha h)\sinh(\beta z)}{2\mu\Delta_a}\right], \tag{5.37}$$

and

$$N_z^s(z,k,\omega) = \alpha\left[\frac{(k^2+\beta^2)\sinh(\alpha z)\sinh(\beta h) - 2k^2\sinh(\alpha h)\sinh(\beta z)}{2\mu\Delta_s}\right] \tag{5.38}$$

$$N_z^a(z,k,\omega) = \alpha\left[\frac{(k^2+\beta^2)\cosh(\alpha z)\cosh(\beta h) - 2k^2\cosh(\alpha h)\cosh(\beta z)}{2\mu\Delta_a}\right]. \tag{5.39}$$

Since it is of our particular interest to consider the case on the upper surface, i.e., $z = h$, the corresponding material responses are

$$N_x^s(h,k,\omega) = jk\left[\frac{(k^2+\beta^2)\cosh(\alpha h)\sinh(\beta h) - 2\alpha\beta\sinh(\alpha h)\cosh(\beta h)}{2\mu\Delta_s}\right] \tag{5.40}$$

$$N_x^a(h,k,\omega) = jk\left[\frac{(k^2+\beta^2)\sinh(\alpha h)\cosh(\beta h) - 2\alpha\beta\cosh(\alpha h)\sinh(\beta h)}{2\mu\Delta_a}\right], \tag{5.41}$$

and

$$N_z^s(h,k,\omega) = \alpha\left[\frac{(-k^2+\beta^2)\sinh(\alpha h)\sinh(\beta h)}{2\mu\Delta_s}\right] \tag{5.42}$$

$$N_z^a(h,k,\omega) = \alpha\left[\frac{(-k^2+\beta^2)\cosh(\alpha h)\cosh(\beta h)}{2\mu\Delta_a}\right]. \tag{5.43}$$

In the following, we will discuss the material responses on the surface, i.e., $N_x^s(h,k,\omega)$ and $N_z^s(h,k,\omega)$. For the same reason, the displacements on the surface $u_n(h,x,t)$ will be determined.

5.2.3 Surface Displacements

The surface displacements can be obtained through the inverse FT of $\hat{u}_n(h,k,\omega)$. In a similar way, the displacements are considered as the sum of the symmetric and antisymmetric components:

$$u_n(h,x,t) = u_n^a(h,x,t) + u_n^s(h,x,t)\ , \tag{5.44}$$

where

$$u_n^s(h,x,t) = \frac{1}{4\pi^2}\int_{-\infty}^{+\infty}\int_{-\infty}^{+\infty} N_n^s(h,k,\omega)\cdot\hat{f}(k,\omega)\cdot e^{j(kx-\omega t)}dkd\omega \tag{5.45}$$

$$u_n^a(h,x,t) = \frac{1}{4\pi^2}\int_{-\infty}^{+\infty}\int_{-\infty}^{+\infty} N_n^a(h,k,\omega)\cdot\hat{f}(k,\omega)\cdot e^{j(kx-\omega t)}dkd\omega\ . \tag{5.46}$$

Since the functions $N_n^s(h,k,\omega)$ and $N_n^a(h,k,\omega)$ contain an infinitely large number of poles corresponding to the roots of the Rayleigh-Lamb dispersion equations, it is convenient to use the residue theorem for evaluating the integrals over the wavenumber k. The integral over the wavenumber k can be evaluated by integrating in the complex k-plane along the contour shown in Fig. 5.2. The contour contains the real k-axis and a semi-circle on the upper half of the complex k-plane. The contributions to the perturbed displacement fields come from all the residues of the integrand within the contour. For a given frequency, there are finite number of real poles and an infinite number of complex poles with nonzero imaginary parts within the contour for the given integrand. Since the superposition of two modes with complex wavenumbers, $\hat{u}(h,k,\omega) + \hat{u}(h,k^*,\omega)$, forms a standing wave without carrying any energy from the source, the only modes propagating in the far field are those with real wavenumbers. Solving, both the in-plane and out-of-plane surface displacements are obtained as

$$u_n^s(h,x,t) = \frac{1}{2\pi}\int_{-\infty}^{+\infty}\sum_{k_s} H_n^s(h,\omega)\cdot\hat{f}(k,\omega)\cdot e^{j(kx-\omega t)}d\omega \tag{5.47}$$

$$u_n^a(h,x,t) = \frac{1}{2\pi}\int_{-\infty}^{+\infty}\sum_{k_a} H_n^a(h,\omega)\cdot\hat{f}(k,\omega)\cdot e^{j(kx-\omega t)}d\omega \tag{5.48}$$

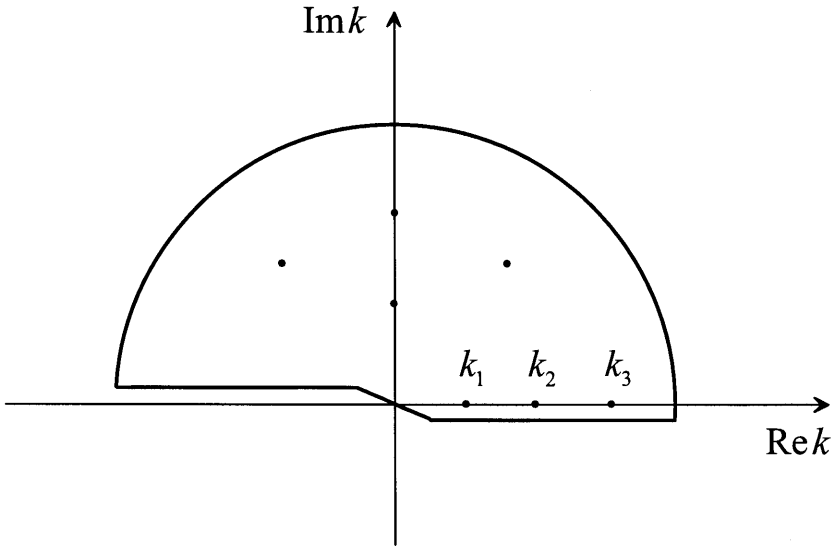

Figure 5.2: The contour of integration in the complex k-plane with poles in the upper half plane.

where $H_n^s(h,\omega)$ and $H_n^s(h,\omega)$ are the material responses of the individual modes, expressed as

$$H_x^s(h,\omega) = \frac{-j(k^4-\beta^4)\cosh(\alpha h)\sinh(\beta h)}{8\mu\Delta_s'} \tag{5.49}$$

$$H_x^a(h,\omega) = \frac{-j(k^4-\beta^4)\sinh(\alpha h)\cosh(\beta h)}{8\mu\Delta_a'} \tag{5.50}$$

$$H_z^s(h,\omega) = \frac{-j\alpha(k^2-\beta^2)\sinh(\alpha h)\sinh(\beta h)}{4\mu\Delta_s'} \tag{5.51}$$

$$H_z^a(h,\omega) = \frac{-j\alpha(k^2-\beta^2)\cosh(\alpha h)\cosh(\beta h)}{4\mu\Delta_a'}\,. \tag{5.52}$$

Here Δ_s' and Δ_a' represent the derivatives of Δ_s and Δ_a with respect to the wavenumber k:

$$\begin{aligned}\Delta_s' =& 8k(k^2+\beta^2)\cosh(\alpha h)\sinh(\beta h) - 8k\alpha\beta\sinh(\alpha h)\cosh(\beta h) - \\ & 4hk^3\beta\cosh(\alpha h)\cosh(\beta h) - 4hk^3\alpha\sinh(\alpha h)\sinh(\beta h) + \\ & \frac{hk(k^2+\beta^2)^2\sinh(\alpha h)\sinh(\beta h)}{\alpha} + \frac{hk(k^2+\beta^2)^2\cosh(\alpha h)\cosh(\beta h)}{\beta} - \\ & \frac{4k^3\beta\sinh(\alpha h)\cosh(\beta h)}{\alpha} - \frac{4k^3\alpha\sinh(\alpha h)\cosh(\beta h)}{\beta},\end{aligned} \tag{5.53}$$

and

$$\begin{aligned}\Delta_a' =& 8k(k^2+\beta^2)\sinh(\alpha h)\cosh(\beta h) - 8k\alpha\beta\cosh(\alpha h)\sinh(\beta h) - \\ & 4hk^3\beta\sinh(\alpha h)\sinh(\beta h) - 4hk^3\alpha\cosh(\alpha h)\cosh(\beta h) + \\ & \frac{hk(k^2+\beta^2)^2\cosh(\alpha h)\cosh(\beta h)}{\alpha} + \frac{hk(k^2+\beta^2)^2\sinh(\alpha h)\sinh(\beta h)}{\beta} - \\ & \frac{4k^3\beta\cosh(\alpha h)\sinh(\beta h)}{\alpha} - \frac{4k^3\alpha\cosh(\alpha h)\sinh(\beta h)}{\beta}.\end{aligned} \tag{5.54}$$

Note that the summations are carried out for the real wavenumbers k_s and k_a to represent the propagating waves in the far field.

5.2.4 Excitation Efficiencies

It is shown above that the Fourier responses of the surface displacements can be generally expressed as the product of the material response and the loading term in the transformed domain. Both $N_n(h,k,\omega)$ and $H_n(h,\omega)$ represent the responses of the material to external loading. They are similar, in that they are independent of the loading condition and both represent the efficiency for generating certain modes; they are different, in that the former consists of the terms for all the modes, while the latter is the factored term for individual modes. From this point of view, both functions may be referred to as the *excitation efficiency* of Lamb wave modes.

$N_n(h, k, \omega)$ — Overall Excitation Efficiency

Figure 5.3 displays the out-of-plane excitation efficiency for a steel plate ($c_L = 5850$ m/s, $c_T = 3240$ m/s), in which the intensity or pixel values represent the magnitude of the function $N_z(h, k, \omega)$. By comparing this image plot with the dispersion curves shown in Fig. 5.4, we can observe that the image shows the same dispersion characteristics as those obtained from the Rayleigh-Lamb frequency equations. Moreover, the excitation efficiency plot is more informative than the dispersion curves, since it shows the distribution of energy for all the wave modes in addition to the dispersion relations. For example, it can be observed that the A_0 mode (represented by the curve at the lowest position) carries the highest energy among the existing modes. Likewise, the in-plane excitation efficiency $N_x(h, k, \omega)$ is shown in Fig. 5.5. Although this plot exhibits the same dispersion characteristics, its energy distribution is different from that of Figure 5.3.

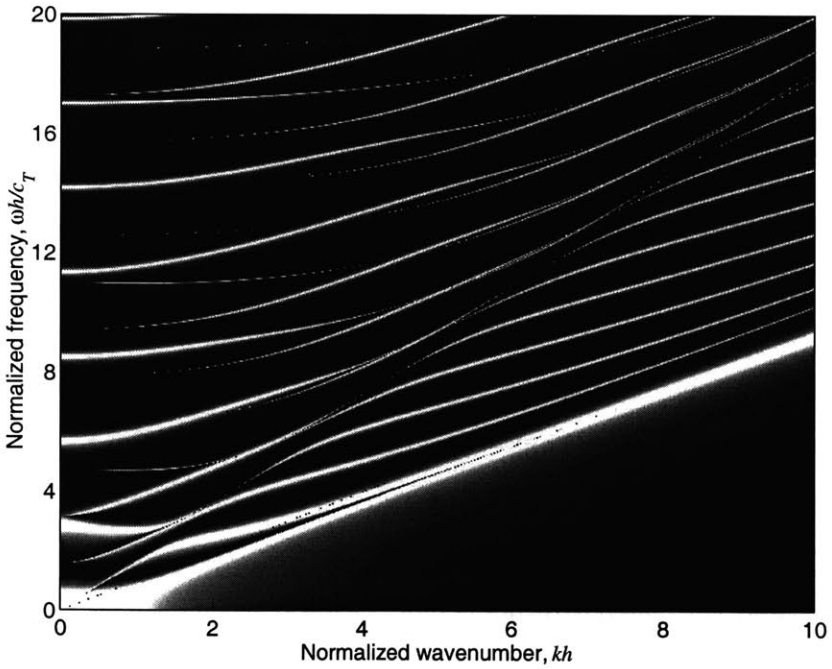

Figure 5.3: Image visualization of material response $N_z(h, k, \omega)$ for out-of-plane Lamb wave modes in a steel plate, where the longitudinal velocity $c_L = 5850$ m/s and transverse velocity $c_T = 3240$ m/s.

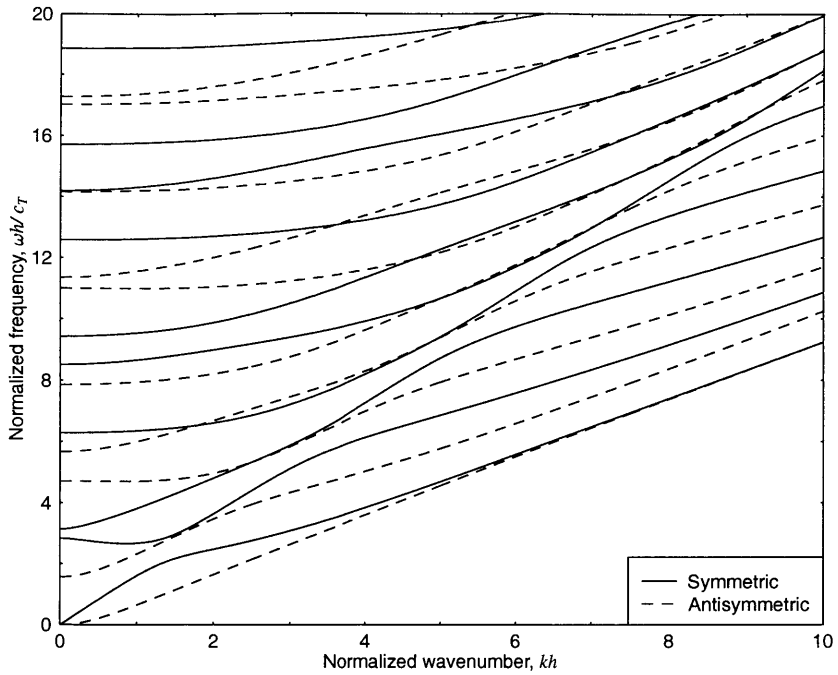

Figure 5.4: Dispersion curves of Lamb wave modes in a steel plate ($c_L = 5850$ m/s and $c_T = 3240$ m/s), where the solid lines stand for symmetric case and dashed lines for the antisymmetric case.

$H_n(h,\omega)$ — Modal Excitation Efficiency

The function $H_n(h,\omega)$ is also a material response function dependent only on the material properties. It is in fact an integral of the function $N_n(h,k,\omega)$ over the wavenumber for certain frequency. Compared with $N_n(h,k,\omega)$, it is a more direct criterion to evaluate the excitation efficiency for each wave mode, which is equivalent to the *excitability function* introduced by Ditri and Rose [70] or the *tensorial transfer function* defined by Núñez *et al* [72]. To differentiate from $N_n(h,k,\omega)$, this function may be referred to as the *modal excitation efficiency.*

In Figs. 5.6 and 5.7, the out-of-plane modal excitation efficiencies of an aluminum plate ($c_L = 6420$ m/s, $c_T = 3040$ m/s), $H_z^s(h,\omega)$ and $H_z^a(h,\omega)$, are plotted as a function of normalized frequency $\omega h/c_T$ for the 10 lowest symmetric and antisymmetric modes. It can be observed from these plots that all the symmetric modes except the S_0 mode produce at least sharp drops at certain frequencies. For example, the S_1

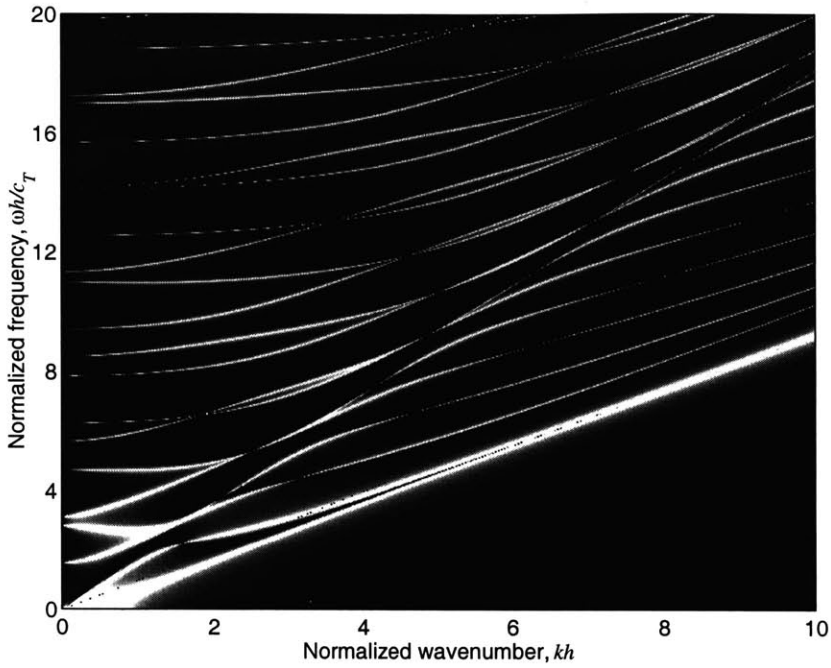

Figure 5.5: Image visualization of material response $N_x(h, k, \omega)$ for in-plane Lamb wave modes in a steel plate, where the longitudinal velocity $c_L = 5850$ m/s and transverse velocity $c_T = 3240$ m/s.

mode has a local minimum near the normalized frequency of 3.5 and the minimum for the S_2 mode occurs at that of 7.2. This means that the wave at those frequencies (at the dips) are not easily generated. It is therefore recommended to avoid excitation at those frequencies. The antisymmetric modes also show similar trends except that both A_0 and A_1 modes have no significant local minimum, as shown in Fig. 5.7. These results are also in good agreement with the tensorial transfer function computed by Núñez *et al* [72]. This confirms that the expressions for the displacements $u_n(z, x, t)$ are essentially the same as those obtained using the normal mode expansion method.

5.2.5 Loading Conditions

We now consider the loading conditions. Although the derived expressions allow us to consider arbitrary loads distributed over an area, we will consider only a point or hairline source at this moment for the sake of simplicity. In other words, we assume

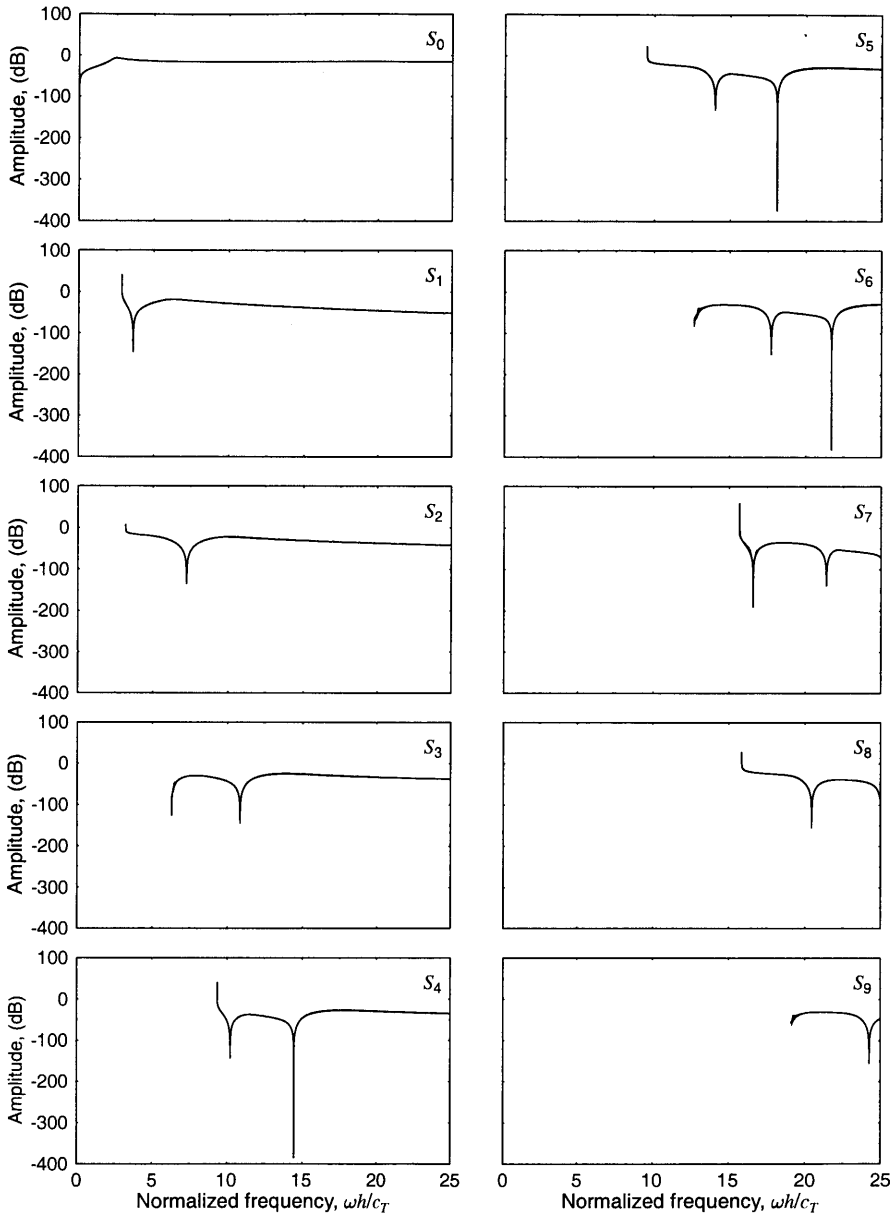

Figure 5.6: The response function $H_z^s(h,\omega)$ for symmetric out-of-plane Lamb wave modes in an aluminum plate, where the longitudinal wave velocity $c_L = 6420$ m/s and transverse wave velocity $c_T = 3040$ m/s.

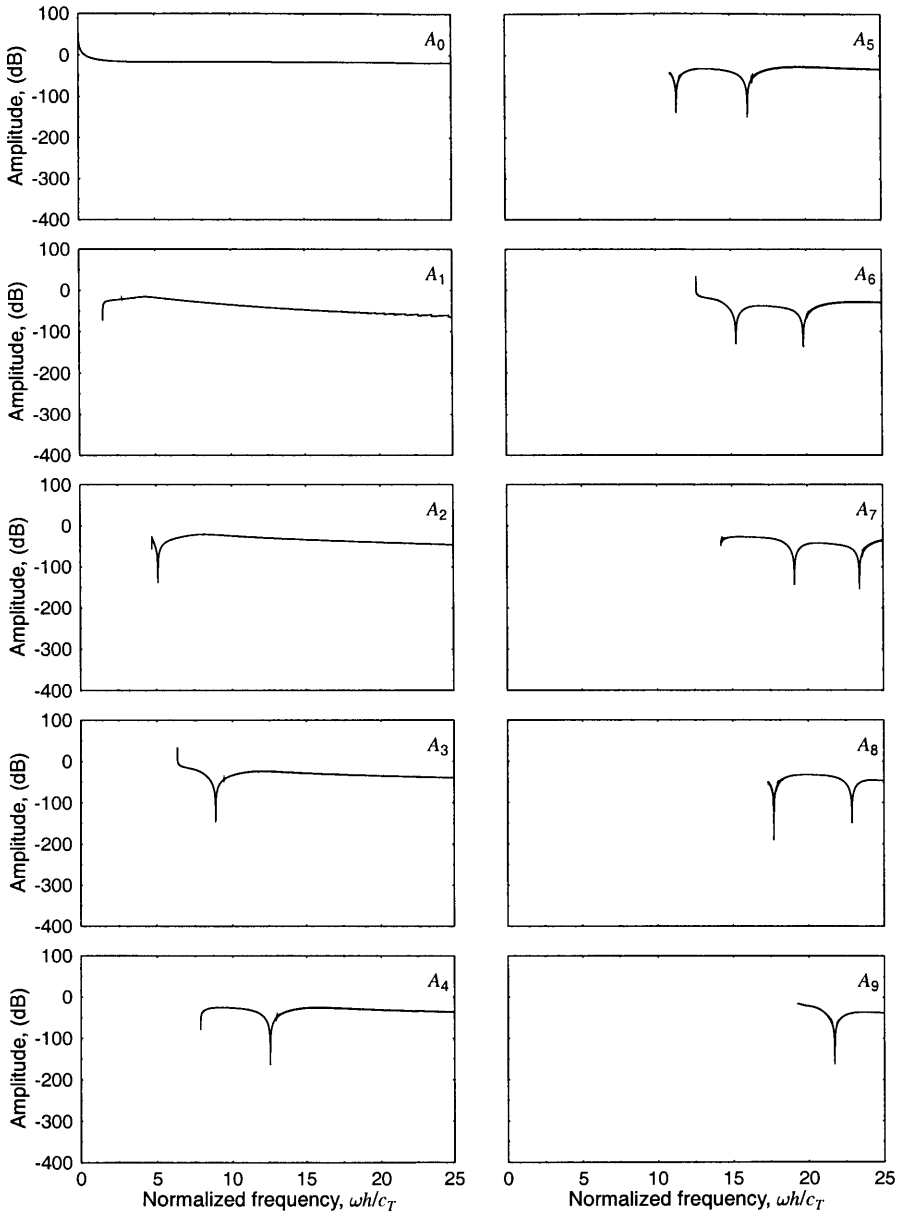

Figure 5.7: The response function $H_z(h, \omega)$ for antisymmetric out-of-plane Lamb wave modes in an aluminum plate, where the longitudinal wave velocity $c_L = 6420$ m/s and transverse wave velocity $c_T = 3040$ m/s.

the traction is of the form:

$$f(x,t) = \delta(x - x_0)g(t) \ , \tag{5.55}$$

so that the excitation response is written as a function of only the frequency ω, i.e.,

$$\hat{f}(k,\omega) = \hat{g}(\omega)e^{-jkx_0} \ , \tag{5.56}$$

where $\delta(x - x_0)$ is a spatial Dirac delta function, x_0 is the source location, and $g(t)$ is a transient excitation signal. For an impulse loading, $g(t) = \delta(t)$, the corresponding Fourier integral is a constant, i.e., $\hat{f}(k,\omega) = 1$, so that the 2-D FT of the displacements are equal to the excitation efficiency as already shown in Figs. 5.3 and 5.5. This means that $N_n(h,k,\omega)$ is the impulse response of the material system.

Without loss of generality, the effect of excitation signal characteristics can be studied by considering a Gaussian spike pulse with the center angular frequency ω_0 and bandwidth B (rad), which can be written as

$$g(t) = \frac{1}{2\pi}e^{-j\omega_0 t}e^{-B^2t^2/8} \ , \tag{5.57}$$

whose Fourier transform is obtained as (see Appendix A)

$$\hat{g}(\omega) = \frac{2}{B\sqrt{2\pi}}e^{-2(\omega-\omega_0)^2/B^2} \ . \tag{5.58}$$

Figures 5.10 and 5.11 show the theoretical 2-D FT of the out-of-plane displacements, $\hat{u}_z(h,k,\omega)$, for a steel plate of thickness $2h = 2$ mm. For comparison, two different bandwidths $B/2\pi = 2.0$ MHz (wide band) and $B/2\pi = 0.5$ MHz (narrow band) are used for the same center frequency $\omega_0/2\pi = 2.25$ MHz. Figures 5.8 and 5.9 depict the waveforms and amplitude spectrum for these two signals.

It is obviously observed that the energy distribution for the broadband excitation signal is relatively uniform over the wide range of frequencies. On the other hand, the distribution is limited in a narrow range of frequencies for the narrow-band excitation

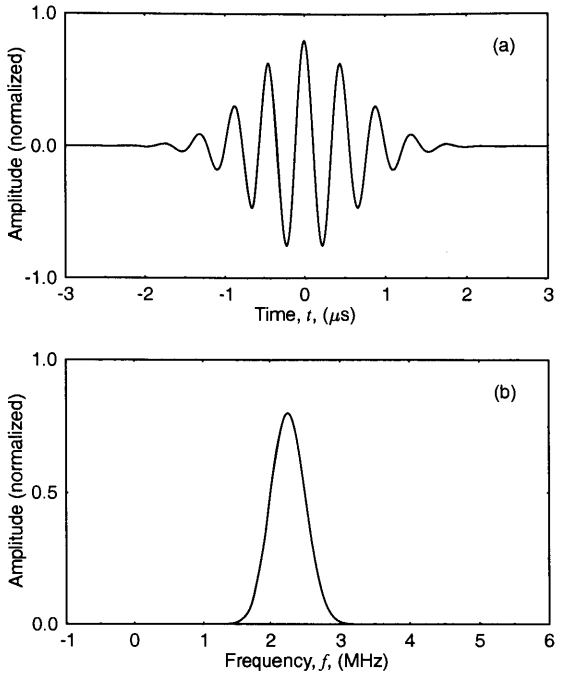

Figure 5.8: Gaussian spike pulse with the center frequency $\omega_0/2\pi = 2.25$ MHz and bandwidth $B/2\pi = 0.5$ MHz (Narrow band case), where (a) is $g(t)$ and (b) is $\hat{g}(\omega)$.

signal. From this reason, the number of well-excited wave modes decreases as the bandwidth is narrowed. Therefore, it can be envisioned that a bandwidth control of excitation signals should be used effectively for exclusively selecting the wave modes of interest.

5.3 Comparison with the FEM Results

It is interesting to compare the results obtained by various approaches. It was shown that our expressions for the displacements are in fact equivalent to those obtained by the normal mode expansion method. In this section, we compare our analytical results with the numerical (FEM) results published by Alleyne and Cawley [16–18]. To do this, it is necessary to review the parameters used in their numerical procedure. In the FEM model, plane strain condition was assumed in the xz plane. A uniform square mesh of four-noded quadrilateral elements was created with more than 10 nodes per

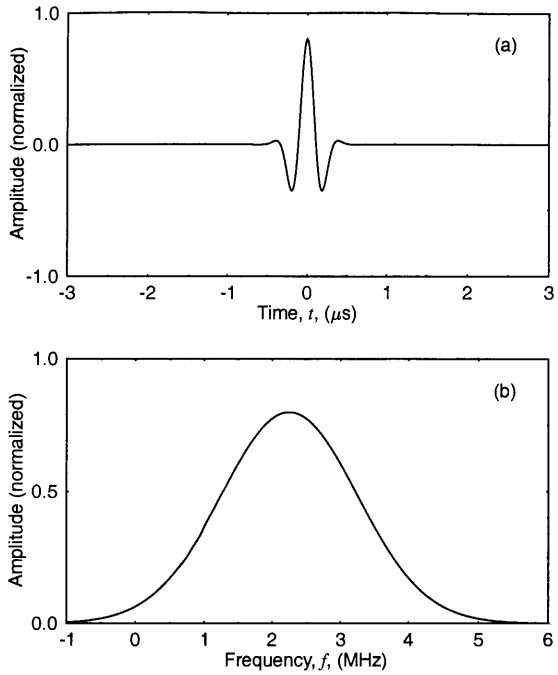

Figure 5.9: Gaussian spike pulse with the center frequency $\omega_0/2\pi = 2.25$ MHz and bandwidth $B/2\pi = 2.0$ MHz (Broad band case), where (a) is $g(t)$ and (b) is $\hat{g}(\omega)$.

wavelength. An explicit central difference scheme was employed to produce the time marching solution, the time step being chosen to be less than the time taken for the longitudinal wave to travel between two adjacent nodes. To control the bandwidth, the input was assumed as a toneburst enclosed in a Hanning window.

5.3.1 Loading Conditions

Consider an m-cycle sinusoidal toneburst with the center frequency f_0 (or angular frequency $\omega_0 = 2\pi f_0$). Accordingly the spatiotemporal traction $f(x,t)$ can be represented as

$$f(x,t) = \delta(x)\exp(-j\omega_0 t)w_H(t)\ , \tag{5.59}$$

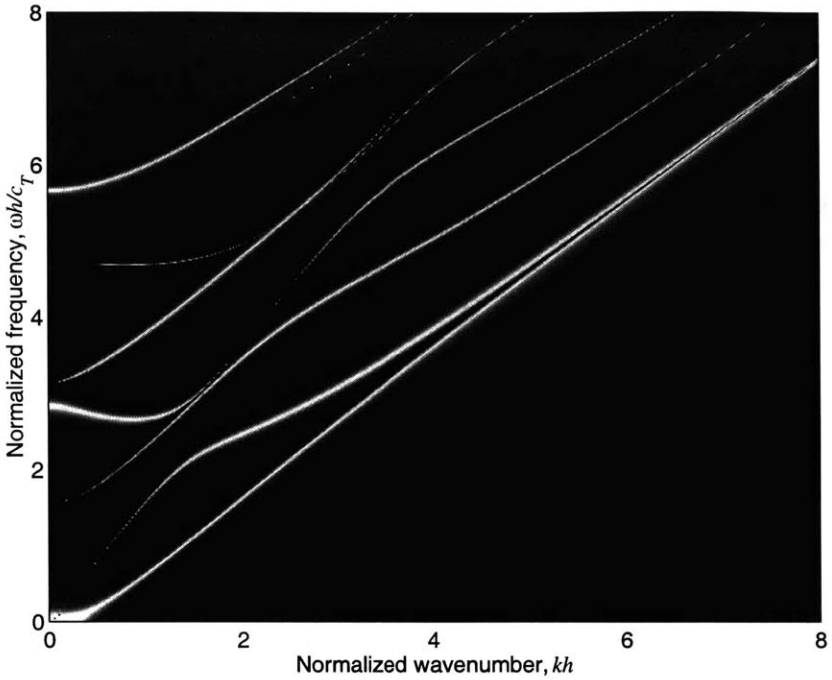

Figure 5.10: Image representing the 2-D FT of the out-of-plane surface displacements, i.e., $\hat{u}_z(h,k,\omega)$ for a steel plate of thickness $2h = 2$ mm ($c_L = 5,850$ m/s and $c_T = 3,240$ m/s) excited by a Gaussian spike pulse with the center frequency $\omega_0/2\pi = 2.25$ MHz and bandwidth $B/2\pi = 2.0$ MHz (Broad band case).

where $w_H(t)$ is the Hanning window of duration $t_0 = m/f_0$ (see Appendix B),

$$\begin{aligned} w_H(t) &= \frac{1}{2}\Big\{1 - \cos(2\pi t/t_0)\Big\}\Big\{H(t) - H(t-t_0)\Big\} \\ &= \frac{1}{2}\Big\{1 - \cos(\omega_0 t/m)\Big\}\Big\{H(t) - H(t-m/f_0)\Big\}\,. \end{aligned} \tag{5.60}$$

Thus, the Fourier transform $\hat{f}(k,\omega)$ is obtained as (see Appendix B)

$$\begin{aligned} \hat{f}(k,\omega) &= \int_{-\infty}^{\infty} \delta(x) e^{-jkx} dx \int_{-\infty}^{\infty} w_H(t) e^{-j\omega_0 t} e^{j\omega t} dt \\ &= \frac{1}{2}(\Lambda_1 + \Lambda_2 + \Lambda_3)\,, \end{aligned} \tag{5.61}$$

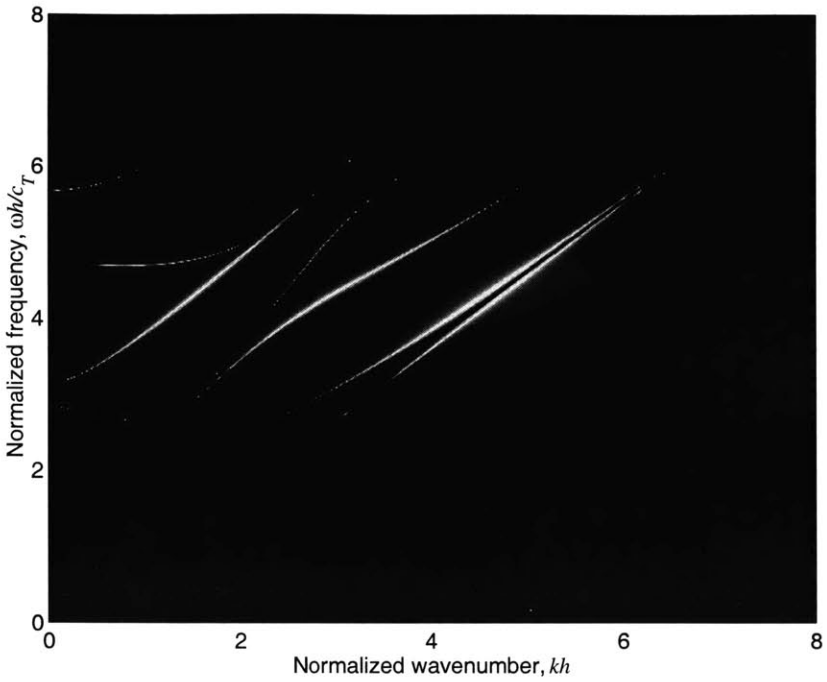

Figure 5.11: Image representing the 2-D FT of the out-of-plane surface displacements, i.e., $\hat{u}_z(h,k,\omega)$ for a steel plate of thickness $2h = 2$ mm ($c_L = 5,850$ m/s and $c_T = 3,240$ m/s) excited by a Gaussian spike pulse with the center frequency $\omega_0/2\pi = 2.25$ MHz and bandwidth $B/2\pi = 0.5$ MHz (Narrow band case).

where

$$\Lambda_1 = \frac{2\sin\left[\frac{\pi m(\omega-\omega_0)}{\omega_0}\right]}{\omega-\omega_0}\exp\left[\frac{j\pi m(\omega-\omega_0)}{\omega_0}\right], \tag{5.62}$$

$$\Lambda_2 = -\frac{\sin\left[\frac{\pi m(\omega-\omega_0-\omega_0/m)}{\omega_0}\right]}{\omega-\omega_0-\omega_0/m}\exp\left[\frac{j\pi m(\omega-\omega_0-\omega_0/m)}{\omega_0}\right], \tag{5.63}$$

$$\Lambda_3 = -\frac{\sin\left[\frac{\pi m(\omega-\omega_0-\omega_0/m)}{\omega_0}\right]}{\omega+\omega_0-\omega_0/m}\exp\left[\frac{j\pi m(\omega+\omega_0-\omega_0/m)}{\omega_0}\right]. \tag{5.64}$$

After substituting Eq. (5.61) into the displacement equations, Eqs. (5.47) and (5.48), for individual wave modes, we are able to predict the propagation behavior of these modes. These theoretical waveforms are compared with those obtained from the finite element simulation using the same excitation condition [16–18].

5.3.2 Prediction of Waveforms for Individual Modes

The propagation behavior of S_0 mode in a steel plate of thickness $2h = 3.0$ mm is predicted. The excitation signal is a 10-cycle sinusoidal toneburst enclosed in a Hanning window, with center frequencies of $f_0 = 0.450$ MHz, and $f_0 = 0.667$ MHz. Figure 5.12 shows the dispersion curves for steel. The longitudinal and transverse wave velocities in steel are $c_L = 5960$ m/s and $c_T = 3260$ m/s, respectively.

Figure 5.13 shows the predicted waveforms of S_0 mode at the distances of (a) $x = 0$ mm, and (b) $x = 500$ mm, for $f_0 = 0.450$ MHz. One can observe that the wave shape is well maintained over such a significant distance. This is because for the corresponding frequency-thickness product, $2f_0h = 1.35$ MHz-mm, the dispersion curve of S_0 mode is flat, as shown in Fig. 5.12. These waveforms are almost exactly the same as the finite element simulation results shown in Figs. 5.14(a) and (b) [17].

Figure 5.15 illustrates the predicted waveforms at the distances of (a) $x = 0$ mm; (b) $x = 100$ mm; (c) $x = 200$ mm, and (d) $x = 500$ mm for $f_0 = 0.667$ MHz. Together with the corresponding FEM results shown in Figs. 5.16(a), (b), (c) and

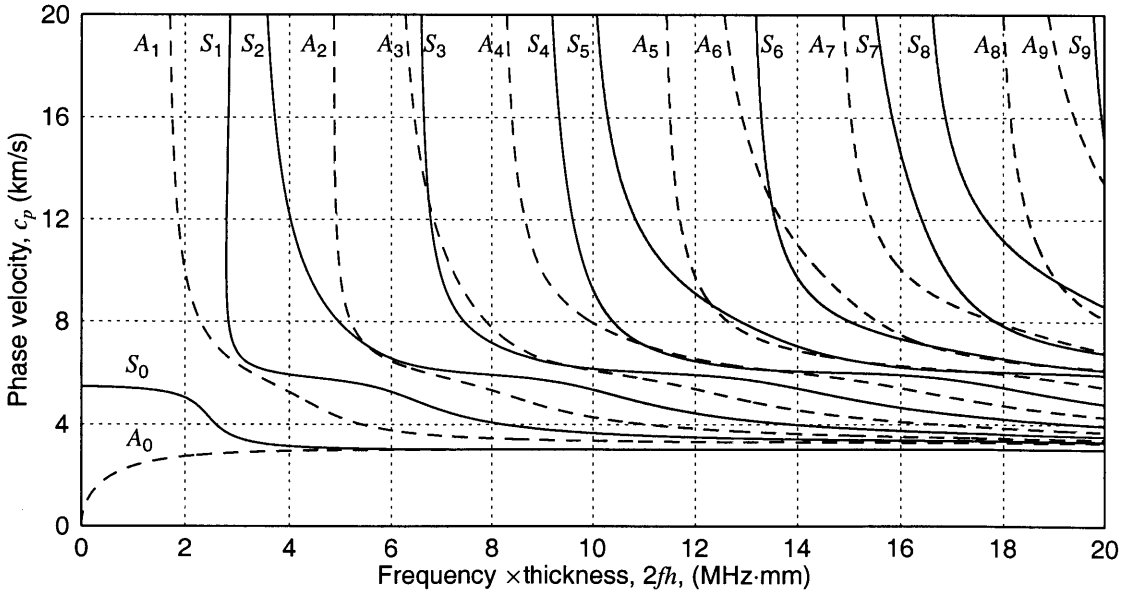

Figure 5.12: Phase velocity dispersion curves for steel ($c_L = 5960$ m/s and $c_T = 3260$ m/s).

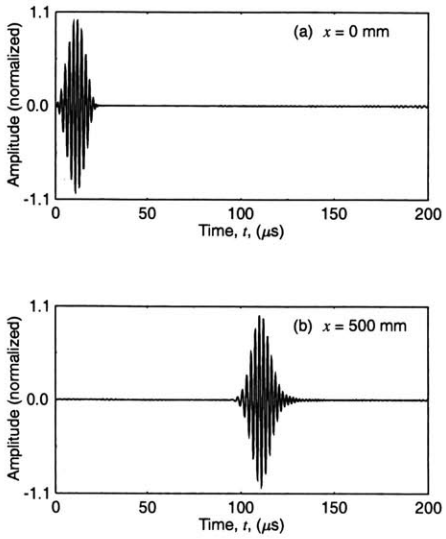

Figure 5.13: Theoretical prediction of the propagation of S_0 mode along a steel plate of thickness $2h = 3.0$ mm at the distances of (a) $x = 0$ mm; and (b) $x = 500$ mm, where the excitation signal is a 10-cycle sinusoidal toneburst enclosed in a Hanning window and the center frequency is $f_0 = 0.45$ MHz.

(d) [17], one can observe the dispersion effect, i.e., the wave shape changes as the wave propagates. This can be explained by the fact that for the corresponding frequency-thickness product, $2f_0h = 2.0$ MHz-mm, the dispersion curve of S_0 mode does not remain flat, as shown in Fig. 5.12.

5.3.3 2-D FFT of Single Mode Waveforms

As described earlier in this chapter, the 2-D FT, providing the amplitude information in the frequency-wavenumber domain, can be used effectively to identify wave modes or to construct dispersion curves. For the efficiency of computation, the 2-D FT is represented by the two-dimensional fast Fourier transform (2-D FFT). In the following, we will compare our results again with the FEM results. The excitation signal is a 5-cycle sinusoidal toneburst enclosed in a Hanning window, with $f_0 = 1.0$ MHz.

Figure 5.17(a) shows the predicted waveform of S_0 mode at a distance of $x = 100$ mm for a steel plate of thickness $2h = 0.5$ mm. Figure 5.17 (b) shows the 2-D FFT of the 64 sequential waveforms collected between $x = 100$ mm and $x = 163$ mm at a

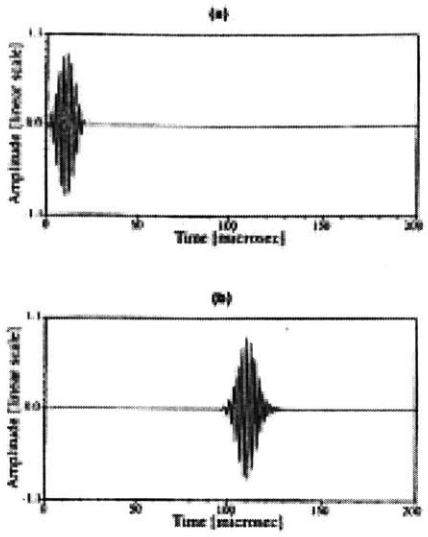

Figure 5.14: Finite element prediction of the propagation of S_0 mode along a steel plate of thickness $2h = 3.0$ mm at the distances of (a) $x = 0$ mm; and (b) $x = 500$ mm, where the excitation signal is a 10-cycle sinusoidal toneburst enclosed in a Hanning window and the center frequency is $f_0 = 0.45$ MHz [17].

spatial sampling interval of 1.0 mm. The results are represented in the form of a 3-D plot of amplitude as a function of frequency and wavenumber. For all frequencies, the amplitude is significant only at one single wavenumber, indicating that only one mode (S_0) is present in this frequency range. Also note the amplitude reaches its maximum at the center frequency of the toneburst signal, $f_0 = 1.0$ MHz. For comparison, the corresponding FEM results are shown in Figs. 5.18(a) and (b) [16].

Similarly, the results for A_0 mode in a steel plate of thickness $2h = 3.0$ mm are shown in Figs. 5.19 and 5.20 [16], for a distance of $x = 50$ mm. For the predictions, waveforms are collected between $x = 30$ mm and $x = 67.8$ mm at an interval of $\Delta x = 0.6$ mm.

The results for A_1 mode in a steel plate of thickness $2h = 3.0$ mm are shown in Figs. 5.21 and 5.22, for the distances of $x = 50$ mm. Note that the wave shape of this mode is quite different from that of A_0 mode as shown in Fig. 5.19(a), although the excitation conditions are the same for both modes. The 2-D FFT results shown

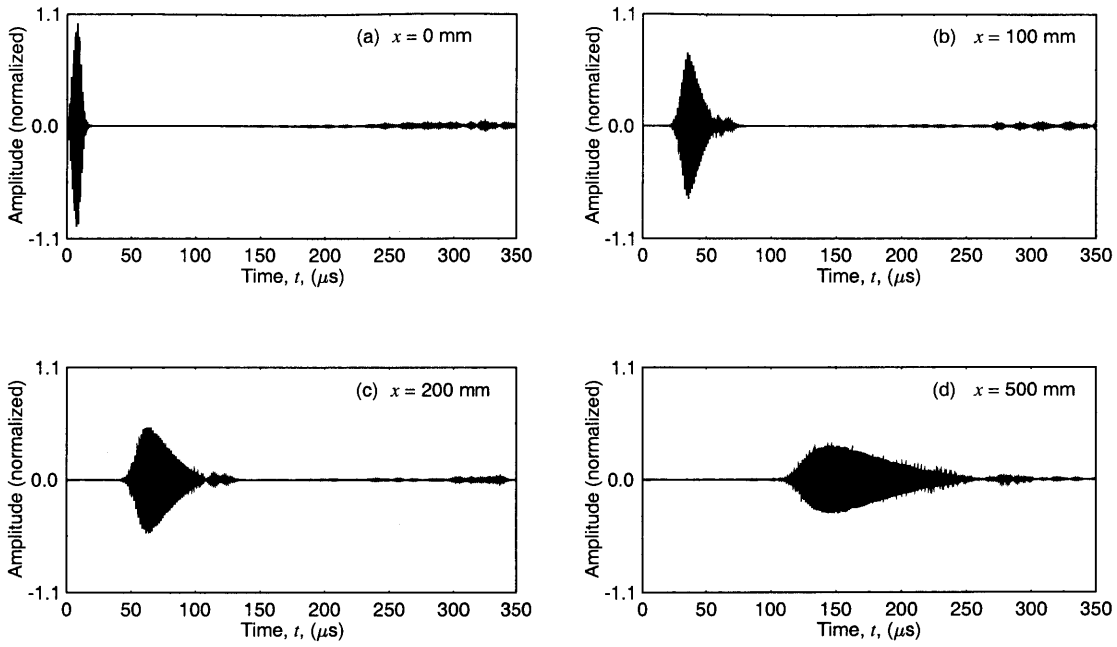

Figure 5.15: Theoretical prediction of the propagation of S_0 mode along a steel plate of thickness $2h = 3.0$ mm at the distances of (a) $x = 0$ mm; (b) $x = 100$ mm; (c) $x = 200$ mm and (d) $x = 500$ mm, where the excitation signal is a 10-cycle sinusoidal toneburst enclosed in a Hanning window and the center frequency is $f_0 = 0.667$ MHz.

in Fig. 5.21 are obtained by processing the 64 sequential waveforms collected between $x = 30$ mm and $x = 67.8$ mm at an interval of $\Delta x = 0.6$ mm.

5.4 Conclusions

In this chapter, the dispersion of Lamb waves in an elastic plate excited by an arbitrary traction force was analyzed by seeking the integral transform solutions of the surface displacements. Since the solution turns out to be the product of the excitation efficiency and loading, we could conveniently to study the influences of both material properties and the excitation function in the frequency-wavenumber domain, which provides the information not available in the time-space domain. The displacements are obtained by carrying out the inverse Fourier transforms.

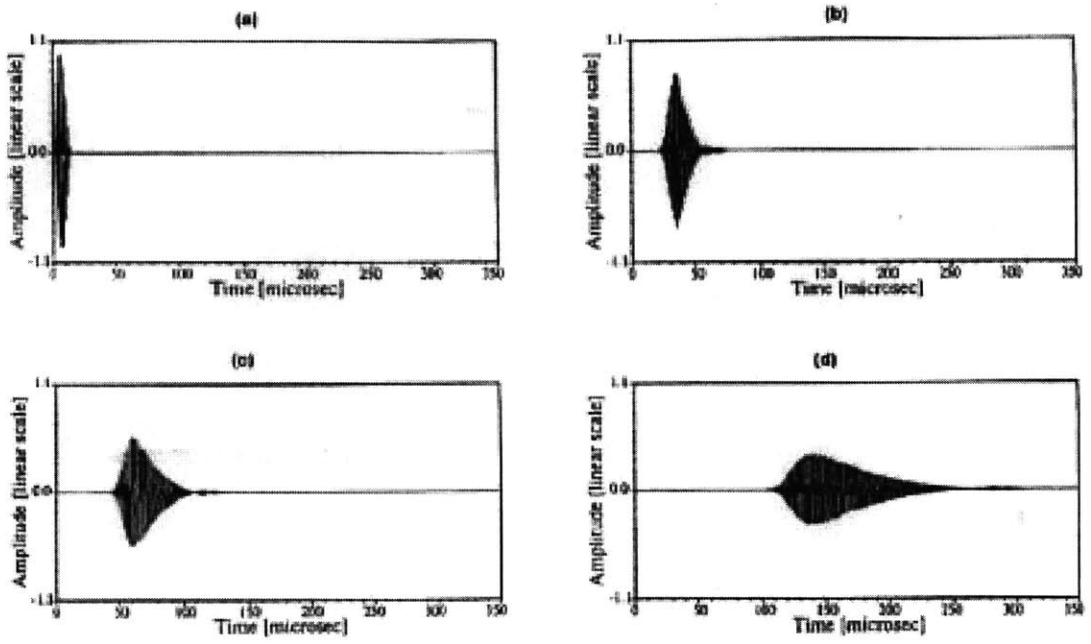

Figure 5.16: Finite element prediction of the propagation of S_0 mode along a steel plate of thickness $2h = 3.0$ mm at the distances of (a) $x = 0$ mm; (b) $x = 100$ mm; (c) $x = 200$ mm and (d) $x = 500$ mm, where the excitation signal is a 10-cycle sinusoidal toneburst enclosed in a Hanning window and the center frequency is $f_0 = 0.667$ MHz [17].

Our approach is in fact virtually identical to the integral transform method, except that we consider information in both the frequency-wavenumber and spatiotemporal domains. Meanwhile, it is shown that the solutions for the displacements are essentially the same as those obtained using the normal mode expansion method. Finally, the analytical results of our method are in excellent agreement with the numerical results from the finite element method studies [16–18].

Our method is advantageous compared with the conventional integral transform and the normal mode expansion methods. In these two methods, the displacement responses of individual wave mode are computed independently in the spatiotemporal domain, from which the total response is obtained by summing the contributions made by all the modes. That procedure is tedious and sometimes unnecessary, especially if we are only interested in selecting the modes of a strong displacement response.

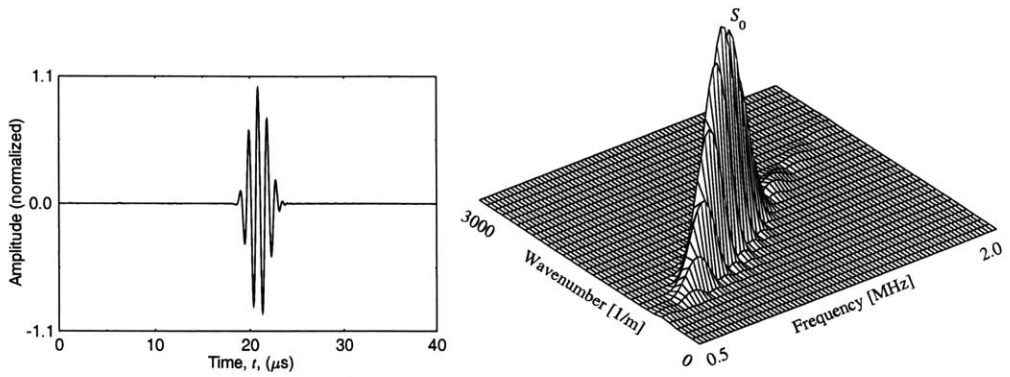

Figure 5.17: (a) Predicted waveform of S_0 mode on the surface of a steel plate of thickness $2h = 0.5$ mm at the distance of $x = 100$ mm using the 2-D FT method. (b) Normalized 3-D plot of the 2-D FFT results of the case in (a), showing the propagating S_0 mode.

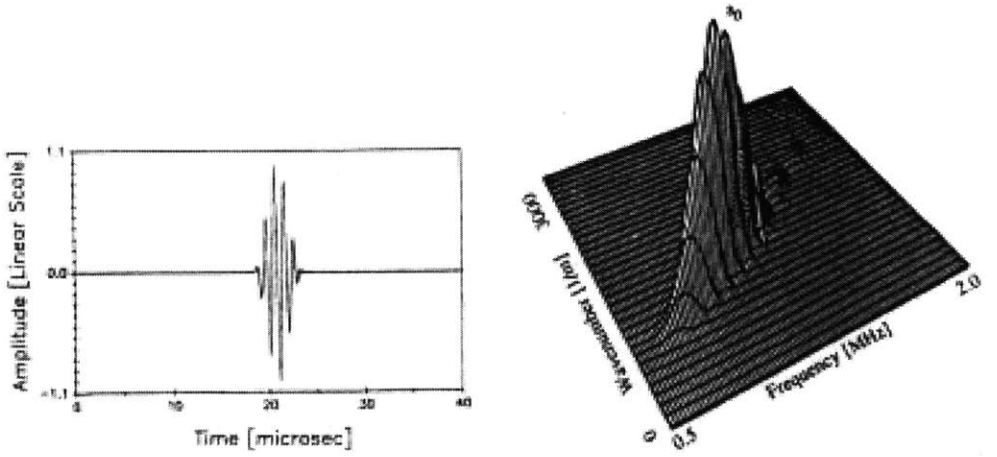

Figure 5.18: (a) Predicted waveform of S_0 mode on the surface of a steel plate of thickness $2h = 0.5$ mm at the distance of $x = 100$ mm using FEM. (b) Normalized 3-D plot of the 2-D FFT results of the case in (a), showing the propagating S_0 mode [16].

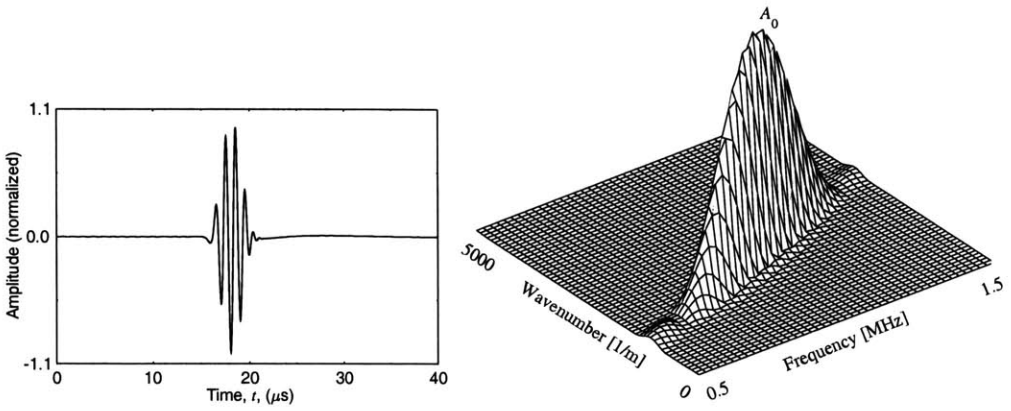

Figure 5.19: (a) Predicted waveform of A_0 mode on the surface of a steel plate of thickness $2h = 3.0$ mm at the distance $x = 50$ mm using the 2-D FT method. (b) Normalized 3-D plot of the 2-D FFT results of the case in (a), showing the propagating A_0 mode.

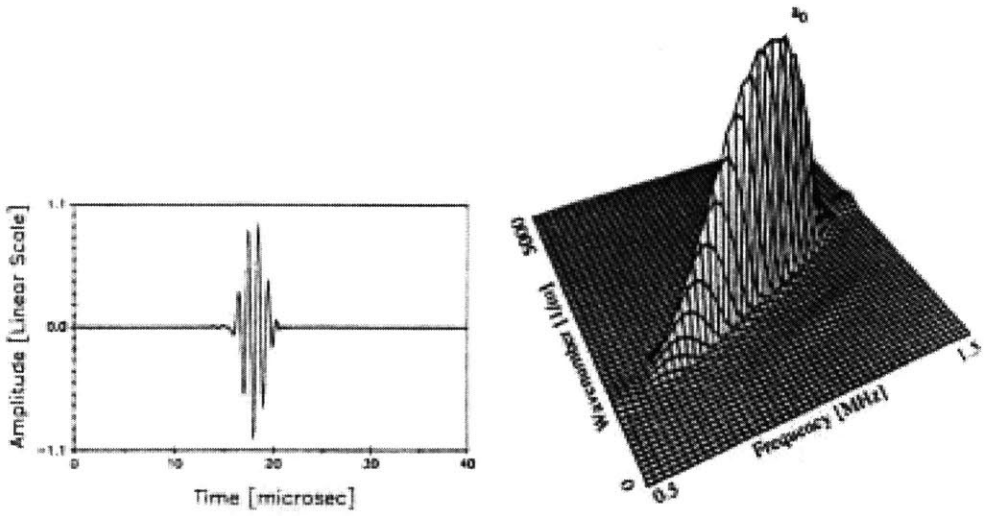

Figure 5.20: (a) Predicted waveform of A_0 mode on the surface of a steel plate of thickness $2h = 3.0$ mm at the distance of $x = 50$ mm using FEM. (b) Normalized 3-D plot of the 2-D FFT results of the case in (a), showing the propagating A_0 mode [16].

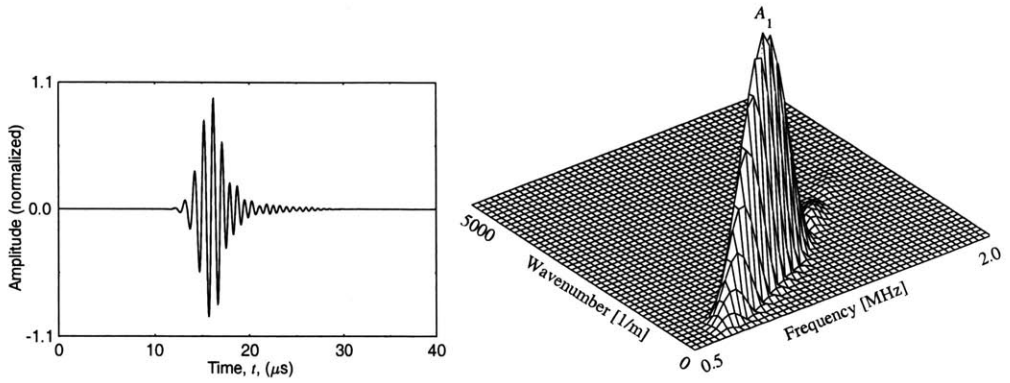

Figure 5.21: (a) Predicted waveform of A_1 mode on the surface of a steel plate of thickness $2h = 3.0$ mm at the distance of $x = 50$ mm using the 2-D FT method. (b) Normalized 3-D plot of the 2-D FFT results of the case in (a), showing the propagating A_1 mode.

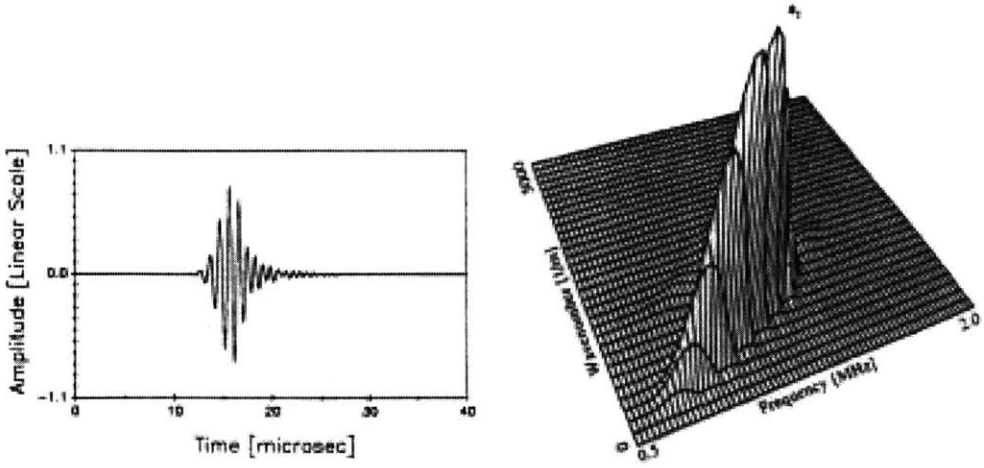

Figure 5.22: (a) Predicted waveform of A_1 mode on the surface of a steel plate of thickness $2h = 3.0$ mm at the distance of $x = 50$ mm using FEM. (b) Normalized 3-D plot of the 2-D FFT results of the case in (a), showing the propagating A_1 mode [16].

Chapter 6

Analysis of Angle Wedge Transducer Tuning

6.1 Introduction

In Chapter 5, an analytical model was developed to study the behavior of transient Lamb waves in an elastic plate subject to an arbitrary loading. This model, allowing for the study of generation efficiencies of waves modes due to both the internal (material properties) and external factors (loadings), is extended in this chapter to investigate quantitatively the angle wedge transducer tuning of Lamb waves.

These two tuning techniques have been studied experimentally Chapters 3 and 4, respectively. As one representative and important broadband signal approach of introducing Lamb waves, the laser generation method will also be studied using the analytical model. These investigations may lead us to find an optimum tuning scenario for Lamb waves, which is also one of the major objectives of this research. On the other hand, this provides us with an opportunity to further verify our analytical model.

In this chapter, the angle wedge transducer tuning is studied from a quantitative point of view. Compared with other tuning techniques, this technique is economical and simple to operate though its disadvantages are obvious. For example, not all the modes are tunable, multiple interfaces exist in the wedge assembly, and the results

are sensitive to the angle of incidence, etc. Despite these limitations, the angle wedge transducer tuning technique is widely used.

Some work has been done to study the mechanism of this tuning technique. For example, using the one-dimensional Fourier transform, Viktorov [13] developed a model to predict the displacements of Lamb wave modes under the assumption of monochromatic excitation, which is not pragmatic. Besides, Ditri and Rose [70] utilized the normal mode expansion method to study this excitation problem where bandwidth effect was incorporated. However, their study did not provide predicted or experimental waveforms. With the normal mode expansion method, Jia [71] performed modal analysis of Lamb wave generation in elastic plates by liquid wedge transducers, taking into account the effects of wave reflection and radiation. Only two fundamental modes — A_0 and S_0 were chosen to excite in the study, and their theoretical and experimental peak-to-peak amplitudes were illustrated with respect to the frequency-thickness product. However, the issue regarding the tuning efficiencies of wave modes was not discussed.

In summary, these studies did not provide the guidance for tuning effect underlying the angle wedge transducer tuning method. Our knowledge of this tuning technique is more or less limited to Snell's law governing the angle of incidence. This is certainly not enough to well apply this technique comfortably, especially in view of the fact that discrepancy in the tuning efficiencies exists for different wave modes.

To best illustrate the tuning effect of angle wedge transducers, we consider a case without tuning, i.e., the generation of Lamb waves using normal contact transducers. The analytical model will be extended by taking into account the excitation conditions for both transducers. Then effectiveness of tuning will be studied theoretically and experimentally by showing the 2-D FT of displacements and the waveforms of individual modes.

6.2 Excitation Conditions

The solutions to the transient Lamb waves due to an arbitrary loading depend on both the excitation efficiency, $N(h,k,\omega)$, and the Fourier transform of the loading, $\hat{f}(k,\omega)$. Since $N(h,k,\omega)$ is already known for a given material, we only need to enter the expressions for the loading $f(x,t)$ in order to obtain general.

For convenience, we may express the external loading, $f(x,t)$, as the product of a space excitation function, $p(x)$, and a time excitation function, $g(t)$, i.e.,

$$f(x,t) = p(x)g(t) \; . \tag{6.1}$$

Since the functions $p(x)$ and $g(t)$ are independent, the Fourier transform of the loading, $\hat{f}(k,\omega)$, is the product of the spatial Fourier transform, $\hat{p}(k)$, and the temporal Fourier transform, $\hat{g}(\omega)$, i.e.,

$$\hat{f}(k,\omega) = \int_{-\infty}^{+\infty} p(x)e^{-jkx}dx \int_{-\infty}^{+\infty} g(t)e^{j\omega t}dt = \hat{p}(k)\hat{g}(\omega) \; . \tag{6.2}$$

We will now consider various excitation functions to represent the loading conditions.

6.2.1 Normal Contact Transducers

As shown in Fig. 6.1, a normal contact transducer of size a is assumed to produce harmonic pressure on the upper surface of an elastic plate of thickness $2h$. To control the frequency range of excitation, a sinusoidal toneburst is chosen as the excitation signal. For an m-cycle toneburst of the center frequency f_0, the time excitation function, $g(t)$, is expressed as

$$g(t) = [H(t) - H(t-t_0)]\exp[-j\omega_0 t] \; , \tag{6.3}$$

where t_0 is the duration of the signal ($t_0 = m/f_0$), ω_0 is the center angular frequency $\omega_0 = 2\pi f_0$, and $H(t)$ is the Heaviside unit step function. It is straightforward to

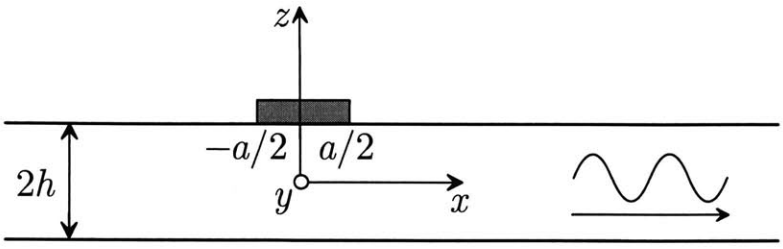

Figure 6.1: Generation of Lamb waves in a plate of thickness $2h$ using a normal contact transducer of size a.

express the temporal Fourier transform as

$$\hat{g}(\omega) = \int_{-\infty}^{+\infty} [H(t) - H(t-t_0)] e^{-j\omega_0 t} e^{j\omega t} dt = \frac{\sin[(\omega-\omega_0)m/2f_0]}{(\omega-\omega_0)/2} e^{j(\omega-\omega_0)m/2f_0} . \tag{6.4}$$

For a rectangular transducer, it is reasonable to assume that the pressure distribution is uniform. The space excitation function $p(x)$ is then assumed to be

$$p(x) = [H(x+a/2) - H(x-a/2)] , \tag{6.5}$$

which yields the spatial Fourier transform as

$$\hat{p}(k) = \int_{-\infty}^{+\infty} [H(x+a/2) - H(x-a/2)] e^{-jkx} dx = \frac{\sin(ka/2)}{k/2} . \tag{6.6}$$

Consequently, the Fourier transform of the traction $f(x,t)$ is obtained as

$$\hat{f}(k,\omega) = \frac{a}{f_0} \frac{\sin(ka/2)}{ka/2} \frac{\sin[(\omega-\omega_0)m/2f_0]}{(\omega-\omega_0)/2f_0} e^{j(\omega-\omega_0)m/2f_0} . \tag{6.7}$$

6.2.2 Angle Wedge Transducers

In the case of angle wedge excitation, the transducer is assumed to produce a time-harmonic plane wave that travels through the wedge and strikes the plate at an incident angle θ_w, as shown in Fig. 6.2. For the sake of simplicity, we ignore the

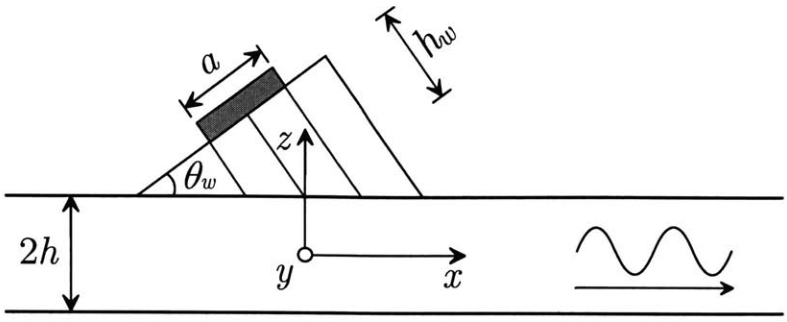

Figure 6.2: Generation of Lamb waves in a plate of thickness $2h$ using an angle wedge transducer of size a, where the angle of incidence is θ_w and the average propagation distance in the wedge is h_w.

effects of beam spreading and shifting upon striking the plate, as done by Viktorov [13] and Ditri and Rose [70]. Also assumed is that the wedge is coupled to the plate by a thin layer of non-viscous liquid so that only the normal tractions are transferred and the shear tractions vanish.

We still denote c_w as longitudinal wave velocity in the wedge and h_w the average propagation distance in the wedge. Assuming the excitation signal is an m-cycle sinusoidal toneburst of the center frequency f_0, the time excitation function $g(t)$ is expressed as

$$g(t) = [H(t - t_w) - H(t - t_w - t_0)] \exp[-j\omega_0 t] \,, \tag{6.8}$$

where t_w is the average time of the longitudinal wave in the wedge ($t_w = h_w/c_w$), and t_0 is the duration of the toneburst signal. The temporal Fourier transform can be written as

$$\hat{g}(\omega) = \frac{2}{(\omega - \omega_0)} \sin\left[\frac{(\omega - \omega_0)m}{2f_0}\right] \exp\left[j(\omega - \omega_0)\left(\frac{h_w}{c_w} + \frac{m}{2f_0}\right)\right] \,, \tag{6.9}$$

Here it is still assumed that the transducer is a source producing uniformly distributed traction across the transducer-wedge interface. Then the space excitation

function $p(x)$ is

$$p(x) = |R(\theta_w)|[H(x + a/2\cos\theta_w) - H(x - a/2\cos\theta_w)]\exp[jk_w \sin\theta_w x] \ , \qquad (6.10)$$

where the factor $R(\theta_w)$ is equal to the amplitude ratio of the normal stress at the wedge-plate interface to that at the transducer-wedge interface. Further discussion of $R(\theta_w)$ was done by Ditri and Rose [70] and it will not be discussed in this thesis. The exponential term in Eq. (6.10) accounts for the propagation in the positive x direction in the wedge, where k_w is the wavenumber in the wedge. The spatial Fourier transform can be obtained as

$$\hat{p}(k) = \frac{2|R(\theta_w)|}{(k - k_w \sin\theta_w)} \sin\left[\frac{(k - k_w \sin\theta_w)a}{2\cos\theta_w}\right] \ , \qquad (6.11)$$

and the Fourier transform of the traction is written as

$$\begin{aligned}\hat{f}(k,\omega) =& \frac{4|R(\theta_w)|}{(k - k_w \sin\theta_w)(\omega - \omega_0)} \sin\left[\frac{(k - k_w \sin\theta_w)a}{2\cos\theta_w}\right] \sin\left[\frac{(\omega - \omega_0)m}{2f_0}\right] \times \\ & \exp\left[j(\omega - \omega_0)\left(\frac{h_w}{c_w} + \frac{m}{2f_0}\right)\right] \ .\end{aligned} \qquad (6.12)$$

From Eq. (6.12), one can observe that there are two terms representing the contribution by the angle of incidence θ_w. Since the first term $R(\theta_w)$ is not discussed in this thesis, we may take a look at the second term, which is denoted as

$$\mathfrak{F} = \frac{2\sin\left[\dfrac{(k - k_w \sin\theta_w)a}{2\cos\theta_w}\right]}{(k - k_w \sin\theta_w)} \ . \qquad (6.13)$$

We can observe that $\mathfrak{F}$ is identical to the result obtained by Viktorov [13] and Ditri and Rose [70]. Also observed is that Snell's law is that rigorously applicable, which assumes only a single wavenumber (or frequency). This indicates that when Snell's law is not obeyed, wave modes can still be generated, albeit less efficiently. However, when the wavenumber k approaches $k_w \sin\theta_w$, the term $\mathfrak{F}$ approaches its maximum

value $a/\cos\theta_w$, which could result in tuning effect. These observations are the same as those made by Ditri and Rose [70].

6.3 Theoretical Analysis

The expressions of the external loading in the Fourier domain, Eqs. (6.7) and (6.12), enable us to obtain the surface displacements as well as their transformation in the frequency-wavenumber domain. Note that in practical situations, the frequency responses of the transducer system (including the transmitter and receiver) should be also taken into account.

The excitation conditions used in the theoretical analysis are determined from the experimental parameters for the purpose of comparison. Three 5-cycle sinusoidal toneburst signals are used with the center frequencies of 0.48, 0.96 and 2.25 MHz, respectively. The thickness of the aluminum plate under investigation ($2h$) is 2.0 mm, the transducer width (a) is 12.7 mm, and the average propagation distance in the wedge (h_w)is 35.0 mm. The distance x is set at 162 mm, measured from the center of the beam at the wedge-plate interface. Note that there is an additional delay in the wedge. Table 6.1 summarizes the respective conditions used in the normal contact and angle wedge transducer generation of Lamb waves.

Table 6.1: Conditions used in the normal contact and angle wedge transducer generation of Lamb waves.

Parameter	Value
Plate material	Aluminum
Longitudinal wavespeed, c_L, (m/s)	6320
Transverse wavespeed, c_T, (m/s)	3130
Center frequency of toneburst, f_0, (MHz)	0.48, 0.96, 2.25
Number of cycles of toneburst, m	5
Plate thickness, $2h$, (mm)	2.0
Transducer size, a, (mm)	12.7
Propagation distance in wedge, h_w, (mm)	35.0
Longitudinal wavespeed in wedge, c_w, (m/s)	2720
Propagation distance in plate, x, (mm)	162.0

For a given frequency, we may find the existing wave modes from the dispersion curves as shown in Fig. 2.6. Table 6.2 tabulates the wave modes, and their phase and group velocities corresponding to the three excitation frequencies. Also shown in Table 6.2 are the required angles of incidence for tuning the respective modes.

Table 6.2: The phase and group velocities of individual wave modes in an aluminum plate of thickness $2h = 2$ mm for the excitation frequencies f_0, as well as the required angles of incidence to tune these modes.

Frequency f_0, (MHz)	Wave mode	Phase velocity c_p, (m/s)	Group velocity c_g, (m/s)	Angle of Incidence θ_w, (deg)
0.48	S_0	5,356	5,176	30.5
	A_0	2,311	3,142	N.A.
0.96	A_1	9,776	3,075	16.2
	S_0	4,880	3,399	33.9
	A_0	2,669	3,142	N.A.
2.25	S_2	9,846	3,568	16.0
	S_1	5,834	4,171	27.8
	A_1	4,269	2,161	39.6
	S_0	2,961	2,704	66.7
	A_0	2,861	2,980	71.9

The 2-D FTs and the corresponding waveforms of the untuned case (normal contact) at $f_0 = 0.48$ MHz ($\omega_0 h/c_T = 0.96$) are shown in Figs. 6.3 and 6.4, respectively. Note that the intensity of the image shown in Figs. 6.3(a) and (b) represents the level of energy distribution. It can be observed that the A_0 mode carries much higher energy than the S_0 mode at about $f_0 = 0.48$ MHz . This means that the amplitude of the A_0 mode is higher than that of the S_0 mode, which is confirmed by the respective waveforms shown in Fig. 6.4(a). From Table 6.2 we realize that the only mode that can be tuned using an angle wedge transducer is the S_0 mode. The A_0 mode can not be tuned since its phase velocity ($c_p = 2311$ m/s) is smaller than the longitudinal wave velocity in the wedge ($c_w = 2720$ m/s). Figure 6.3(b) shows the transformed displacement $\hat{u}(h, k, \omega)$ for the angle wedge transducer tuning. It is observed that the relative energy level of the S_0 mode is considerably enhanced compared with that of the untuned case. However, it is still lower than that of the A_0 mode, meaning that

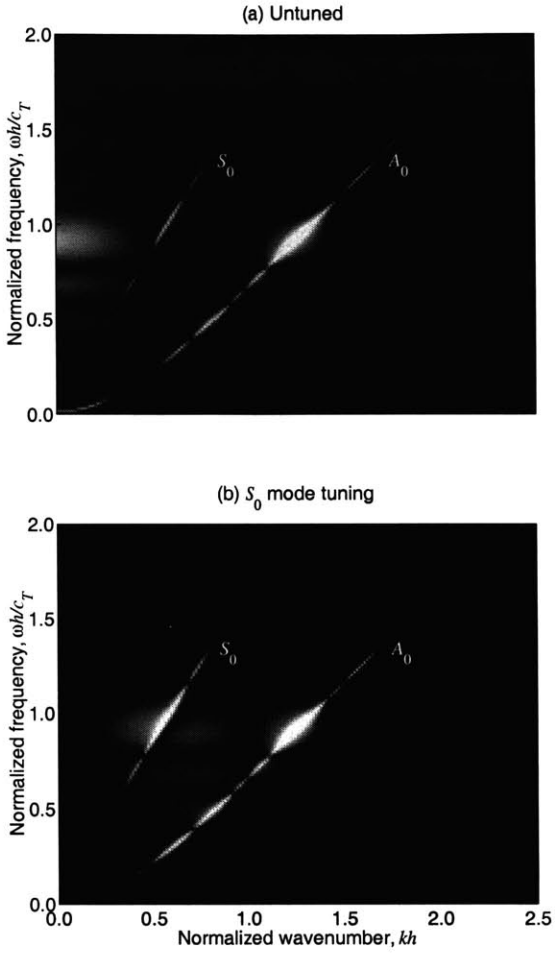

Figure 6.3: Image visualization of 2-D FT $\hat{u}_z(h, k, \omega)$ of Lamb wave displacements for the normal contact transducer and an angle wedge transducer generation with an excitation toneburst signal of center frequency $f_0 = 0.48$ MHz: (a) untuned case, (b) S_0 mode tuning.

the A_0 mode is still a dominant mode. This is assured in Fig. 6.4(b), where the S_0 mode has a much lower amplitude than that of the A_0 mode. This concludes that it is not desirable to tune the S_0 mode at this frequency. Although the A_0 mode can not be tuned, the high amplitude ratio between the A_0 and S_0 mode allows the use of A_0 mode at this frequency range.

Figures 6.5 and 6.6 illustrate the effect of tuning at the frequency $f_0 = 0.96$ MHz ($\omega_0 h/c_T = 1.93$). Figure 6.5(a) shows the result for the untuned case. In addition to the three modes (A_0, S_0, A_1) expected from the dispersion curve containing high

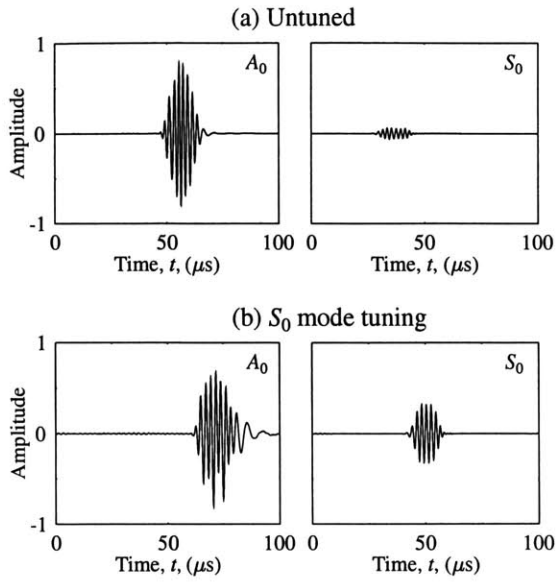

Figure 6.4: Predicted waveforms of individual wave modes generated by a normal contact transducer and an angle wedge transducer with an excitation toneburst signal of center frequency $f_0 = 0.48$ MHz: (a) untuned case, (b) S_0 mode tuning.

energy approximately at 0.96 MHz, there are additional two modes appearing in the figure: S_1 and S_2. This is because the excitation toneburst signal has certain bandwidth so that the cutoff frequencies of these two modes are reached. Among the three dominant modes, A_0 can not be tuned by angle wedge transducers for the same reason as that of the previous case. Figure 6.5(b) shows the 2-D FT of the S_0 tuned wave, in which it can be observed that the relative energy level of the S_0 mode is significantly enhanced and much higher than those remaining modes including A_0 and A_1, indicating that the S_0 mode is now well tuned. This is also confirmed in Fig. 6.6(b) by the predicted waveforms. Shown in Figs. 6.5(c) and 6.6(c) are the results for the A_1 mode tuning. The energy of the A_1 mode is the highest but that of S_0 mode is significantly high as well.This indicates that the A_1 mode tuning is not desirable.

With the increase of $2f_0h$ value, the number of wave modes increases. Shown in Figs. 6.7, 6.8 and 6.9 are the results at the frequency $f_0 = 2.25$ MHz ($\omega_0 h/c_T = 4.52$). One can observe that there are three additional modes (A_2, A_3, and S_3) exist in addition to the five expected modes (A_0, S_0, A_1, S_1 and S_2) at the given frequency.

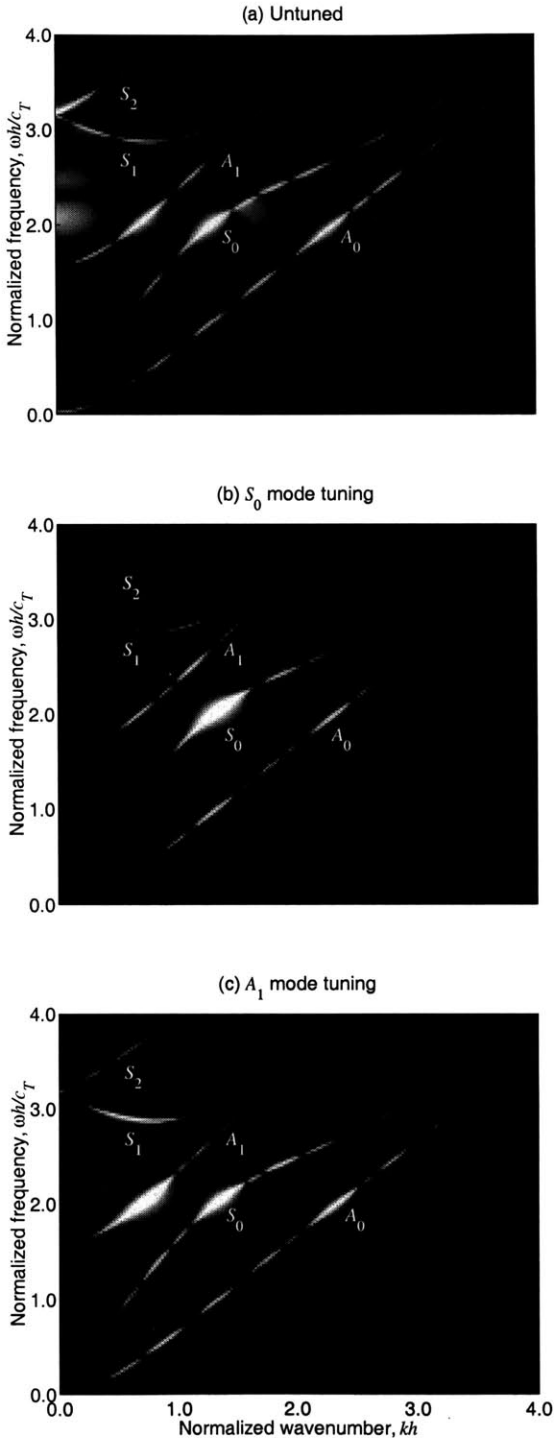

Figure 6.5: Predicted waveforms of individual mode generated by a normal contact transducer and an angle wedge transducer with an excitation toneburst signal of the center frequency $f_0 = 0.96$ MHz: (a) untuned case, (b) S_0 mode tuning, and (c) A_1 mode tuning.

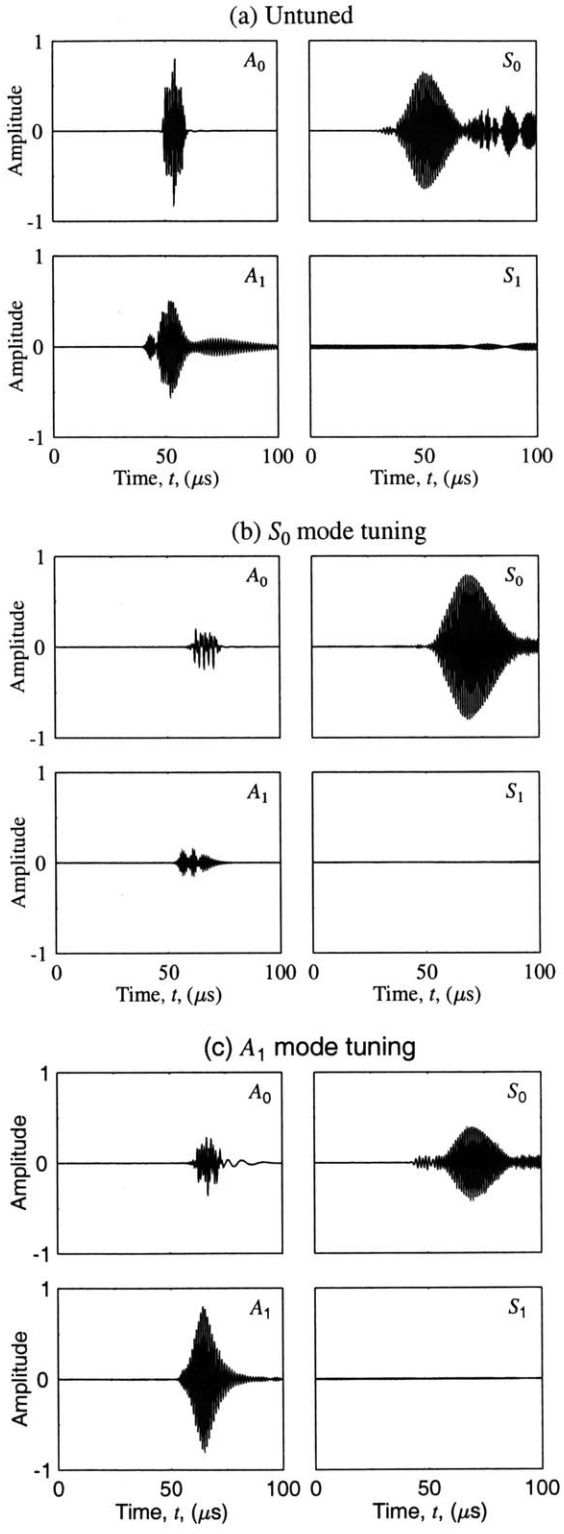

Figure 6.6: Predicted waveforms of individual modes for the normal contact transducer and angle wedge transducer generation of Lamb waves with an excitation toneburst signal of center frequency $f_0 = 0.96$ MHz: (a) untuned case, (b) S_0 mode tuning, and (c) A_1 mode tuning.

Figure 6.7(a) show the 2-D FT result for the untuned case. The energy levels at 2.25 MHz are ranked in a descending order as S_2, A_1, S_0 and A_0. The remaining two modes, S_1 and A_2, have much lower energy. The observations made are consistent with those made from the waveforms of individual modes shown in Fig. 6.8(a).

Figures 6.7(b) and 6.8(b) show the results for the S_1 mode tuning. The selection of this mode for tuning may not be desired since the level of energy is distributed approximately equal for both S_1 and A_1 modes, resulting in two dominating modes excited at the same time.

Shown in Figs. 6.7(c) and 6.8(c) are the results for the A_0 mode tuning, while Figs. 6.7(d) and 6.9(a) are those for the S_0 mode tuning. Since the phase velocities of these two modes (2861 m/s and 2961 m/s) are very close, the required angles of incidence for tuning are also very close. Consequently, tuning one of these modes also boosts the other mode. The tuned waves arrive at a similar time. As a result, these modes may not be desirable for tuning, either.

The results for the A_1 mode tuning are shown in Fig. 6.7(e) and 6.9(b), from which we can observe that the A_1 mode has much higher energy than all the other modes. This indicates that A_1 can be used for tuning. Similarly, the tuning of S_2 mode is excellent, as shown in in Figs. 6.7(f) and 6.9(c).

6.4 Experimental Investigation

The tuning effect of angle wedge transducers has been demonstrated in the above analysis. In this section, we will validate the tuning effect experimentally using the measured set of data.

6.4.1 Experimental Setup

Figure 6.10 illustrates the schematic diagram of the experimental setup used for the generation and detection of Lamb waves in a plate using a normal contact transducer. The distance x is measured from the center of the transmitter to the receiver. The receiver is a 0.5 mm wide broadband PVDF transducer. The effect of averaging

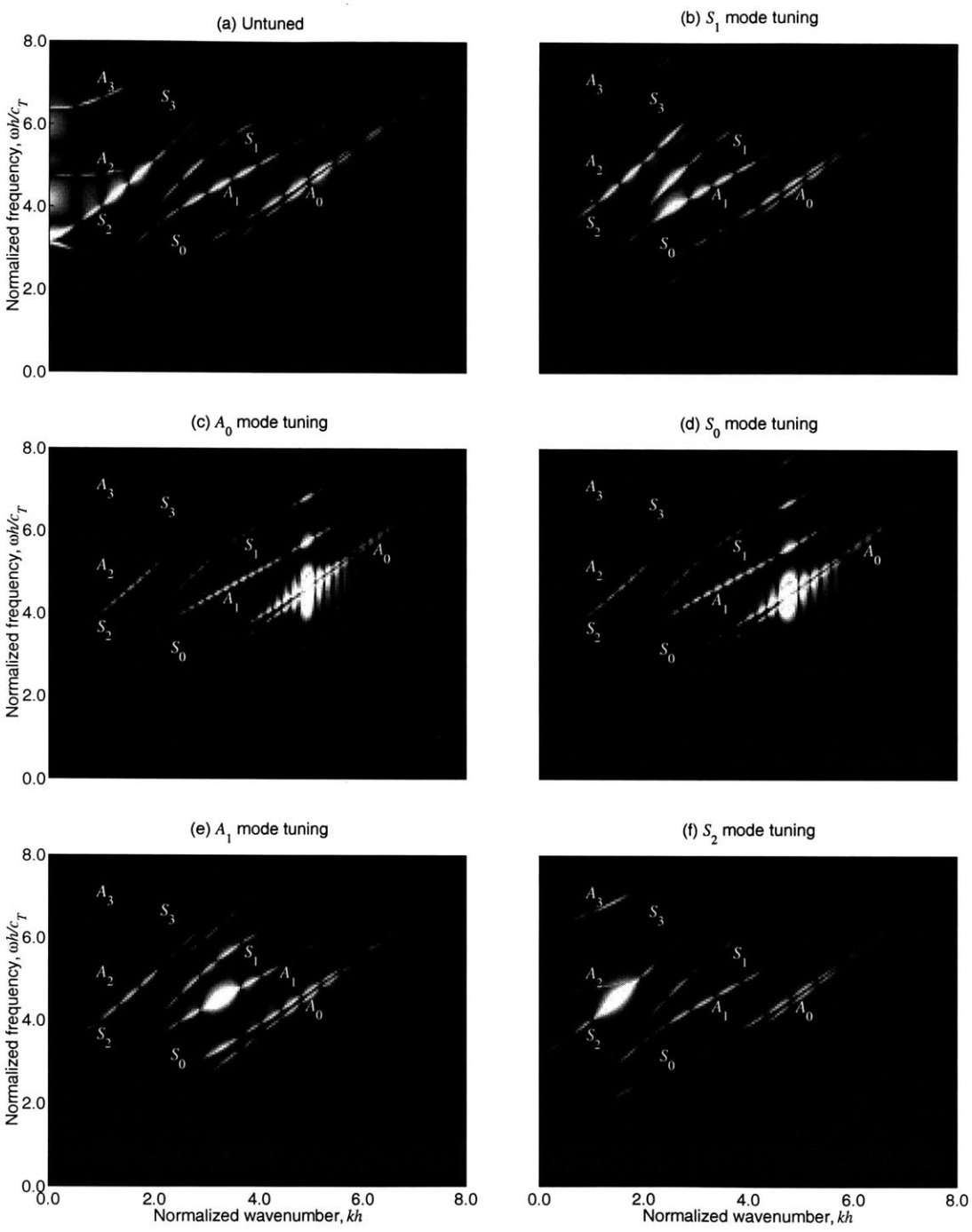

Figure 6.7: Image visualization of 2-D FT $\hat{u}_z(h, k, \omega)$ of displacements for the normal contact transducer and angle wedge transducer generation of Lamb waves with an excitation toneburst signal of center frequency $f_0 = 2.25$ MHz: (a) untuned case, (b) S_1 mode tuned, (c) A_0 mode tuning, (d) S_0 mode tuning, (e) A_1 mode tuning, and (f) S_2 mode tuning.

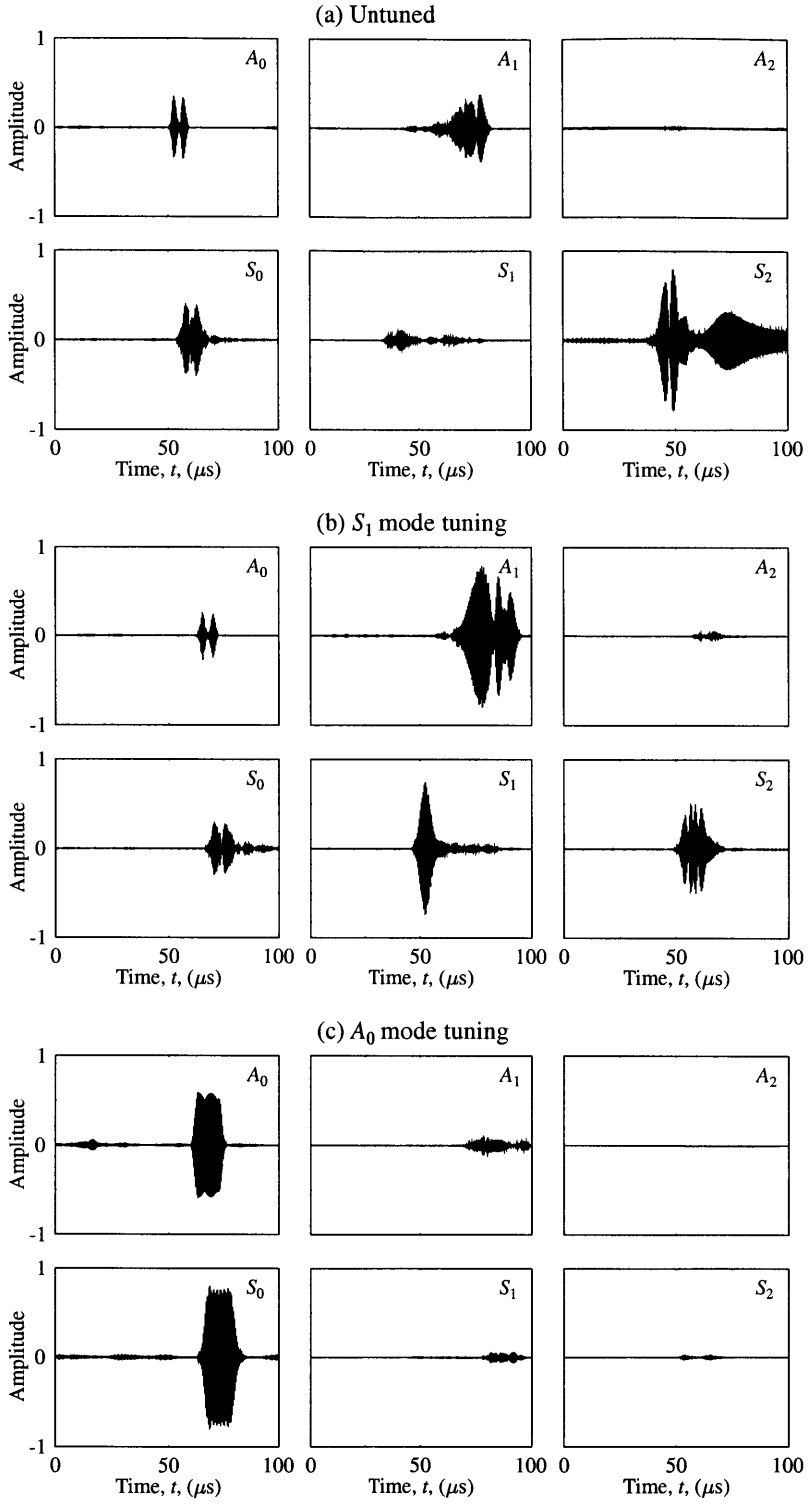

Figure 6.8: Predicted waveforms of individual modes for the normal contact transducer and angle wedge transducer generation of Lamb waves with an excitation toneburst signal of center frequency $f_0 = 2.25$ MHz: (a) untuned case, (b) S_1 mode tuning, and (c) A_0 mode tuning.

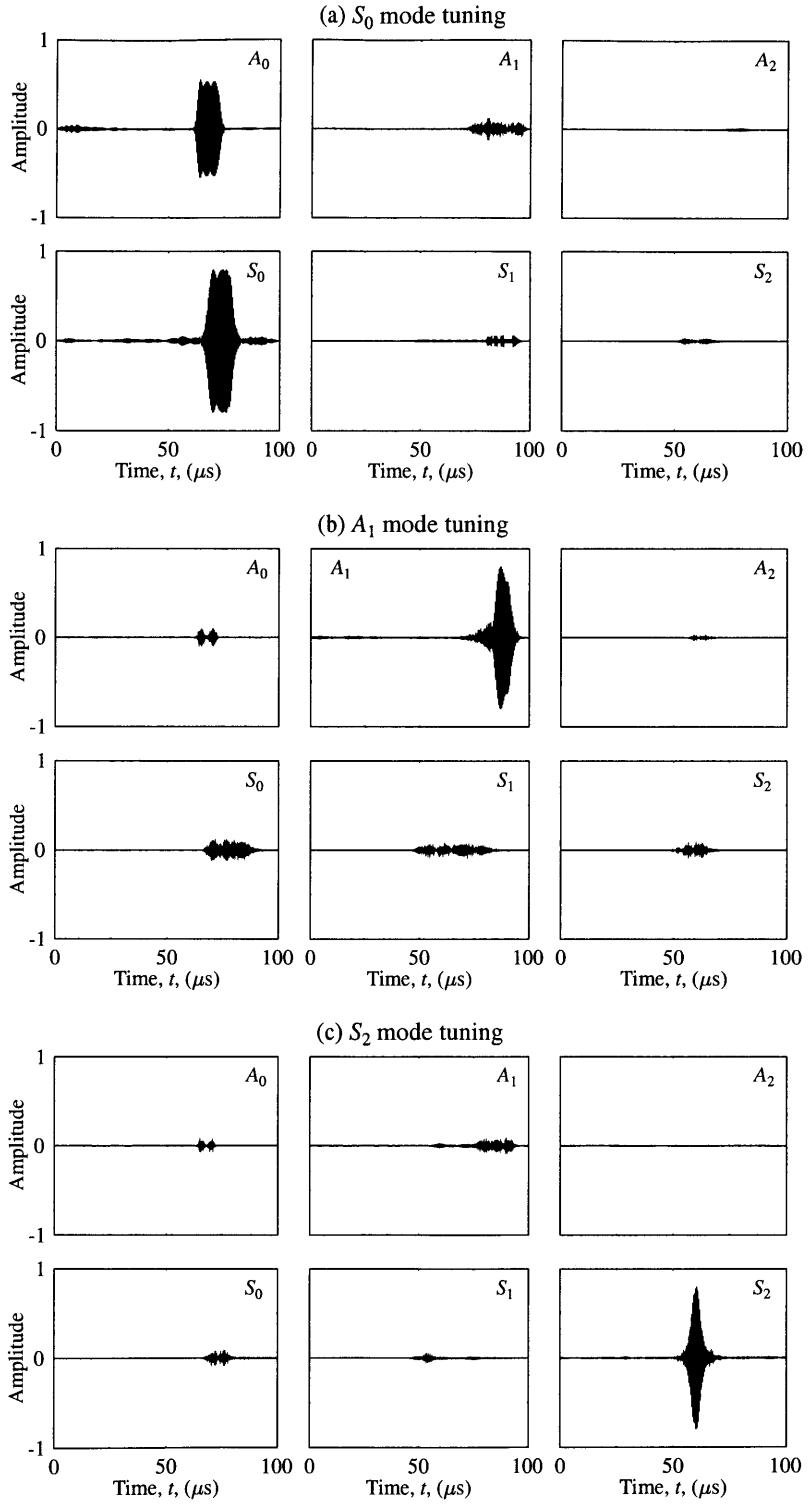

Figure 6.9: Predicted waveforms of individual modes for the normal contact transducer and angle wedge transducer generation of Lamb waves with an excitation toneburst signal of center frequency $f_0 = 2.25$ MHz: (a) S_0 mode tuning, (b) A_1 mode tuning, and (c) S_2 mode tuning.

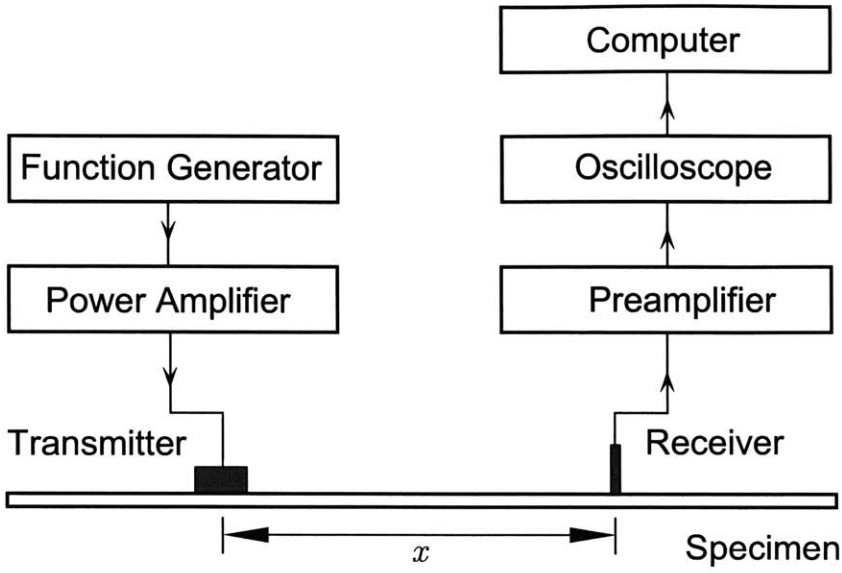

Figure 6.10: Experimental setup for the generation of Lamb waves using a normal contact transducer.

across the face of the sensor is minimized due to the small size, so that the receding transducer can be approximated as a point receiver. The transmitter is excited using a sinusoidal toneburst signal, generated by a function generator and amplified by a power amplifier to produce Lamb waves in the plate. The received signal is pre-amplified and transferred to the oscilloscope. Then , the signal is downloaded to a computer through GPIB. The experimental conditions are the same as those used in the theoretical condition as listed in Table 6.1.

For the angle wedge transducer tuning, we simply replace the normal contact transducer with an angle wedge transducer, as shown in Fig. 6.11, where the distance x is measured from the center of the beam at the wedge-plate interface to the receiver. Note that both the travel time in the wedge and that in the plate should be take into account to evaluate the group delay (or time of arrival).

6.4.2 Experimental Results

Since it is impossible to extract waveforms of single modes from the acquired waveforms, the comparisons are made with the predicted signal contributed by all the

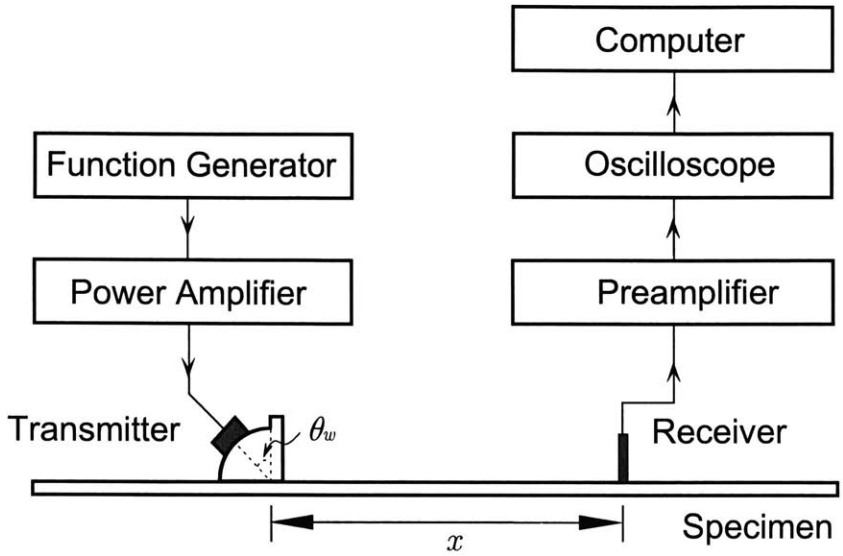

Figure 6.11: Experimental setup for the generation of Lamb waves using an angle wedge transducer.

modes. Figures 6.12 through 6.15 show the predicted and measured waveforms for various (and untuned) modes at the respective center frequencies of 0.48, 0.96, and 2.25 MHz.

In general, the predicted waveforms are in good agreement with the experimental results. From these waveform data, we can make the following observations:

The waveforms received in the experiment come from the overall contributions of the generated wave modes. They will be compared with the theoretical waveforms which are obtained from the summation of those of individual modes. As in the theoretical analysis, here we also give the comparison results in the order of the excitation frequencies.

Figures 6.12 show the comparison of theoretical and experimental waveforms for the excitation frequency of $f_0 = 0.48$ MHz, where Figs. 6.12(a) and (b) are the theoretical and experimental waveforms for the untuned case (normal contact generation), Figs. 6.12(c) and (d) are the theoretical and experimental waveforms for S_0 mode tuning. As we can see, S_0 and A_0 modes are distinguishable in both cases since they have quite different group velocities, as shown in Table 6.2. Also, the agreement between

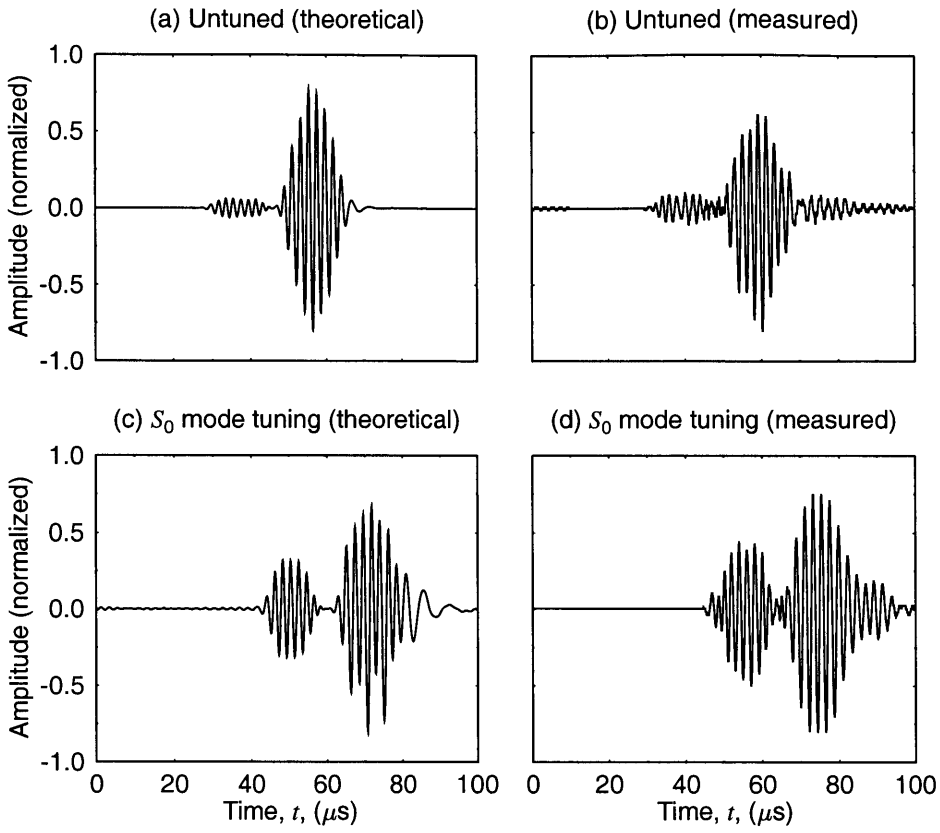

Figure 6.12: Theoretical and experimental waveforms for normal contact transducer and angle wedge transducer generation of Lamb waves with an excitation toneburst signal of frequency $f_0 = 0.48$ MHz: (a) untuned (theoretical), (b) untuned (measured), (c) S_0 mode tuning (theoretical), and (d) S_0 mode tuning (measured).

theoretical and experimental results for both untuned case and S_0 mode tuning is good. This confirms the theoretical observation that S_0 mode can not be tuned well using the angle wedge transducer in this case.

Shown in Figures 6.13 is the comparison of theoretical and experimental results for the excitation frequency of $f_0 = 0.96$ MHz, where Figs. 6.13(a) and (b) are the theoretical and experimental waveforms for the untuned case (normal beam generation), Figs. 6.13(c) and (d) are the theoretical and experimental waveforms for A_1 mode tuning, and Figs. 6.13(e) and (f) are the theoretical and experimental waveforms for S_0 mode tuning. As we can see, no single mode can be distinguished from the overall waveforms for the untuned case, as shown in Fig. 6.13(a) and confirmed

by Fig. 6.13(b). This is because the three modes (A_0, S_0 and A_1) have close energy distribution and group velocities, as mentioned above. For the case of A_1 mode tuning, the overall waveform is mainly composed of A_1 and S_0 modes, thus still no single mode can be watched. In contrast, a single S_0 mode can be identified in Fig. 6.13(e), which is consistent with the previous observation in the previous theoretical analysis that S_0 mode is the dominant mode. Moreover, this is well confirmed by Fig. 6.13(f). Hence S_0 mode has excellent tuning efficiency except that the wave package is wide in terms of resolution requirement for practical purpose.

Figures 6.14 and Figures 6.15 illustrate the comparison of theoretical and experimental results for the excitation frequency of $f_0 = 2.25$ MHz, where Fig. 6.14(a) and Fig. 6.15(a) are the theoretical and experimental waveforms for the untuned case, Fig. 6.14(b) and Fig. 6.15(b) correspond to the case of S_1 mode tuning, Fig. 6.14(c) and Fig. 6.15(c) correspond to the case of A_0 mode tuning, Fig. 6.14(d) and Fig. 6.15(d) correspond to the case of S_0 mode tuning, Fig. 6.14(e) and Fig. 6.15(e) correspond to the case of A_1 mode tuning, and Fig. 6.14(f) and Fig. 6.15(f) correspond to the case of S_2 mode tuning. Referring back to Fig. 6.7(a), we can understand that the overall waveform for the untuned case, as shown in Fig. 6.14(a), has many peaks since several modes coexist. This indicates the necessity of mode tuning. As we have already pointed out after looking at the 2-D FT of displacements or Figs. 6.7 that A_1 and S_2 modes are tuned well while A_0, S_0 and S_1 modes are not. This prediction is demonstrated by the waveforms as shown in Figs. 6.14. For the cases of A_1 and S_2 mode tuning, a single peak corresponding to the mode of tuning appears in the waveform, while for the cases of A_0, S_0 and S_1 mode tuning, no single peak corresponding to the mode of tuning exists in the waveform. In addition, the observation is confirmed by the experimental waveforms shown in Figs. 6.15. It is worth pointing out that the agreement between the theoretical and experimental waveforms is quite good though difference in similarity level is shown.

6.5 Conclusions

The angle wedge transducer tuning method was investigated quantitatively in this chapter, based on the theoretical model proposed in Chapter 5. The generation of Lamb waves by normal contact transducers was also considered in order to highlight the tuning effect of angle wedge transducers. Good agreement was observed between the theoretical results and experimental results, for various excitation frequencies.

It was shown that the tuning effect can be achieved by the oblique incidence. Although Snell's law is not rigorously applicable if the excitation signal has certain bandwidth, the displacement amplitude of the wave mode reaches its maximum value at the required incident angle. It was also shown that the tuning efficiencies of wave modes can be effectively illustrated by the waveforms of individual modes and the Fourier spectrum of displacements. The transient wave model proposed in Chapter 5 was validated.

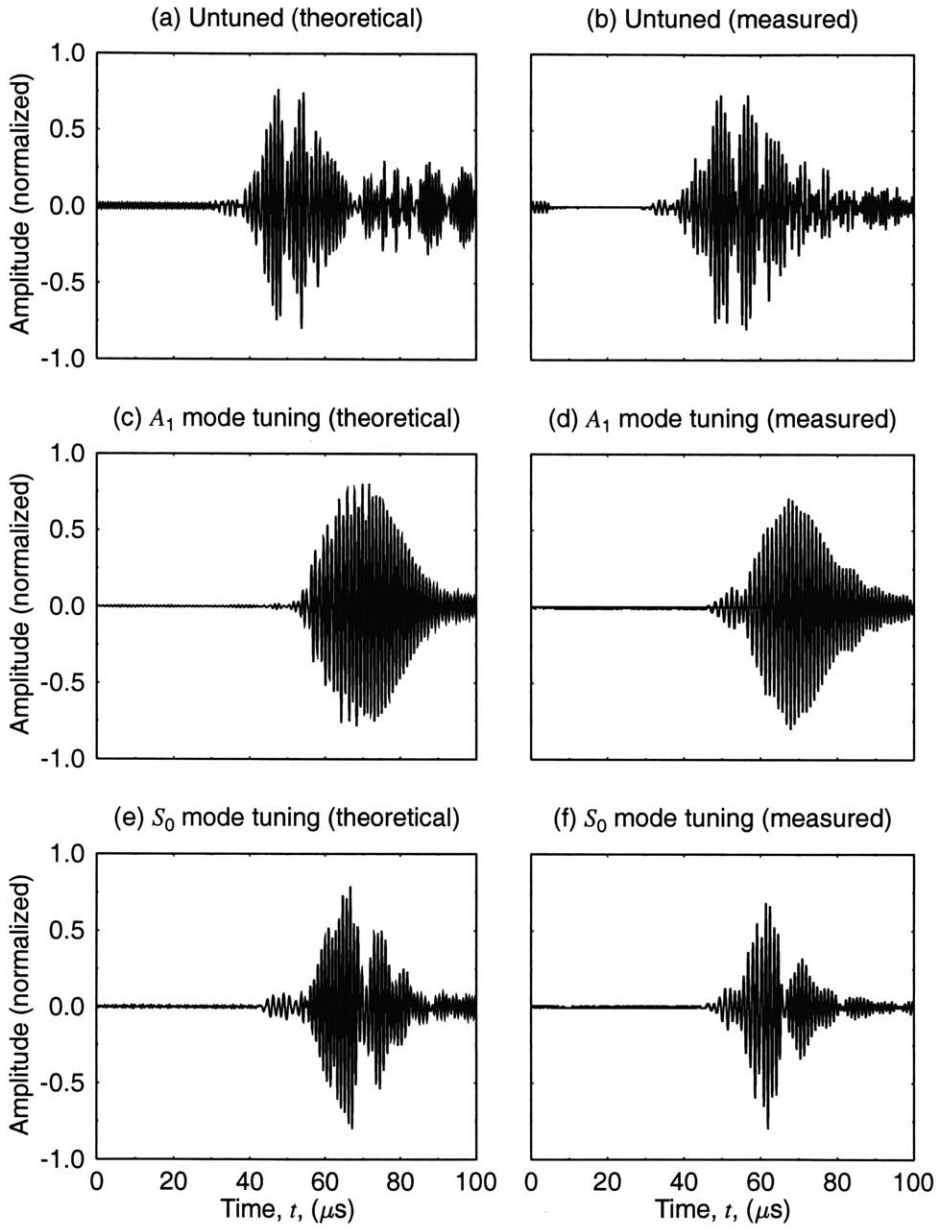

Figure 6.13: Theoretical and experimental waveforms for normal contact transducer and angle wedge transducer generation of Lamb waves with an excitation toneburst signal of frequency $f_0 = 0.96$ MHz: (a) untuned (theoretical), (b) untuned (measured), (c) A_1 mode tuning (theoretical), (d) A_1 mode tuning (measured), (e) S_0 mode tuning (theoretical), and (f) S_0 mode tuning (measured).

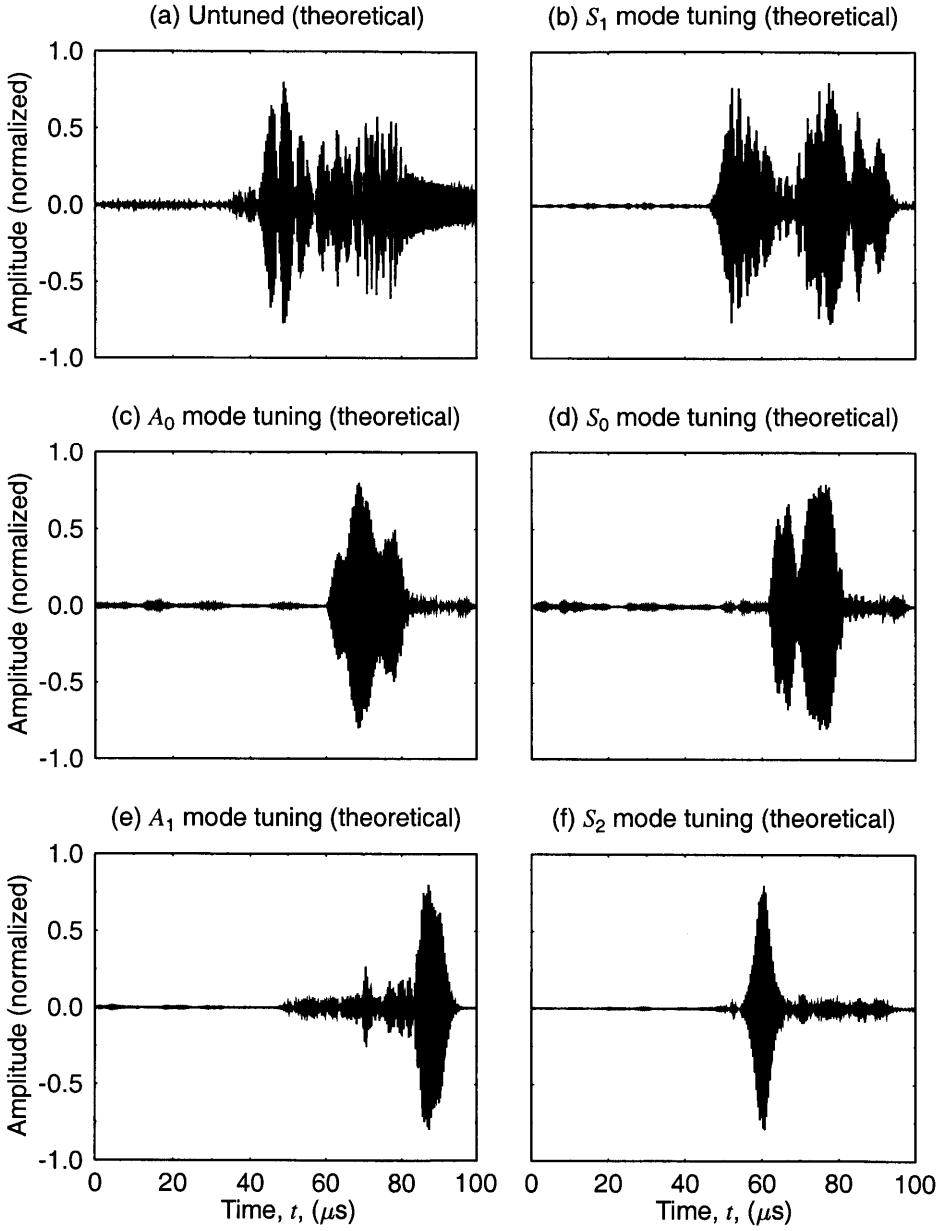

Figure 6.14: Theoretical waveforms for the normal contact transducer and angle wedge transducer generation of Lamb waves with an excitation toneburst signal of frequency $f_0 = 2.25$ MHz: (a) untuned case, (b) S_1 mode tuned, (c) A_0 mode tuning, (d) S_0 mode tuning, (e) A_1 mode tuning, and (f) S_2 mode tuning.

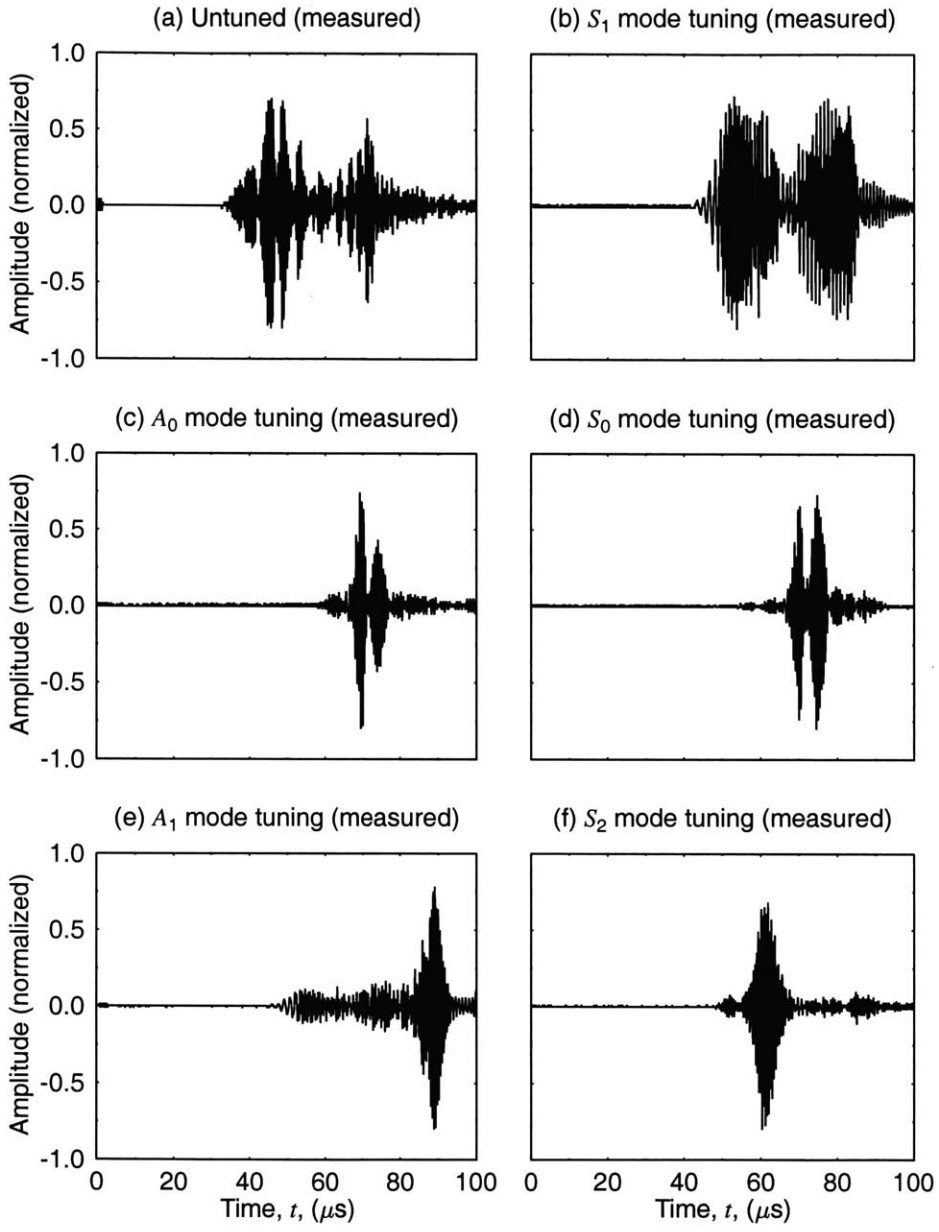

Figure 6.15: Experimental waveforms for the normal contact transducer and angle wedge transducer generation of Lamb waves with an excitation toneburst signal of frequency $f_0 = 2.25$ MHz: (a) untuned case, (b) S_1 mode tuned, (c) A_0 mode tuning, (d) S_0 mode tuning, (e) A_1 mode tuning, and (f) S_2 mode tuning.

Chapter 7

Analysis of Synthetic Phase Tuning

7.1 Introduction

The concepts of phased array and synthetic phase tuning were introduced in Chapters 3 and 4. Although the mechanism of tuning is understood and the feasibility of approaches is verified experimentally, it is still necessary to study the tuning behavior for better understanding and finding of optimum tuning. In Chapter 6, we have investigated the angle wedge transducer tuning mechanism, using the transient analysis model developed in Chapter 5. In this chapter, we will extend the theory to predict the behavior of phase tuning using an array, based on the single element excitation model and the principle of superposition.

It should be pointed out that in Chapter 4 the signals were processed using the pseudo pulse-echo (PPE) scheme, where a single array transducer was used both as a transmitter and receiver to process the signal reflected off a discontinuity.

The reflection of the propagating waves at the discontinuity could involve complex phenomenon such as energy loss and mode conversion. Although the signals are tuned in the forward direction, the tuning effect can be disturbed due to the mode conversion. Therefore, it is needed to tune the waves again in the backward direction. This "full tuning" concept can be applied without any analytical tools. However, the analysis of such problem requires rigorous models, which is beyond the scope of this thesis. For simplicity, we will analyze the array tuning for the pseudo pitch-

catch (PPC) operation, which eliminates the need to take into account the problems associated with the reflection or mode conversion.

In operation, we consider two different scenarios: half-way tuning and full tuning. In both cases, an array transducer is used to transmit phase tuned waves. In the former, the transmitted signals are received by a single-element receiver; in the latter, the signals are received and tuned by a secondary array transducer.

7.2 Theoretical Development

7.2.1 Single Element Excitation

Before analyzing the array-tuned scenarios, we will consider the condition where Lamb waves are generated by a single element transducer and received by another single element transducer located at a distance x, as shown in Fig. 7.1. For reference, we may use indices m and n to denote the transmitting and receiving elements, respectively. If the element size a is small, e.g., $a < 1$ mm, it is reasonable to assume the receiving transducer as a point receiver. Otherwise, the size of the receiving element should be taken into account in the analysis. We will treat the receiving element transducer as a point receiver for simplicity.

The analysis is based on the transient wave model treated in Chapter 5, except that we express the equations using the indices m and n. The key equations are the displacements expressed in terms of the overall excitation efficiency:

$$u_{mn}(h,x,t) = \frac{1}{4\pi^2}\int_{-\infty}^{+\infty}\int_{-\infty}^{+\infty} N(h,k,\omega)\cdot\hat{f}(k,\omega)\cdot e^{j(kx-\omega t)}dkd\omega\ , \tag{7.1}$$

and those expressed in terms of the modal excitation efficiency:

$$u_{mn}(h,x,t) = \frac{1}{2\pi}\int_{-\infty}^{+\infty}\sum H(h,\omega)\cdot\hat{f}(k,\omega)\cdot e^{j(kx-\omega t)}dkd\omega\ . \tag{7.2}$$

where the summation is carried out for all the modes. Note that the displacements $u_{mn}(h,x,t)$ refer to the out-of-plane displacements. For simplicity, the superscripts

s (symmetric) and a (antisymmetric) are omitted in Eqs. (7.1) and (7.2), and the subscript mn represents the transmitter-receiver pair (m, n).

The expressions for the overall excitation efficiency $N(h, k, \omega)$ and the modal excitation efficiency $H(h, \omega)$ can be readily found in Chapter 5. In this study, we consider the same excitation condition as those used in Chapter 6, i.e., the time excitation function of an m_0-cycle toneburst with the center frequency f_0, and the uniformly distributed space excitation function over the element, represented by the function

$$f(x,t) = [H(x + a/2) - H(x - a/2)][H(t) - H(x - m_0/f_0)] \exp[-j\omega_0 t] \,, \tag{7.3}$$

whose Fourier transform is the same as Eq. (6.7):

$$\hat{f}(k,\omega) = \frac{a}{f_0} \frac{\sin(ka/2)}{ka/2} \frac{\sin[(\omega - \omega_0)m_0/2f_0]}{(\omega - \omega_0)/2f_0} e^{j(\omega-\omega_0)m_0/2f_0} \,. \tag{7.4}$$

Recall that the displacement in the transformed domain is expressed in the form:

$$\hat{u}_{mn}(h,k,\omega) = N(h,k,\omega)\hat{f}(k,\omega) \,. \tag{7.5}$$

7.2.2 Half-way Tuning

Figure 7.2 schematically illustrates the first scenarios, in which Lamb waves are generated using an M-element linear array of element size a and inter-element spacing d, and received by the n-th element of the receiving array. The distance between

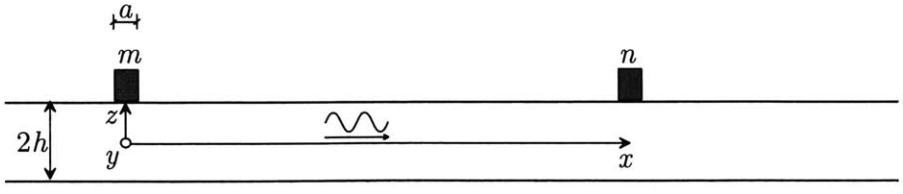

Figure 7.1: Generation of Lamb waves in an elastic plate of thickness $2h$ using a single element of size a. The distance between the receiving and the transmitting elements is x.

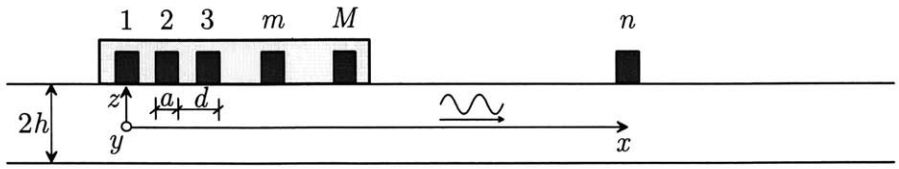

Figure 7.2: Tuning of Lamb waves in an elastic plate of thickness $2h$ using an M-element linear phased array (half-way tuning in PPC operation), where the element size is a, the inter-element spacing is d. The distance between the receiver and the first transmitting element is x.

the first transmitting element and the receiving element (n) is x. Recall that the time delay between two neighboring elements required for synthetic phase tuning or phased array tuning is given as

$$\Delta\tau = d/c_p \ . \tag{7.6}$$

If we choose the position of the first element in the transmitting array as the origin of the x-coordinate, the displacement contributed by the m-th transmitting element can be expressed as

$$u_{mn}(h, x, t) = u_{1n}(h, x - (m-1)d, t - (m-1)\Delta\tau) \ , \tag{7.7}$$

assuming that characteristics of the elements are identical.

The phase tuned displacement is obtained by summing the contributions made by all the elements as

$$u_n(h, x, t) = \sum_{m=1}^{M} u_{mn}(h, x, t) = \sum_{m=1}^{M} u_{1n}(h, x - (m-1)d, t - (m-1)\Delta\tau) \ . \tag{7.8}$$

By substituting Eqs. (7.1) and (7.6) into Eq. (7.8), and using the relationship:

$$\sum_{m=1}^{M} e^{-j(m-1)(kd-\omega\Delta\tau)} = \frac{1 - e^{-jM(kd-\omega\Delta\tau)}}{1 - e^{-j(kd-\omega\Delta\tau)}} = \frac{\sin[M(kd-\omega\Delta\tau)/2]}{\sin[(kd-\omega\Delta\tau)/2]} e^{-j(M-1)(kd-\omega\Delta\tau)/2} \ , \tag{7.9}$$

the displacement can be written in terms of the inverse double Fourier transform as

$$u_n(h,x,t) = \frac{1}{4\pi^2}\int_{-\infty}^{+\infty}\int_{-\infty}^{+\infty} N(h,k,\omega)\cdot\hat{f}(k,\omega)\cdot\frac{\sin[M(kd-\omega\Delta\tau)/2]}{\sin[(kd-\omega\Delta\tau)/2]}\times e^{-j(M-1)(kd-\omega\Delta\tau)/2}\cdot e^{j(kx-\omega t)}dkd\omega\ , \tag{7.10}$$

or it can be expressed in terms of the response of individual mode as

$$u_n(h,x,t) = \frac{1}{2\pi}\int_{-\infty}^{+\infty}\sum H(h,\omega)\cdot\hat{f}(k,\omega)\cdot\frac{\sin[M(kd-\omega\Delta\tau)/2]}{\sin[(kd-\omega\Delta\tau)/2]}\times e^{j(kx-\omega t)}\cdot e^{-j(M-1)(kd-\omega\Delta\tau)/2}d\omega\ . \tag{7.11}$$

From Eq. (7.10), we can show that the displacement in the Fourier domain is written as

$$\hat{u}_n(h,k,\omega) = N(h,k,\omega)\cdot\hat{f}(k,\omega)\cdot\frac{\sin[M(kd-\omega\Delta\tau)/2]}{\sin[(kd-\omega\Delta\tau)/2]}\ . \tag{7.12}$$

Note from Eqs. (7.11) and (7.12) that the tuning effect is contributed by the term $\frac{\sin[M(kd-\omega\Delta\tau)/2]}{\sin[(kd-\omega\Delta\tau)/2]}$.

7.2.3 Full Tuning

Now we consider the second scenario, in which the array tuning takes place both in transmission and reception.

Figure 7.3 schematically illustrates the operation of full tuning in PPC, where the transmitting and receiving arrays have M and N elements, respectively. The two arrays have the same element size a and inter-element spacing d, and the distance between the first receiving element and the first transmitting element is x. The time delay between two neighboring elements is still set according to Eq. (7.6).

If we choose the first element in the receiving array as a reference, the half-way tuned wave displacement obtained by the n-th receiving element can be expressed as

$$u_n(h,x,t) = u_1(h,x-(n-1)d,t-(n-1)\Delta\tau)\ . \tag{7.13}$$

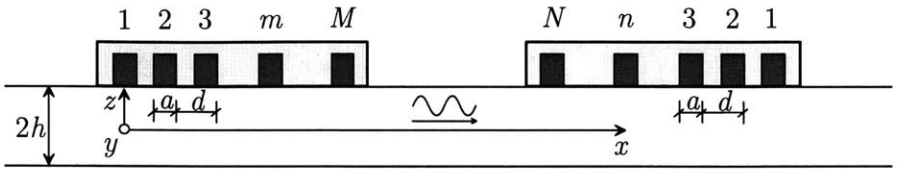

Figure 7.3: Tuning of Lamb waves using an array of M elements, where the receiver is an array of N elements (full tuning in PPC operation). The distance between the first receiving element and the first transmitting element is x.

Carrying out the summation for all the receiving elements, we obtain the fully tuned displacement in the form

$$u(h,x,t) = \sum_{n=1}^{N} u_n(h,x,t) = \sum_{n=1}^{N} u_1(h,x-(n-1)d, t-(n-1)\Delta\tau) \; . \tag{7.14}$$

which can be expanded by substituting Eqs. (7.10) and (7.6) into Eq. (7.14) as

$$\begin{aligned} u(h,x,t) = & \frac{1}{4\pi^2} \int_{-\infty}^{+\infty} \int_{-\infty}^{+\infty} N(h,k,\omega) \cdot \hat{f}(k,\omega) \cdot \frac{\sin[M(kd-\omega\Delta\tau)/2]}{\sin[(kd-\omega\Delta\tau)/2]} \times \\ & \frac{\sin[N(kd-\omega\Delta\tau)/2]}{\sin[(kd-\omega\Delta\tau)/2]} \cdot e^{-j(M+N-2)(kd-\omega\Delta\tau)/2} \cdot e^{j(kx-\omega t)} dk d\omega \; , \end{aligned} \tag{7.15}$$

or in terms of the individual modes as

$$\begin{aligned} u(h,x,t) = & \frac{1}{2\pi} \int_{-\infty}^{+\infty} \sum H(h,\omega) \cdot \hat{f}(k,\omega) \cdot \frac{\sin[M(kd-\omega\Delta\tau)/2]}{\sin[(kd-\omega\Delta\tau)/2]} \cdot \frac{\sin[N(kd-\omega\Delta\tau)/2]}{\sin[(kd-\omega\Delta\tau)/2]} \times \\ & e^{-j(M+N-2)(kd-\omega\Delta\tau)/2} \cdot e^{j(kx-\omega t)} d\omega \; . \end{aligned} \tag{7.16}$$

The displacements in the transformed domain are

$$\begin{aligned} \hat{u}(h,k,\omega) = & N(h,k,\omega) \cdot \hat{f}(k,\omega) \cdot \frac{\sin[M(kd-\omega\Delta\tau)/2]}{\sin[(kd-\omega\Delta\tau)/2]} \cdot \frac{\sin[N(kd-\omega\Delta\tau)/2]}{\sin[(kd-\omega\Delta\tau)/2]} \times \\ & e^{-j(M+N-2)(kd-\omega\Delta\tau)/2} \; . \end{aligned} \tag{7.17}$$

If two identical arrays are used for transmitter and receiver ($M = N$), then the corresponding equations are rewritten as

$$u(h,x,t) = \frac{1}{4\pi^2}\int_{-\infty}^{+\infty}\int_{-\infty}^{+\infty} N(h,k,\omega)\cdot\hat{f}(k,\omega)\cdot\left\{\frac{\sin[M(kd-\omega\Delta\tau)/2]}{\sin[(kd-\omega\Delta\tau)/2]}\right\}^2 \times e^{-j(M-1)(kd-\omega\Delta\tau)}\cdot e^{j(kx-\omega t)}dkd\omega\,, \tag{7.18}$$

$$u(h,x,t) = \frac{1}{2\pi}\int_{-\infty}^{+\infty}\sum H(h,\omega)\cdot\hat{f}(k,\omega)\cdot\left\{\frac{\sin[M(kd-\omega\Delta\tau)/2]}{\sin[(kd-\omega\Delta\tau)/2]}\right\}^2 \times e^{-j(M-1)(kd-\omega\Delta\tau)}\cdot e^{j(kx-\omega t)}d\omega\,, \tag{7.19}$$

and

$$\hat{u}(h,k,\omega) = N(h,k,\omega)\cdot\hat{f}(k,\omega)\cdot\left\{\frac{\sin[M(kd-\omega\Delta\tau)/2]}{\sin[(kd-\omega\Delta\tau)/2]}\right\}^2\cdot e^{-j(M-1)(kd-\omega\Delta\tau)}\,. \tag{7.20}$$

Observe from Eqs. (7.11) and (7.12) that the full tuning effect comes from the term $\left\{\frac{\sin[M(kd-\omega\Delta\tau)/2]}{\sin[(kd-\omega\Delta\tau)/2]}\right\}^2$, which is exactly the square of the contributing term for the half-way tuning.

7.3 Simulation Examples

We will now examine the tuning efficiencies for various modes through a simulation study by giving examples of the half-way and fully tuned waves. To be consistent, we use the same excitation conditions, i.e., a five-cycle toneburst signal of center frequency $f_0 = 2.25$ MHz is used as excitation signal. Both transmitting and receiving transducers are 16-element arrays, the inter-element spacing is $d = 0.7$ mm, and element size $a = 0.4$ mm.

7.3.1 Half-way Tuning

The parameters used in the half-way tuning simulation are summarized in Table 7.1.

Table 7.1: Parameters used in the half-way tuning simulation.

Parameter	Value
Material	Aluminum
Longitudinal wavespeed, c_L, (m/s)	6320
Transverse wavespeed, c_T, (m/s)	3130
Number of elements (transmitting), M	16
Inter-element spacing, d, (mm)	0.7
Element width, a, (mm)	0.4
Toneburst frequency, f_0, (MHz)	2.25
Number of toneburst cycles, m_0	5
Plate thickness, $2h$, (mm)	2.0
$2f_0h$ value, (MHz-mm)	4.5
Transducer distance, x, (mm)	168.0

According to the dispersion curves shown in Fig. 2.6, at the given center frequency ($2f_0h = 4.5$ MHz-mm, $\omega_0 h/c_T = 4.52$), there are five coexisting modes: A_0, S_0, A_1, S_1 and S_2, whose phase and group velocities as well as the required time delays are given in Table 7.2.

Table 7.2: Required parameters for half-way tuning of various wave modes.

Wave mode	Phase velocity c_p, (m/s)	Group velocity c_g, (m/s)	Time delay $\Delta\tau$, (ns)
S_2	9,846	3,568	71
S_1	5,834	4,171	120
A_1	4,269	2,161	164
S_0	2,961	2,704	236
A_0	2,861	2,980	245

Simulation results for half-way tuning are shown in Figs. 7.4, 7.5 and 7.6. As is the case for angle wedge transducer tuning, additional modes (A_2, A_3 and S_3) appear in the images shown in Fig. 7.4, due to the bandwidths of the excitation signal. Of course, these modes are not dominant, so that their individual waveforms are not shown.

Figure 7.4(a) is the result for the untuned case ($\Delta\tau = 0$ ns). At the center frequency of 2.25 MHz, the energy levels of the A_0 and S_0 modes are much higher than those of other modes, which is also shown in Fig. 7.5(a).

Figures 7.4(b) and 7.5(b) show the result of S_1 mode tuning ($\Delta\tau = 120$ ns), which is not quite successful since the energy is distributed almost evenly to all existing modes.

Shown in Figs. 7.4(c) 7.5(c) are the result for A_0 mode tuning ($\Delta\tau = 245$ ns). TheA_0 mode can be boosted, but it may not be a good choice for tuning since the phase velocities and required time delays are approximately the same for both A_0 and S_0 modes. Similar conclusions can be drawn for tuning S_0 mode ($\Delta\tau = 236$ ns), as shown in Figs. 7.4(d) and 7.6(a).

It seems that the best tuning modes are A_1 ($\Delta\tau = 164$ ns) and S_2 ($\Delta\tau = 71$ ns) as shown in Figs. 7.4(e), 7.6(b), 7.4(f), and 7.6(c). The tuned modes carry the highest energy (or amplitude) while the undesired modes are virtually squelched.

By summing the signals of individual wave modes depicted in Figs. 7.5 and 7.6, we can simulate the actual signal received by the transducer, as shown in Fig. 7.7. The signals shown in Figs. 7.7(a), through (d) are either bi-modal or multi-modal, whereas the waves in Figs. 7.7(e) and (f) are clearly tuned into single mode. Thus, it is desirable to use these modes (A_1 and S_2) for the given parameters.

7.3.2 Full Tuning

Now we extend our simulation study to full tuning. The main difference is that the tuning is carried out in receiving as well, using a second array. The simulation parameters found in Table 7.1 are used, except that an identical array is used as receiver and $x = 168.0$ mm refers to the distance between the first elements in the transmitting and receiving arrays.

The results are shown in Figs. 7.8 to 7.7. Comparing them with Figs. 7.4 to 7.7, we can clearly see that the tuning effect is enhanced for all the tuning cases. However, this does not change the conclusions on desired modes. For the S_1, S_0 and A_0 modes which are not well tuned in the half-way tuning, the improvement of tuning effect is

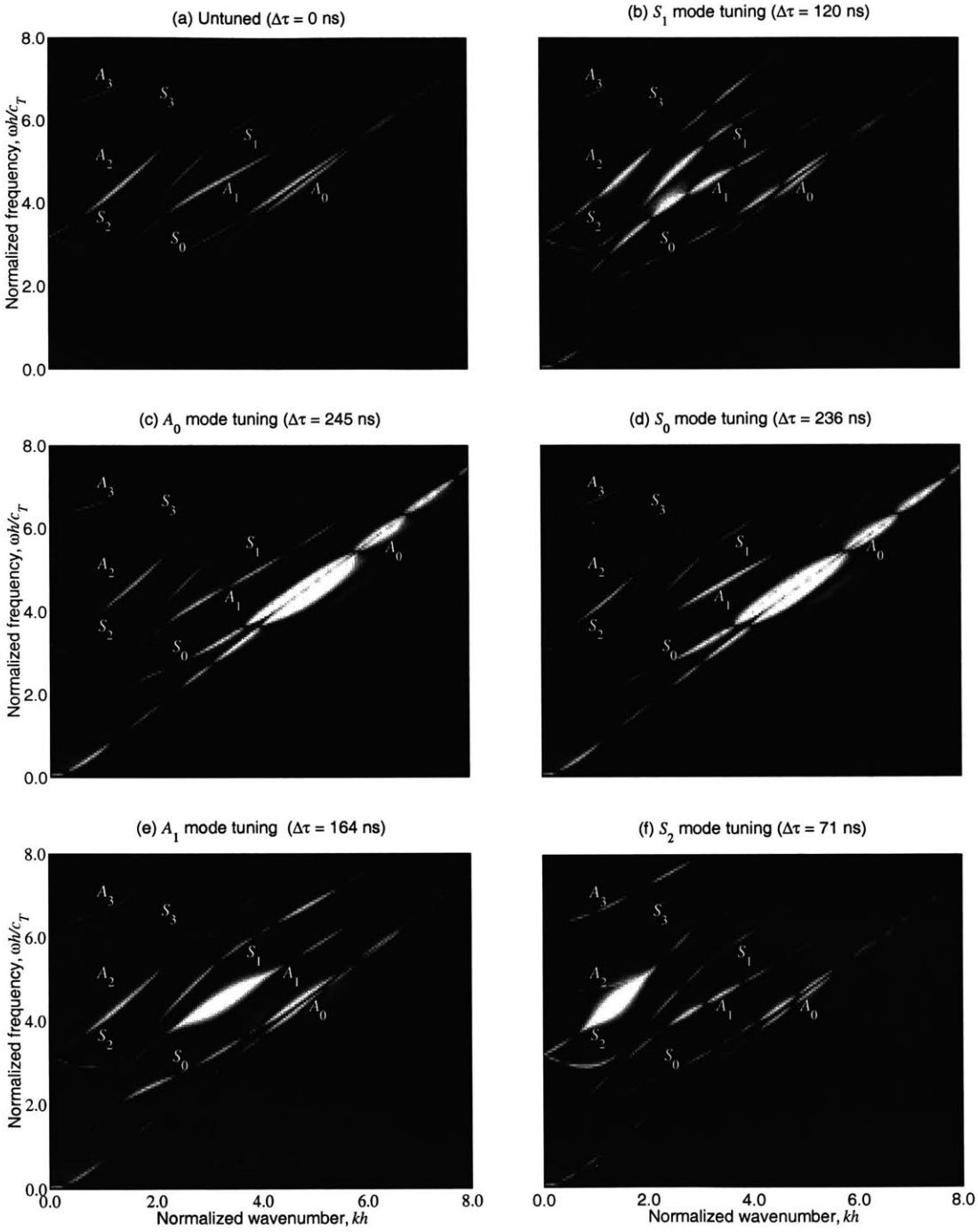

Figure 7.4: Image visualization of 2-D FT of displacements, $\hat{u}(h, k, \omega)$, for the halfway tuning with an excitation toneburst signal of center frequency $f_0 = 2.25$ MHz: (a) untuned case ($\Delta\tau = 0$ ns), (b) S_1 mode tuning ($\Delta\tau = 120$ ns), (c) A_0 mode tuning ($\Delta\tau = 245$ ns), (d) S_0 mode tuning ($\Delta\tau = 236$ ns), (e) A_1 mode tuning ($\Delta\tau = 164$ ns), and (f) S_2 mode tuning ($\Delta\tau = 71$ ns).

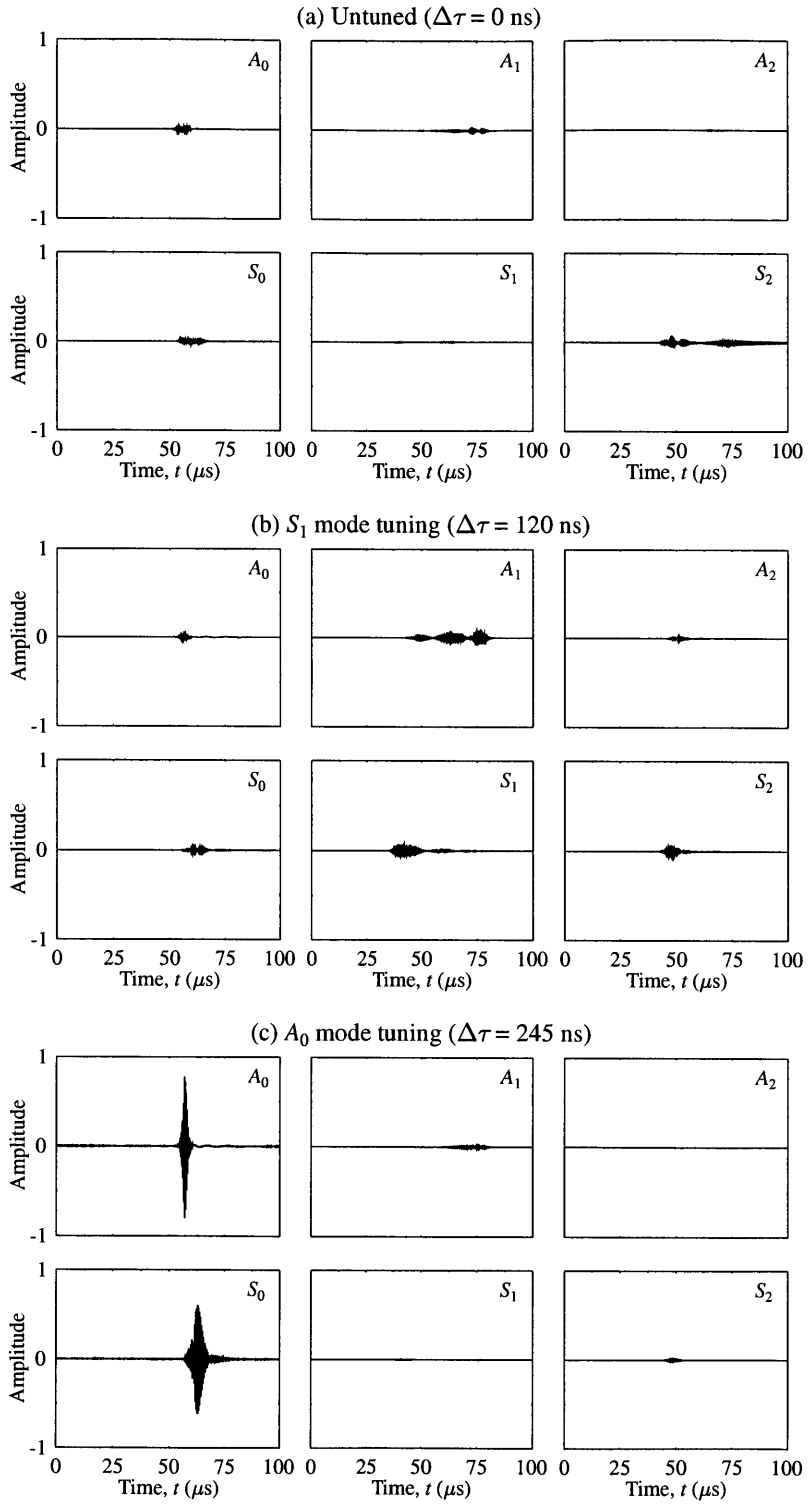

Figure 7.5: Predicted waveforms of individual modes for the half-way tuning with an excitation toneburst signal of center frequency $f_0 = 2.25$ MHz: (a) untuned case ($\Delta\tau = 0$ ns), (b) S_1 mode tuning ($\Delta\tau = 120$ ns), (c) A_0 mode tuning ($\Delta\tau = 245$ ns).

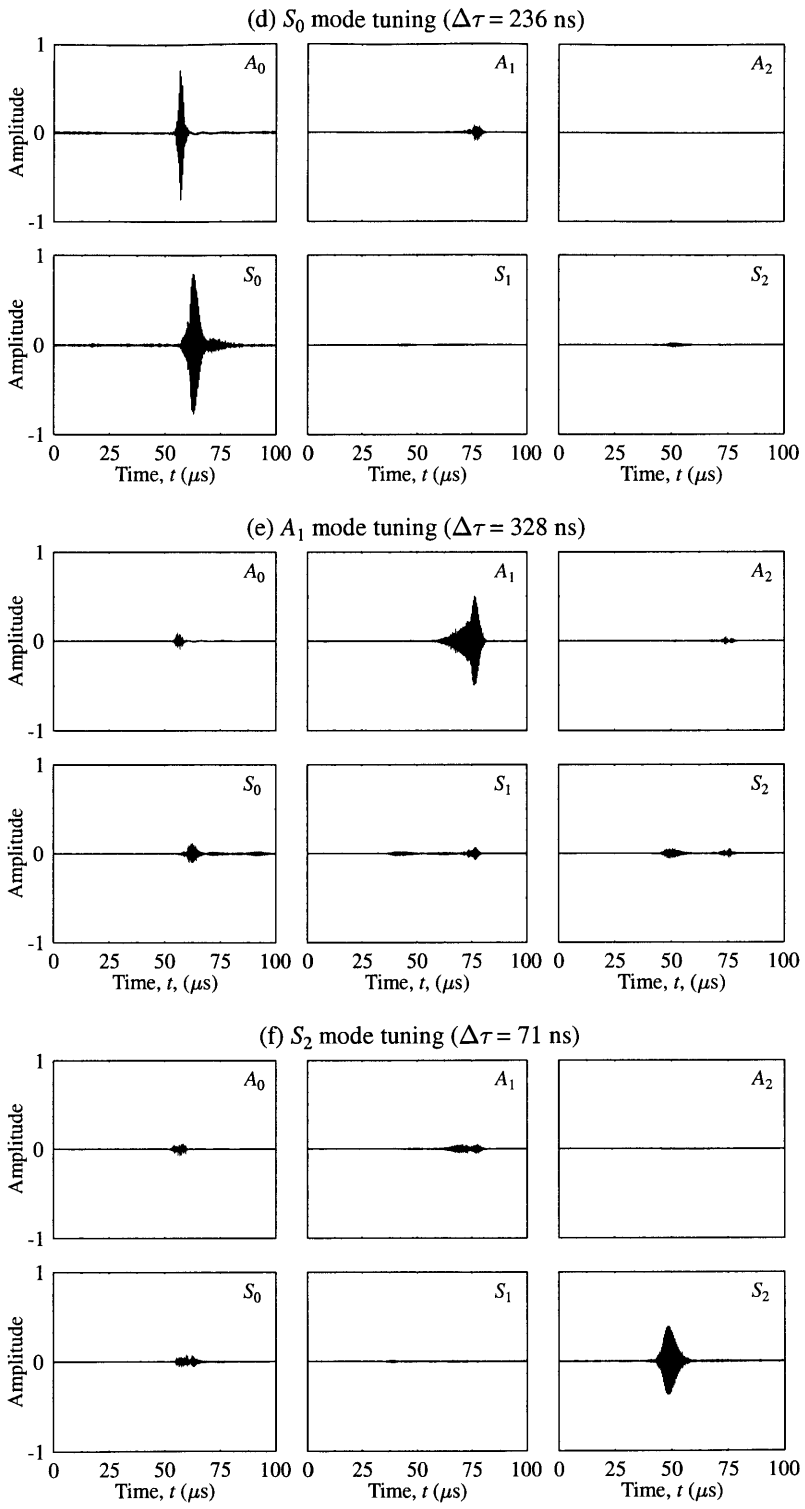

Figure 7.6: Predicted waveforms of individual modes for the half-way tuning with an excitation toneburst signal of center frequency $f_0 = 2.25$ MHz: (a) S_0 mode tuning ($\Delta\tau = 236$ ns), (b) A_1 mode tuning ($\Delta\tau = 164$ ns), and (c) S_2 mode tuning ($\Delta\tau = 71$ ns).

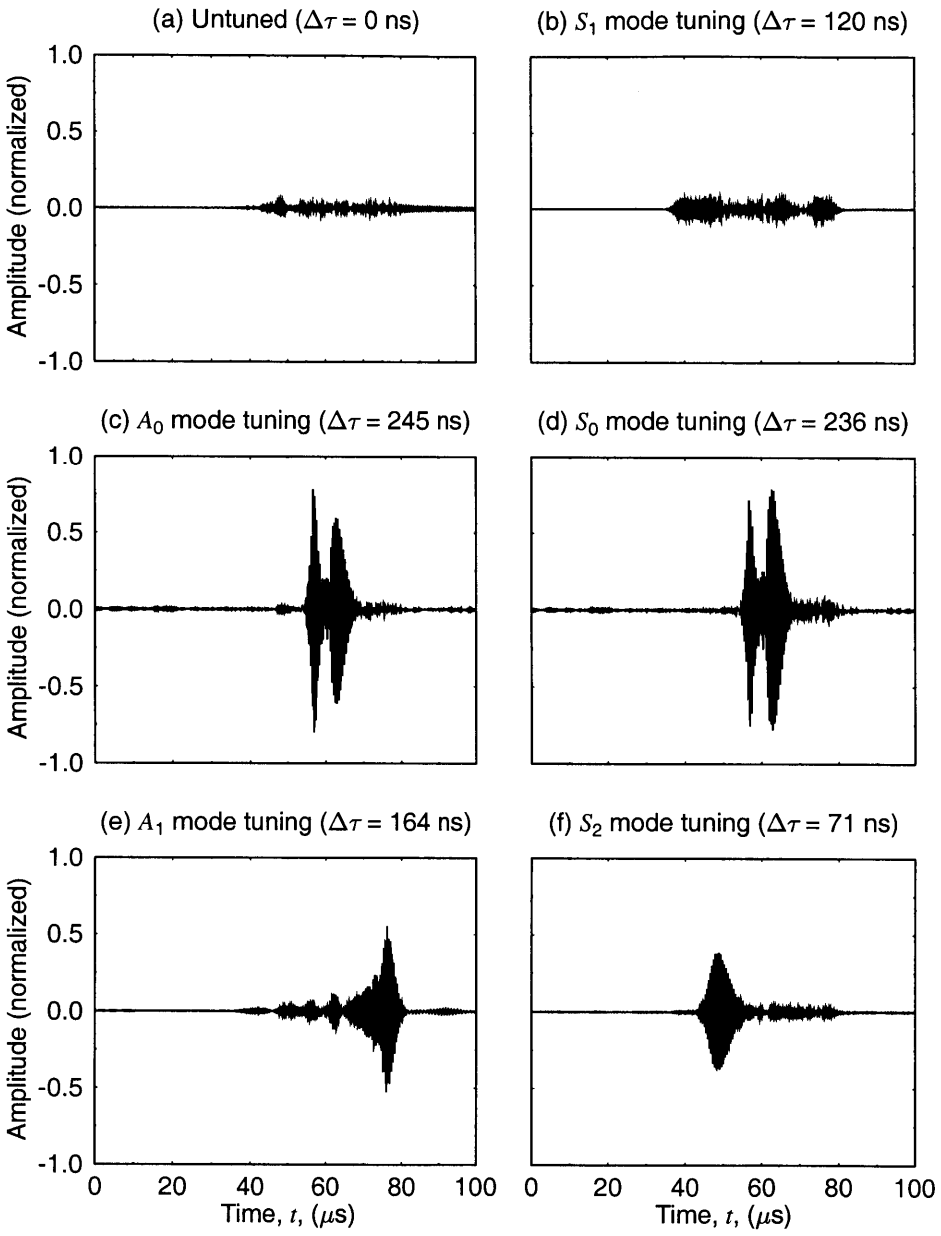

Figure 7.7: Predicted waveforms for the half-way tuning of Lamb waves with a 5-cycle toneburst signal of frequency $f_0 = 2.25$ MHz: (a) untuned case ($\Delta\tau = 0$ ns), (b) S_1 mode tuning ($\Delta\tau = 120$ ns), (c) A_0 mode tuning ($\Delta\tau = 245$ ns), (d) S_0 mode tuning ($\Delta\tau = 236$ ns), (e) A_1 mode tuning ($\Delta\tau = 164$ ns), and (f) S_2 mode tuning ($\Delta\tau = 71$ ns).

not significant enough to make them a desirable choice. For the A_1 and S_2 modes which are already well tuned in the half-way tuning, the improvement of tuning effect makes them a more desirable choice.

7.4 Experimental Investigation

The simulation results are validated in this section by comparing the predicted waveforms with those obtained experimentally. The investigation is limited only for half-way tuning, for the sake of simplicity.

Figure 7.12 illustrates the schematic diagram of the experimental setup for the half-way tuning. This setup is identical to that used in the angle wedge transducer tuning experiment, except that the wedge is replaced by a PVDF array transducer. For consistency, the same parameters given in the simulation study are used, which can be found in Tables 7.1 and 7.2.

Figure 7.13 shows the as-obtained waves transmitted by the 16 transmitting elements and received by the single-element receiver. Note that the waveforms vary from one transmitting element to the other, which is perhaps caused by not only the dispersive nature of Lamb waves but also the response disparity of array elements.

This deficiency may influence the tuning result, but can be alleviated with improved array transducers. Tuned waves are constructed synthetically using the formula

$$u_n(h, x, t) = \sum_{m=1}^{M} u_{mn}(h, x, t - (m-1)\Delta\tau) \ . \tag{7.21}$$

as introduced in Chapter 4.

The experimental tuning results for various wave modes are shown in Fig. 7.14. If we compare the theoretical results shown in Fig. 7.7 with these experimental results, we can observe that the agreement is good in general while the difference is not trivial.

Both results show that the S_1, A_0 and S_0 modes are not well tuned while the A_1 and S_2 modes are well tuned, as compared with the untuned case. Furthermore, the

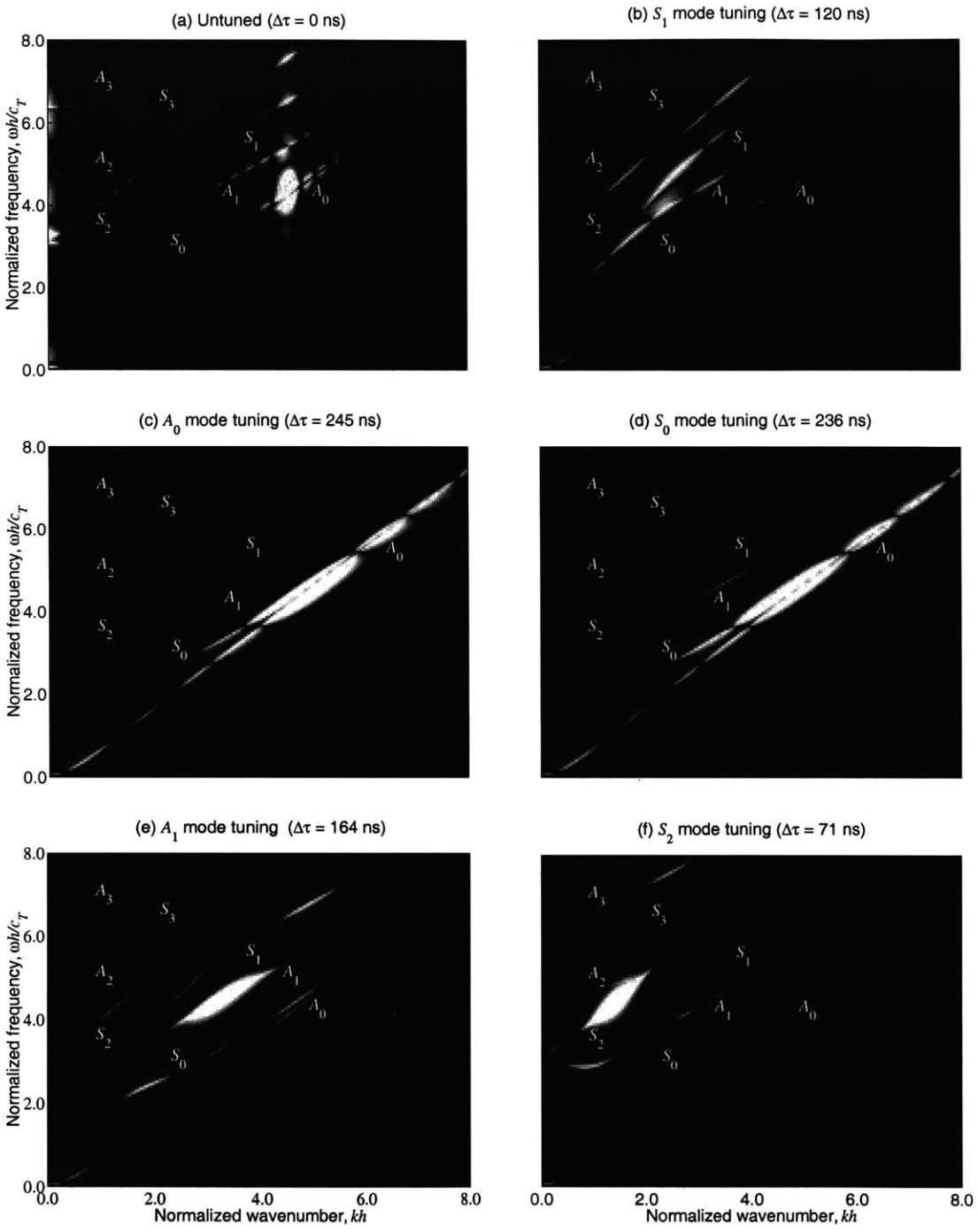

Figure 7.8: Image visualization of 2-D FT of displacements, $\hat{u}(h, k, \omega)$, for the full tuning of Lamb waves with an excitation toneburst signal of center frequency $f_0 = 2.25$ MHz: (a) untuned case ($\Delta\tau = 0$ ns), (b) S_1 mode tuning ($\Delta\tau = 120$ ns), (c) A_0 mode tuning ($\Delta\tau = 245$ ns), (d) S_0 mode tuning ($\Delta\tau = 236$ ns), (e) A_1 mode tuning ($\Delta\tau = 164$ ns), and (f) S_2 mode tuning ($\Delta\tau = 71$ ns).

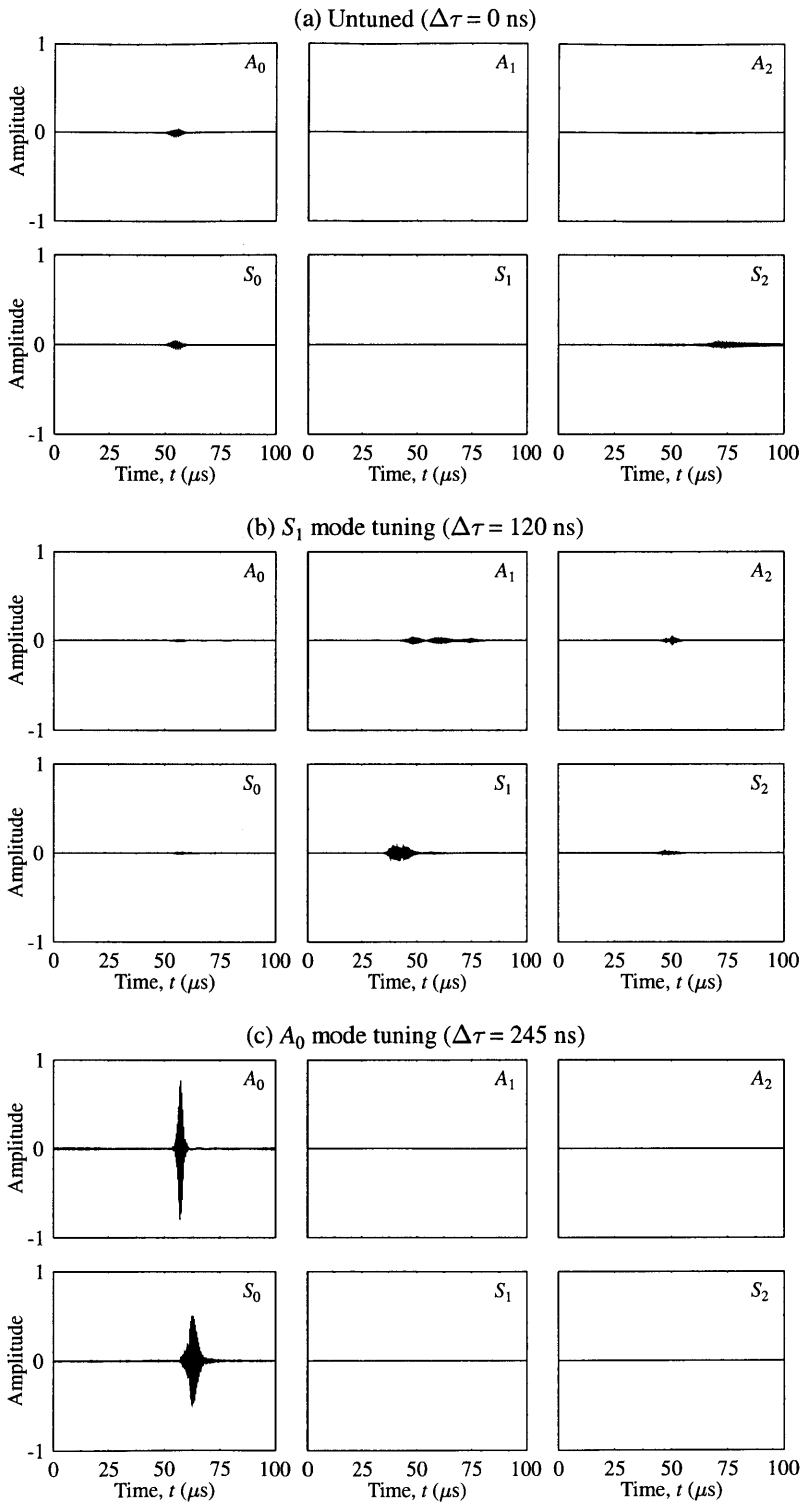

Figure 7.9: Predicted waveforms of individual modes for the full tuning of Lamb waves with an excitation toneburst signal of center frequency $f_0 = 2.25$ MHz: (a) untuned case ($\Delta\tau = 0$ ns), (b) S_1 mode tuning ($\Delta\tau = 120$ ns), (c) A_0 mode tuning ($\Delta\tau = 245$ ns).

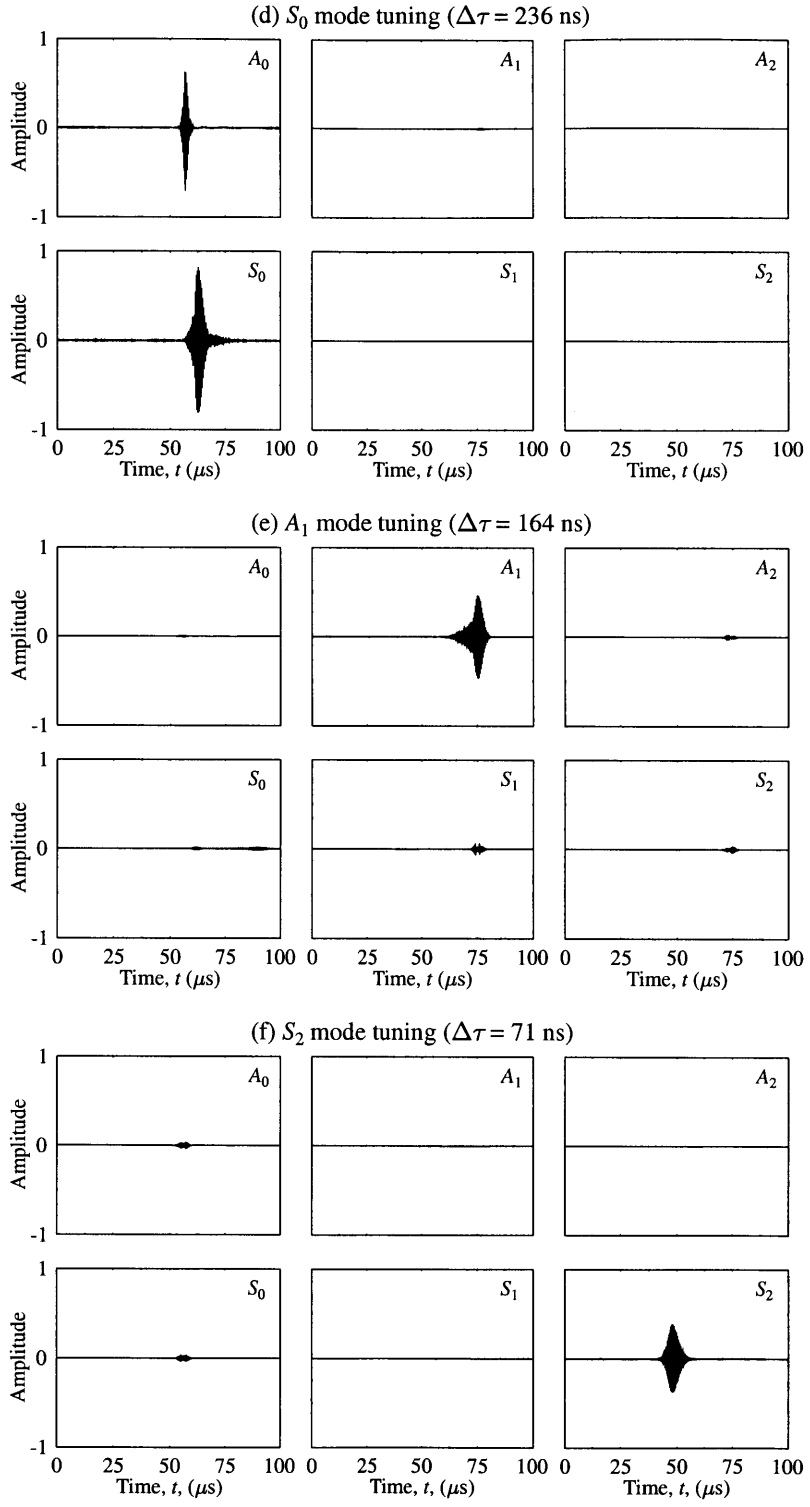

Figure 7.10: Predicted waveforms of individual modes for the full tuning with an excitation toneburst signal of center frequency $f_0 = 2.25$ MHz: (a) S_0 mode tuning ($\Delta\tau = 236$ ns), (b) A_1 mode tuning ($\Delta\tau = 164$ ns), and (c) S_2 mode tuning ($\Delta\tau = 71$ ns).

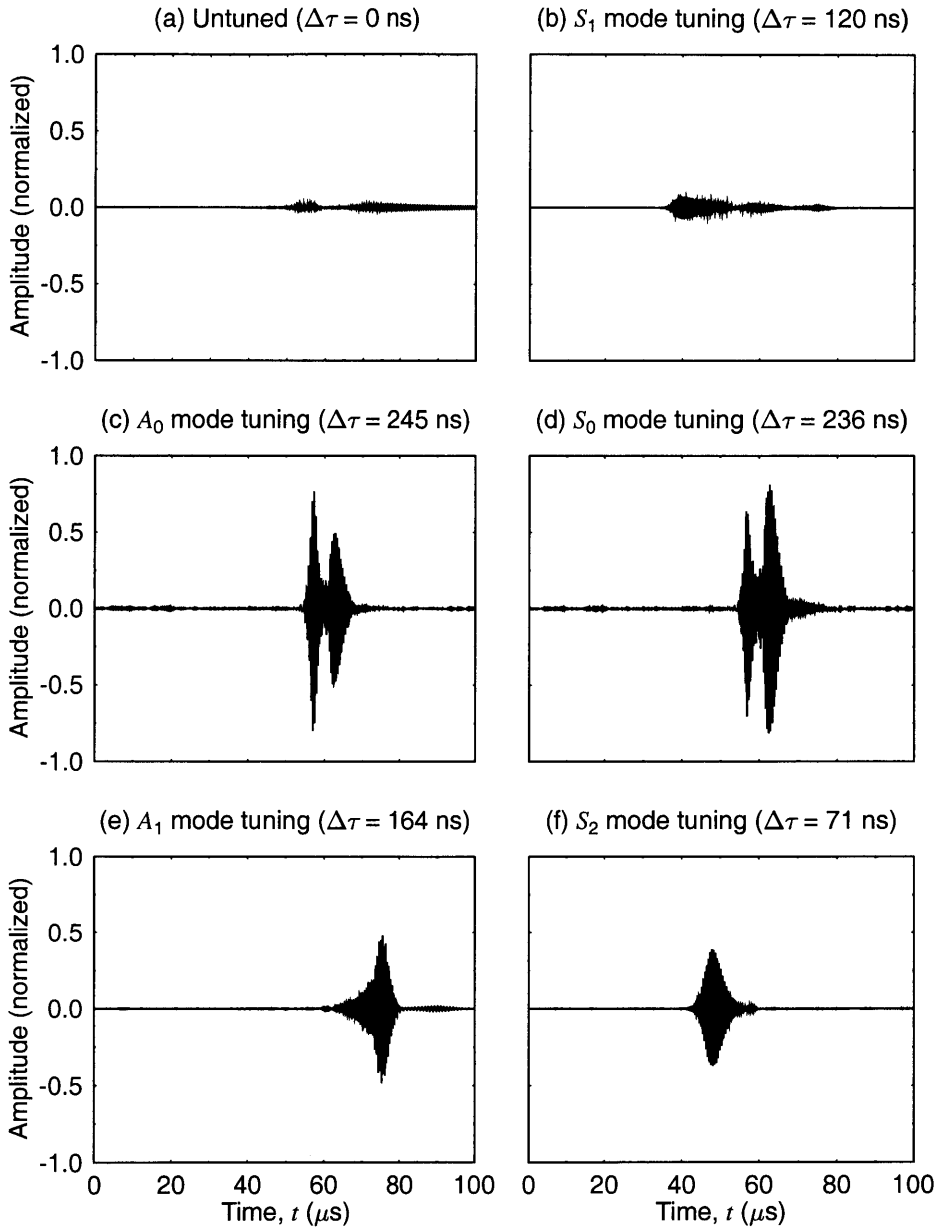

Figure 7.11: Theoretical waveforms for the full tuning with a 5-cycle toneburst signal of frequency $f_0 = 2.25$ MHz: (a) untuned case ($\Delta\tau = 0$ ns), (b) S_1 mode tuning ($\Delta\tau = 120$ ns), (c) A_0 mode tuning ($\Delta\tau = 245$ ns), (d) S_0 mode tuning ($\Delta\tau = 236$ ns), (e) A_1 mode tuning ($\Delta\tau = 164$ ns), and (f) S_2 mode tuning ($\Delta\tau = 71$ ns).

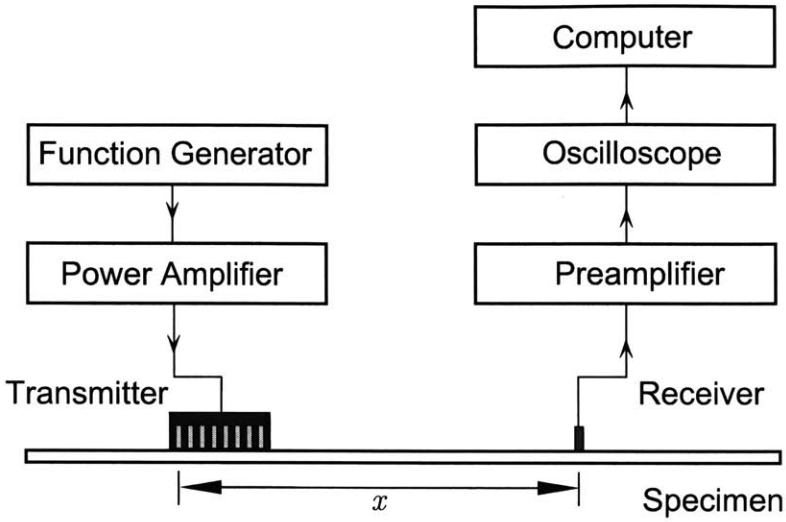

Figure 7.12: Experimental setup for half-way tuning of Lamb waves, where tuned Lamb waves are generated by an array of 16 elements and received by one single-element transducer.

experimental waveforms for A_1 and S_2 mode tuning are quite similar to the theoretical waveforms.

The big difference between Fig. 7.14 and Fig. 7.7 is the relative amplitude of the A_0 and S_0 tuned waves, which is experimentally very low while theoretically very high. There are two possible causes for this difference. The first cause is that the array elements might have different characteristics, while in the theoretical calculation we assume that all the elements are identical. The second cause is that the measured frequency response (of a representative element) has a center frequency of f_0 at about 6 MHz, while in the tuning experiment we observed that the received signals became very weak when the frequency of the excitation toneburst signal was higher than 3 MHz. Note that in the theoretical waveforms of A_0 and S_0 modes, high frequency components are strong, as shown in Figs. 7.4(c) and (d). Currently, we can not understand this phenomenon.

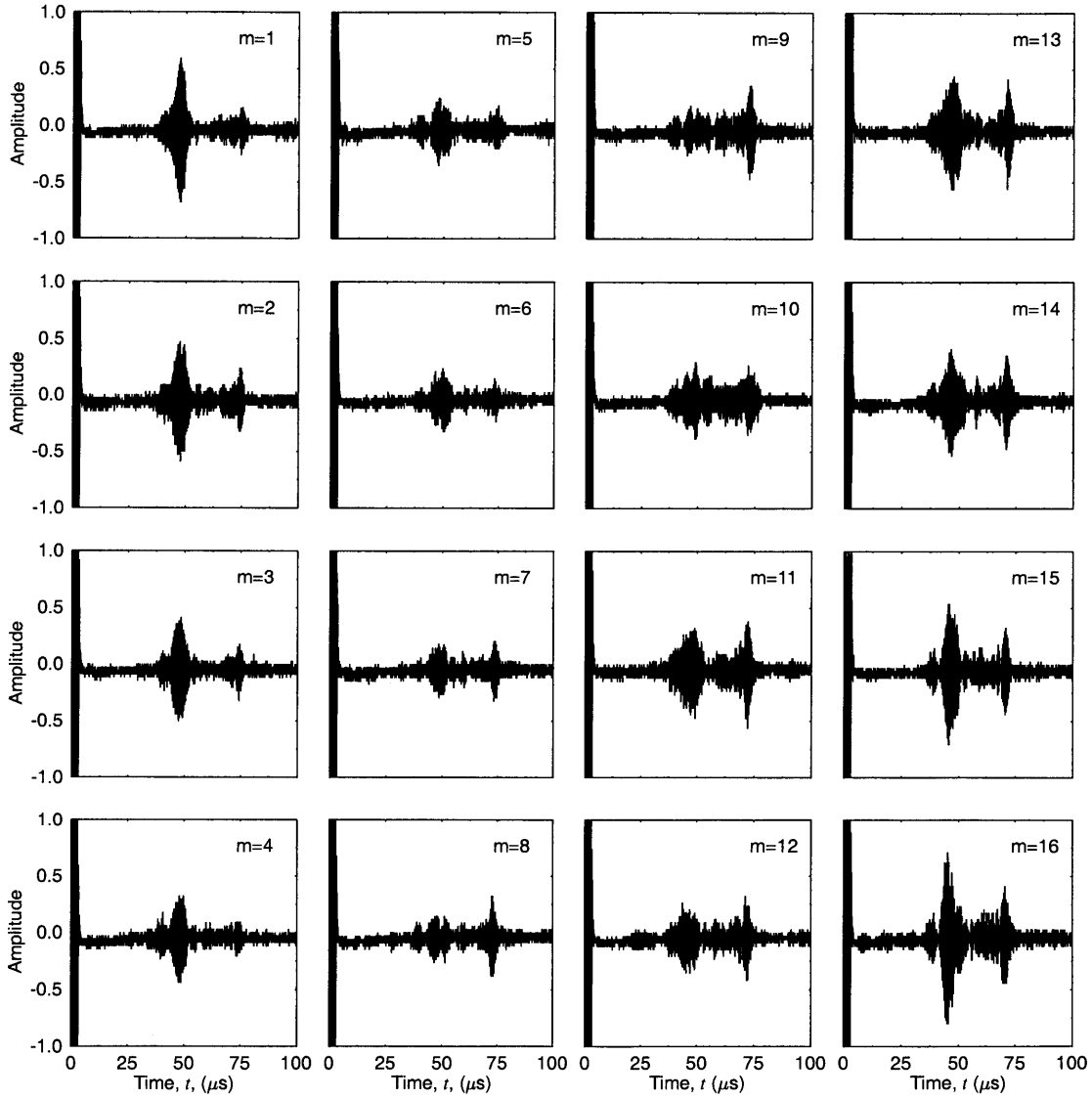

Figure 7.13: As-obtained individual waveforms generated by the 16 elements of the transmitting array and received by the receiving element.

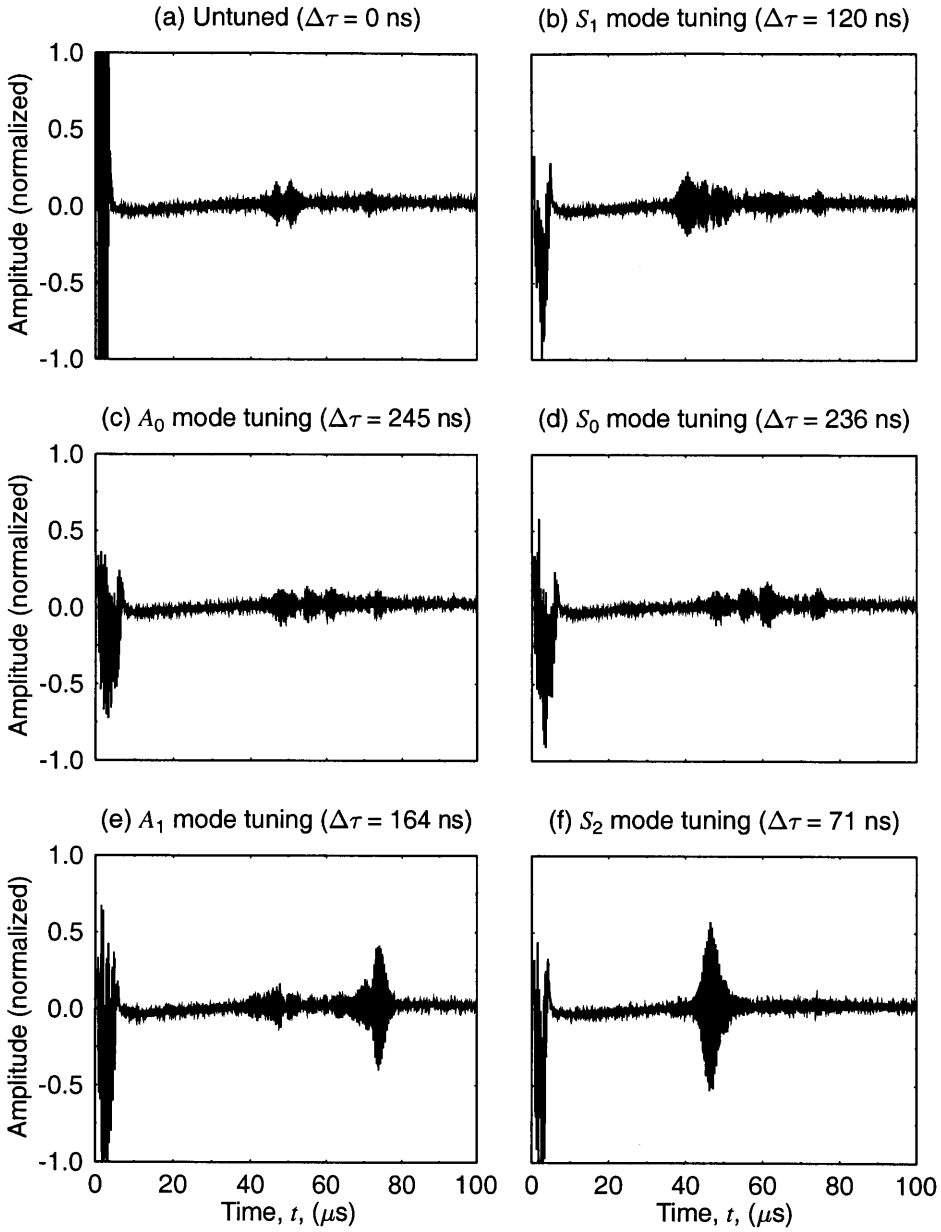

Figure 7.14: Experimental waveforms for the half-way tuning testing of Lamb waves with a 5-cycle toneburst signal of frequency $f_0 = 2.25$ MHz: (a) untuned case ($\Delta\tau = 0$ ns), (b) S_1 mode tuning ($\Delta\tau = 120$ ns), (c) A_0 mode tuning ($\Delta\tau = 245$ ns), (d) S_0 mode tuning ($\Delta\tau = 236$ ns), (e) A_1 mode tuning ($\Delta\tau = 164$ ns), and (f) S_2 mode tuning ($\Delta\tau = 71$ ns).

7.5 Conclusions

The synthetic phase tuning (SPT) in the pseudo pitch-catch (PPC) operation was investigated quantitatively, based on the analytical model of transient waves. Simulation examples were provided to illustrate tuning effect of SPT, including the half-way tuning and full tuning. Experimental waveforms were also obtained for the half-way tuning.

It was shown that the theoretical predications were in general consistent with the experimental observations. We can conclude that the array tuning effect is achieved by providing time delays for the transmitting array elements. Also learned is that the tuning effect is improved by replacing the single-element receiver with a second array transducer, i.e., full tuning is better than half-way tuning.

As pointed out in Chapter 4, the SPT method is advantageous than the angle wedge transducer tuning method. This was further confirmed in this chapter. First, it is possible to tune all the wave modes using array transducers. By contrast, wave modes with low phase velocities can not be tuned using angle wedge transducers. Second, the SPT enables accurate control of the time delays while it is difficult to set the angle of incidence accurately. Third, array transducers are directly coupled to the specimen, eliminating the problem caused by multiple interfaces in the wedge assembly.

Note that the influence of the array parameters such as the number of elements, M (and N), and the inter-element distance, d, on the tuning effect of this approach was not studied. An extensive investigation on this topic will be recommended for the future work.

Chapter 8

Analysis of Laser Generation of Lamb Waves

8.1 Introduction

Up to now, we have used toneburst signals to excite piezoelectric transducers for producing Lamb waves. The narrow bandwidth of the signals allows for simple signal processing schemes because the influence of dispersion are minimally attributed. However, it is often desirable to use broadband signals because the information over a wide range of frequency can be processed without sweeping the frequency. One of the candidate sources to produce broadband ultrasonic signals is laser. Another good reason to use laser sources is that they are non-contact. Due to the many advantages, laser ultrasonics is finding more and more application in flaw detection and material characterization, as summarized by Scruby [76] and Davies *et al.* [77].

Depending on the specimen geometry, lasers can produce bulk, Rayleigh, Lamb, and other waves. In the early stage of the development, bulk waves were most commonly used. With the increasing awareness of Lamb waves NDE, lasers become common energy sources to produce Lamb waves. They have been employed to construct dispersion curves [78–80], to measure the thickness of thin metal sheet [81], to measure elastic constants of paper [79, 82] and to assess damages in paper [83].

The mechanism of laser generation of ultrasound in solids has been studied by many investigators [84–86]. Basically, there are two types of acoustic sources representing the generation process: *thermoelastic regime* and *ablation regime*, as schematically shown in Fig. 8.1. In the thermoelastic regime where the laser power density is low, the optical energy is converted to acoustic energy primarily due to the thermoelastic expansion of materials. As a result, the induced stresses are primarily in directions parallel to the surface (shear stresses). In the ablation regime, on the other hand, the high laser power density level causes the formation of plasma and the removal of material from the surface. As a result of the momentum transfer, normal stresses will be induced.

Laser-generated ultrasound in bulk materials has been studied by numerous investigators [76, 84, 87–97], both theoretically and experimentally. By contrast, the analytical studies on the generation of Lamb waves are limited. Spicer *et al.* [98] developed a quantitative model using Hankel-Laplace transform to study ultrasonic waves in thin plates excited thermoelastically by a laser pulse. Using the normal mode expansion method, Cheng *et al.* [99–103] studied the waves caused by thermoelastic excitation or oil-coating evaporation (ablation regime), although their theoretical results were not confirmed by experiments. Most of the work on Lamb wave generation is limited to the experimental measurements.

This chapter is mainly devoted to the development of an analytical model to study the transient behavior of Lamb waves generated by a laser source in the ablation range. The circular cross-section of a laser beam produces a circular illumination area (source). However, it is often advantageous to use a source of strip (line) shape in some cases, e.g., to enhance the wave directivity [95]. This is practically possible by focusing the laser beam into a line source, using a cylindrical lens [94, 96]. It is easier to analyze such line source since a simple two-dimensional model is sufficient to describe the nature, thus some of the mathematical complexity associated with circular sources can be relaxed. The model developed in Chapter 5 can be directly used by taking into account the different loading conditions.

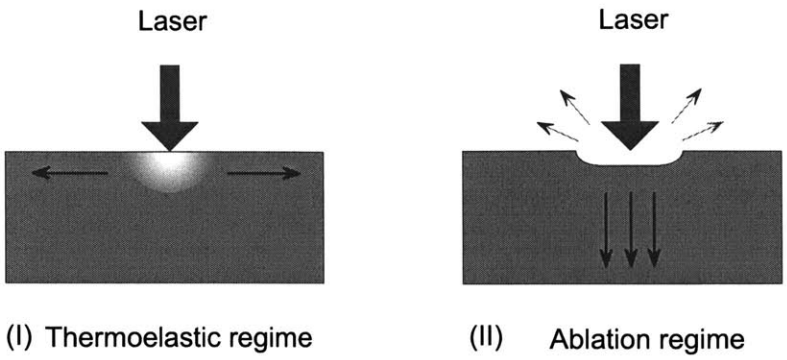

Figure 8.1: Schematic diagram of laser generation of ultrasound: (a) thermoelastic regime; (b) ablation regime.

Besides, this chapter will also investigate the tuning of laser-generated Lamb waves. Since broadband signals can be decomposed into multiple narrowband signals, it is possible to illustrate the tuning effect at different frequencies. The virtually tuned waves can be obtained by applying the synthetic phase tuning (SPT) scheme described in Chapter 4. Due to the aforementioned superior feature of laser ultrasound, tuning of laser-generated Lamb waves is very attractive. This study will greatly expand the application of broadband Lamb waves.

We will start with the development of an analytical model to study the propagation of transient waves originated from a circular source. Solutions will be obtained using the Fourier and Hankel transform for the wave mode displacements. Then, the loading conditions will be prescribed to represent the line and circular sources. The Lamb wave displacement responses due to a line source are analyzed using the 2-D FT of displacements and group velocity dispersion curves. Finally, laser-generated waveforms are obtained, and used to construct experimental dispersion curves as well as virtually tuned waves. The theoretical results will be compared with the experimental results.

8.2 Transient Response to a Circular Source

The analytical model of transient waves developed in Chapter 5 can be directly applied to a line source, where the Cartesian coordinates are used and the plain strain condition is assumed. Such waves are often called *straight-crested waves* [14]. In contrast, a circular source loading is actually an axisymmetric problem, which requires cylindrical coordinates for analysis. Waves under this condition are often called *circular-crested waves* [14]. In the following, an analytical model is developed to obtain the solutions of transient circular-crested waves due to a circular source using the Fourier and Hankel transform. The derivation procedure is similar to that used in obtaining the solutions of transient straight-crested waves from a line source.

8.2.1 Problem Statement

Consider a cylindrical coordinate system as shown in Fig. 8.2, where a plate of thickness $2h$ is subjected to a normal load $f(r,t)$ distributed in a circular area. [1] The stress boundary conditions can be prescribed as

$$\sigma_{zz}(r,t) = \begin{cases} f(r,t) & \text{at} \quad z = +h \\ 0 & \text{at} \quad z = -h \end{cases} \tag{8.2}$$

$$\sigma_{rz}(x,t) = 0 \qquad \text{at} \quad z = \pm h\,. \tag{8.3}$$

For an axisymmetric case, we have the condition $u_\theta = \partial/\partial\theta = 0$. Then the resulting equations of motion can be expressed in terms of displacement as [104]

$$(\lambda + 2\mu)\frac{\partial \Delta}{\partial r} + \mu\frac{\partial \Omega}{\partial z} = \rho\frac{\partial^2 u_r}{\partial t^2} \tag{8.4}$$

$$(\lambda + 2\mu)\frac{\partial \Delta}{\partial z} - \frac{\mu}{r}\frac{\partial (r\Omega)}{\partial r} = \rho\frac{\partial^2 u_z}{\partial t^2}\,, \tag{8.5}$$

[1] A particular case of circular load is the point load ($r \to 0$), represented by the form

$$f(r,t) = \frac{\delta(r)}{2\pi r} g(t)\,, \tag{8.1}$$

where $g(t)$ is the time dependence of the source, or the time excitation function.

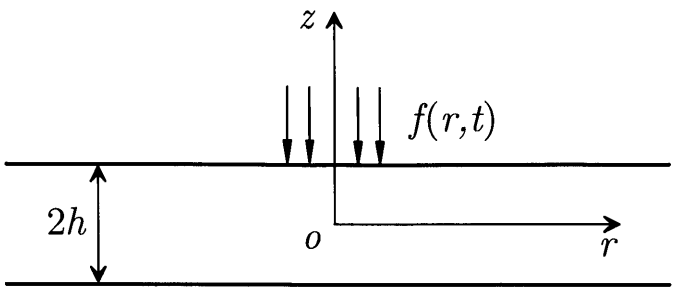

Figure 8.2: An isotropic plate of thickness $2h$ subjected to a normal load $f(r,t)$ distributed circularly on the top surface ($z = h$).

where Δ and Ω are defined as

$$\Delta = \frac{\partial u_r}{\partial r} + \frac{u_r}{r} + \frac{\partial u_z}{\partial z} \tag{8.6}$$

$$\Omega = \frac{\partial u_r}{\partial z} - \frac{\partial u_z}{\partial r} \, . \tag{8.7}$$

Our interest is to obtain the transformed displacements $\hat{u}_n(z,k,\omega)$ induced by the normal load $f(x,t)$, where the subscript n denotes the axis, i.e., $n = r$ (in-plane) or $n = z$ (out-of-plane). In the cylindrical coordinates, Fourier transform is applied to the time variable t, and Hankel transform is applied to the spatial variables r and z. To utilize the properties of the Hankel transform, the zeroth-order Hankel transform is used to compute the out-of-plane displacement $u_z(z,r,t)$, while the first-order Hankel transform is used for the in-plane displacement $u_r(z,r,t)$. Thus, the Fourier-Hankel transform of the displacements are defined as

$$\hat{u}_z(z,k,\omega) = \int_{-\infty}^{+\infty} \int_0^{+\infty} u_z(z,r,t) r J_0(kr) e^{j\omega t} dr dt \tag{8.8}$$

$$\hat{u}_r(z,k,\omega) = \int_{-\infty}^{+\infty} \int_0^{+\infty} u_r(z,r,t) r J_1(kr) e^{j\omega t} dr dt \, , \tag{8.9}$$

with the inverse transform pair as

$$u_z(z,r,t) = \frac{1}{2\pi}\int_{-\infty}^{+\infty}\int_{0}^{+\infty} \hat{u}_z(z,k,\omega) k J_0(kr) e^{-j\omega t} dk d\omega \tag{8.10}$$

$$u_r(z,r,t) = \frac{1}{2\pi}\int_{-\infty}^{+\infty}\int_{0}^{+\infty} \hat{u}_r(z,k,\omega) k J_1(kr) e^{-j\omega t} dk d\omega \ , \tag{8.11}$$

where $J_0(kr)$ and $J_1(kr)$ are the Bessel functions of the zeroth and first-order, respectively. The solution $\hat{u}_n(z,k,\omega)$ can be obtained simply by substituting the displacements $u_n(z,x,t)$ in the form of inverse Fourier-Hankel transform into the equations of motion and satisfying the boundary conditions. This procedure is described as follows.

8.2.2 Fourier-Hankel Transform

The derivatives of the displacements with respect to the spatial variables r and z are obtained as

$$\frac{\partial u_r}{\partial r} = \frac{1}{2\pi}\int_{-\infty}^{+\infty}\int_{0}^{+\infty} \hat{u}_r k^2 J_1'(kr) e^{-j\omega t} dk d\omega \tag{8.12}$$

$$\frac{\partial u_r}{\partial z} = \frac{1}{2\pi}\int_{-\infty}^{+\infty}\int_{0}^{+\infty} \frac{d\hat{u}_r}{dz} k J_1(kr) e^{-j\omega t} dk d\omega \tag{8.13}$$

$$\frac{\partial u_z}{\partial r} = \frac{1}{2\pi}\int_{-\infty}^{+\infty}\int_{0}^{+\infty} \hat{u}_z k^2 J_0'(kr) e^{-j\omega t} dk d\omega \tag{8.14}$$

$$\frac{\partial u_z}{\partial z} = \frac{1}{2\pi}\int_{-\infty}^{+\infty}\int_{0}^{+\infty} \frac{d\hat{u}_z}{dz} k J_0(kr) e^{-j\omega t} dk d\omega \ . \tag{8.15}$$

From Eqs. (8.6) and (8.7) the parameters Δ and Ω are expressed as

$$\Delta = \frac{1}{2\pi}\int_{-\infty}^{+\infty}\int_{0}^{+\infty} \left[k\hat{u}_r + \frac{d\hat{u}_z}{dz}\right] k J_0(kr) e^{-j\omega t} dk d\omega \tag{8.16}$$

$$\Omega = \frac{1}{2\pi}\int_{-\infty}^{+\infty}\int_{0}^{+\infty} \left[\frac{d\hat{u}_r}{dz} + k\hat{u}_z\right] k J_1(kr) e^{-j\omega t} dk d\omega \tag{8.17}$$

where the following properties of the Bessel functions are utilized:

$$J_0'(kr) = -J_1(kr) \tag{8.18}$$

$$J_1(kr) + krJ_1'(kr) = krJ_0(kr)\ . \tag{8.19}$$

Hence, the derivatives of Δ and Ω with respect to the variables r and z are obtained as

$$\frac{\partial \Delta}{\partial r} = \frac{1}{2\pi}\int_{-\infty}^{+\infty}\int_{0}^{+\infty}\left[k\hat{u}_r + \frac{d\hat{u}_z}{dz}\right]k^2 J_0'(kr)e^{-j\omega t}dkd\omega \tag{8.20}$$

$$\frac{\partial \Delta}{\partial z} = \frac{1}{2\pi}\int_{-\infty}^{+\infty}\int_{0}^{+\infty}\left[k\frac{d\hat{u}_r}{dz} + \frac{d^2\hat{u}_z}{dz^2}\right]kJ_0(kr)e^{-j\omega t}dkd\omega \tag{8.21}$$

$$\frac{\partial \Omega}{\partial r} = \frac{1}{2\pi}\int_{-\infty}^{+\infty}\int_{0}^{+\infty}\left[\frac{d\hat{u}_r}{dz} + k\hat{u}_z\right]k^2 J_1'(kr)e^{-j\omega t}dkd\omega \tag{8.22}$$

$$\frac{\partial \Omega}{\partial z} = \frac{1}{2\pi}\int_{-\infty}^{+\infty}\int_{0}^{+\infty}\left[\frac{d^2\hat{u}_r}{dz^2} + k\frac{d\hat{u}_z}{dz}\right]kJ_1(kr)e^{-j\omega t}dkd\omega \tag{8.23}$$

$$\frac{1}{r}\frac{\partial (r\Omega)}{\partial r} = \frac{1}{2\pi}\int_{-\infty}^{+\infty}\int_{0}^{+\infty}\left[\frac{d\hat{u}_r}{dz} + k\hat{u}_z\right]k^2 J_0(kr)e^{-j\omega t}dkd\omega \tag{8.24}$$

Also note that the derivatives of the displacements with respect to the time variable t can be obtained as

$$\frac{\partial^2 u_r}{\partial t^2} = \frac{1}{2\pi}\int_{-\infty}^{+\infty}\int_{0}^{+\infty}\hat{u}_r kJ_1(kr)(-\omega^2)e^{-j\omega t}dkd\omega \tag{8.25}$$

$$\frac{\partial^2 u_z}{\partial t^2} = \frac{1}{2\pi}\int_{-\infty}^{+\infty}\int_{0}^{+\infty}\hat{u}_z kJ_0(kr)(-\omega^2)e^{-j\omega t}dkd\omega\ . \tag{8.26}$$

By substituting Eqs. (8.20) – (8.26) into the governing equations of motion, Eqs. (8.4) and (8.5), we would have the following set of ordinary differential equations:

$$\mu\frac{d^2\hat{u}_r}{dz^2} - [(\lambda+\mu)k]\frac{d\hat{u}_z}{dz} + [\rho\omega^2 - k^2(\lambda+2\mu)]\hat{u}_r = 0 \tag{8.27}$$

$$(\lambda+2\mu)\frac{d^2\hat{u}_z}{dz^2} + [(\lambda+\mu)k]\frac{d\hat{u}_r}{dz} + [\rho\omega^2 - \mu k^2]\hat{u}_z = 0\ . \tag{8.28}$$

Solving, the general solutions for the transformed displacements can be represented by the form:

$$\hat{u}_r = \{A_s k \cosh(\alpha z) - D_s \beta \cosh(\beta z)\} + \{B_a k \sinh(\alpha z) - C_a \beta \sinh(\beta z)\} \tag{8.29}$$

$$\hat{u}_z = \{-A_s \alpha \sinh(\alpha z) + D_s k \sinh(\beta z)\} + \{-B_a \alpha \cosh(\alpha z) + C_a k \cosh(\beta z)\} \ , \tag{8.30}$$

where A_s, D_s, B_a and C_a are arbitrary constants to be determined. and the variables α and β are defined as

$$\alpha^2 = k^2 - \frac{\omega^2}{c_L^2} \ , \qquad \beta^2 = k^2 - \frac{\omega^2}{c_T^2} \ , \tag{8.31}$$

where c_L and c_T are the longitudinal and transverse wave velocities, respectively.

Since the stresses are related to the displacements by virtue of the constitutive law, i.e.,

$$\sigma_{zz} = \lambda \left(\frac{\partial u_r}{\partial r} + \frac{u_r}{r} + \frac{\partial u_z}{\partial z} \right) + 2\mu \frac{\partial u_z}{\partial z} \tag{8.32}$$

$$\sigma_{zr} = \mu \left(\frac{\partial u_r}{\partial z} + \frac{\partial u_z}{\partial r} \right) \ , \tag{8.33}$$

the stress boundary conditions

$$\sigma_{zz} = \begin{cases} \dfrac{1}{2\pi} \displaystyle\int_{-\infty}^{+\infty} \int_{0}^{+\infty} \hat{f}(k,\omega) k J_0(kr) e^{-j\omega t} dk d\omega & \text{at} \quad z = +h \\ 0 & \text{at} \quad z = -h \end{cases} \tag{8.34}$$

$$\sigma_{rz} = 0 \qquad \text{at} \quad z = \pm h \tag{8.35}$$

can be satisfied in terms of displacements, where $\hat{f}(k,\omega)$ is the Fourier-Hankel transform of the circular load $f(x,t)$. As a result, the constants are determined to be

$$A_s = \frac{-(k^2+\beta^2)\sinh(\beta h) \cdot \hat{f}(k,\omega)}{2\mu\Delta_s} \ , \qquad D_s = \frac{-k\alpha \sinh(\alpha h) \cdot \hat{f}(k,\omega)}{\mu\Delta_s} \tag{8.36}$$

$$B_a = \frac{-(k^2+\beta^2)\cosh(\beta h) \cdot \hat{f}(k,\omega)}{2\mu\Delta_a} \ , \qquad C_a = \frac{-k\alpha \cosh(\alpha h) \cdot \hat{f}(k,\omega)}{\mu\Delta_a} \tag{8.37}$$

where

$$\Delta_s = (k^2+\beta^2)^2 \cosh(\alpha h)\sinh(\beta h) - 4k^2\alpha\beta \sinh(\alpha h)\cosh(\beta h) \tag{8.38}$$

$$\Delta_a = (k^2+\beta^2)^2 \sinh(\alpha h)\cosh(\beta h) - 4k^2\alpha\beta \cosh(\alpha h)\sinh(\beta h)\,. \tag{8.39}$$

Note that the conditions for $\Delta_s = 0$ and $\Delta_a = 0$ represent the Rayleigh-Lamb frequency equations for symmetric and antisymmetric wave modes, respectively. Also noticeable is that the frequency equations for circular-crested waves are the same as those for straight-crested waves [104].

It is straightforward to compute $\hat{u}_n(z,k,\omega)$ at an arbitrary position z. But it is of our interest to evaluate those on the upper surface, i.e., $\hat{u}_n(h,k,\omega)$, which can be expressed as the sum of symmetric and antisymmetric parts:

$$\hat{u}_n(h,k,\omega) = \hat{u}_n^s(h,k,\omega) + \hat{u}_n^a(h,k,\omega) \tag{8.40}$$

where

$$\hat{u}_n^s(h,k,\omega) = N_n^s(h,k,\omega)\cdot \hat{f}(k,\omega) \tag{8.41}$$

$$\hat{u}_n^a(h,k,\omega) = N_n^a(h,k,\omega)\cdot \hat{f}(k,\omega)\,, \tag{8.42}$$

and

$$N_r^s(h,k,\omega) = -k\left[\frac{(k^2+\beta^2)\cosh(\alpha h)\sinh(\beta h) - 2\alpha\beta\sinh(\alpha h)\cosh(\beta h)}{2\mu\Delta_s}\right] \tag{8.43}$$

$$N_r^a(h,k,\omega) = -k\left[\frac{(k^2+\beta^2)\sinh(\alpha h)\cosh(\beta h) - 2\alpha\beta\cosh(\alpha h)\sinh(\beta h)}{2\mu\Delta_a}\right] \tag{8.44}$$

$$N_z^s(h,k,\omega) = \alpha\left[\frac{(-k^2+\beta^2)\sinh(\alpha h)\sinh(\beta h)}{2\mu\Delta_s}\right] \tag{8.45}$$

$$N_z^a(h,k,\omega) = \alpha\left[\frac{(-k^2+\beta^2)\cosh(\alpha h)\cosh(\beta h)}{2\mu\Delta_a}\right]. \tag{8.46}$$

This is the analytical solution representing the transient response of the Lamb waves generated by an axisymmetric normal load. It should be pointed out that

$\hat{u}_n^s(h,k,\omega)$ or $\hat{u}_n^a(h,k,\omega)$ are the product of two independent terms, where $\hat{f}(k,\omega)$ is the loading in the transformed domain and $N_n^s(h,k,\omega)$ and $N_n^a(h,k,\omega)$ are the material responses (or overall excitation efficiencies) for the symmetric and antisymmetric wave modes, respectively.

8.2.3 Surface Displacements

We extend our study to compute the displacements induced by the same excitation source. The surface displacements at $z = h$ are also considered as the sum of symmetric and antisymmetric components:

$$u_n(h,x,t) = u_n^s(h,x,t) + u_n^a(h,x,t) \tag{8.47}$$

where

$$\begin{aligned}
u_z^s(h,x,t) &= \frac{1}{2\pi}\int_{-\infty}^{+\infty}\int_0^{+\infty} N_z^s(h,k,\omega)\hat{f}(k,\omega)kJ_0(kr)e^{-j\omega t}dkd\omega \\
u_z^a(h,x,t) &= \frac{1}{2\pi}\int_{-\infty}^{+\infty}\int_0^{+\infty} N_z^a(h,k,\omega)\hat{f}(k,\omega)kJ_0(kr)e^{-j\omega t}dkd\omega \\
u_r^s(h,x,t) &= \frac{1}{2\pi}\int_{-\infty}^{+\infty}\int_0^{+\infty} N_r^s(h,k,\omega)\hat{f}(k,\omega)kJ_1(kr)e^{-j\omega t}dkd\omega \\
u_r^a(h,x,t) &= \frac{1}{2\pi}\int_{-\infty}^{+\infty}\int_0^{+\infty} N_r^a(h,k,\omega)\hat{f}(k,\omega)kJ_1(kr)e^{-j\omega t}dkd\omega\,.
\end{aligned} \tag{8.48}$$

Since the functions $N_n^s(h,k,\omega)$ and $N_n^a(h,k,\omega)$ contain an infinitely large number of poles corresponding to the roots of the dispersion equations for circular-crested waves, it is convenient to use the residue theorem for evaluating the integrals over the wavenumber k. Accordingly, the in-plane and out-of-plane surface displacements

are obtained as

$$u_z^s(h,x,t) = \int_{-\infty}^{+\infty} \sum_{k_s} H_z^s(h,\omega)\hat{f}(k,\omega)kJ_0(kr)e^{-j\omega t}d\omega \tag{8.49}$$

$$u_z^a(h,x,t) = \int_{-\infty}^{+\infty} \sum_{k_a} H_z^a(h,\omega)\hat{f}(k,\omega)kJ_0(kr)e^{-j\omega t}d\omega \tag{8.50}$$

$$u_r^s(h,x,t) = \int_{-\infty}^{+\infty} \sum_{k_s} H_r^s(h,\omega)\hat{f}(k,\omega)kJ_1(kr)e^{-j\omega t}d\omega \tag{8.51}$$

$$u_r^a(h,x,t) = \int_{-\infty}^{+\infty} \sum_{k_a} H_r^a(h,\omega)\hat{f}(k,\omega)kJ_1(kr)e^{-j\omega t}d\omega\,, \tag{8.52}$$

where $H_n^s(h,\omega)$ and $H_n^a(h,\omega)$ are the material responses (or modal excitation efficiencies) for symmetric and antisymmetric wave modes, expressed as

$$H_r^s(h,\omega) = \frac{j(k_s^4-\beta^4)\cosh(\alpha h)\sinh(\beta h)}{8k_s\mu\Delta_s'} \tag{8.53}$$

$$H_r^a(h,\omega) = \frac{j(k_a^4-\beta^4)\sinh(\alpha h)\cosh(\beta h)}{8k_s\mu\Delta_a'} \tag{8.54}$$

$$H_z^s(h,\omega) = \frac{-j\alpha(k_s^2-\beta^2)\sinh(\alpha h)\sinh(\beta h)}{4\mu\Delta_s'} \tag{8.55}$$

$$H_z^a(h,\omega) = \frac{-j\alpha(k_a^2-\beta^2)\cosh(\alpha h)\cosh(\beta h)}{4\mu\Delta_a'}\,. \tag{8.56}$$

Here Δ_s' and Δ_a' are the derivatives of Δ_s and Δ_a with respect to the wavenumber k. The summations are carried out for the real wavenumbers to represent the propagating waves in the far field.

Theses displacement expressions are similar to those for a line source given in Chapter 5. The only difference is that the Hankel transform instead of the Fourier transform is used in the space domain.

8.3 Laser Source Loading Models

In order to find the displacements of transient waves due to the laser source, we need to find the expression for the line source $f(x,t)$ or the circular source $f(r,t)$, which

is considered as the product of the time excitation function $g(t)$ and space excitation function $p(x)$ or $p(r)$.

For simplicity, the time excitation function is assumed to be a Dirac delta function, since the duration of the broadband laser pulse is in general very short (less than 10 ns). Figure 8.3 shows two types of space excitation functions: (a) uniform distribution function which has constant amplitude over the beam area, and (b) elliptical distribution function in which the intensity decreases elliptically from the center of the beam. If the beam size a is small, it is reasonable to imagine that the uniform distribution is equivalent to the elliptical distribution. Thus, in the following, we simply assume the uniform distribution space function.

8.3.1 Line Source

The spatiotemporal loading for a line source can be represented by

$$f(x,t) = [H(x+a/2) - H(x-a/2)]\delta(t) \,, \tag{8.57}$$

where $H(x)$ is the Heaviside step function. The corresponding spatial and temporal Fourier transform is obtained as

$$\hat{f}(k,\omega) = \int_{-\infty}^{+\infty} \delta(t) e^{j\omega t} dt \int_{-\infty}^{+\infty} [H(x+a/2) - H(x-a/2)] e^{-jkx} dx = \frac{\sin(ka/2)}{k/2} \,. \tag{8.58}$$

8.3.2 Circular Source

The spatiotemporal loading for a circular source can be expressed as

$$f(r,t) = [H(r) - H(r-a/2)]\delta(t) \,, \tag{8.59}$$

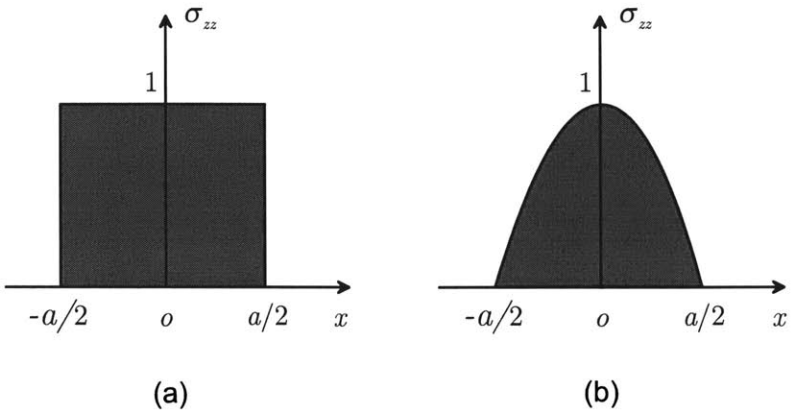

Figure 8.3: Spatial loading distribution: (a) uniform distribution; (b) elliptical distribution, where a is the beam size.

and the Fourier-Hankel transform is

$$\hat{f}(k,\omega) = \int_{-\infty}^{+\infty} \delta(t) e^{j\omega t} dt \int_{0}^{+\infty} [H(r) - H(r - a/2)] r J_0(kr) dr = \frac{a J_1(ka/2)}{2k} . \quad (8.60)$$

8.4 Predicted Waveforms

The expressions for $\hat{f}(k,\omega)$ enable us to predict the transient waves due to a line and circular source. Consider a laser source of diameter $a = 0.5$ mm at the surface of an aluminum plate of thickness $2h = 3.2$ mm. The distance between the receiving point and the coordinate origin is set as $x = 135$ mm. These conditions used for the prediction are summarized in Table 8.1.

Table 8.1: Theoretical conditions used for simulating laser generation.

Parameter	Value
Material	Aluminum
Longitudinal wavespeed, c_L, (m/s)	6320
Transverse wavespeed, c_T, (m/s)	3130
Plate thickness, $2h$, (mm)	3.2
Source diameter, a, (mm)	0.5
Propagation distance, x, (mm)	135

Figures 8.4 and 8.5 show the predicted waveforms for individual wave modes, for the line and circular source loading models, respectively. Here we only display the four lowest antisymmetric modes (A_0, A_1, A_2, A_3) and symmetric modes (S_0, S_1, S_2, S_3). These two models give rise to similar results. Figures 8.6(a) and (b) show the overall displacements for the line source and circular source, obtained from the summation of individual modes. As expected, these two waveforms look similar.

8.5 Discussion

We are interested in analyzing the predicted waveforms such as the ones shown in Fig. 8.6. Of particular interest are the arrival times corresponding to the longitudinal (L), transverse (T), and Rayleigh waves (R) as well as their corresponding wave amplitudes. Since the total response can be represented by summing the individual responses of wave modes, we start with analyzing the individual responses as shown in Fig. 8.4.

Before we proceed, it is of importance to examine the similar work by Weaver and Pao [105]. They explained the responses of individual Lamb wave modes to a point source in detail, by virtue of the group velocity dispersion curves and "modal factors" of the wave modes which were defined as the amplitudes of displacements. Specifically, the group velocity was used for determining the time of arrivals, and the modal factors were used for estimating the waveform amplitudes at these arrivals.

In our analysis, we will use group velocities for determining the times of arrival, as was done by Weaver and Pao [105]. However, we will use the spatial and temporal Fourier transform of the displacements, $\hat{u}(k, \omega)$, for examining the amplitudes, as compared to the normal mode expansion method. Furthermore, we assume a uniformly distributed space excitation function and Dirac delta time excitation function, while they used Dirac delta space excitation function and a Heaviside step time excitation function.

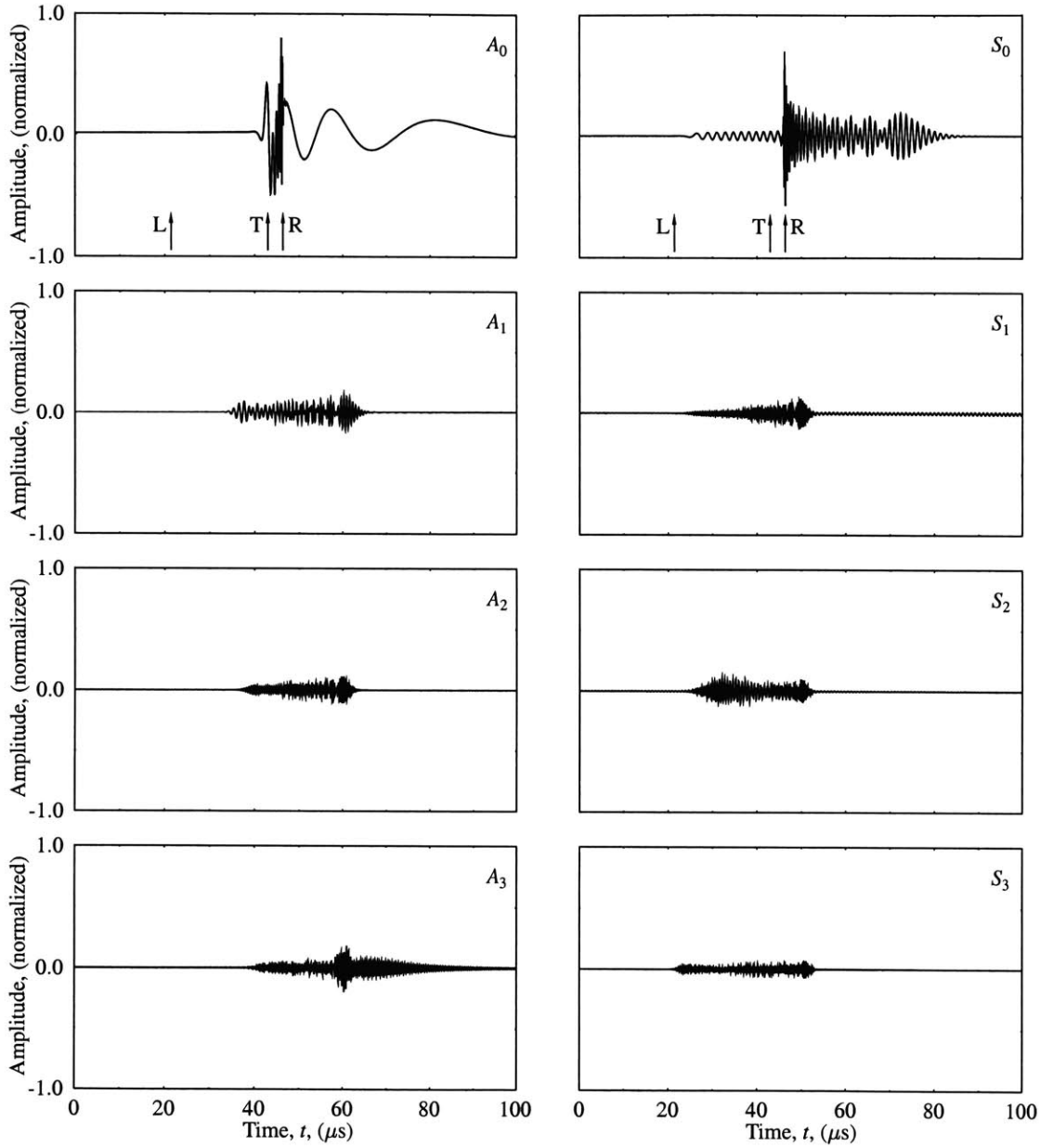

Figure 8.4: Theoretical waveforms of individual Lamb waves modes (A_0, A_1, A_2, A_3, S_0, S_1, S_2 and S_3) in an aluminum plate of thickness $2h = 3.2$ mm at a distance of $x = 135$ mm, where uniformly distributed line source is assumed with a beam diameter of $a = 0.5$ mm.

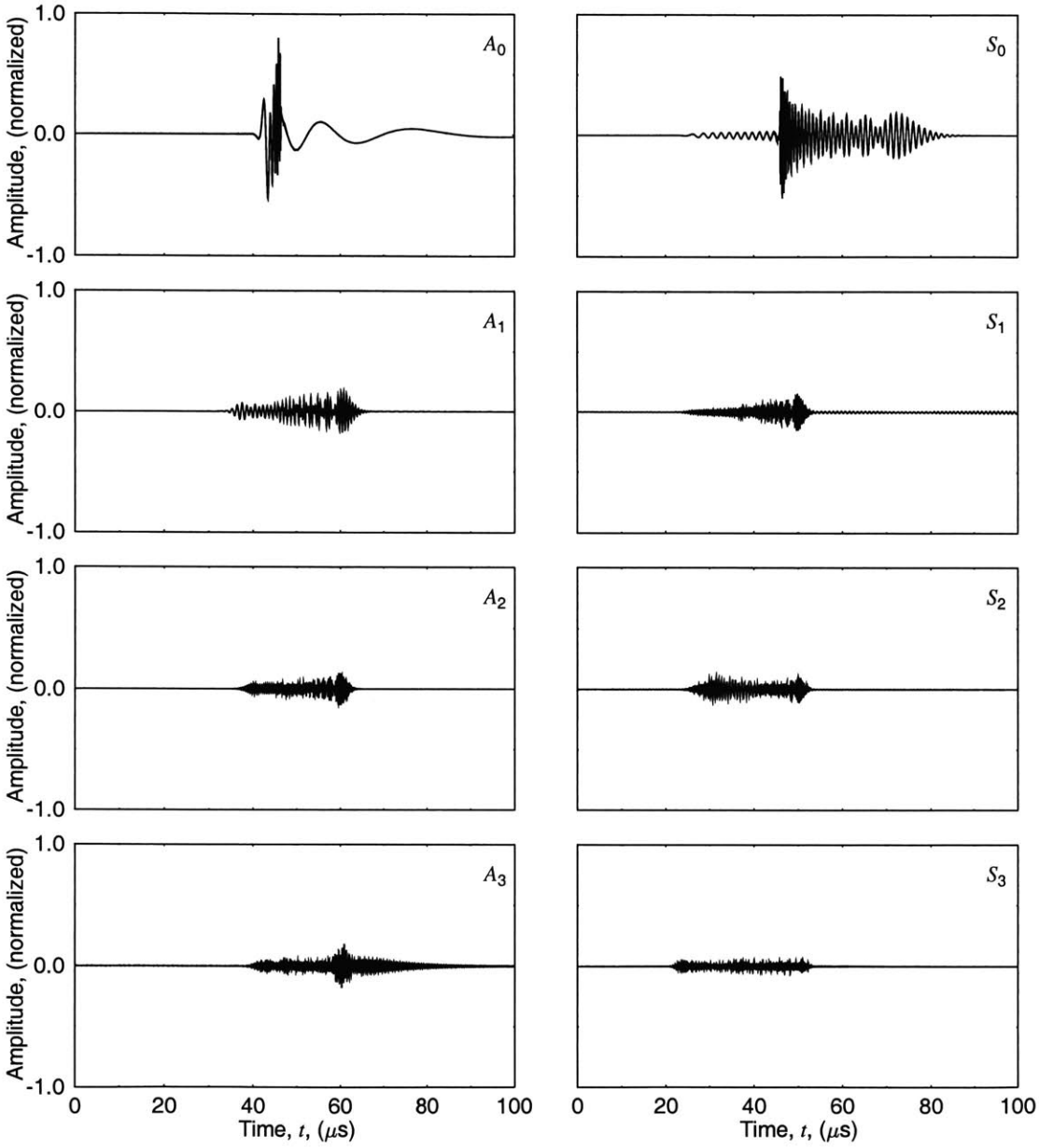

Figure 8.5: Theoretical waveforms of individual Lamb waves modes (A_0, A_1, A_2, A_3, S_0, S_1, S_2 and S_3) in an aluminum plate of thickness $2h = 3.2$ mm at a distance of $x = 135$ mm, where uniformly distributed circular source is assumed with a beam size of $a = 0.5$ mm.

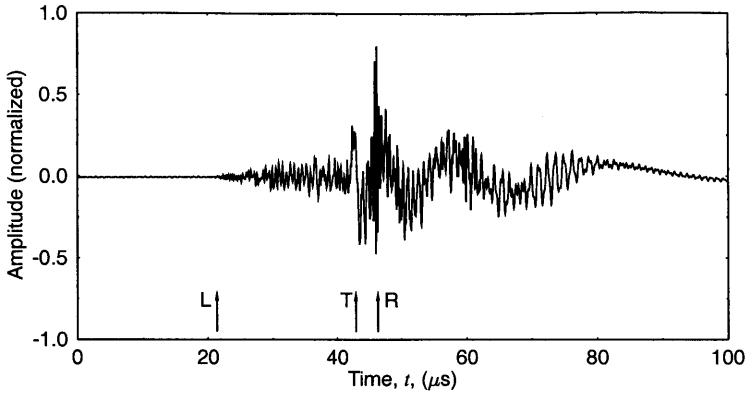

(a)

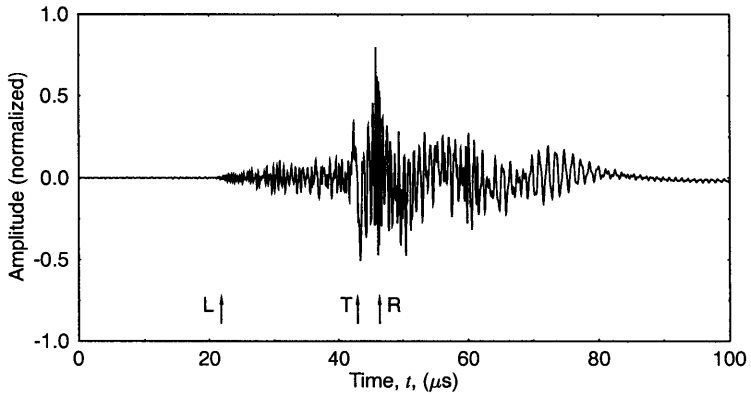

(b)

Figure 8.6: Theoretical waveform of Lamb waves in an aluminum plate of thickness $2h = 3.2$ mm at a distance of $x = 135$ mm, where (a) uniformly distributed line source, and (b) uniformly distributed circular source are assumed with a beam size of $a = 0.5$ mm.

8.5.1 Dispersion curves and Fourier Spectrum

We begin our discussion by observing the dispersion curves relating the group velocity and frequency, as shown in Fig 8.7. As we can see, each wave mode has a maximum group velocity, for example, $(c_g)_{max} = 3,168$ m/s for the A_0 mode and $(c_g)_{max} = 5,438$ m/s for the S_0 mode. It is noticeable that the group velocities of the symmetric modes are significantly larger than those of the antisymmetric modes. In addition, the lowest symmetric and antisymmetric modes (S_0 and A_0) have asymptotic group velocities equal to the wavespeed of Rayleigh waves (c_R). In contrast, all the other

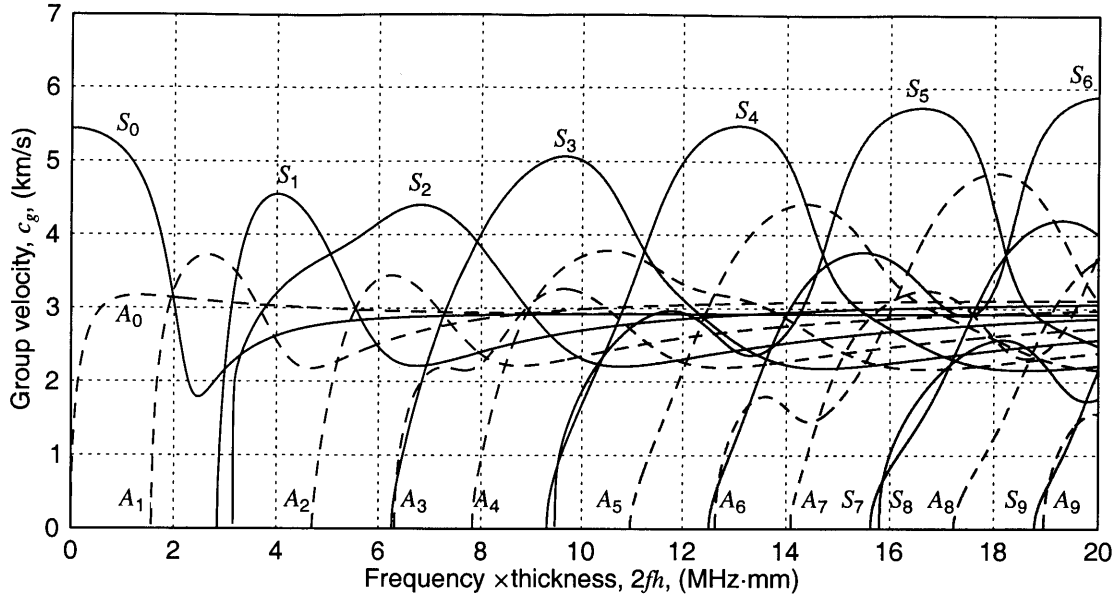

Figure 8.7: Group velocity dispersion curves of Lamb waves in an aluminum plate ($c_L = 6,320$ m/s, $c_T = 3,130$ m/s and $c_R = 2,910$ m/s).

modes have asymptotic group velocities equal to the transverse wavespeed (c_T). None of the group velocities exceed the longitudinal wavespeed (c_L).

Figure 8.8 displays the Fourier transform of the displacement, $\hat{u}(h, k, \omega)$, for the lowest four symmetric and antisymmetric modes, which shows not only the dispersion relations but also the associated energy distribution of the wave modes. The gray lines OR, OT and OL represent the Rayleigh, transverse, and longitudinal waves, respectively. As we know, $\hat{u}(h, k, \omega)$ is the product of excitation efficiency $N(h, k, \omega)$ and external loading $\hat{f}(k, \omega)$, thus it accounts for the influences of both the material properties and external excitation.

Note that the group velocities are represented by the slope of the dispersion curves in the frequency (ω) and wavenumber (k) domain. From Fig. 8.8 we can qualitatively obtain the information about not only the group velocities but also the change of energy distribution as a function of frequency for each mode. For example, the group velocity of the A_0 mode increases from nearly zero to its maximum value and then asymptotically approaches the wavespeed of Rayleigh waves (c_R), as the frequency

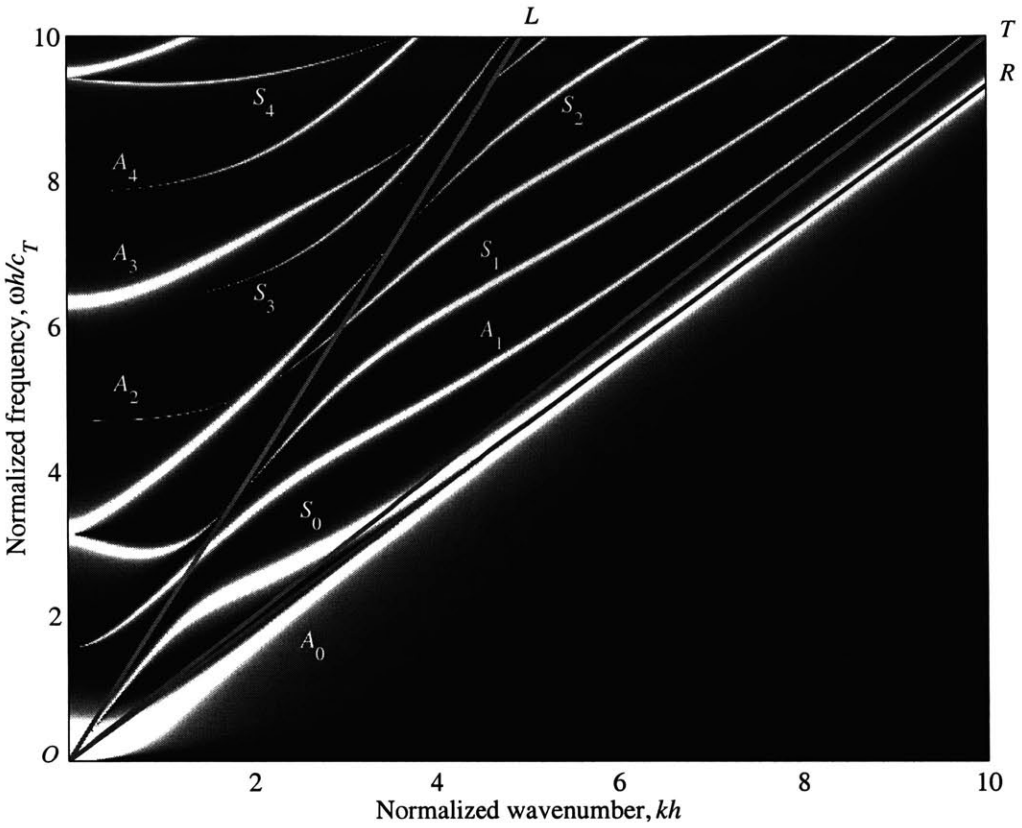

Figure 8.8: Image representing the 2-D FT of the out-of-plane surface displacements, i.e., $\hat{u}_z(h, k, \omega)$ for an aluminum plate of thickness $2h = 3.2$ mm, where uniform distribution space excitation source is assumed with a beam size $a = 0.5$ mm.

increases. On the other hand, the energy decreases. This is consistent with the observations made from Fig. 8.7.

Both the S_0 and A_0 modes have asymptotic group velocities equal to the Rayleigh wave speed (c_R). In contrast, all the other modes have asymptotic group velocities equal to the transverse wave speed (c_T). Moreover, by tracing the line OL and dispersion branches, it is of interest to notice that compared with the antisymmetric modes, the symmetric modes have larger maximum slopes (or maximum group velocities) of their dispersion curves, which has been already confirmed in Fig. 8.7. However, for the symmetric modes, the energy is low at the frequencies corresponding to the individual maximum group velocities. For example, the maximum group velocity of S_0

mode is close to the longitudinal wave speed ($(c_g)_{max}$ = 5438 m/s = 0.86 c_L) when the frequency is nearly zero; but as shown in Fig. 8.8, the energy for that frequency is very low.

8.5.2 Predicted Waveforms

With these observations, we will explain the responses of individual wave modes as shown in Fig. 8.4. The following key observations are made:

- For each mode, the earliest arrival time of in the signal corresponds to its maximum group velocity, i.e., $t_{min} = x/(c_g)_{max}$. For example, the calculated earliest arrival time for the A_0 mode is $t_{min} = 42.7\,\mu$s.

- The high amplitudes of the A_0 and S_0 mode signals shown in Fig. 8.4 are consistent with the energy distribution shown in Fig. 8.8. It is also consistent that the amplitude of the A_0 mode is higher than that of the S_0 mode at low frequency ($\omega h/c_T < 2$).

- In the A_0 mode signal, one can observe that a signal of moderately high amplitude and low frequency, arriving at the time equivalent to that of transverse waves (T). This is due to the fact that the maximum group velocity of A_0 mode is very close to the transverse wavespeed ($(c_g)_{max} \approx c_T$) at the frequency $\omega h/c_T = 1.33$ and the energy contained at that frequency is high.

- We can also observe a sharp high peak standing at the time equivalent to the arrival time of Rayleigh waves, which corresponds to the high-frequency asymptotic (minimum) group velocity.

- The moderately large-amplitude signal following Rayleigh waves is the low frequency flexural motion, as observed by Weaver and Pao [105]. Note that A_0 mode has very high energy at low frequency.

- The time of the earliest arriving S_0 signal is $t_{min} = 24.9\,\mu$s, computed from the maximum group velocity $(c_g)_{max} = 5,438$ m/s (at $\omega h/c_T \approx 0$). The amplitude of this signal is small due to the low energy at this frequency.

- As in the case of the A_0 mode, there is also a sharp peak in the S_0 mode signal at the Rayleigh wavespeed. This can be understood that the local maximum group velocity approaches the transverse wavespeed at high frequency where S_0 mode has high energy.

Similar observations can be made for the other modes. Summing the individual waveforms, the total response is obtained as shown in Fig 8.6(a). Still, our interest is the arrivals and amplitudes of L-wave, T-wave and R-wave. Here of particular interest is that the maximum group velocities of symmetric are kind of close to the longitudinal wave speed, where the closest case among the modes in Fig. 8.4 is $(c_g)_{max} = 0.86\ c_L$ for S_0 mode. However, it is shown that the energy of these modes associated with the maximum group velocities is small. This explains the fact that in the total response there is very low amplitude at the arrival of longitudinal wave, as shown in Fig 8.6(a).

It is worth pointing out that the moderately high peak at the arrival time of transverse waves is largely contributed by the A_0 mode. In fact, there is very low amplitude at this speed in the waveforms of individual modes except A_0. This is contrast to the fact that all the modes except A_0 and S_0 have asymptotic group velocities equal to the transverse wavespeed at high frequency. However, as we have pointed out, the energy tends to decrease as frequency decreases, meaning that the peak of the transverse wavespeed comes largely from the A_0 mode which has much higher energy than the other modes except S_0.

Finally it is natural to understand that there is a huge peak corresponding to the time arrival of Rayleigh wave in the total response waveform. This shall be mainly attributed to the A_0 and S_0 modes. On the one hand, both the A_0 and S_0 modes have asymptotic group velocities equal to the Rayleigh wave speed at high frequency. On the other hand, both modes have much higher energy compared with the other modes at high frequency.

8.6 Experimental Results

Figure 8.9 shows the schematic of the experimental setup used for the laser generation and detection of Lamb waves in an aluminum plate. The excitation (source) laser was a flash-lamp pumped, Q-switched Nd:YAG laser operating at a wavelength of 1064 nm. The pulse energy was about 90 mJ and the pulse width was 6–8 ns. The smallest beam diameter achieved by focusing was approximately 0.5 mm, reduced from unfocused beam diameter of approximately 3.75 mm. The excitation laser head was mounted on a custom-made linear sliding table with a scanning resolution of 25.4 μm.

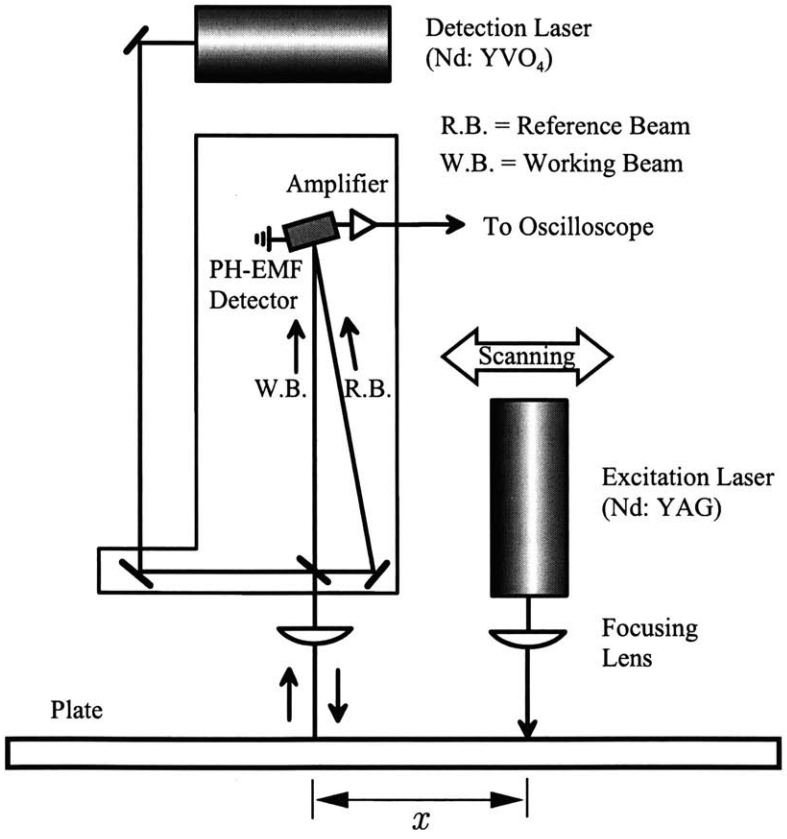

Figure 8.9: Experimental schematic of the laser generation and detection of Lamb waves in a plate.

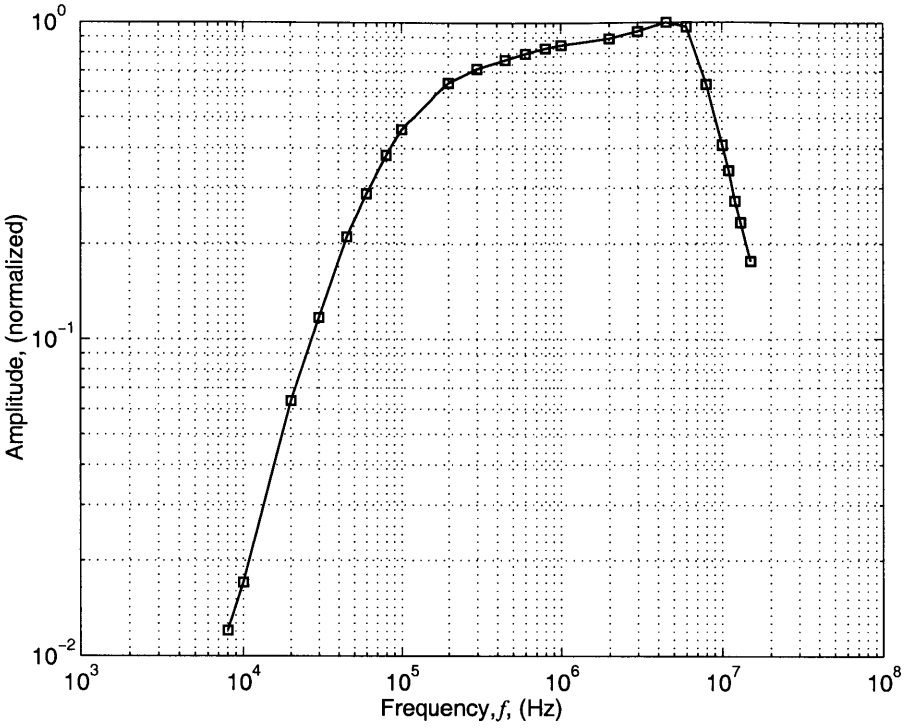

Figure 8.10: Frequency response of the Lasson EMF-500 laser ultrasonic receiver (courtesy of Lasson Technologies).

The out-of-plane displacements were detected by a laser interferometer powered by a continuous wave Nd:YVO_4 laser and a photo-EMF detector operating at a wavelength of 532 nm. The output power was usually set at 1.0 W. The frequency response of the photo-emf detector is shown in Fig. 8.10. In the experiment, the receiving laser remained at a fixed position. The source-receiver distance x was controlled by moving the sliding table (or the source laser). The signals detected by the interferometer were digitized by a digital oscilloscope with a maximum sampling rate of 60 MHz and then transferred to a computer for storage and analysis.

The total of 128 waveforms were recorded for each position at a spatial sampling interval of 0.8255 mm. Figure 8.11 shows three sample waveforms measured at the source-receiver distances of (a) $x = 133$ mm, (b) $x = 185$ mm, and (c) $x = 223$ mm. With the increase of the source-receiver distance, the amplitudes of the waveforms tend to decrease.

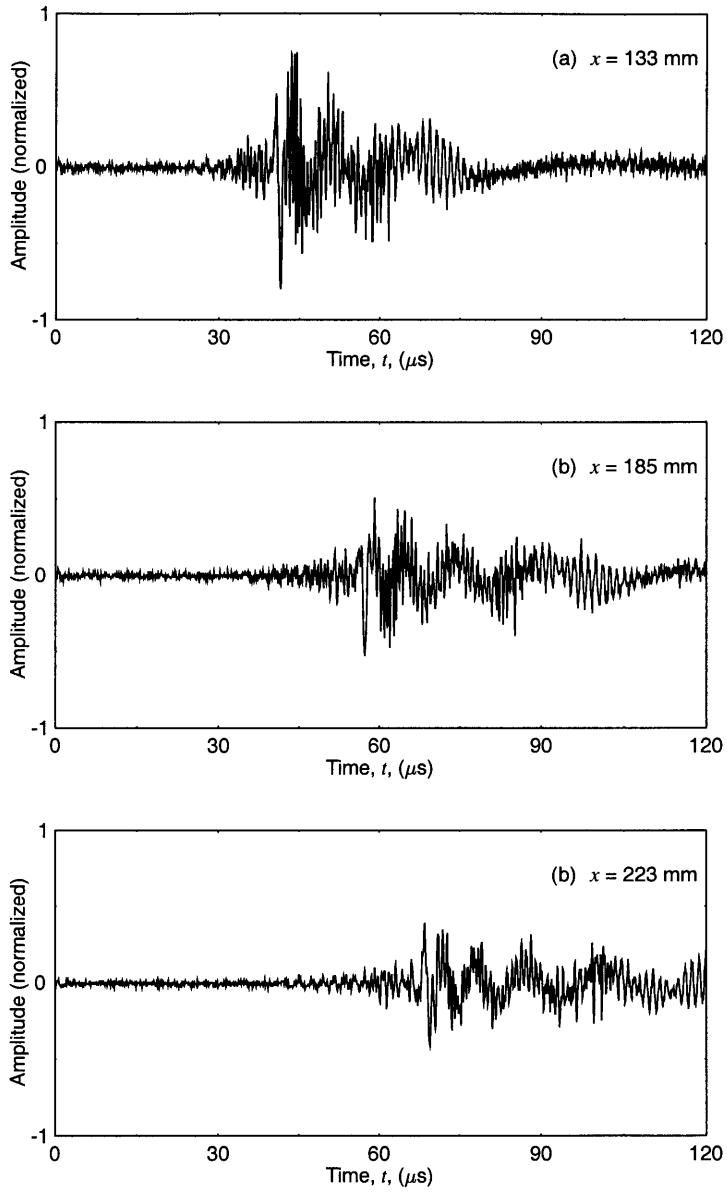

Figure 8.11: Sample experimental waveforms of Lamb waves in an aluminum plate of thickness $2h = 3.2$ mm at the distances (a) 133 mm, (b) 185 mm, and (c) 223 mm, where the excitation source is a Nd:YAG pulsed laser and the receiver is a Lasson EMF-500 laser receiver.

Although we have demonstrated that the predicted waveforms at a distance of 135.0 mm are similar for a line and circular source of small size (diameter), it is still interesting to compare the experimental waveforms shown in Fig. 8.11 with the predicted waveforms for these two loading models, as shown in Figs. 8.12 and 8.13, respectively.[2] We can observe that the agreement between the theoretical results for both two loading models and the experimental results is excellent.

From the 128 waveforms obtained at various spatial locations, we can obtain dispersion curves using a fast 2-D FFT, which is presented as a gray scale image as shown in Fig. 8.14. The image shows the amplitude-wavenumber information at discrete frequencies, through which the individual Lamb wave modes are identified. A Hanning window was used to reduce the leakage in the wavenumber domain. Figure 8.14 also shows the predicted Fourier spectrum, $\hat{u}(h, k, \omega)$, of Lamb waves in the aluminum plate, for a uniform distribution space excitation over the beam diameter $a = 0.5$ mm. The experimental result agrees very well with the theoretical result.

8.7 Construction of Virtually Tuned Waves

The laser-generated signals at various spatial locations can be used to construct virtually tuned waves. Specifically, the broadband signals are decomposed into narrowband signals with certain center frequency and bandwidth, and then virtually tuned waves are constructed according to the SPT scheme.

In this case, the inter-element spacing is equivalent to the space sampling interval ($d = \Delta x = 0.8255$ mm), the number of transmitting elements is equivalent to the number of scanning locations ($M = 128$), and the number of receiving elements is equivalent to the number of receiving locations ($N = 1$). Referring to Chapter 4, the

[2]In the experiment, the cylindrical lens for producing line sources was not available. Thus theoretically speaking, the circular source loading model should be more suitable.

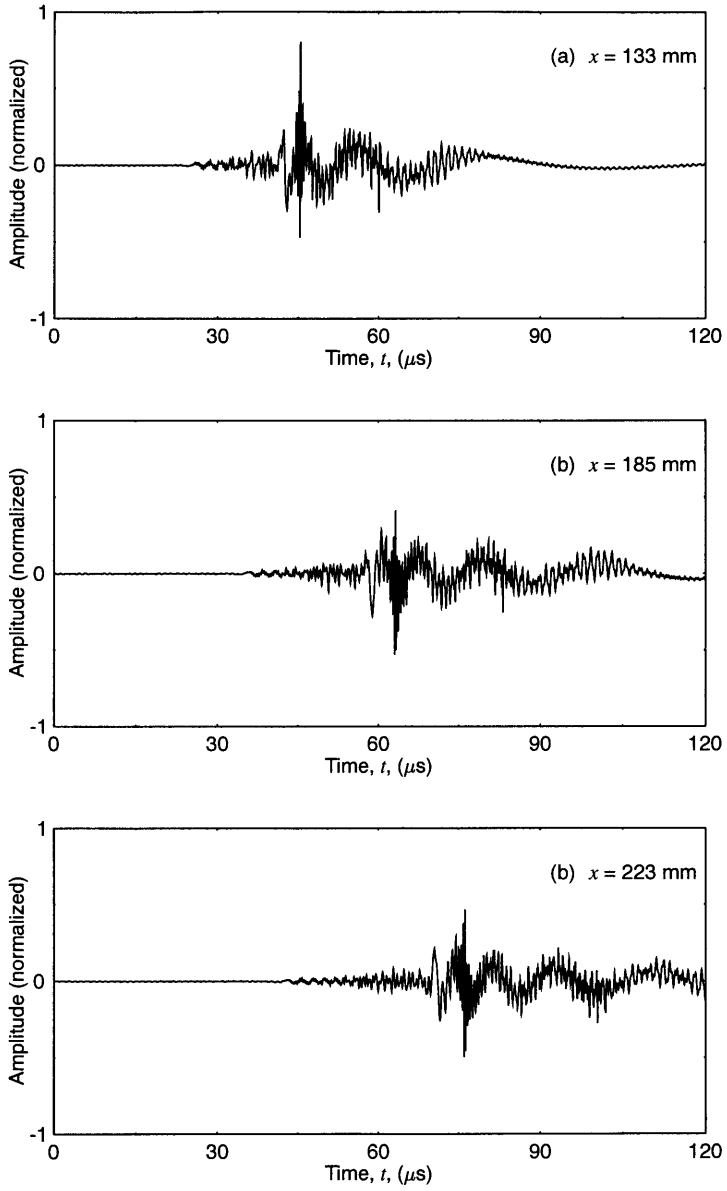

Figure 8.12: Predicted waveforms of Lamb waves in an aluminum plate of thickness $2h = 3.2$ mm at the distances (a) $x_1 = 133$ mm, (b) $x_2 = 185$ mm, and (c) $x_3 = 223$ mm, where the excitation source is a line source of width $a = 0.5$ mm.

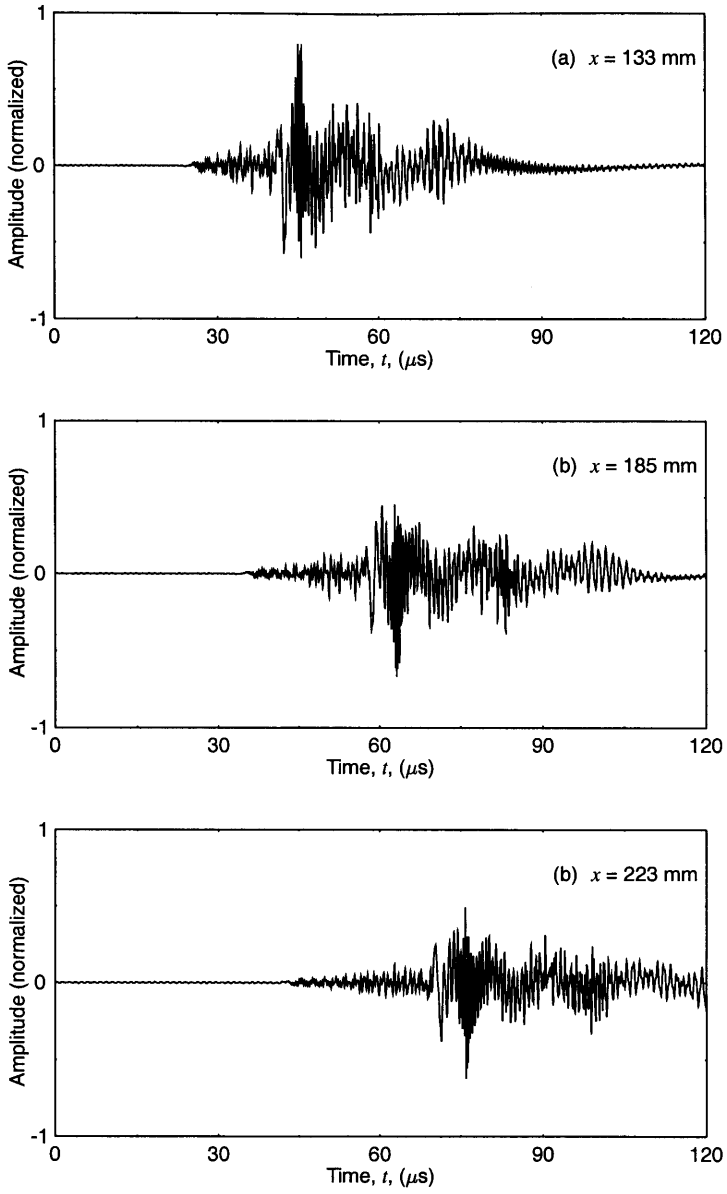

Figure 8.13: Predicted waveforms of Lamb waves in an aluminum plate of thickness $2h = 3.2$ mm at the distances (a) $r_1 = 133$ mm, (b) $r_2 = 185$ mm, and (c) $r_3 = 223$ mm, where the excitation source is a circular source of diameter $a = 0.5$ mm.

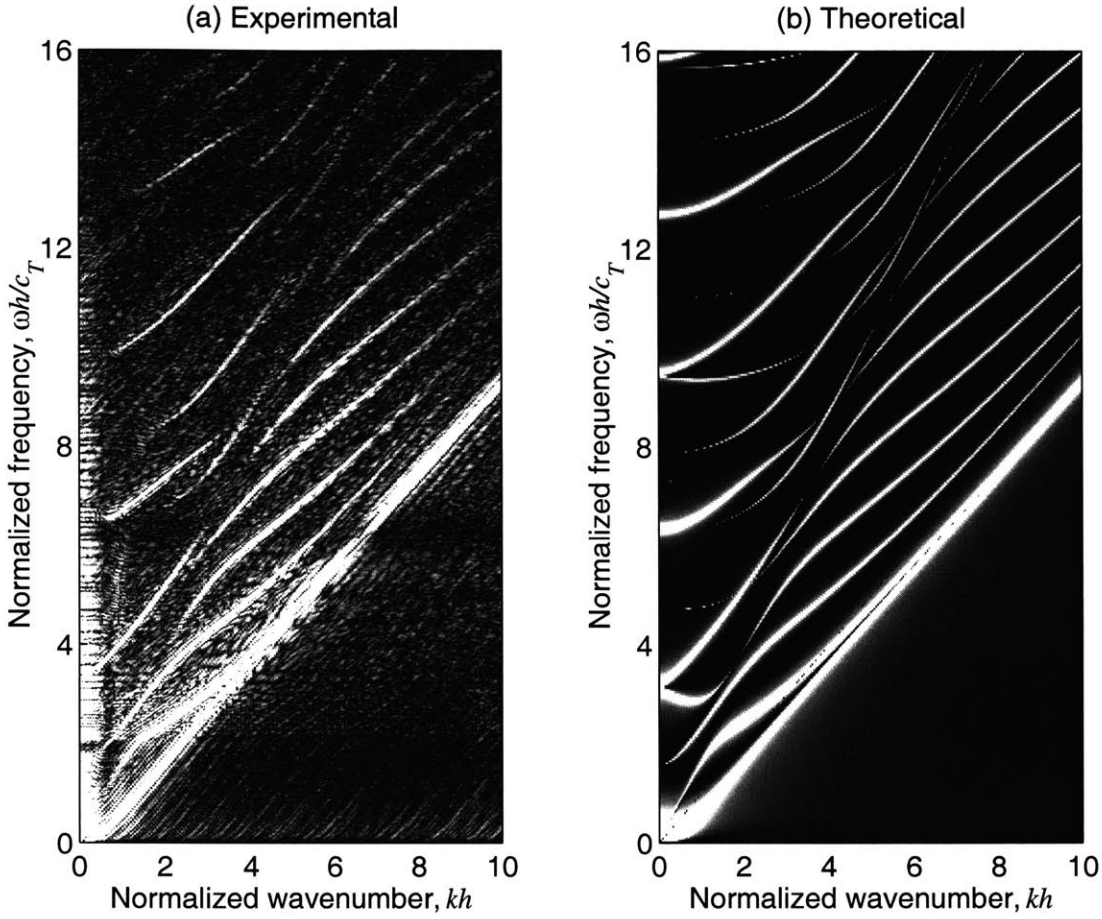

Figure 8.14: Comparison of the experimental 2-D FFT and theoretical 2-D FT of Lamb waves in an aluminum plate of thickness $2h = 3.2$ mm, where the uniform distribution space excitation is assumed with beam size $a = 0.5$ mm.

construction process can be represented in the time domain by the following formula:

$$s(t) = \sum_{m=1}^{M} \sum_{n=1}^{N} s_{mn}(t - (m + n - 2)\Delta\tau) \otimes h(t) \ , \tag{8.61}$$

where as before, $s_{mn}(t)$ are the signals obtained from the transmitter-receiver pair (m,n), $\Delta\tau$ is the required time delay at a certain frequency, $\otimes$ represents the convolution, and $h(t)$ is the filtering function (usually bandpass). It is often convenient to make the computation in the frequency domain. According to the frequency shifting

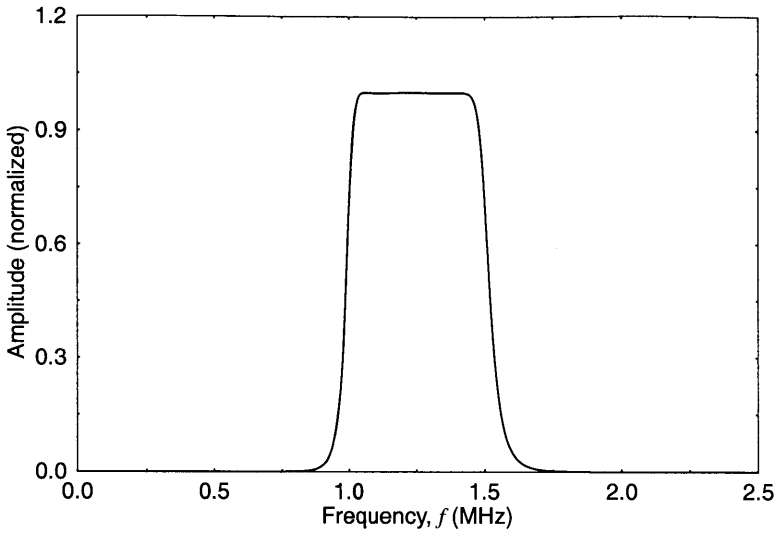

Figure 8.15: Magnitude of the bandpass Butterworth filter's frequency response.

and convolution properties of Fourier transform, we have

$$\hat{s}(\omega) = \sum_{m=1}^{M} \sum_{n=1}^{N} \hat{s}_{mn}(\omega) e^{j\omega(m+n-2)\Delta\tau} \cdot \hat{h}(\omega) \,, \tag{8.62}$$

where $\hat{s}(\omega)$, $\hat{s}_{mn}$ and $\hat{h}(\omega)$ are the Fourier transform of $s(t)$, $s_{mn}(t)$ and $h(t)$, respectively.

The filter design is critical for the tuning effect, which is decided by the chosen center frequency and bandwidth of the narrowband signals. According to the dispersion curves of aluminum shown in Fig. 2.6(a), we choose a frequency-thickness value of $2f_0h = 4.0$ MHz-mm. This means that the center frequency is $f_0 = 1.25$ MHz, since the plate thickness is $2h = 3.2$ mm. Correspondingly, a Butterworth bandpass filter of order 20 is used, where the lower- and upper-bound frequency are 1.0 and 1.5 MHz. Figure 8.15 shows the magnitude of the filter's frequency response.

For the frequency-thickness value of 4.0 MHz-mm, there are five wave modes: A_0, A_1, S_0, S_1 and S_2. The phase (and group) velocities along with the required time delay and group delays for these modes are tabulated in Table 8.2.

Table 8.2: Required parameters for tuning laser-generated waves ($2f_0h$ = 4.0 MHz-mm, d = 0.825 mm, and x = 238 mm).

Wave mode	Phase velocity c_p, (m/s)	Group velocity c_g, (m/s)	Time delay $\Delta\tau$, (ns)	Group delay t_g, (μs)
S_2	12,520	3,196	65.9	42.2
S_1	6,072	4,548	135.9	29.7
A_1	4,887	2,554	168.8	52.9
S_0	3,030	2,618	287.8	51.6
A_0	2,867	3,026	272.3	44.6

Shown in Fig. 8.7 are the tuning results of laser-generated Lamb waves, where the dashed lines represent the arrival times of individual wave modes. We can observe that among these modes, A_0 and S_0 are tuned well while A_1, S_1, and S_2 are not.

8.8 Conclusions

The laser generation of Lamb waves was studied in this chapter. Both the line source and circular source were used to model the laser generation of Lamb waves. For this, an analytical model was developed to analyze the transient waves due to a circular source.

It was shown that the line source model and circular source model predict similar waveforms, which are close to the experimental waveforms. We can conclude that both source models are valid for lasers in the ablation regime. In addition, the line source can link the theoretical 2-D FT (or theoretical dispersion curves) with the experimental 2-D FFT result (or experimental dispersion curves).

The tuning of laser-generated Lamb waves was also investigated. The SPT scheme was applied to a set of filtered signals. It was shown that it is possible to tune various wave modes at different frequencies by processing the broadband signals.

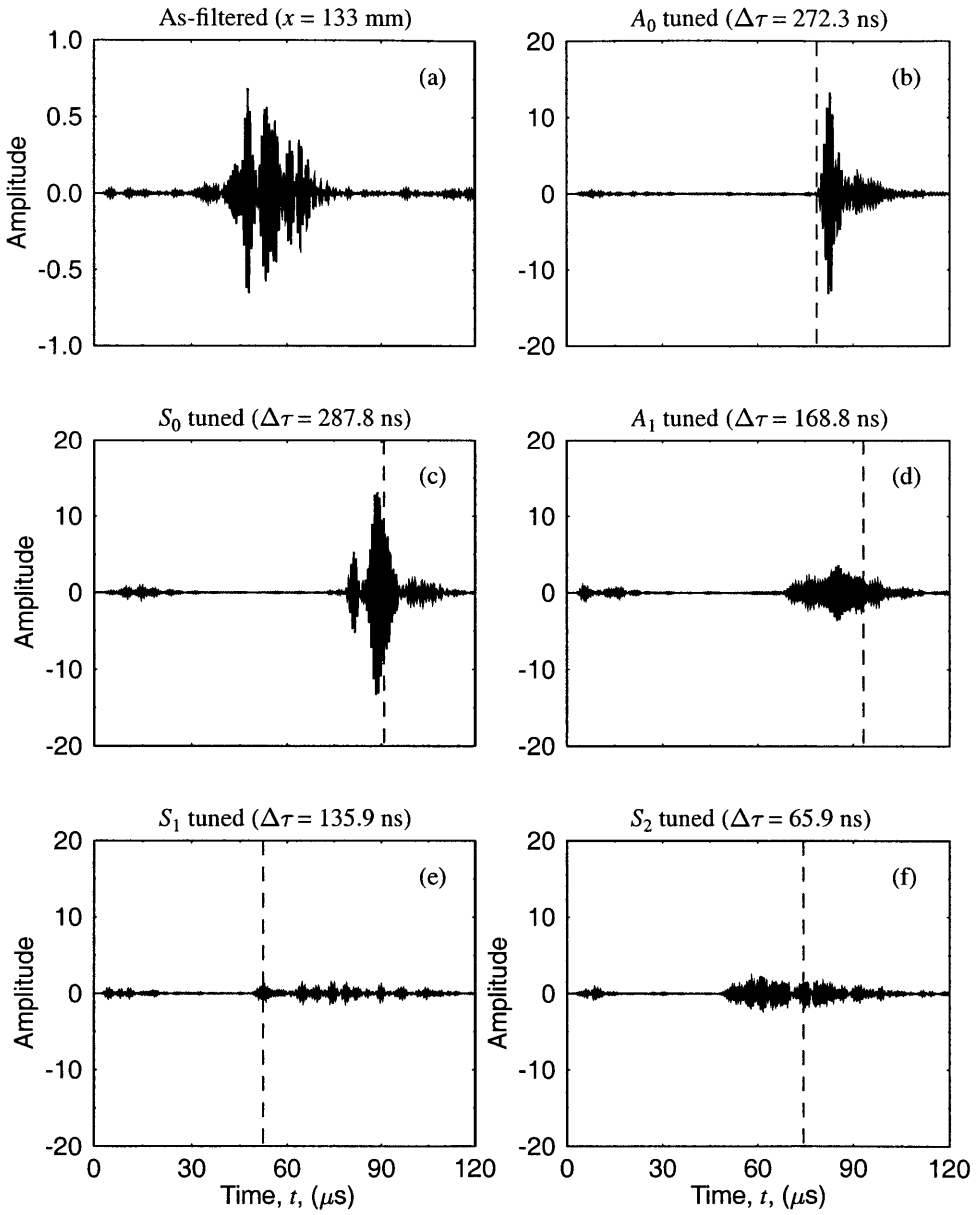

Figure 8.16: Virtually tuned waves obtained from the laser-generated Lamb waves for $2f_0h = 4.0$ MHz-mm: (a) as-filtered case ($x = 133$ mm), (b) A_0 mode tuning ($\Delta\tau = 272.3$ ns), (c) S_0 mode tuning ($\Delta\tau = 287.8$ ns), (d) A_1 mode tuning ($\Delta\tau = 168.8$ ns), (e) S_1 mode tuning ($\Delta\tau = 135.9$ ns), and (f) S_2 mode tuning ($\Delta\tau = 65.9$ ns).

Chapter 9

Transient Waves in Transversely Isotropic Composites

9.1 Introduction

By far the tuning of Lamb waves has been investigated for homogeneous isotropic plates. It was shown that the synthetic phase tuning method is effective as compared to the other tuning techniques and that the analytical model for studying transient Lamb waves can be used to investigate the tuning efficiencies of various wave modes. The results show that it is important to select proper Lamb wave modes for the nondestructive evaluation of thin-walled structures. It is the interest of this chapter to study the tuning of Lamb waves in composite materials.

Due to their high strength to weight ratio, composite materials are finding extensive applications in many industries especially the aerospace industry. As a result, it is of extreme importance to determine material properties for stress analysis and design. In addition, detection of failure in composites is critical to their safe use. Ultrasonic techniques are considered as the most commonly used techniques for measuring elastic constants of composites and detecting flaws in composites.

The elastic constants of composite materials can be measured nondestructively using bulk waves [106–109] and Rayleigh surface waves [110]. The properties are also

measurable using Lamb waves [12, 82, 111] and leaky Lamb waves [8, 112–114]. [1] In addition, matrix cracking and delamination in composites can be detected using leaky Lamb waves [115] and Lamb waves [116].

Hence, Lamb wave tuning techniques have a great potential in determining elastic constants and detecting flaw in composite plates. However, composite materials are anisotropic, so that a great deal of efforts should be made to study the propagation of Lamb waves in composite laminates before analyzing the tuning mechanism. For this reason, the focus of this chapter is on investigating transient Lamb waves in transversely isotropic composite plates, rather than the tuning of Lamb waves in composites.

The choice of transversely isotropic composites is that unidirectional fiber reinforced composites (such as carbon/epoxy, glass/epoxy composites) falling into this category are widely used and have only 5 independent elastic constants. The investigation in this chapter is intended to serve as the basis for future research work on the tuning of Lamb waves in composite plates.

In fact, in the measurement of elastic constants of composites, bulk waves and Lamb waves are used together. In this chapter, the propagation of bulk (or plane) waves in transversely isotropic composites will be introduced first, which refers to the publications by Wu and Liu [82], and Wooh and Daniel [106] . This will be useful for understanding the methods for measuring elastic constants of composites. The governing equations of motion for plane waves will also be used to derive the dispersion relationship in the principal directions (parallel and normal to the fiber direction), from which the dispersion curves will be constructed. More detail on the derivation of dispersion relation can be found in the work by Habeger *et al.* [117], and Dayal and Kinra [115]. Afterwards, the transient Lamb waves in the principal directions due to an arbitrary loading will be investigated, which will be very useful for understanding the tuning capabilities of waves modes. Finally, experiment will be done to generate Lamb waves in the composite principal directions using laser

[1] When the plate is immersed in a fluid, Lamb waves traveling in the plate leak energy into the surrounding fluid and sensed by a receiver. These waves in the fluid are named "leaky Lamb waves".

sources. The waveforms collected in multiple receiving locations will be will be used to construct experimental dispersion curves using the two-dimensional fast Fourier transform (2-D FFT) algorithm which has been utilized in Chapters 5 and 8.

9.2 Plane Waves Propagation

For an elastic medium, the constitutive relation or Hooke's Law relates the stress and strain components by:

$$\sigma_{ij} = C_{ijkl}\varepsilon_{kl} \,, \qquad \text{for} \quad i,j,k,l = 1,2,3 \,, \tag{9.1}$$

where σ_{ij} is the stress tensor, C_{ijkl} is the tensor of elastic constants, and ε_{kl} is the strain tensor. The equations of motion are expressed as

$$\frac{\partial \sigma_{ij}}{\partial x_i} = \rho \frac{\partial^2 u_i}{\partial t^2} \,, \qquad i = 1,2,3 \,, \tag{9.2}$$

where u_i is the displacement, and ρ is the density. The strain-displacement relation can be written as

$$\varepsilon_{ij} = (u_{i,j} + u_{j,i})/2, \qquad \text{for} \quad i,j = 1,2,3 \,. \tag{9.3}$$

For a plane wave without external boundaries, the displacements are given as

$$u_m = U_m \exp[jk(n_i x_i - ct)] \,, \tag{9.4}$$

where k is the wave number, j is the unit imaginary number, n_i is the direction cosines of the normal to the wave front, U_m is the displacement amplitude, and c the wave speed. By substituting Eq. (9.4) into Eq. (9.1), we obtain the following eigenvalue equation:

$$(C_{ijkl}n_j n_l - \rho c^2 \delta_{ik})U_k = 0 \,, \tag{9.5}$$

where δ_{ik} is the Kronecker delta. This is the well-known Christoffel equation.

A general anisotropic material without any plane of symmetry has 21 independent elastic constants. If a material has three mutually orthogonal planes of material property symmetry, it is called an *orthotropic material.* In this case, the number of independent elastic constants reduces to 9. The stress-strain relations in coordinates aligned with principal material directions are

$$\begin{pmatrix} \sigma_{11} \\ \sigma_{22} \\ \sigma_{33} \\ \sigma_{23} \\ \sigma_{13} \\ \sigma_{12} \end{pmatrix} = \begin{pmatrix} C_{11} & C_{12} & C_{13} & 0 & 0 & 0 \\ C_{12} & C_{22} & C_{23} & 0 & 0 & 0 \\ C_{13} & C_{23} & C_{33} & 0 & 0 & 0 \\ 0 & 0 & 0 & 2C_{44} & 0 & 0 \\ 0 & 0 & 0 & 0 & 2C_{55} & 0 \\ 0 & 0 & 0 & 0 & 0 & 2C_{66} \end{pmatrix} \begin{pmatrix} \varepsilon_{11} \\ \varepsilon_{22} \\ \varepsilon_{33} \\ \varepsilon_{23} \\ \varepsilon_{13} \\ \varepsilon_{12} \end{pmatrix} . \tag{9.6}$$

Hence Eq. (9.5) takes the form

$$\begin{pmatrix} \Gamma_{11} - \rho c^2 & \Gamma_{12} & \Gamma_{13} \\ \Gamma_{12} & \Gamma_{22} - \rho c^2 & \Gamma_{23} \\ \Gamma_{13} & \Gamma_{23} & \Gamma_{33} - \rho c^2 \end{pmatrix} \begin{pmatrix} U_1 \\ U_2 \\ U_3 \end{pmatrix} = \begin{pmatrix} 0 \\ 0 \\ 0 \end{pmatrix} \tag{9.7}$$

where the so-called Christoffel stiffnesses Γ_{ij} are given by

$$\begin{aligned} \Gamma_{11} &= n_1^2 C_{11} + n_2^2 C_{66} + n_3^2 C_{55} , \\ \Gamma_{22} &= n_1^2 C_{66} + n_2^2 C_{22} + n_3^2 C_{44} , \\ \Gamma_{33} &= n_1^2 C_{55} + n_2^2 C_{44} + n_3^2 C_{33} , \\ \Gamma_{12} &= n_1 n_2 (C_{12} + C_{66}) , \\ \Gamma_{23} &= n_2 n_3 (C_{23} + C_{44}) , \\ \Gamma_{13} &= n_1 n_3 (C_{13} + C_{55}) . \end{aligned} \tag{9.8}$$

For nontrivial solution of the displacement vector $\mathbf{U}$, the characteristic determinant of Eq. (9.7) is set to be zero:

$$\begin{vmatrix} \Gamma_{11} - \rho c^2 & \Gamma_{12} & \Gamma_{13} \\ \Gamma_{12} & \Gamma_{22} - \rho c^2 & \Gamma_{23} \\ \Gamma_{13} & \Gamma_{23} & \Gamma_{33} - \rho c^2 \end{vmatrix} = 0 \,. \tag{9.9}$$

An orthotropic material is called *transversely isotropic* when one of its planes is a plane of isotropy, as shown in Fig. 9.1. By assuming the 2-3 plane is the plane of isotropy, the elastic constants satisfy the following relationship:

$$C_{12} = C_{13} \,, \qquad C_{22} = C_{33} \,, \qquad C_{55} = C_{66} \,, \qquad C_{44} = \frac{(C_{22} - C_{23})}{2} \,. \tag{9.10}$$

If the wave propagates in the 3 direction, i.e., $n_1 = n_2 = 0$, $n_3 = 1$, Eq. (9.9) gives three distinct solutions:

$$c_{33L} = \sqrt{\frac{C_{33}}{\rho}} \,, \qquad c_{32T} = \sqrt{\frac{C_{44}}{\rho}} \,, \qquad c_{31T} = \sqrt{\frac{C_{55}}{\rho}} \,. \tag{9.11}$$

where c_{33L} is the longitudinal wave in the 3-axis, c_{32T} is the transverse wave with a polarization in the 2-axis and c_{31T} is the transverse wave with a polarization in the 1-axis. We can see that the three independent elastic constants of a transversely isotropic material: C_{33}, C_{44} and C_{55} can be measured using the conventional bulk wave measurements [82,106]. The remaining two unknown elastic constants C_{11} and C_{12} can be determined using the Lamb wave testing [82]. Specifically, they are determined inversely from the experimental measurements of phase velocity and frequency, or the experimental dispersion curves. This requires the understanding of dispersion of Lamb waves in transversely isotropic plates.

9.3 Dispersion Relation

Consider an infinitely long transversely isotropic composite plate in the coordinate system shown in Fig. 9.1. If we assume plane strain condition, the displacement u_2 and all derivatives with respect to y vanish. Substituting Eqs. (9.6) and (9.3) into Eq. (9.2) yields

$$\rho\ddot{u}_1 = C_{11}u_{1,11} + C_{13}u_{3,31} + C_{55}(u_{1,33} + u_{3,13}) \tag{9.12}$$

$$\rho\ddot{u}_3 = C_{33}u_{3,33} + C_{13}u_{1,13} + C_{55}(u_{1,13} + u_{3,11}) \tag{9.13}$$

For a plane wave with displacements in the x and z directions only, the displacement components can be written as

$$u_1 = U_{10}\exp\{j(k_x x + k_z z - \omega t)\} \tag{9.14}$$

$$u_3 = U_{30}\exp\{j(k_x x + k_z z - \omega t)\}\ , \tag{9.15}$$

where U_{10} and U_{30} are the wave amplitudes. Substituting Eqs. (9.14) and (9.15) into Eqs. (9.12) and (9.13) one obtains

$$\rho U_{10}\omega^2 = C_{11}U_{10}k_x^2 + (C_{13} + C_{55})U_{30}k_x k_z + C_{55}U_{10}k_z^2 \tag{9.16}$$

$$\rho U_{30}\omega^2 = C_{55}U_{30}k_x^2 + (C_{13} + C_{55})U_{10}k_x k_z + C_{33}U_{30}k_z^2\ . \tag{9.17}$$

For a given frequency ω and wavenumber k_x, Eqs. (9.16) and (9.17) can be used to find the wavenumber k_z and corresponding values of wave amplitude ratio U_{30}/U_{10}, where k_z^2 satisfy the following quadratic equation

$$(C_{55} + C_{13})^2 k_x^2 k_z^2 = (\rho\omega^2 - C_{11}k_x^2 - C_{55}k_z^2)(\rho\omega^2 - C_{55}k_x^2 - C_{33}k_z^2) \tag{9.18}$$

and given a value of k_z, U_{30}/U_{10} can be obtained as

$$R = \frac{U_{30}}{U_{10}} = \frac{(\rho\omega^2 - C_{11}k_x^2 - C_{55}k_z^2)}{(C_{55} + C_{13})k_x k_z}\ . \tag{9.19}$$

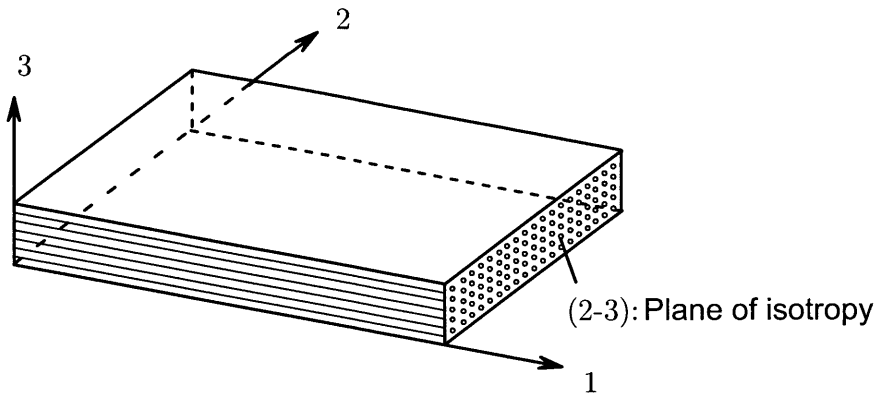

Figure 9.1: Orthotropic material with the 2-3 plane as the plane of transverse isotropy.

From Eq. (9.18), k_z^2 can be represented in terms of k_x

$$k_z^2 = \frac{k_x^2[B \pm \sqrt{B^2 - 4D}]}{2} \tag{9.20}$$

where

$$B = -\frac{\rho[C_{33}(C_{11}/\rho - \omega^2/k_x^2) - C_{13}(2C_{55} + C_{13})/\rho - C_{55}\omega^2/k_x^2]}{C_{33}C_{55}} \tag{9.21}$$

$$D = \frac{\rho^2(\omega^2/k_x^2 - C_{55}/\rho)(\omega^2/k_x^2 - C_{11}/\rho)}{C_{33}C_{55}} \,. \tag{9.22}$$

If we define k_{zp} and k_{zm} as the complex conjugates of the two roots of k_z, i.e., $k_z = \pm jk_{zp}$ and $k_z = \pm jk_{zm}$, then k_{zp}^2 and k_{zm}^2 are the two opposite values of k_z^2 obtained from Eq. (9.20) with + and − signs in the bracket,

$$k_{zp}^2 = \frac{k_x^2[-B + \sqrt{B^2 - 4D}]}{2} \tag{9.23}$$

$$k_{zm}^2 = \frac{k_x^2[-B - \sqrt{B^2 - 4D}]}{2} \,. \tag{9.24}$$

Also, R_p and R_m are the values of R, respectively, when k_{zp} and k_{zm} are substituted into Eq. (9.19) (excluding $-j$),

$$R_p = \frac{(\rho\omega^2 - C_{11}k_x^2 + C_{55}k_{zp}^2)}{(C_{55} + C_{13})k_x k_{zp}} \tag{9.25}$$

$$R_m = \frac{(\rho\omega^2 - C_{11}k_x^2 + C_{55}k_{zm}^2)}{(C_{55} + C_{13})k_x k_{zm}} \, . \tag{9.26}$$

The equations in the above stand for the bulk waves traveling in an unbounded medium. The plate wave solution is obtained if these bulk waves add up such that the free boundary conditions are met at $z = \pm h$. The two possible plate wave displacements have the following forms:

$$\begin{aligned} u_1 = &\exp[j(k_x x - \omega t)][M\exp(-k_{zp}z) + N\exp(k_{zp}z) \\ &+ P\exp(-k_{zm}z) + Q\exp(k_{zm}z)] \end{aligned} \tag{9.27}$$

and

$$\begin{aligned} u_3 = &\exp[j(k_x x - \omega t)]\{-jR_p[M\exp(-k_{zp}z) - N\exp(k_{zp}z)] \\ &- jR_m[P\exp(-k_{zm}z) - Q\exp(k_{zm}z)]\} \, , \end{aligned} \tag{9.28}$$

where M, N, P, Q are arbitrary constants.

The free boundary conditions to be satisfies at $z = \pm h$ gives

$$\sigma_{33} = C_{33}u_{3,3} + C_{13}u_{1,1} = 0 \tag{9.29}$$

$$\sigma_{31} = C_{55}u_{1,3} + C_{55}u_{3,1} = 0 \, . \tag{9.30}$$

Substituting u_1 and u_3 from Eqs. (9.27) and (9.28) into Eqs. (9.29) and (9.30) imposes the four following conditions on M, N, P and Q:

$$\begin{pmatrix} G_p \exp(-k_{zp}h) & G_p \exp(k_{zp}h) & G_m \exp(-k_{zm}h) & G_m \exp(k_{zm}h) \\ G_p \exp(k_{zp}h) & G_p \exp(-k_{zp}h) & G_m \exp(k_{zm}h) & G_m \exp(-k_{zm}h) \\ -H_p \exp(-k_{zp}h) & H_p \exp(k_{zp}h) & -H_m \exp(-k_{zm}h) & H_m \exp(k_{zm}h) \\ -H_p \exp(k_{zp}h) & H_p \exp(-k_{zp}h) & -H_m \exp(k_{zm}h) & H_m \exp(-k_{zm}h) \end{pmatrix} \begin{pmatrix} M \\ N \\ P \\ Q \end{pmatrix} = \begin{pmatrix} 0 \\ 0 \\ 0 \\ 0 \end{pmatrix} \tag{9.31}$$

where G_p and G_m are defined as

$$G_p = C_{33}k_{zp}R_p + C_{13}k_x \tag{9.32}$$

$$G_m = C_{33}k_{zm}R_m + C_{13}k_x \ , \tag{9.33}$$

and H_p and H_m are defined as

$$H_p = k_{zp} - k_x R_p \tag{9.34}$$

$$H_m = k_{zm} - k_x R_m \ . \tag{9.35}$$

There are non-zero solutions for M, N, P and Q only if the determinant of the matrix in Eq. (9.31) is equal to zero, which yields

$$G_p H_m \cosh(k_{zp}h)\sinh(k_{zm}h) - G_m H_p \sinh(k_{zp}h)\cosh(k_{zm}h) = 0 \tag{9.36}$$

$$G_p H_m \sinh(k_{zp}h)\cosh(k_{zm}h) - G_m H_p \cosh(k_{zp}h)\sinh(k_{zm}h) = 0 \ . \tag{9.37}$$

This further results in

$$\frac{\tanh(k_{zp}h)}{\tanh(k_{zm}h)} = \frac{G_p H_m}{G_m H_p} \tag{9.38}$$

for symmetric modes, and

$$\frac{\tanh(k_{zp}h)}{\tanh(k_{zm}h)} = \frac{G_m H_p}{G_p H_m} \tag{9.39}$$

for antisymmetric modes. These are the dispersion equations for transversely isotropic composite plates in the fiber direction. [2] This involves four of the five elastic constants: C_{11}, C_{13}, C_{33} and C_{55}. Similar procedures can be applied to obtain the dispersion relations normal to the fiber direction, where the four elastic constants: C_{22}, C_{23}, C_{33} and C_{44} are used.

Figure 9.2 shows the dispersion curves of Lamb waves in the fiber direction for a 7-ply unidirectional carbon/epoxy composite plate of thickness $2h = 0.92$ mm. The material properties used are: $\rho = 1.55$ g/cm^3, $C_{11} = 154.02$ GPa, $C_{13} = 3.29$ GPa, $C_{33} = 10.96$ GPa, and $C_{55} = 5.59$ GPa. This composite plate will be used for the experimental work later in this Chapter. If we compare this figure with the dispersion curves for aluminum plates, we can see they are quite different.

9.4 Transient Response to an External Loading

In Chapter 5, we analyzed the transient response of a homogeneous isotropic plate to an arbitrary loading (normal direction) using the integral transform method. The double Fourier transform was applied to the time variable t and space variable x. Solutions were obtained for the surface displacements of Lamb waves and their 2-D FTs. In this section, we use the same method to analyze the transient response of an orthotropic composite plate to an arbitrary loading.

9.4.1 Problem Statement

Consider an orthotropic plate of thickness $2h$ loaded by an arbitrary traction $f(x,t)$. The problem geometry along with the coordinate system is shown in Fig. 9.3, in which

[2] In fact, the dispersion equations are valid for orthotropic composite plates.

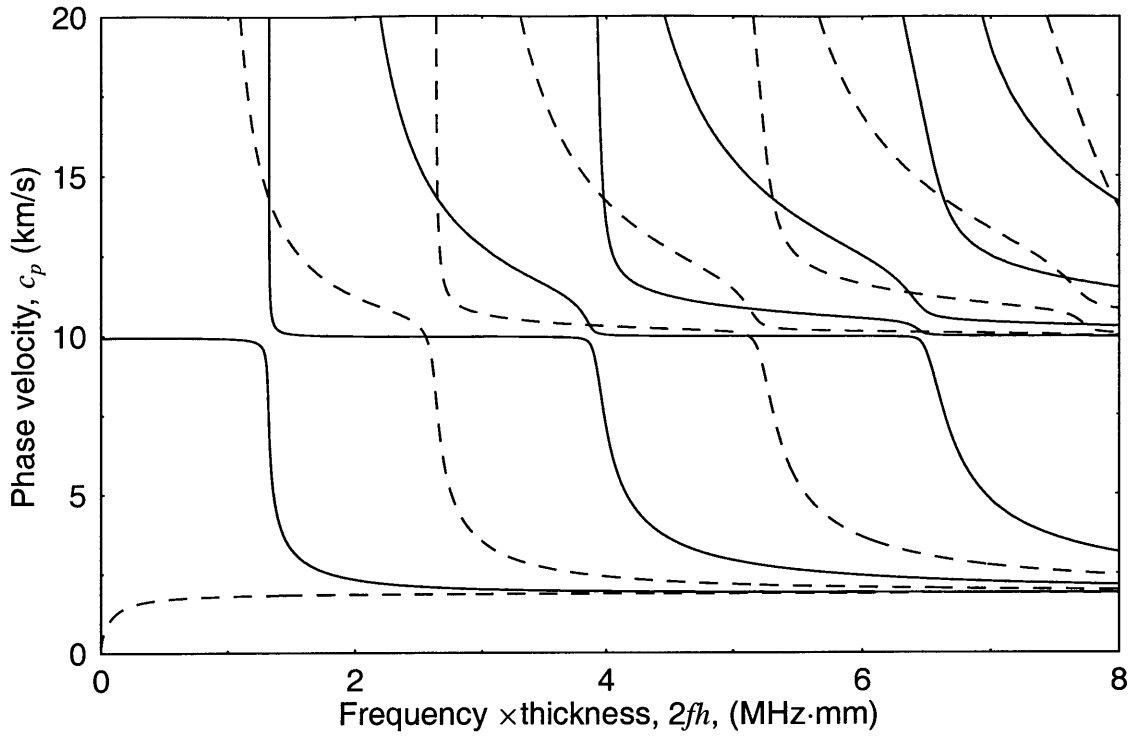

Figure 9.2: Dispersion curves of Lamb waves in the fiber direction of a 7-ply unidirectional carbon/epoxy composite plate.

the stress boundary conditions are prescribed as

$$\sigma_{zz}(x,t) = \begin{cases} f(x,t) & \text{at} \quad z = +h \\ 0 & \text{at} \quad z = -h \end{cases} \tag{9.40}$$

$$\sigma_{xz}(x,t) = 0 \qquad \text{at} \quad z = \pm h \ , \tag{9.41}$$

Assuming the state of plane strain, the equations of motion can be expressed in terms of displacements as:

$$\begin{aligned} \rho \ddot{u_1} &= C_{11}u_{1,11} + C_{13}u_{3,31} + C_{55}(u_{1,33} + u_{3,13}) \\ \rho \ddot{u_3} &= C_{33}u_{3,33} + C_{13}u_{1,13} + C_{55}(u_{1,13} + u_{3,11}) \ , \end{aligned} \tag{9.42}$$

where λ and μ are Lamé constants, and ρ is the mass density.

Our objective is to obtain the 2-D FT of the displacements $u_n(z,x,t)$ induced by the loading $f(x,t)$, which is defined as

$$\hat{u}_n(z,k,\omega) = \int_{-\infty}^{+\infty}\int_{-\infty}^{+\infty} u_n(z,x,t)e^{-j(kx-\omega t)}dxdt\ , \tag{9.43}$$

where where k and ω are the wavenumber and angular frequency. The subscript n denotes the axis, i.e., $n = x$ (in-plane) or $n = z$ (out-of-plane). Correspondingly, the inverse FT is defined as

$$u_n(z,x,t) = \frac{1}{4\pi^2}\int_{-\infty}^{+\infty}\int_{-\infty}^{+\infty} \hat{u}_n(z,k,\omega)e^{j(kx-\omega t)}dkd\omega\ , \tag{9.44}$$

The solution $\hat{u}_n(z,k,\omega)$ can be obtained simply by substituting the displacements $u_n(z,x,t)$ in the form of inverse 2-D Fourier transform into the equations of motion and satisfying the boundary conditions. This procedure is described as follows.

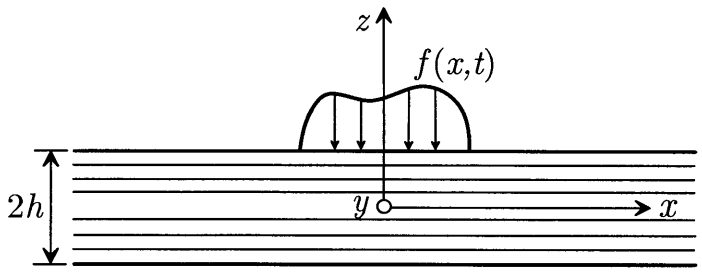

Figure 9.3: Problem geometry. An orthotropic plate of thickness $2h$ is loaded by an arbitrary traction $f(x,t)$ on the top surface ($z = h$).

9.4.2 Two-Dimensional Fourier Transform

The derivatives of $u_x(z,x,t)$ and $u_z(z,x,t)$ with respect to the variables x, z and t are obtained as

$$\frac{\partial u_x}{\partial x} = \frac{1}{4\pi^2}\int_{-\infty}^{+\infty}\int_{-\infty}^{+\infty} \hat{u}_x(jk)\exp[j(kx-\omega t)]dkd\omega \tag{9.45}$$

$$\frac{\partial^2 u_x}{\partial x^2} = \frac{1}{4\pi^2}\int_{-\infty}^{+\infty}\int_{-\infty}^{+\infty} \hat{u}_x(-k^2)\exp[j(kx-\omega t)]dkd\omega \tag{9.46}$$

$$\frac{\partial^2 u_x}{\partial x \partial z} = \frac{1}{4\pi^2}\int_{-\infty}^{+\infty}\int_{-\infty}^{+\infty} \frac{d\hat{u}_x}{dz}(jk)\exp[j(kx-\omega t)]dkd\omega \tag{9.47}$$

$$\frac{\partial^2 u_x}{\partial t^2} = \frac{1}{4\pi^2}\int_{-\infty}^{+\infty}\int_{-\infty}^{+\infty} \hat{u}_x(-\omega^2)\exp[j(kx-\omega t)]dkd\omega\ , \tag{9.48}$$

and

$$\frac{\partial u_z}{\partial z} = \frac{1}{4\pi^2}\int_{-\infty}^{+\infty}\int_{-\infty}^{+\infty} \frac{d\hat{u}_z}{dz}\exp[j(kx-\omega t)]dkd\omega \tag{9.49}$$

$$\frac{\partial^2 u_z}{\partial z^2} = \frac{1}{4\pi^2}\int_{-\infty}^{+\infty}\int_{-\infty}^{+\infty} \frac{d^2\hat{u}_z}{dz^2}\exp[j(kx-\omega t)]dkd\omega \tag{9.50}$$

$$\frac{\partial^2 u_z}{\partial z \partial x} = \frac{1}{4\pi^2}\int_{-\infty}^{+\infty}\int_{-\infty}^{+\infty} \frac{d\hat{u}_z}{dz}(jk)\exp[j(kx-\omega t)]dkd\omega \tag{9.51}$$

$$\frac{\partial^2 u_z}{\partial t^2} = \frac{1}{4\pi^2}\int_{-\infty}^{+\infty}\int_{-\infty}^{+\infty} \hat{u}_z(-\omega^2)\exp[j(kx-\omega t)]dkd\omega\ . \tag{9.52}$$

By substituting these into the governing equations of motion or Eqs. (9.42), we would have the ordinary differential equations:

$$C_{55}\frac{d^2\hat{u}_x}{dz^2} + [(C_{13}+C_{55})(jk)]\frac{d\hat{u}_z}{dz} + [\rho\omega^2 - C_{11}k^2]\hat{u}_x = 0 \tag{9.53}$$

$$C_{33}\frac{d^2\hat{u}_z}{dz^2} + [(C_{13}+C_{55})(jk)]\frac{d\hat{u}_x}{dz} + [\rho\omega^2 - C_{55}k^2]\hat{u}_z = 0\ . \tag{9.54}$$

Solving, the general solutions of $\hat{u}_n(z,k,\omega)$ can be thus written in the form:

$$\begin{aligned}\hat{u}_x(z,k,\omega) =& \{-jA_sH_m\cosh(k_{zp}z) + D_sH_p\cosh(k_{zm}z)\} + \\ & \{-jB_aH_m\sinh(k_{zp}z) + C_aH_p\sinh(k_{zm}z)\}\end{aligned} \tag{9.55}$$

$$\begin{aligned}\hat{u}_z(z,k,\omega) =& \{A_s R_p H_m \sinh(k_{zp}z) + jD_s R_m H_p \sinh(k_{zm}z)\} + \\ & \{B_a R_p H_m \cosh(k_{zp}z) + jC_a R_m H_p \cosh(k_{zm}z)\} ,\end{aligned} \tag{9.56}$$

where the parameters k_{zp} and k_{zm} are defined in Eqs. (9.23) and (9.24), R_p and R_m are defined in Eqs. (9.25) and (9.26), H_p and H_m are defined in Eqs. (9.34) and (9.26). A_s, D_s, B_a and C_a are the constants to be determined through satisfying the stress boundary conditions. By far we can express the displacements in terms of these constants using Eq. (9.44).

Since the stresses are related to the displacements by virtue of the constitutive law, i.e.,

$$\sigma_{33} = C_{33}u_{3,3} + C_{13}u_{1,1} , \qquad \sigma_{31} = C_{55}u_{1,3} + C_{55}u_{3,1} , \tag{9.57}$$

the stresses can be expressed in terms of the constants A_s, D_s, B_a and C_a:

$$\begin{aligned}\sigma_{zz} =& \frac{1}{4\pi^2}\int_{-\infty}^{+\infty}\int_{-\infty}^{+\infty}\Big[G_p H_m\Big]\Big[A_s\cosh(k_{zp}z) + B_a\sinh(k_{zp}z)\Big]e^{j(kx-\omega t)}dkd\omega + \\ & \frac{1}{4\pi^2}\int_{-\infty}^{+\infty}\int_{-\infty}^{+\infty}\Big[G_m H_p\Big]\Big[jD_s\cosh(k_{zm}z) + jC_a\sinh(k_{zm}z)\Big]e^{j(kx-\omega t)}dkd\omega ,\end{aligned} \tag{9.58}$$

and

$$\begin{aligned}\sigma_{zx} =& \frac{1}{4\pi^2}\int_{-\infty}^{+\infty}\int_{-\infty}^{+\infty}\Big[C_{55}H_p H_m\Big]\Big[-jA_s\sinh(k_{zp}z) - jB_a\cosh(k_{zp}z)\Big]e^{j(kx-\omega t)}dkd\omega - \\ & \frac{1}{4\pi^2}\int_{-\infty}^{+\infty}\int_{-\infty}^{+\infty}\Big[C_{55}H_p H_m\Big]\Big[D_s\sinh(k_{zm}z) + C_a\cosh(k_{zm}z)\Big]e^{j(kx-\omega t)}dkd\omega .\end{aligned} \tag{9.59}$$

where the parameters G_p and G_m are defined in Eqs. (9.32) and (9.26).

In the meantime, via the inverse 2-D FT the stress boundary conditions can be expressed as

$$\sigma_{zz}(x,t) = \begin{cases} \dfrac{1}{4\pi^2}\displaystyle\int_{-\infty}^{+\infty}\int_{-\infty}^{+\infty} \hat{f}(k,\omega)e^{j(kx-\omega t)}dkd\omega & \text{at} \quad z = +h \\ 0 & \text{at} \quad z = -h \end{cases} \tag{9.60}$$

$$\sigma_{xz}(x,t) = 0 \qquad \text{at} \quad z = \pm h \tag{9.61}$$

where $\hat{f}(k,\omega)$ is the 2-D FT of the traction $f(x,t)$:

$$\hat{f}(k,\omega) = \int_{-\infty}^{+\infty}\int_{-\infty}^{+\infty} f(x,t)e^{-j(kx-\omega t)}dxdt \; . \tag{9.62}$$

By satisfying the stress boundary conditions, the constants are determined as

$$A_s = \frac{-\sinh(k_{zm}h)\cdot\hat{f}(k,\omega)}{2\Delta_s}, \qquad D_s = \frac{-j\sinh(k_{zp}h)\cdot\hat{f}(k,\omega)}{2\Delta_s}, \tag{9.63}$$

$$B_a = \frac{-\cosh(k_{zm}h)\cdot\hat{f}(k,\omega)}{2\Delta_a}, \qquad C_a = \frac{-j\cosh(k_{zp}h)\cdot\hat{f}(k,\omega)}{2\Delta_a}, \tag{9.64}$$

where

$$\Delta_s = G_p H_m \cosh(k_{zp}h)\sinh(k_{zm}h) - G_m H_p \sinh(k_{zp}h)\cosh(k_{zm}h) \tag{9.65}$$

$$\Delta_a = G_p H_m \sinh(k_{zp}h)\cosh(k_{zm}h) - G_m H_p \cosh(k_{zp}h)\sinh(k_{zm}h) \; . \tag{9.66}$$

Note that the conditions for $\Delta_s = 0$ and $\Delta_a = 0$ represent the frequency equations for symmetric and antisymmetric Lamb wave modes, respectively [117].

From Eqs. (9.55) and (9.56), it is straightforward to compute $\hat{u}_n(z,k,\omega)$ at an arbitrary position z, which can be expressed as the sum of symmetric and antisymmetric parts:

$$\hat{u}_n(z,k,\omega) = u_n^a(z,k,\omega) + u_n^s(z,k,\omega) \; , \tag{9.67}$$

where

$$\hat{u}_x^s = j\left[\frac{H_m \cosh(k_{zp}z)\sinh(k_{zm}h) - H_p \cosh(k_{zm}z)\sinh(k_{zp}h)}{2\Delta_s}\right] \cdot \hat{f}(k,\omega) \quad (9.68)$$

$$\hat{u}_x^a = j\left[\frac{H_m \cosh(k_{zm}h)\sinh(k_{zp}z) - H_p \cosh(k_{zp}h)\sinh(k_{zm}z)}{2\Delta_a}\right] \cdot \hat{f}(k,\omega) \quad (9.69)$$

and

$$\hat{u}_z^s = \left[\frac{R_m H_p \sinh(k_{zm}z)\sinh(k_{zp}h) - R_p H_m \sinh(k_{zp}z)\sinh(k_{zm}h)}{2\Delta_s}\right] \cdot \hat{f}(k,\omega) \quad (9.70)$$

$$\hat{u}_z^a = \left[\frac{R_m H_p \cosh(k_{zm}z)\cosh(k_{zp}h) - R_p H_m \cosh(k_{zp}z)\cosh(k_{zm}h)}{2\Delta_a}\right] \cdot \hat{f}(k,\omega) \quad (9.71)$$

This is the analytical solution representing the transient Lamb waves generated by an arbitrary traction. It can be observed that the 2-D FT $u_n^s(z,k,\omega)$ and $u_n^a(z,k,\omega)$ are the product of two independent terms: the first is the material response which is only dependent on the material properties, and the second term is the loading in the transformed domain which is only dependent on the external loading. As for the case of isotropic plate, we denote the material responses $N_n^s(z,k,\omega)$ and $N_n^a(z,k,\omega)$ as the *overall excitation efficiencies*, i.e.,

$$\hat{u}_n^s(z,k,\omega) = N_n^s(z,k,\omega) \cdot \hat{f}(k,\omega) \quad (9.72)$$

$$\hat{u}_n^a(z,k,\omega) = N_n^a(z,k,\omega) \cdot \hat{f}(k,\omega)\ , \quad (9.73)$$

where

$$N_x^s(z,k,\omega) = j\left[\frac{H_m \cosh(k_{zp}z)\sinh(k_{zm}h) - H_p \cosh(k_{zm}z)\sinh(k_{zp}h)}{2\Delta_s}\right] \quad (9.74)$$

$$N_x^a(z,k,\omega) = j\left[\frac{H_m \cosh(k_{zm}h)\sinh(k_{zp}z) - H_p \cosh(k_{zp}h)\sinh(k_{zm}z)}{2\Delta_a}\right]\ , \quad (9.75)$$

and

$$N_z^s(z,k,\omega) = \left[\frac{H_m \cosh(k_{zp}z)\sinh(k_{zm}h) - H_p \cosh(k_{zm}z)\sinh(k_{zp}h)}{2\Delta_s}\right] \tag{9.76}$$

$$N_z^a(z,k,\omega) = \left[\frac{R_m H_p \cosh(k_{zm}z)\cosh(k_{zp}h) - R_p H_m \cosh(k_{zp}z)\cosh(k_{zm}h)}{2\Delta_a}\right] . \tag{9.77}$$

Since it is of our particular interest to consider the case on the upper surface, i.e., $z = h$, the corresponding overall excitation efficiencies are

$$N_x^s(h,k,\omega) = j\left[\frac{H_m \cosh(k_{zp}h)\sinh(k_{zm}h) - H_p \cosh(k_{zm}h)\sinh(k_{zp}h)}{2\Delta_s}\right] \tag{9.78}$$

$$N_x^a(h,k,\omega) = j\left[\frac{H_m \cosh(k_{zm}h)\sinh(k_{zp}h) - H_p \cosh(k_{zp}h)\sinh(k_{zm}h)}{2\Delta_a}\right] , \tag{9.79}$$

and

$$N_z^s(h,k,\omega) = \left[\frac{(R_m H_p - R_p H_m)\sinh(k_{zp}h)\sinh(k_{zm}h)}{2\Delta_s}\right] \tag{9.80}$$

$$N_z^a(h,k,\omega) = \left[\frac{(R_m H_p - R_p H_m)\cosh(k_{zp}h)\cosh(k_{zm}h)}{2\Delta_a}\right] . \tag{9.81}$$

9.4.3 Surface Displacements

Now that the 2-D FT $\hat{u}_n(h,k,\omega)$ is obtained, the displacements on the surface can be obtained through the inverse FT. In a similar way, the displacements are considered as the sum of the symmetric and antisymmetric components:

$$u_n(h,x,t) = u_n^a(h,x,t) + u_n^s(h,x,t) , \tag{9.82}$$

where

$$u_n^s(h,x,t) = \frac{1}{4\pi^2}\int_{-\infty}^{+\infty}\int_{-\infty}^{+\infty} N_n^s(h,k,\omega)\cdot\hat{f}(k,\omega)\cdot e^{j(kx-\omega t)}dkd\omega \tag{9.83}$$

$$u_n^a(h,x,t) = \frac{1}{4\pi^2}\int_{-\infty}^{+\infty}\int_{-\infty}^{+\infty} N_n^a(h,k,\omega)\cdot\hat{f}(k,\omega)\cdot e^{j(kx-\omega t)}dkd\omega . \tag{9.84}$$

Similar to the case of transient waves in an isotropic and homogeneous plate, the functions $N_n^s(h,k,\omega)$ and $N_n^a(h,k,\omega)$ contain an infinitely large number of poles corresponding to the roots of dispersion equations in the composite principal directions. Thus, it is again convenient to use the residue theorem for evaluating the integrals over the wavenumber k. Referring to Chapter 5, both the in-plane and out-of-plane surface displacements are obtained as

$$u_n^s(h,x,t) = \frac{1}{2\pi}\int_{-\infty}^{+\infty}\sum_{k_s} H_n^s(h,\omega)\cdot\hat{f}(k,\omega)\cdot e^{j(kx-\omega t)}d\omega \tag{9.85}$$

$$u_n^a(h,x,t) = \frac{1}{2\pi}\int_{-\infty}^{+\infty}\sum_{k_a} H_n^a(h,\omega)\cdot\hat{f}(k,\omega)\cdot e^{j(kx-\omega t)}d\omega \tag{9.86}$$

where $H_n^s(h,\omega)$ and $H_n^s(h,\omega)$ are the *modal excitation efficiencies*, expressed as

$$H_x^s(h,\omega) = \frac{H_m(G_p/G_m-1)\cosh(k_{zp}h)\sinh(k_{zm}h)}{4\Delta_s'} \tag{9.87}$$

$$H_x^a(h,\omega) = \frac{H_m(G_p/G_m-1)\sinh(k_{zp}h)\cosh(k_{zm}h)}{4\Delta_a'} \tag{9.88}$$

$$H_z^s(h,\omega) = \frac{j(R_mH_p-R_pH_m)\sinh(k_{zp}h)\sinh(k_{zm}h)}{4\Delta_s'} \tag{9.89}$$

$$H_z^a(h,\omega) = \frac{j(R_mH_p-R_pH_m)\cosh(k_{zp}h)\cosh(k_{zm}h)}{4\Delta_a'}\,. \tag{9.90}$$

Here Δ_s' and Δ_a' represent the derivatives of Δ_s and Δ_a with respect to the wavenumber k, which can be obtained numerically. Notice that the summations are carried out for the real wavenumbers k_s and k_a to represent the propagating waves in the far field.

9.5 Experimental Investigation

Experiment is conducted to investigate the Lamb wave propagation in the principal directions (parallel and normal to the fiber direction) of the 7-ply unidirectional carbon/epoxy composite plate of thickness $2h = 0.92$ mm using laser sources. The dispersion curves in the fiber direction of this specimen have been shown in Fig. 9.2.

The experimental setup is basically the same as that for the laser generation of Lamb waves in an aluminum plate as shown in Fig. 8.9. In the fiber direction (0°), 128 waveforms were recorded for varying source-receiver distances with a spatial sampling interval of 0.8255 mm. In the normal-to-fiber direction (90°), only 54 waveforms were recorded for varying source-receiver distances with a spatial sampling interval of 0.508 mm. The amplitude of the signal is proportional to the out-of-plane displacements on the plate surface.

Figure 9.4 illustrates three sample waveforms parallel to the fiber direction at the source-receiver distances of (a) $x_1 = 114$ mm, (b) $x_2 = 166$ mm, and (c) $x_3 = 219$ mm. Notice that the signal amplitudes are normalized by the same value. As we can see, there are only two fundamental modes obtained: A_0 and S_0 modes, and S_0 mode arrives earlier than A_0 mode, while the amplitude of S_0 mode is much smaller than that of A_0 mode. For A_0 mode, the dispersion effect is obvious since the higher frequency part arrives earlier than the lower frequency part and the wave shape changes with the change of source-receiver distance. This observation is the same as some publication on laser-generated Lamb waves in composites [82]. The lack of high frequency and high order modes could be caused by the high attenuation of high frequency signals in composites. Also noticeable is that the amplitude of the waveform at the distance of $x_3 = 219$ mm is larger than the one at the distance of $x_2 = 166$ mm, which is inconsistent with the expectation that the waveform amplitude tends to decrease with the increase of distance. This is because the detection laser was not working very steady during the experiment.

Figure 9.5 shows three sample waveforms normal to the fiber direction at the source-receiver distances of (a) $x_1 = 71.0$ mm, (b) $x_2 = 83.2$ mm, and (c) $x_3 = 95.9$ mm. The signal amplitudes are also normalized by the same value. As we can see, as in this case of waveforms in the fiber direction, there are only two fundamental modes shown: A_0 and S_0 modes, and S_0 mode arrives earlier than A_0 mode. Furthermore, the amplitude of S_0 modes is so small that it is almost non-visible. For A_0 mode, the higher frequency part arrives earlier than the lower frequency part and the wave shape changes with the change of source-receiver distance, indicative of the

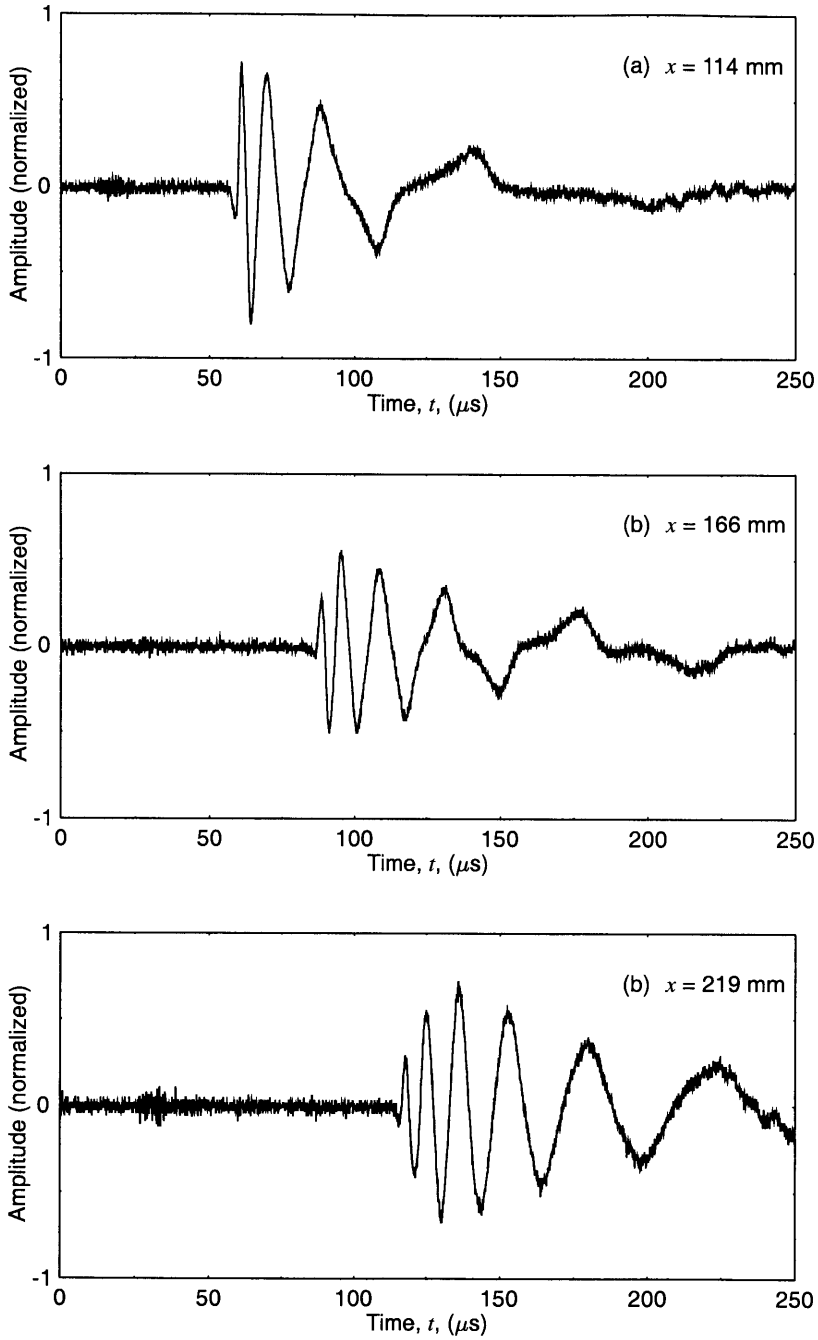

Figure 9.4: Experimental waveforms of Lamb waves parallel to the fiber direction in a 7-ply unidirectional carbon/epoxy composite plate of thickness $2h = 0.92$ mm at the distances of (a) $x_1 = 114$ mm, (b) $x_2 = 166$ mm, and (c) $x_3 = 219$ mm, where the signals are generated by an Nd:YAG pulsed laser and received by a Lasson EMF-500 laser receiver.

dispersion. The waveforms collected normal to the fiber direction are quite different from those collected in the fiber direction, indicating the anisotropic feature of composites.

After experimental waveforms of Lamb waves are obtained in multiple locations, it is interesting to see if experimental dispersion curves will be resulted, like the case of laser experiment on an aluminum plate (see Chapter 8). A two-dimensional fast Fourier transform (2-D FFT) is applied to the 128 waveforms obtained in the fiber direction, where a Hanning window is utilized in order to reduce the leakage in the wavenumber domain. Figure 9.6 illustrates the comparison of the experimental 2-D FFT and theoretical 2-D FT of Lamb waves in the fiber direction, where the excitation laser beam is assumed to be beam size $a = 0.5$ mm. It is observed that only a faint agreement exists at the low frequency range. This result is not surprising since only low-frequency A_0 and S_0 modes are observed in the experimental waveforms. The theoretical model does not take the attenuation in composites (especially the high frequency modes) into account.

9.6 Conclusions

This chapter was intended to serve as a basis for the future work on the Lamb wave tuning in composites. A limited investigation on the transient Lamb waves in transversely isotropic composite plates was conducted. The propagation of plane waves in composites was firstly reviewed, which gave the guidance for elastic constants measurement using bulk waves and Lamb waves. The dispersion equations in the principal directions (parallel or normal to the fiber direction) of composites were reviewed and sample dispersion curves were constructed. Afterwards, the transient Lamb waves in the principal directions of composites subject to an arbitrary loading was analyzed using the integral transform method. Expressions were derived for the displacements and their 2-D FTs. Finally, laser-generated experimental Lamb waves in the principal directions were obtained on a unidirectional carbon/epoxy composite plate.

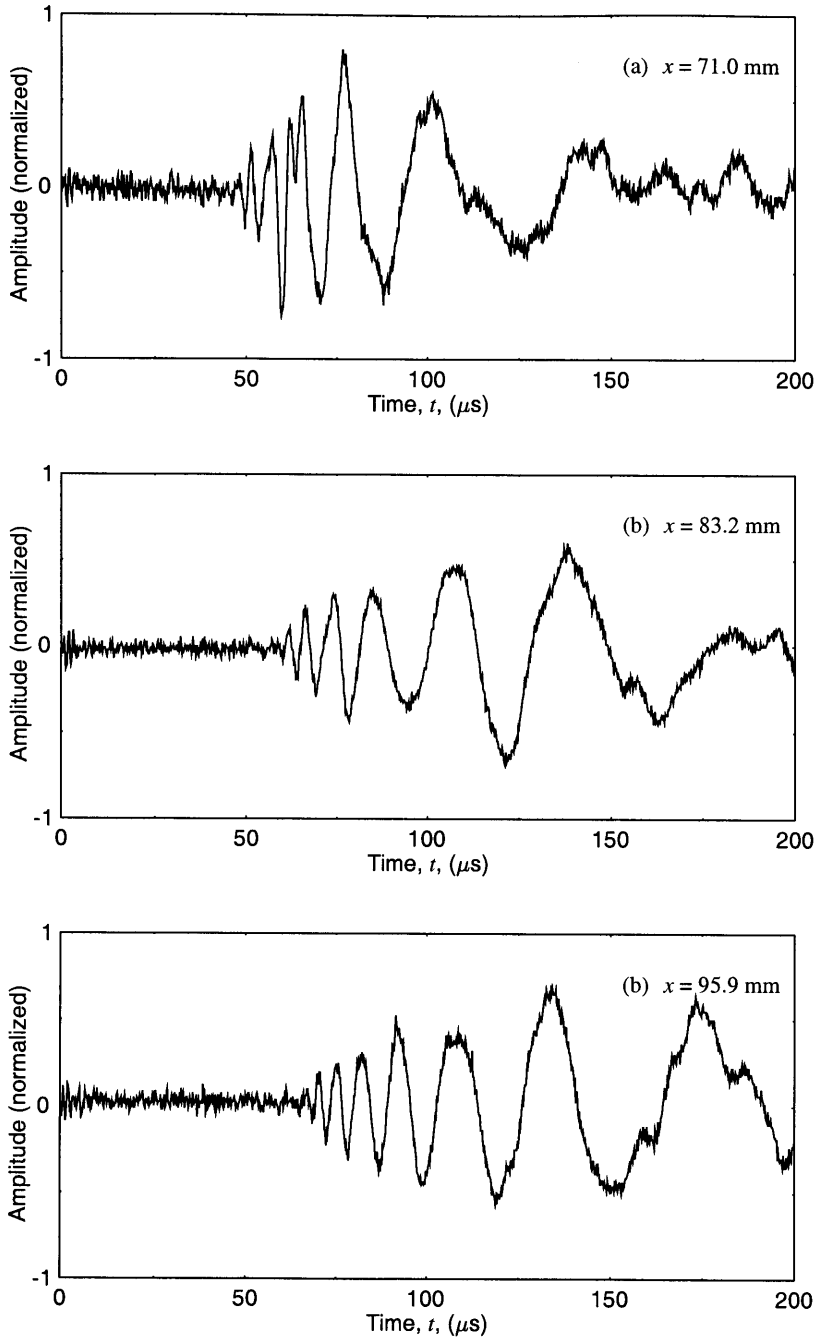

Figure 9.5: Experimental waveforms of Lamb waves normal to the fiber direction in a 7-ply unidirectional carbon/epoxy composite plate of thickness $2h = 0.92$ mm at the distances of (a) $x_1 = 71.0$ mm, (b) $x_2 = 83.2$ mm, and (c) $x_3 = 95.9$ mm, where the signals are generated by an Nd:YAG pulsed laser and received by a Lasson EMF-500 laser receiver.

From the study we can learn that the wave propagation behavior in directions parallel to the fiber direction is quite different from that in directions normal to the fiber direction. Also, only two fundamental wave modes A_0 and S_0 modes are found in the experimental waveforms, and A_0 mode is dominant. Since the waveforms are of low frequency, we may conclude that the attenuation of high frequency wave modes is high in composites. This also partially explains the observation that he experimental dispersion curves obtained from the 2-D FFT results are not very close to the theoretical curves.

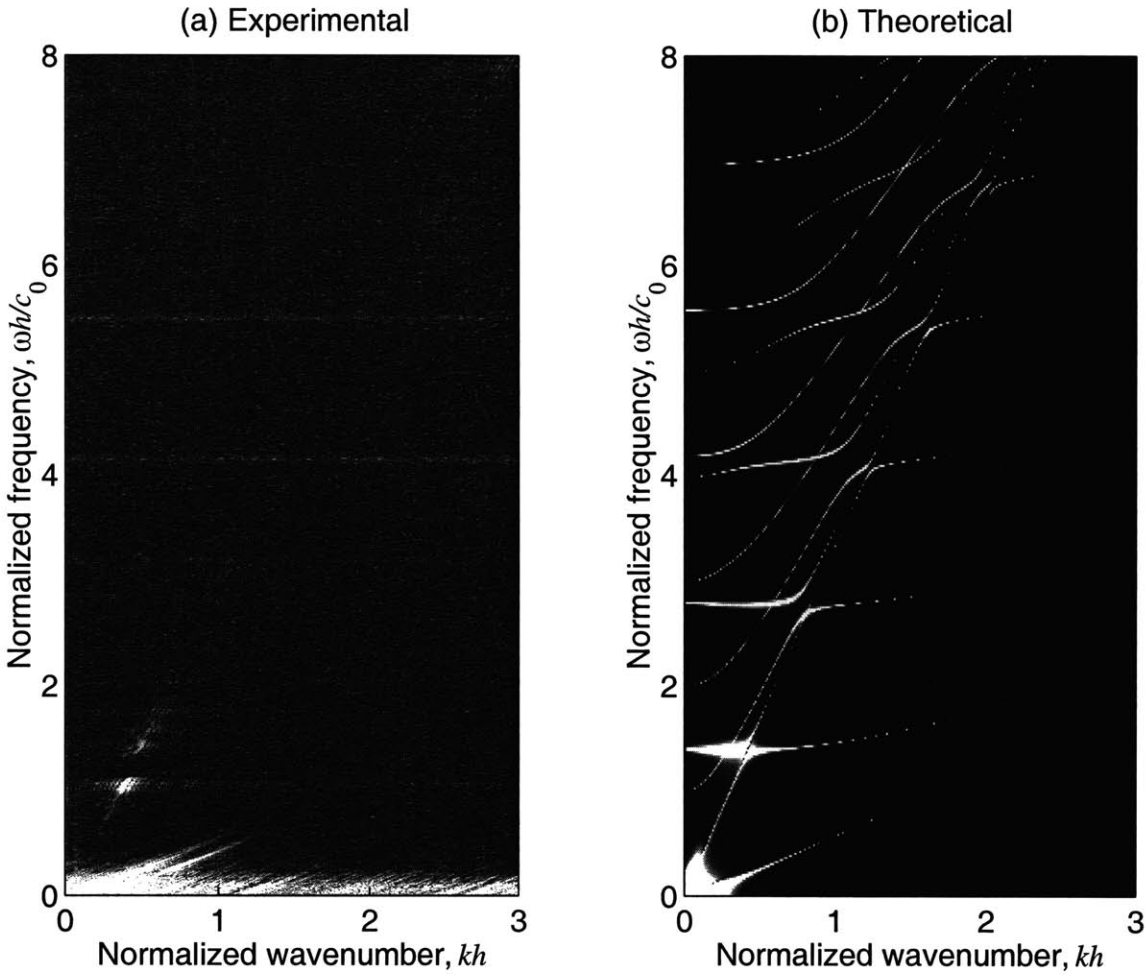

Figure 9.6: Comparison of the experimental 2-D FFT and theoretical 2-D FT of Lamb waves in a plate unidirectional carbon/epoxy composite plate of thickness $2h = 0.92$ mm, where the excitation source is a Nd:YAG pulsed laser of beam size $a = 0.5$ mm.

Chapter 10

Summary and Conclusions

10.1 Summary

In this thesis, the tuning of Lamb waves in elastic plates was studied theoretically and experimentally. A dynamic phase tuning concept employing array transducers was proposed, and compared with the traditional angle wedge and comb transducer tuning methods. This tuning concept was implemented in two ways — phased array tuning and synthetic phase tuning. The former was based on physical time delays, while in the latter numerical time delays are provided to array elements.

To understand the tuning efficiency of each wave mode, an analytical model was developed and the transient response of an elastic plate to an arbitrary loading was analyzed, using an integral transform method (double Fourier integrals applied in both space and time). The analytical expressions were used to compute the surface displacements as well as their temporal and spatial Fourier spectrum, which were then used to illustrate the tuning efficiency of each wave mode.

The analytical model was then extended to investigate the tuning mechanism of angle wedge and array transducers, by taking into account their excitation conditions. The surface displacements of individual modes and their Fourier spectrum were derived and used to study the tuning behavior. The analytical results were compared with the experimental results as well as the numerical results obtained from the finite element simulation studies.

In dealing with broadband signals, laser-generated Lamb waves were investigated. Both line and circular source loading models were considered for lasers in the ablation regime. The predicted waveforms and dispersion curves were compared with the experimental results. Virtually tuned waves were also constructed by processing a set of laser-generated Lamb waves, based on the SPT scheme.

A limited investigation of Lamb waves in transversely isotropic composite plates was also carried out. Solutions were obtained for transient waves in the principal directions. Experimental waveforms were obtained in the principal directions using laser sources. This investigation was intended to serve as a basis for the future study of Lamb wave tuning in composite plates.

10.2 Conclusions

The following conclusions are drawn from this study:

- The phase tuning using an array transducer is effective in that it can tune the modes propagating at low phase velocities and that the propagation direction of tuned waves can be controlled.
- The synthetic phase tuning technique is flexible and cost-effective.
- The tuning efficiency varies from wave mode to wave mode and from frequency to frequency.
- The analytical solutions for the displacements of wave modes and their Fourier spectrum can be used to investigate the tuning mechanism of various methods and tuning efficiencies of various wave modes.
- The analytical results are consistent with the numerical results obtained from the finite element simulation studies.
- The tuning effect of angle wedge transducers is achieved by controlling the angle of incidence.

- For the angle wedge transducer tuning, Snell's law is not rigorously obeyed if the excitation signal has certain bandwidth.
- The tuning effect of phased array transducers is achieved by providing time delays between elements.
- The tuning effect is improved from the half-way tuning to the full tuning.
- Both line and circular source loading models are valid for lasers in the ablation regime.
- The SPT scheme can be applied to broadband signals to construct virtually tuned waves, combined with signal processing algorithms.
- It is feasible to obtain optimum tuning effect through this study.
- For Lamb waves in a transversely isotropic composite plate, the propagation behavior parallel to the fiber direction is different from that normal to the fiber direction. Only two fundamental modes (A_0 and S_0) exist in the experimental signals and the amplitude of A_0 mode is much larger than that of S_0 mode. In addition, the attenuation of high frequency components in composites is severe.

10.3 Contributions of the Thesis

The contributions of this thesis include:

- Development of the synthetic phase tuning technique.
- Development of an analytical model for studying transient Lamb waves using an integral transform method (Fourier transform in both space and time).
- Theoretical and experimental investigation of the tuning mechanism of angle wedge transducers.
- Theoretical and experimental investigation of the tuning mechanism of array transducers (synthetic phase tuning).

- Theoretical and experimental investigation of laser-generated Lamb waves.
- Development of an analytical model for studying transient Lamb waves originated from a circular source using Fourier and Hankel transform.
- Study of the feasibility of tuning laser-generated Lamb waves.
- Development of an analytical model for studying transient Lamb waves in the principal directions of transversely isotropic composite plates.

10.4 Recommendations for Future Work

Based on the thesis work, major future research work is recommended as follows:

- Reflection of Lamb waves

  When investigating the synthetic phase tuning under pseudo pulse-echo operation, we assumed a perfect reflection of Lamb waves from the plate edge. In fact, there are energy loss and mode conversion associated with the wave reflection.

- Attenuation of Lamb waves

  Lamb waves have energy loss during their propagation in waveguides, which is related to the frequency. The attenuation is severe in composite plates, especially for wave modes of high order.

- Experimental investigation of full synthetic phase tuning in PPC operation

  In the thesis research, theoretical results were given for the full synthetic phase tuning, but were not confirmed by experimental results.

- Influence of array parameters

  It is of importance to investigate the influence of array parameters on the tuning effect, including the number of elements N, inter-element spacing d, and element size a.

- Influence of the laser beam size

  It is of importance to study the influence of laser beam size (a) on the predicted waveforms, while in the study we only used a single beam size value.

- Time-frequency analysis

  Time-frequency analysis tools such as wavelet transform are very useful for analyzing dispersive signals. They can be applied to laser-generated Lamb wave signals for constructing virtually tuned waves.

- Tuning of Lamb waves in composite plates

  It is important to apply various tuning techniques, including the angle wedge transducer tuning, and synthetic phase tuning methods, to transversely isotropic composite plates.

Appendix

A Fourier Transform of a Gaussian Spike Pulse

Consider a Gaussian spike pulse of the form:

$$f(t) = \frac{1}{2\pi} e^{-j\omega_0 t} e^{-B^2 t^2/8} , \tag{A.1}$$

where ω_0 is the center angular frequency, and B is the bandwidth. The Fourier transform of $f(t)$ is simply expressed as

$$\hat{f}(\omega) = \int_{-\infty}^{+\infty} e^{-j\omega_0 t} e^{-B^2 t^2/8} e^{j\omega t} dt , \tag{A.2}$$

which can be rewritten as

$$\hat{f}(\omega) = \int_{-\infty}^{+\infty} \exp\left[-\frac{B^2}{8} \left(t^2 - \frac{j(\omega - \omega_0)t}{B^2/8} \right) \right] dt . \tag{A.3}$$

By defining τ as

$$\tau = t - \frac{j(\omega - \omega_0)t}{B^2/8} , \tag{A.4}$$

we have the equity

$$t^2 - \frac{j(\omega - \omega_0)t}{B^2/8} = \tau^2 + \frac{(\omega - \omega_0)^2}{B^4/16} . \tag{A.5}$$

Thus the Fourier transform is [1]

$$\hat{f}(\omega) = \int_{-\infty}^{+\infty} \exp\left[-\frac{B^2\tau^2}{8} - \frac{2(\omega-\omega_0)^2}{B^2}\right] d\tau \ . \tag{A.6}$$

Using the quantity

$$\int_{-\infty}^{+\infty} e^{-x^2} dx = \sqrt{\pi} \ , \tag{A.7}$$

finally the Fourier transform of the Gaussian spike pulse is obtained as

$$\hat{f}(\omega) = \frac{2}{B\sqrt{2\pi}} e^{-2(\omega-\omega_0)^2/B^2} \ . \tag{A.8}$$

[1] In this thesis, the Fourier transform over the time t is defined as $\hat{x}(\omega) = \int_{-\infty}^{+\infty} x(t)\exp(j\omega t)dt$. Correspondingly, the inverse Fourier transform is defined as $x(t) = \frac{1}{2\pi}\int_{-\infty}^{+\infty} \hat{x}(\omega)\exp(-j\omega t)d\omega$.

B Toneburst Modulated by Hanning Window

The excitation of narrowband signals is generally implemented by producing sinusoidal. In order to control the bandwidth of the excitation signal, a Hanning window is often applied to modulate the toneburst. The Fourier transform of a sinusoidal toneburst signal modulated by a Hanning window is derived in this Appendix.

A Hanning window can be viewed as a periodic Hanning function modulated by a rectangular (Dirichlet) window. As a result, the toneburst modulated by a Hanning window is equivalent to a sinusoidal signal modulated by a periodic Hanning function which is modulated by a rectangular window, if the duration of the Hanning window is equal to the duration of the toneburst.

Denoting $x(t)$ as the sinusoidal signal, $h(t)$ as the periodic Hanning function and $w_r(t)$ as the rectangular window, the modulated toneburst signal $w_H(t)$ is the product of these three terms:

$$w_H(t) = x(t) \cdot h(t) \cdot w_r(t) \ . \tag{B.1}$$

In the frequency domain, it is represented as the convolution

$$\hat{w}_H(\omega) = \frac{1}{(2\pi)^2} \hat{x}(\omega) \otimes \hat{h}(\omega) \otimes \hat{w}_r(\omega) \ , \tag{B.2}$$

where $\hat{w}_H(\omega)$, $\hat{x}(\omega)$, $\hat{h}(\omega)$ and $\hat{w}_r(\omega)$ are the respective Fourier transform of $w_H(t)$, $x(t)$, $h(t)$ and $w_r(t)$, respectively. The expressions for the signals $x(t)$, $h(t)$ and $w_r(t)$ are simply written as

$$x(t) = \exp(-j\omega_0 t) \tag{B.3}$$

$$h(t) = 0.5 - 0.5\cos(2\pi t/t_0) \tag{B.4}$$

$$w_r(t) = H(t) - H(t - t_0) \ , \tag{B.5}$$

where $\omega_0 = 2\pi f_0$ and f_0 is the frequency of the sinusoidal signal $x(t)$. The time constant t_0 is the duration of both the toneburst and the rectangular window, that

is $t_0 = m/f_0$ for the m-cycles of sinusoids in the signal. The function $H(t)$ is the Heaviside step function, i.e.,

$$H(t) = \begin{cases} 1 & \text{for } t \geq 0 \\ 0 & \text{for } t < 0 \, . \end{cases} \tag{B.6}$$

The Fourier transforms $\hat{x}(\omega)$, $\hat{h}(\omega)$ and $\hat{w}_r(\omega)$ are then obtained as

$$\hat{x}(\omega) = 2\pi\delta(\omega - \omega_0) \tag{B.7}$$

$$\hat{h}(\omega) = \frac{\pi}{2}[2\delta(\omega) - \delta(\omega - 2\pi/t_0) - \delta(\omega + 2\pi/t_0)] \tag{B.8}$$

$$\hat{w}_r(\omega) = \frac{2\sin(\omega t_0/2)}{\omega} \exp(j\omega t_0/2) \, . \tag{B.9}$$

By substituting these into Eq. (B.2), the Fourier transform $\hat{w}_H(\omega)$ is obtained as

$$\hat{w}_H(\omega) = \frac{1}{2}\Big\{\Lambda_1 + \Lambda_2 + \Lambda_3\Big\} \, , \tag{B.10}$$

where

$$\Lambda_1 = \frac{2\sin\left[\frac{\pi m(\omega-\omega_0)}{\omega_0}\right]}{\omega - \omega_0} e^{\dfrac{j\pi m(\omega - \omega_0)}{\omega_0}} \tag{B.11}$$

$$\Lambda_2 = -\frac{\sin\left[\frac{\pi m(\omega-\omega_0-\omega_0/m)}{\omega_0}\right]}{\omega - \omega_0 - \omega_0/m} e^{\dfrac{j\pi m(\omega - \omega_0 - \omega_0/m)}{\omega_0}} \tag{B.12}$$

$$\Lambda_3 = -\frac{\sin\left[\frac{\pi m(\omega-\omega_0-\omega_0/m)}{\omega_0}\right]}{\omega + \omega_0 - \omega_0/m} e^{\dfrac{j\pi m(\omega + \omega_0 - \omega_0/m)}{\omega_0}} \, . \tag{B.13}$$

References

[1] J. Krautkrämer and H. Krautkrämer (1990), *Ultrasonic Testing of Materials*, 4th Ed., Springer-verlag, berlin.

[2] M. G. Silk and K. F. Rainton (1979), "The propagation in metal tubing of ultrasonic wave modes equivalent to Lamb waves," *Ultrasonics*, **17**(1), 11–19.

[3] S. I. Rokhlin, R. J. Mayhan, and L. Adler (1985), "On-line ultrasonic Lamb wave monitoring of spot welds," *Mat. Eval.*, **43**, 879–883.

[4] C. Woodward and K. R. White (1996), "Long range bridge girder evaluation using Lamb waves," *Rev. Progr. Quant. Nondestr. Eval.*, **15**, 1847–1852.

[5] M. H. Park, I. S. Kim, and Y. K. Yoon (1996), "Ultrasonic inspection of long steel pipes using Lamb waves," *NDT&E Int.*, **29**(1), 13–20.

[6] J. L. Rose (2000), "Guided wave nuances for ultrasonic nondestructive evaluation," *IEEE Trans. Ultrason. Ferroelectr. Freq. Control*, **47**(3), 575–583.

[7] A. H. Nayfeh and D. E. Chimenti (1983), "Propagation of guided waves in liquid-coupled plates of fiber-reinforced composites," *J. Acoust. Soc. Am.*, **83**(5), 1736–1743.

[8] D. E. Chimenti and A. H. Nayfeh (1985), "Leaky Lamb waves in fibrous composite laminates", *J. Appl. Phys.*, **58**(12), 4512–4538.

[9] S. K. Datta, A. H. Shah, R. L. Bratton and T. Chakraborty (1988), "Propagation of guided waves in liquid-coupled plates of fiber-reinforced composites," *J. Acoust. Soc. Am.*, **83**(5), 1736–1743.

[10] D. E. Chimenti and R. W. Martin (1991), "Nondestructive evaluation of composite laminates by leaky Lamb waves," *Ultrasonics*, **29**(1), 13–21.

[11] A. K. Mal and Y. Bar-Cohen (1990), "Characterization of composites using combined LLW and PBS methods," *Rev. Progr. Quant. Nondestr. Eval.*, **10**, 1555–1560.

[12] W. P. Rogers (1995), "Elastic property measurement using Rayleigh-Lamb waves," *Res. Nondestr. Eval.*, **6**, 185–208.

[13] I. A. Viktorov (1967), *Rayleigh and Lamb waves: Physical Theory and Applications*, Plenum Press, New York.

[14] K. F. Graff (1975), *Wave Motion in Elastic Solids*, Dover Publications, New York.

[15] P. B. Nagy, W. R. Rose, and L. Adler (1986), "A single transducer broadband technique for leaky Lamb wave detection," *Rev. Progr. Quant. Nondestr. Eval.*, **5**, 483–490.

[16] D. Alleyne and P. Cawley (1991), "A two-dimensional Fourier transform method for the measurement of propagating multimode signals," *J. Acoust. Soc. Am.*, **89**(3), 1159–1168.

[17] D. N. Alleyne and P. Cawley (1992), "Optimization of Lamb wave inspection techniques," *NDT&E Int.*, **25**(1), 11–22.

[18] D. N. Alleyne and P. Cawley (1992), "The interaction of Lamb waves with defects," *IEEE Trans. Ultrason. Ferroelectr. Freq. Control*, **39**(3), 381–397.

[19] W. H. Prosser, M. D. Seale, and B. T. Smith (1999), "Time-frequency analysis of the dispersion of Lamb modes," *J. Acoust. Soc. Am.*, **105**(5), 2669–2676.

[20] M. Niethammer, L. J. Jacobs, J. Qu and J. Jarzynski (2000), "Time-frequency representation of Lamb waves using the reassigned spectrogram," *J. Acoust. Soc. Am.*, **107**(5), L19–24.

[21] K. L. Veroy, S. C. Wooh and Y. Shi (1999), "Analysis of dispersive waves using the wavelet transform," *Rev. Progr. Quant. Nondestr. Eval.*, **18**, 687–694.

[22] J. L. Rose, S. P. Pelts, and M. J. Quarry (1998), "A comb transducer model for guided wave NDE," *Ultrasonics*, **36**(1–5), 163–169.

[23] J. Miklowitz (1978), *The Theory of Elastic Waves and Waveguides*, North-Holland Press, New York.

[24] L. Rayleigh (1889), "On the free vibrations of an infinite plate of homogeneous isotropic elastic matter," *Proc. London Math. Soc.*, **20**, 225–234.

[25] H. Lamb (1889), "On the flexure of an elastic plate (Appendix)," *Proc. London Math. Soc.*, **21**, 70–90.

[26] H. Lamb (1917), "On waves in an elastic plate," *Proc. R. Soc.*, **A93**, 114–128.

[27] R. D. Mindlin (1960), "Waves and vibrations in isotropic, elastic plates," in: *Structural Mechanics*, J. N.Goodier and N. Hoff, eds., Pergammon Press, New York, 199–232.

[28] L. P. Solie and B. A. Auld (1973), "Elastic waves in free anisotropic plates," *J. Acoust. Soc. Am.*, **54**(1), 50–65.

[29] S. K. Datta, A. H. Shah, R. L. Bratton and T. Chakraborty (1988), "Wave propagation in laminated composite plates," *J. Acoust. Soc. Am.*, **83**(6), 2020–2026.

[30] A. H. Nayfeh (1991), "The general problem of elastic wave propagation in multilayered anisotropic media," *J. Acoust. Soc. Am.*, **89**(4), 1521–1531.

[31] B. A. Auld (1973), *Acoustic Fields And Waves in Solids*, John Wiley & Sons, New York.

[32] J. D. Achenbach (1984), *Wave Propagation in Elastic Solids*, North-Holland Press, New York.

[33] J. L. Rose (1999), *Ultrasonic Waves in Solid Media*, Cambridge University Press, New York.

[34] A. Safaeinili, O. I. Lobkis, and D. E. Chimenti (1996), "Quantitative materials characterization using air-coupled leaky Lamb waves," *Ultrasonics*, **34**(2–5), 393–396.

[35] M. Castaings and P. Cawley (1996), "The generation, propagation, and detection of Lamb waves in plates using air-coupled ultrasonic transducers," *J. Acoust. Soc. Am.*, **100**(5), 3070–3077.

[36] J. L. Rose (1996), "An ultrasonic comb transducer for smart materials," *Proc. SPIE*, **3321**, 636–643.

[37] S. P. Pelts, D. Jiao and J. L. Rose, "A comb transducer for guided wave generation and mode selection," *IEEE Ultrasonics Symposium*, 857–860 (1996).

[38] K. Fehr (1995), *Wireless Digital Communications: Modulation and Spread Spectrum Applications*, Prentice-Hall, New Jesery.

[39] R. S. C. Monkhouse, P. D. Wilcox, and P. Cawley (1997), "Flexible interdigital PVDF transducers for the generation of Lamb waves in structures," *Ultrasonics*, **35**(7), 489–498.

[40] M. J. Vellekoop (1998), "Acoustic wave sensors and their technology," *Ultrasonics*, **36**, 7–14.

[41] H. P. Schwarz (1987), "Development of a divided-ring array for three-dimensional beam steering in ultrasonic nondestructive testing: theoretical and experimental results of a prototype," *Mat. Eval.*, **45**, 951–957.

[42] B. D. Steinberg (1976), *Principles of Aperture and Array System Design*, John Wiley & Sons, New York.

[43] D. K. Lemon and G. J. Posakony (1980), "Linear array technology in NDE applications," *Mat. Eval.*, **38**, 34–37.

[44] D. H. Turnbull and S. F. Foster (1991), "Beam steering with pulsed two-dimensional transducer arrays," *IEEE Trans. Ultrasonics, Ferroelectrics, and Frequency Control*, **38**(4), 320–333.

[45] D. H. Turnbull and S. F. Foster (1992), "Fabrication and characterization of transducer elements in two-dimensional arrays for medical ultrasound imaging," *IEEE Trans. Ultrasonics, Ferroelectrics, and Frequency Control*, **39**, 464–475.

[46] G. R. Lockwood, P.-C. Li, M. O'Donnell, and F. S. Foster (1996), "Optimizing the radiation pattern of sparse periodic linear arrays," *IEEE Trans. Ultrasonics, Ferroelectrics, and Frequency Control*, **43**(1), 7–14.

[47] G. R. Lockwood and F. S. Foster (1996), "Optimizing the radiation pattern of sparse periodic two-dimensional arrays," *IEEE Trans. Ultrasonics, Ferroelectrics, and Frequency Control*, **43**(1), 15–19.

[48] Y. Shi (1998), *Modeling of Acoustic Waves for Linear Phased Arrays*, Master of Science thesis, Massacusetts Institute of Technology.

[49] S. C. Wooh and Y. Shi (1998), "Influence of phased array element size on beam steering behavior," *Ultrasonics*, **36**, 737–749.

[50] S. C. Wooh and Y. Shi (1998), "Optimum beam steering of linear phased arrays," *Wave Motion*, **29**(3), 245–265.

[51] S. C. Wooh and Y. Shi (1999), "A simulation study of the beam steering characteristics for linear phased arrays," *J. Nondestr. Eval.*, **18**(2), 39–57.

[52] S. C. Wooh and Y. Shi (1999), "Three-dimensional beam directivity of phase-steered ultrasound," *J. Acoust. Soc. Am.*, **105**(6), 3275–3282.

[53] L . Azar, Y. Shi, and S. C. Wooh (2000), "Beam focusing behavior of linear phased arrays," *NDT&E Int.*, **33**(3), 189–198.

[54] A. McNab and I. Stumpf (1986), "Monolithic phased array for the transmission of ultrasound in NDT ultrasonics," *Ultrasonics*, **24**, 148–155.

[55] A. McNab and M. J. Campbell (1987), "Ultrasonic phased arrays for nondestructive testing," *NDT&E Int.*, **(6)**, 333–337.

[56] M. Lethiecq, C. Pejot, M. Berson, P. Guillemet and A. Roncin (1994), "An ultrasonic array-based system for real-time inspection of carbon-epoxy composite plates," *NDT&E Int.*, **27**(6), 311–315.

[57] M. T. Buchanan and K. Hynynen (1994), "Design and experimental evaluation of an intracavity ultrasound phased array system for hyperthermia," *IEEE Trans. Biomedical Engineering*, **41**(12), 1178–1187.

[58] J. V. Hatfield, N. R. Scales, A. D. Armitage, P. J. Hicks, Q. X. Chen, and P. A. Payne (1994), "An integrated multi-element array transducer for ultrasound imaging," *Sensors and Actuators*, **A(41–42)**, 167–173.

[59] N. R. Scales, P. J. Hicks, A. D. Armitage, P. A. Payne, Q. X. Chen and J. V. Hatfield (1994), "A programmable multi-channel CMOS pulser chip to drive ultrasonic array transducers," *IEEE Journal of Solid-State Circuits*, **29**(8), 992–994.

[60] A. D. Armitage, N. R. Scales, P. J. Hicks, P. A. Payne and Q. X. Chen (1995), "An integrated array transducer receiver for ultrasound imaging," *Sensors and Actuators A*, **46–47**, 542–546.

[61] B. Beardsley, M. Peterson, and J. D. Achenbach (1995), "A simple scheme for self-focusing of an array," *J. Nondestr. Eval.*, **14**(4), 169–179.

[62] A. Lovejoy, P. Pedrick, A. Doran, T. A. Delchar, J. A. Mills, and A. Stamm (1995), "A novel 8-bit ultrasound phased-array controller for hyperthermia applications," *Ultrasonics*, **33**(1), 69–73.

[63] A. C. Clay (1998), *Development and Experimental Characterization of Ultrasonic Phased Arrays for Nondestructive Evaluation*, Master of Science thesis, Massacusetts Institute of Technology.

[64] S. C. Wooh and Y. Shi (2001), "Synthetic phase tuning of guided waves," *IEEE Trans. Ultrasonics, Ferroeletrics and Frequency Control*, **48**(1), 209–223.

[65] A. N. Ceranoglu and Y. H. Pao (1981), "Propagation of elastic pulses and acoustic emission in a plate, Part I. Theory, Part II. Epicentral respnose, Part III. General responses," *ASME J. Appl. Mech.*, **48**, 125–147.

[66] N. Vasudevan and A. K. Mal (1985), "Response of an elastic plate to localized transient sources," *ASME J. Appl. Mech.*, **52**, 356–362.

[67] D. Guo and A. Mal (1998), "Rapid calculation of Lamb waves in plates due to localized sources," *Rev. Progr. Quant. Nondestr. Eval.*, **17**, 485–492.

[68] G. S. Kino (1987), *Acoustic Waves: Devices, Imaging, and Analog Signal Processing*, Prentice-Hall, Englewood Cliffs, New Jersey.

[69] A. Cermal Eringen and Erdoğan S. Şububi (1975), *Elastodynamics*, Academic Press, New York.

[70] J. J. Ditri and J. L. Rose (1994), "Excitation of guided waves in generally anisotropic layers using finite sources," *ASME J. Appl. Mech.*, **61**, 330–338.

[71] X. Jia (1997), "Modal analysis of Lamb wave generation in elastic plates by liquid wedge transducers," *J. Acoust. Soc. Am.*, **101**(2), 834–842.

[72] I. Núñez, R. K. Ing, C. Negreira and M. Fink (2000), "Transfer and Green functions based on modal analysis for Lamb waves generation," *J. Acoust. Soc. Am.*, **107**(5), 2370–2378.

[73] Z. Li and Y. H. Berthelot (2000), "Propagation of transient ultrsound in thick annular waveguides: modeling, experiments, and application," *NDT&E Int.*, **33**(4), 225–232.

[74] Y. Al-Nassar, S. K. Datta and A. H. Shah (1991), "Scattering of Lamb waves by a normal rectangular strip weldment," *Ultrasonics*, **29**, 125–132.

[75] F. Moser, L. J. Jacobs, and J. Qu (1999), "Modeling elastic wave propagation in waveguides with the finite element method," *NDT&E Int.*, **32**(4), 225–234.

[76] C. B. Scruby and L. E. Drain (1990), *Laser Ultrasonics Techniques and Applications*, Adam Hilger, Bristol.

[77] S. J. Davies, C. Edwards, G. S. Taylor and S. B.Palmer (1993), "Laser-generated ultrasound: its properties, mechanisms and multifarious applications," *Journal of Physics D: Applied Physics*, **26**(3), 329–348.

[78] R. D. Costley, Jr. and Y. H. Berthelot (1994), "Dispersion curve analysis of laser-generated Lamb waves," *Ultrasonics*, **32**(4), 249–253.

[79] S. G. Pierce, B. Culshaw, W. R. Philp, F. Lecuyer and R. Farlow (1997), "Broadband Lamb wave measurements in aluminum and carbon/glass fibre reinforced composite materials using non-contacting laser generation and detection," *Ultrasonics*, **35**(2), 105–114.

[80] M. Kley, C. Valle, L. .J. Jacobs, J. Qu and J. Jarzynski (1999), "Development of dispersion curves for two-layered cylinders using laser ultrasonics," *J. Acoust. Soc. Am.*, **106**(2), 582–588.

[81] R. J. Dewhurst, C. Edwards, A. D. W. Mckie, and S. B. Palmer (1987), "Estimation of the thickness of thin metal sheet using laser generated ultrasound," *Appl. Phys. Lett.*, **51**(14), 1066–1068.

[82] T.-T. Wu and Y.-H. Liu (1999), "On the measurement of anisotropic elastic constants of fiber-reinforced composite plate using ultrasonic bulk wave and laser generated Lamb wave," *Ultrasonics*, **37**(6), 405–412.

[83] M. A. Johnson, Y. H. Berthelot, P. H. Brodeur and L. A. Jacobs (1996), "Investigation of laser generation of Lamb waves in copy paper," *Ultrasonics*, **34**, 703–710.

[84] C. B. Scruby, R. J. Dewhurst, D. A. Hutchins, and S. B. Palmer (1980), "Quantitative studies of thermally generated elastic waves in laser-irradiated metals," *J. Appl. Phys.*, **51**(12), 6210–6216.

[85] D. A. Hutchins, R. J. Dewhurst, and S. B. Palmer (1981), "Directivity patterns of laser-generated ultrasound in aluminum," *J. Acoust. Soc. Am.*, **70**(5), 1362–1369.

[86] A. Aindow, R. J. Dewhurst, D. A. Hutchins, and S. B. Palmer (1981), "Laser-generated ultrasonic pulses at free metal surfaces," *J. Acoust. Soc. Am.*, **69**(2), 449–455.

[87] S. N. Hopko and I. C. Ume (1999), "Laser generated ultrasound by material ablation using fiber optic delivery," *Ultrasonics*, **37**(1), 1–7.

[88] S. N. Hopko and I. C. Ume (1999), "Laser ultrasonics: simultaneous generation by means of thermoelastic and material ablation," *J. Nondestr. Eval.*, **18**(3), 91–98.

[89] L. R. F. Rose (1984), "Point-source representation for laser-generated ultrasound," *J. Acoust. Soc. Am.*, **75**(3), 723–732.

[90] L. F. Bresse and D. A. Hutchins (1989), "Transient generation by a wide thermoelastic source at a solid surface," *J. Appl. Phys.*, **65**(4), 1441–1446.

[91] L. F. Bresse and D. A. Hutchins (1989), "Transient generation of elastic waves in solids by a disk-shaped normal force source," *J. Acoust. Soc. Am.*, **86**(2), 810–817.

[92] A. Aharoni, K. M. Jassby, and M. Tur (1992), "The thermoelastic surface strip source for laser-generated ultrasound," *J. Acoust. Soc. Am.*, **92**, 3249–3258.

[93] Y. H. Berthelot (1994), "Half-order derivative formulation for the analysis of laser-generated Rayleigh waves," *Ultrasonics*, **32**, 153–154.

[94] P. A. Doyle and C. M. Scala (1996), "Near-field ultrasonic Rayleigh waves from a laser line source," *Ultrasonics*, **34**, 1–8.

[95] J. R. Bernstein and J. B. Spicer (2000), "Line source representation for laser-generated ultrasonics in aluminum," *J. Acoust. Soc. Am.*, **107**(3), 1352–1357.

[96] D. Royer and C. Chenu (2000), "Experimental and theoretical waveforms of Rayleigh waves generated by a thermoelastic laser line source," *Ultrasonics*, **38**, 891–895.

[97] D. Royer (2001), "Mixed matrix formulation for the analysis of laser-generated acoustic waves by a thermoelastic line source," *Ultrasonics*, **39**, 345–354.

[98] J. B. Spicer, A. D. W. Mckie, and J. W. Wagner (1990), "Quantitative theory for lase ultrasonic waves in a thin plate," *Appl. Phys. Lett.*, **57**(18), 1882–1884.

[99] J. Cheng, L. Wu and S. Zhang (1994), "Thermoelastic response of pulsed photothermal deformation of thin plates," *J. Appl. Phys.*, **76**(2), 716–722.

[100] J. Cheng, S. Zhang and L. Wu (1995), "Excitations of thermoelastic waves in plates by a pulsed laser," *Applied Physics A: Materials Science and Processing*, **61**(3), 311–319.

[101] J. Cheng and Y. Berthelot (1996), "Theory of laser-generated transient Lamb waves in orthotropic plates," *Journal of Physics D: Applied Physics*, **29**, 1857–1867.

[102] J. Cheng and S. Zhang (1999), "Quantitative theory for laser-generated Lamb waves in orthotropic thin plates," *Appl. Phys. Lett.*, **74**(14), 2087–2089.

[103] J. Cheng, T. Wang and S. Zhang (1999), "Normal mode expansion method for laser-generated Lamb waves in orthotropic thin plates," *Applied Physics B: Lasers & Optics*, **74**(14), 57–63.

[104] L. E. Goodman (1952), "Circular-crested vibrations of an elastic solid bounded by two parallel planes," in: *Proc. 1st Natn. Congr. Appl. Mech.*, ASME, New York, 65–73.

[105] R. L. Weaver and Y. H. Pao (1982), "Axisymmetric elastic waves excited by a point source in a plate," *ASME J. Appl. Mech.*, **49**, 821–836.

[106] S. C. Wooh and I. M. Daniel (1991), "Mechanical characterization of unidirectional composite by ultrasonic methods," *J. Acoust. Soc. Am.*, **90**(6), 3248–3253.

[107] Y. C. Chu, A. D. Degtyar, and S. I. Rokhlin (1994), "On determination of orthotropic material moduli from ultrasonic velocity data in nonsymmetry planes," *J. Acoust. Soc. Am.*, **95**(6), 3191–3203.

[108] A. Minachi, D. K. Hsu, and R. B. Thompson (1994), "Single-sided determination of elastic constants of thick composites using acoustoultrasonic technique," *J. Acoust. Soc. Am.*, **96**(1), 353–362.

[109] C. Aristégui and S. Baste (1997), "Optimal determination of the material symmetry axes and associated elasticity tensor from ultrasonic velocity data," *J. Acoust. Soc. Am.*, **102**(3), 1503–1521.

[110] J.-F. Chai and T.-T. Wu (1994), "Determination of anisotropic constants using laser-generated surface waves," *J. Acoust. Soc. Am.*, **95**(6), 3232–3241.

[111] W. R. Rose, S. I. Rokhlin, and I. Adler (1987), "Evaluation of anisotropic properties of graphite-epoxy composites using Lamb waves," *Rev. Progr. Quant. Nondestr. Eval.*, **6**, 1111–1118.

[112] A. H. Nayfeh and D. E. Chimenti (1989), "Free wave propagation in plates of anisotropic media," *J. Appl. Mech.*, **56**, 881–886.

[113] S. I. Rokhlin, and D. E. Chimenti (1990), "Reconstruction of elastic constants from ultrasonic reflectivity data in a fluid coupled composite plate," *Rev. Progr. Quant. Nondestr. Eval.*, **9**, 1411–1418.

[114] M. R.Karim, A. K. Mal, and Y. Bar-Cohen (1990), "Determination of the elastic constants of composites through inversion of leaky Lamb wave data," *Rev. Progr. Quant. Nondestr. Eval.*, **9**, 109–116.

[115] V. Dayal and V. K.Kinra (1991), "Leaky Lamb waves in an anisotropic plate. II: Nondestructive evaluation of matrix cracks in fiber-reinforced composites," *J. Acoust. Soc. Am.*, **89**(4), 1590–1598.

[116] N. Guo and P. Cawley (1993), "The interaction of Lamb waves with delaminations in composite laminates," *J. Acoust. Soc. Am.*, **94**(4), 2240–2246.

[117] C. C. Habeger, R. W. Mann and G. A. Baum (1979), "Ultrasonic plate waves in paper," *Ultrasonics*, **17**, 57–62.

[118] V. Dayal and V. K. Kinra (1989), "Leaky Lamb waves in an anisotropic plate. I: An exact solution and experiments," *J. Acoust. Soc. Am.*, **85**(6), 2268–2276.